Introduction to Astroparticle Physics

Exploring the Universe with multi-messenger astroparticle physics

cosmic rays, gamma rays, neutrinos, gravitational waves

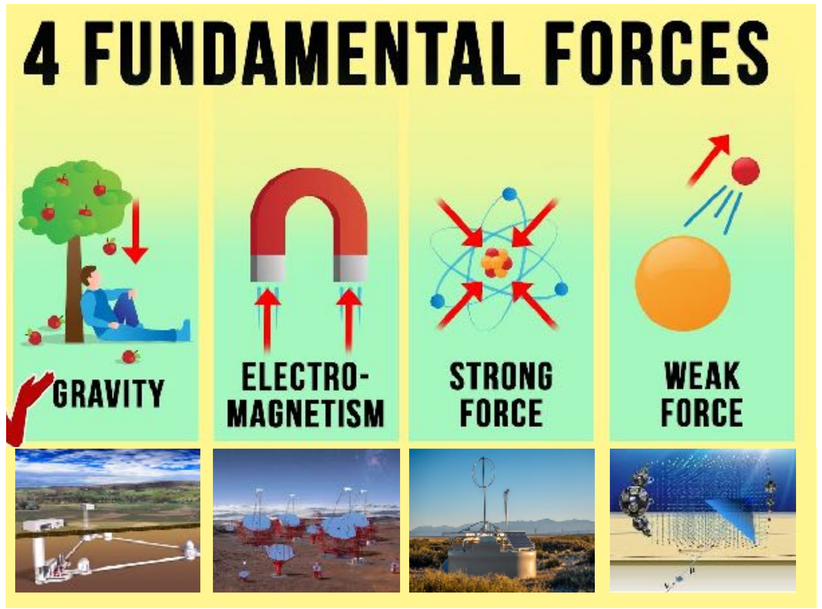

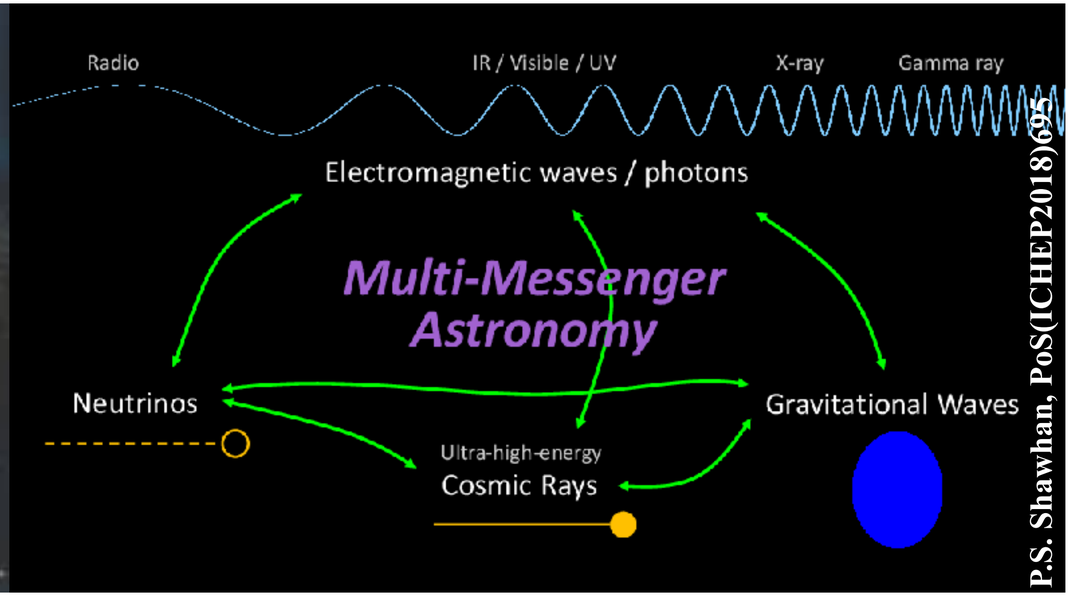

grav. waves gamma rays cosmic rays neutrinos

Jörg R. Hörandel
Radboud Universiteit Nijmegen - Vrije Universiteit Brussel - http://particle.astro.ru.nl

Multi-messenger astroparticle physics

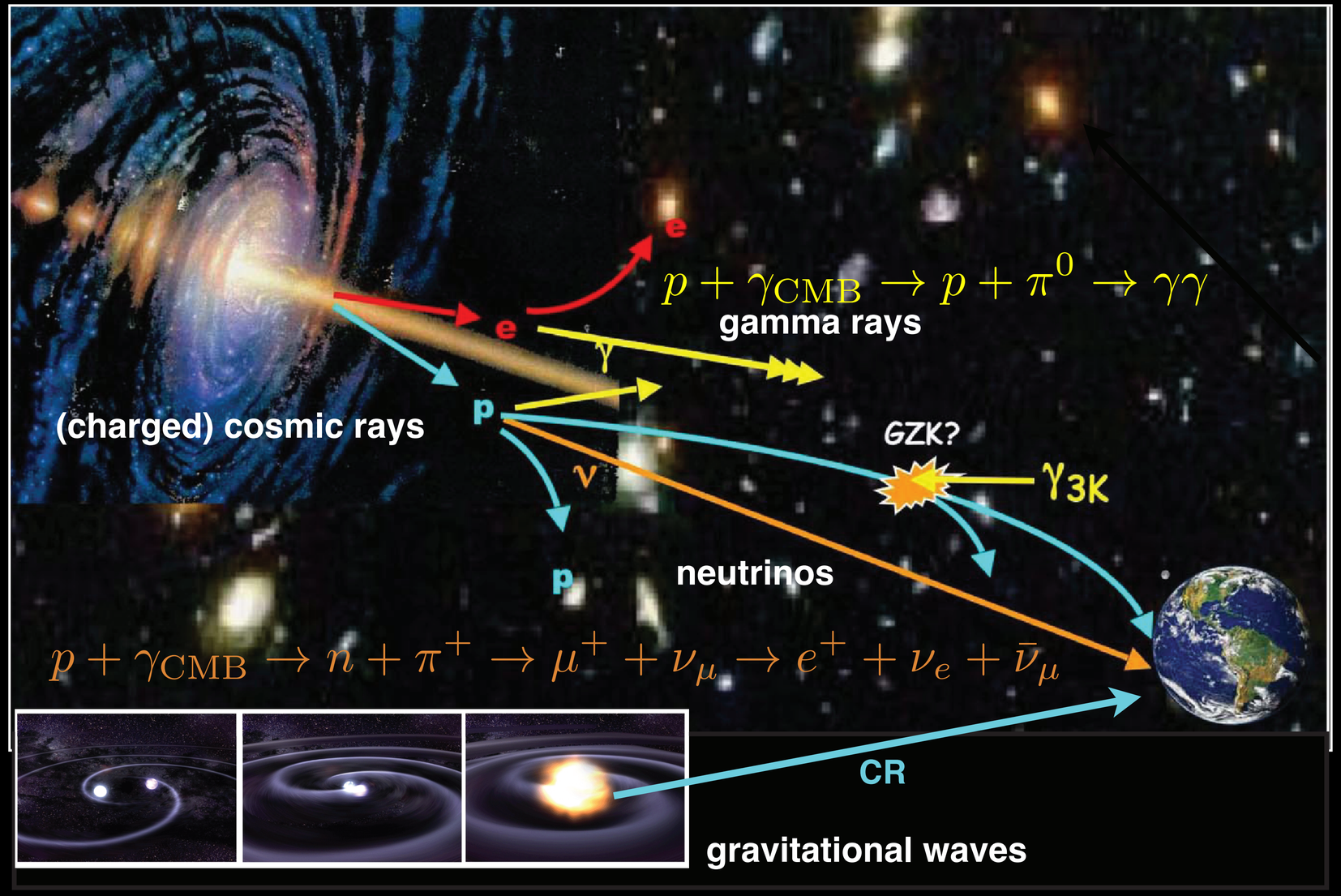

Cosmic rays

ionized atomic nuclei hitting the Earth from outer space

energy density

$$\rho_E = \frac{4\pi}{c} \int \frac{E}{\beta} \frac{dN}{dE} dE \approx 1 \ \frac{\text{eV}}{\text{cm}^3}$$

for comparison:

$$\rho_B = \frac{B^2}{2\mu_0} \approx 0.25 \ \text{eV/cm}^3$$

$$\rho_{SL} \approx 0.3 \ \text{eV/cm}^3$$

$$\rho_{IR} \approx 0.4 \ \text{eV/cm}^3$$

$$\rho_{3K} \approx 0.25 \ \text{eV/cm}^3$$

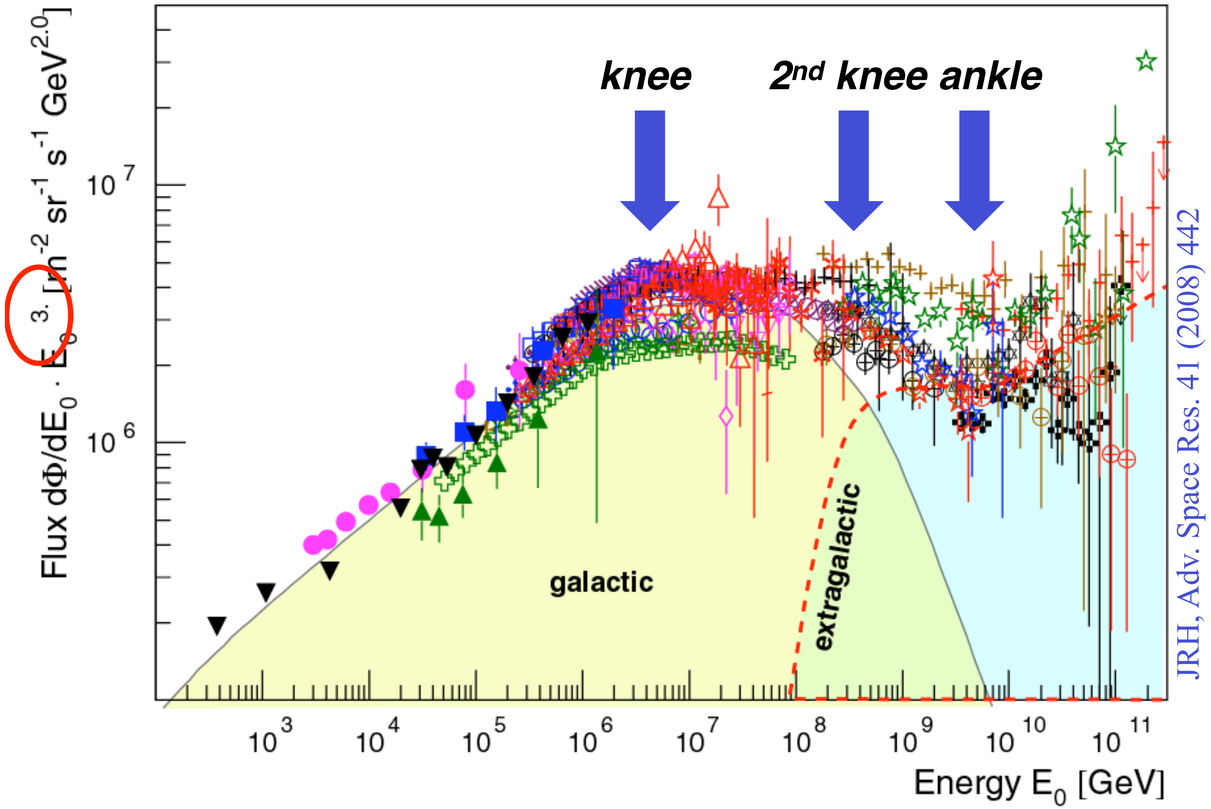

Cosmic rays

Solar flares

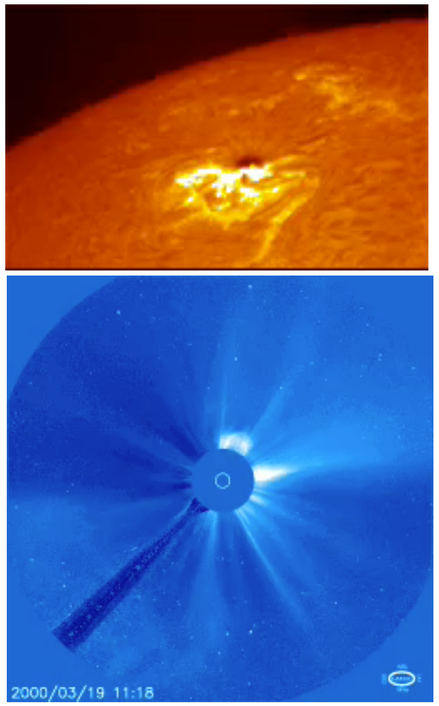

solar particles

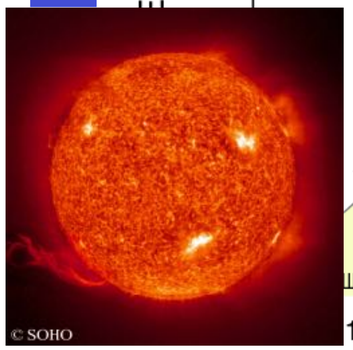

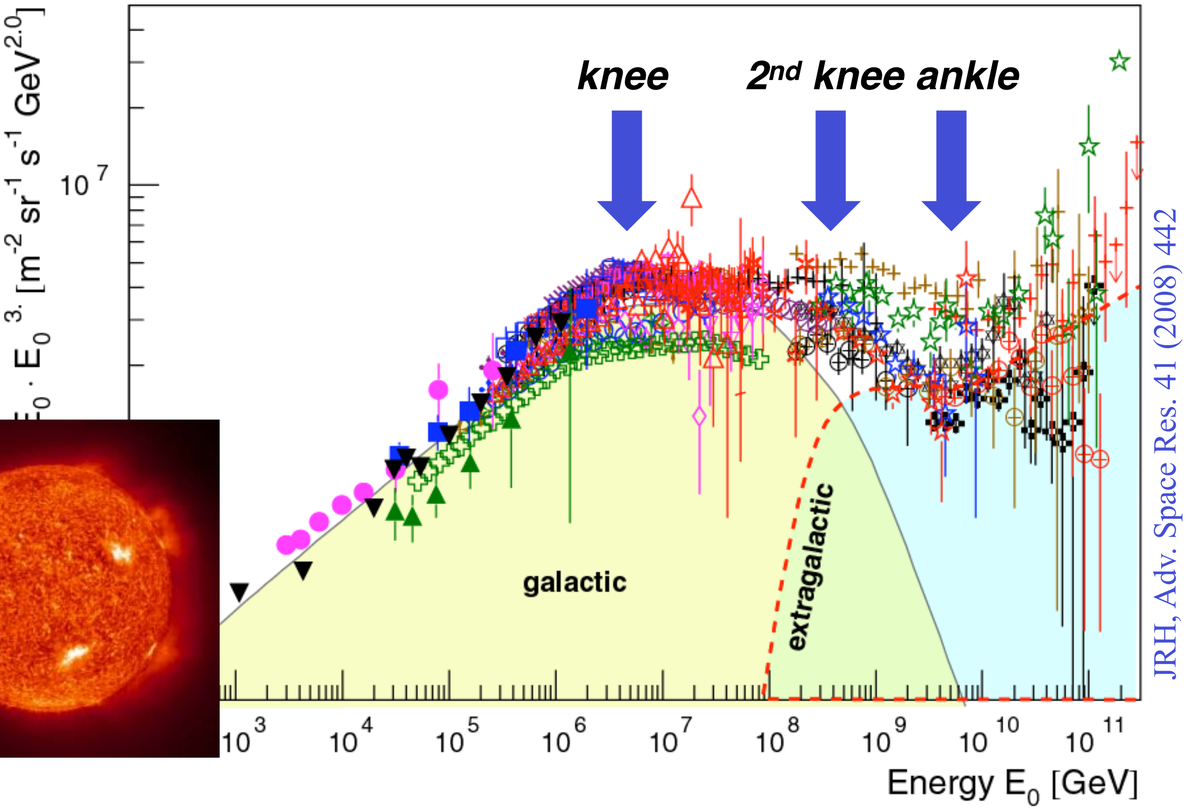

JRH, Adv. Space Res. 41 (2008) 442

Cosmic rays

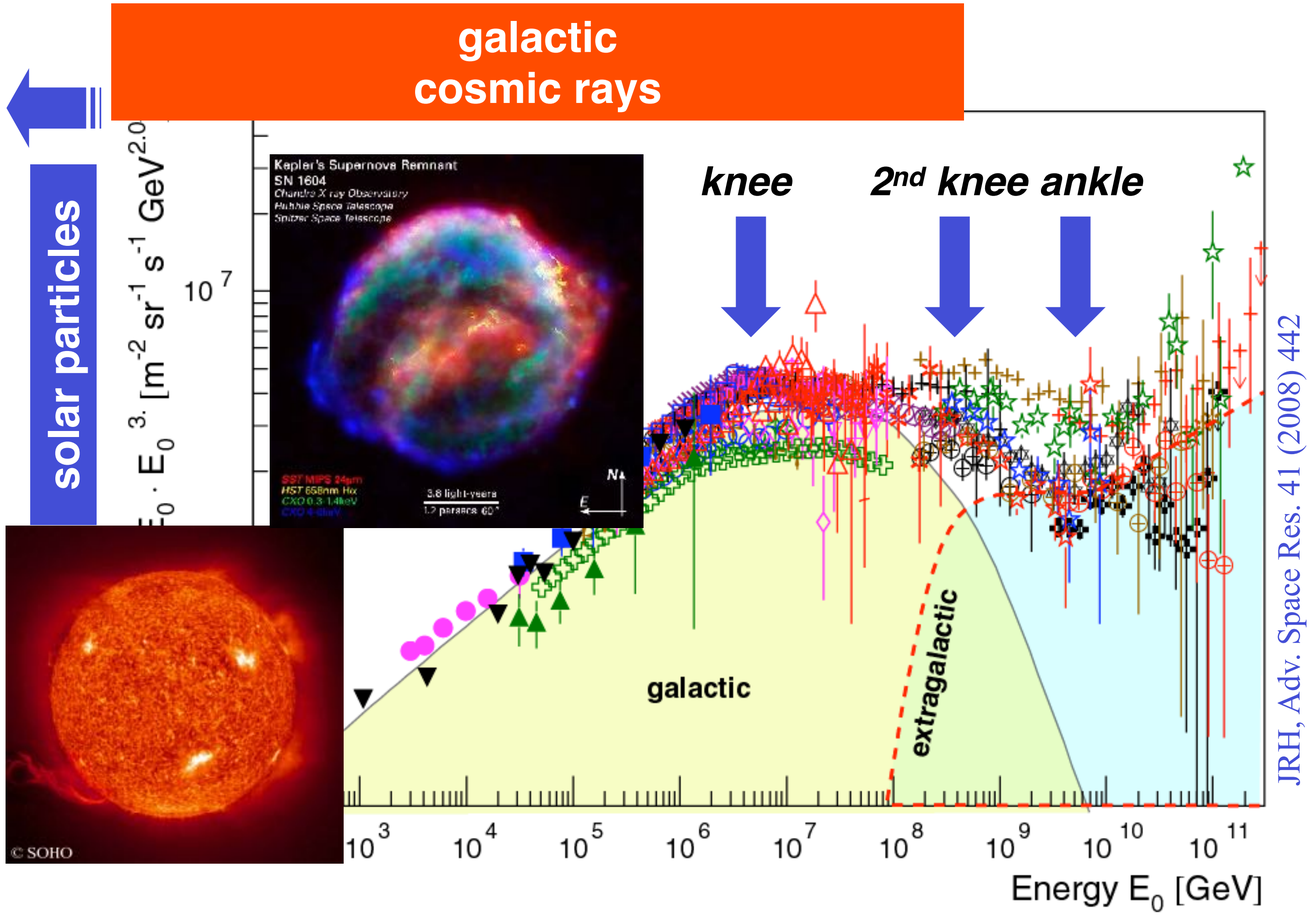
galactic
cosmic rays
solar particles
knee
2nd knee ankle
galactic
extragalactic
Kepler's Supernova Remnant
SN 1604
Chandra X-ray Observatory
Hubble Space Telescope
Spitzer Space Telescope
© SOHO
JRH, Adv. Space Res. 41 (2008) 442
Energy E0 [GeV]

Cosmic rays

Radius of particle in magnetic field

$$r = \frac{p}{ZeB} \qquad r[pc] = 1.08 * \frac{E\ [PeV]}{B\ [\mu G]}$$

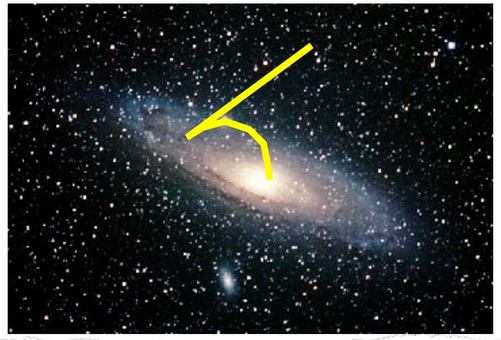

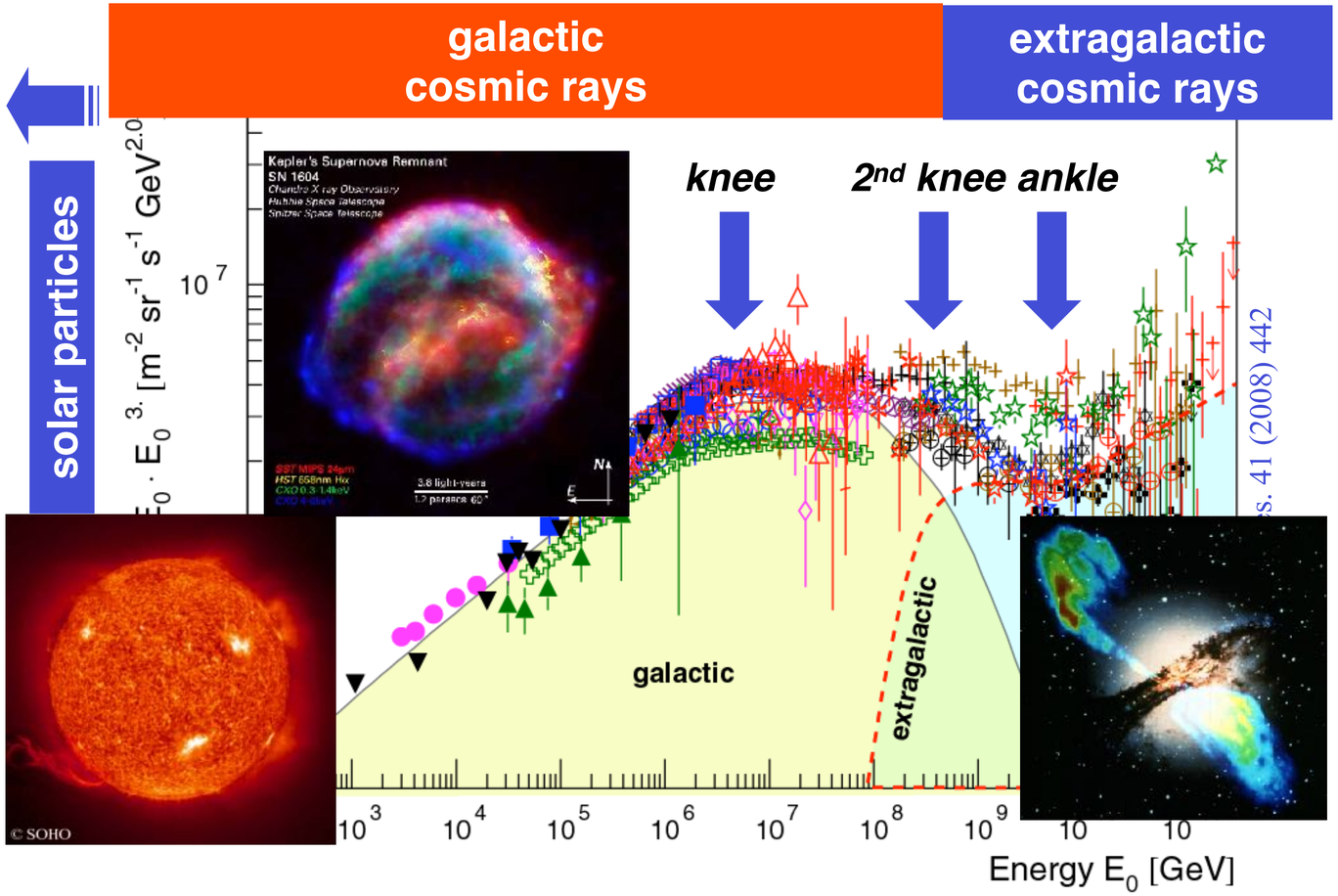

Discovery of Radioactivity

Henri Becquerel

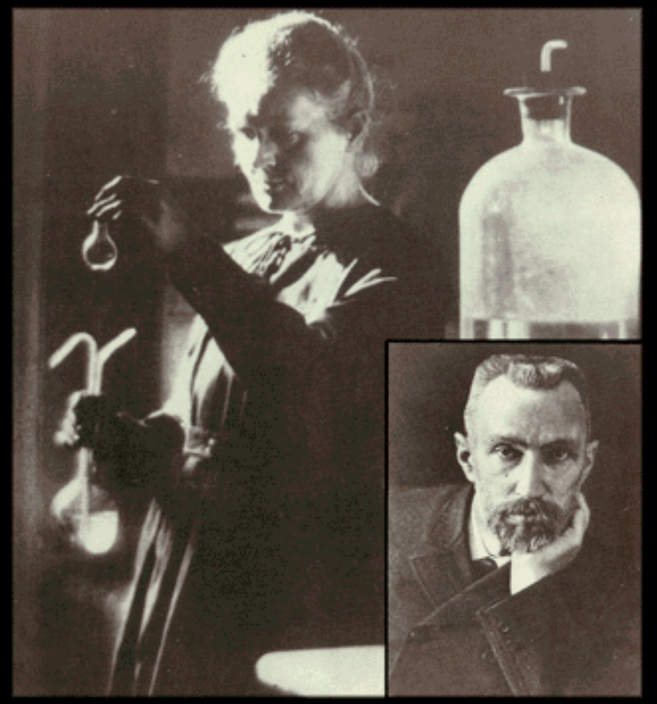

Marie & Pierre Curie

Nobel Prize 1903

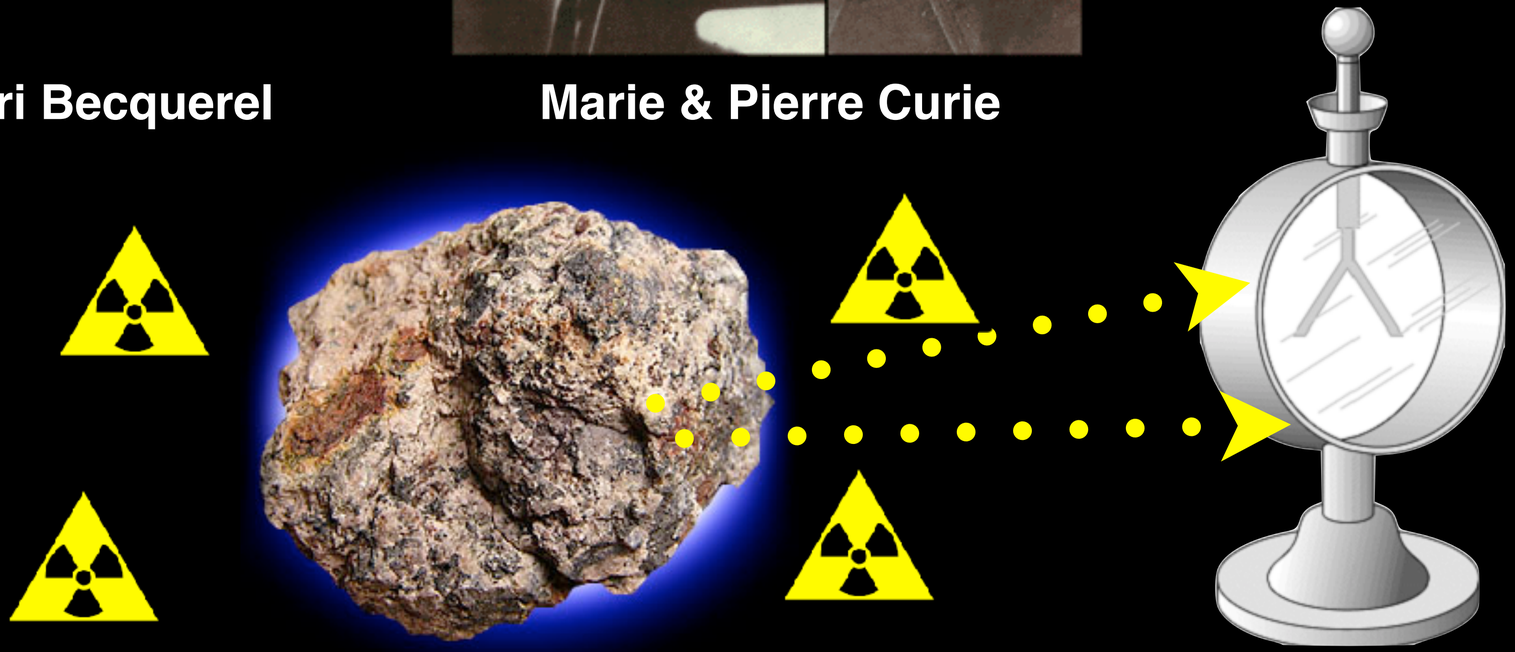

Physikalische Zeitschrift. 10. Jahrgang. No. 8. (1909) 251

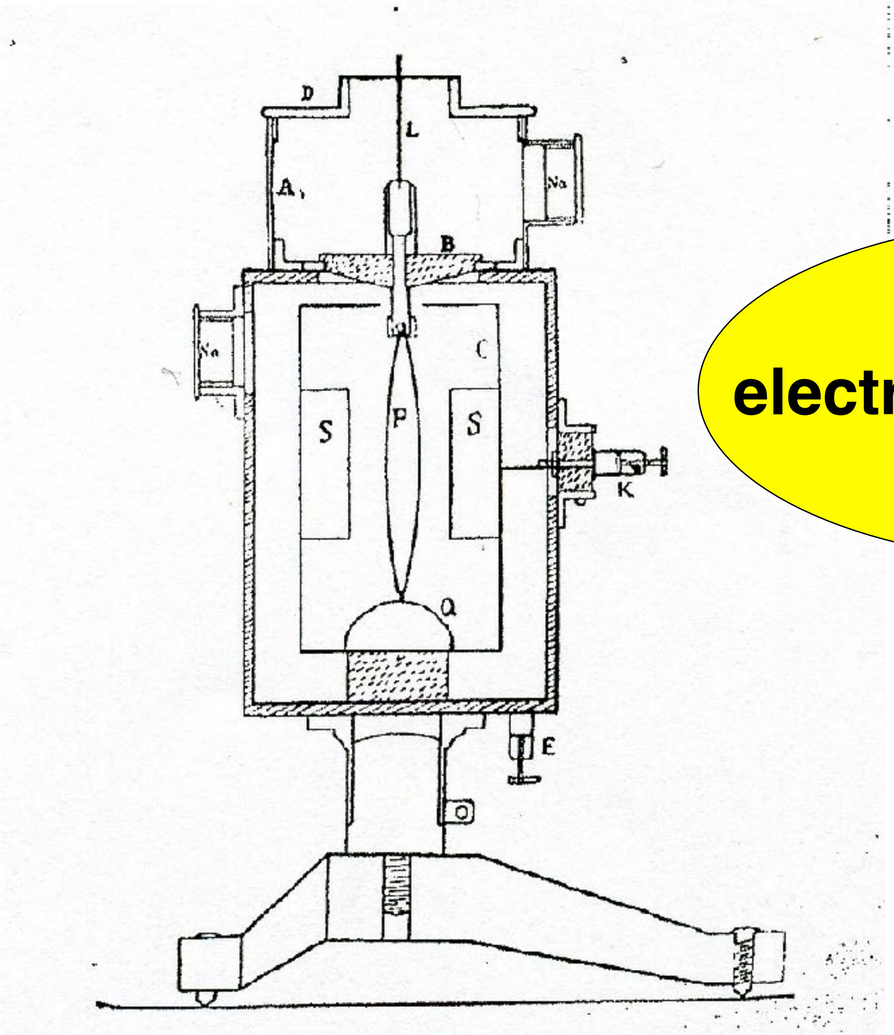

Ein neues Elektrometer für statische Ladungen.

Dritte Mitteilung [1]).

Von Th. Wulf.

Mitteilung enthält einige
ner beschriebenen Appa-
öhung seiner Transport-

a new electrometer for static charges

on the origin of gamma radiation in the atmosphere

Über den Ursprung der in der Atmosphäre vorhandenen γ-Strahlung.

Von Th. Wulf.

Tabelle I.

Strahlung der Wände von Gebäuden.

Ort	Material	Alter	Strahlung Ionen pro ccm u. Sekunde
Abtei Maria Laach bei Andernach a. Rh. . .	Vulkanisch Tuff	50 Jahre	13,7
Valkenburg, Colleg, Holland-L.	Ziegelsteine	15 „	5,7
Löwen, Colleg, Belgien	Ziegelsteine	—	8,0
Namur, Colleg N.D. de la paix, Belgien . . .	Ziegelsteine	ca. 100	3,7
Wynandsrade Kasteel, Holland	Ziegelsteine	200 Jahre	0,0

Nur in dem alten holländischen Kasteel Wynandsrade, vor fast 200 Jahren aus Ziegelsteinen erbaut, zeigte sich kein Unterschied in der Strahlung im Zimmer und im Freien. — Am stärksten war die Strahlung in Maria Laach in einem

Man kann den Inhalt dieser Arbeit kurz so zusammenfassen. Es wird über Versuche berichtet, welche beweisen, daß an dem Beobachtungsort die durchdringende Strahlung von primär radioaktiven Substanzen verursacht wird, welche in den obersten Erdschichten liegen, bis etwa 1 m unter der Oberfläche.

Wenn ein Teil der Strahlung aus der Atmosphäre stammt, so ist er doch so klein, daß er sich mit den gebrauchten Mitteln nicht nachweisen ließ.

Die zeitlichen S… …ränkungen in der γ-Strahlun… …ieben d… …rde …ie …1.,

N… …09.)

the radiation originates from the soil maybe a small contribution from the atmosphere

~1910

Theodor Wulf

1909: Soddy & Russel: attenuation of gamma rays follows an exponential law

$$I = I_0 e^{-\mu L}$$

Discovery of Cosmic Rays
Viktor Franz Hess 7. August 1912

Early cosmic-ray work published in German

Jörg R. Hörandel

Citation: AIP Conf. Proc. **1516**, 52 (2013); doi: 10.1063/1.4792540

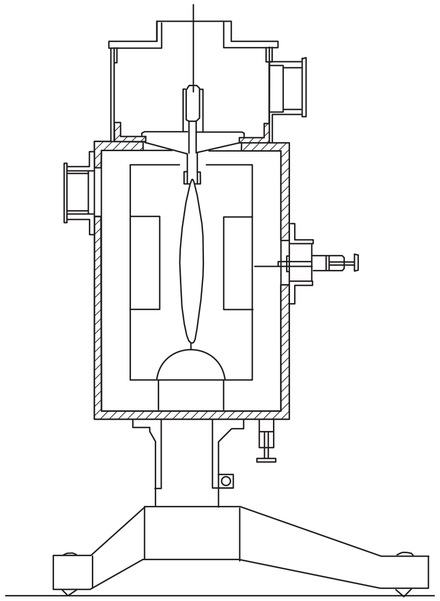

FIGURE 1. *Left*: Electrometer after Th. Wulf [5]. *Right*: Two grandsons of V.F. Hess revealing a plaque to commemorate the discovery of cosmic rays on August 7th, 2012, close to the presumed landing site of V.F. Hess in Pieskow close to Berlin. It reads: "To commemorate the discovery of cosmic rays. On 7 August 1912 landed the Austrian physicist Victor F. Hess with a hydrogen balloon close to Pieskow. On the journey from Lower-Bohemia he reached an altitude of 5300 m and he proved the existence of a penetrating, ionizing radiation from outer space. For the discovery of cosmic rays V.F. Hess has been awarded the Nobel Prize in Physics in 1936. The participants of the symposium '100 years cosmic rays', Bad Saarow-Pieskow, 7 August 2012".

Aeronautisches Gelände im Wiener Prater, vo
seine ersten Freiballon-Forschungsfahrten u
schichtliche Mu

Hess on

Route des Entdeckungsfluges der kosmischen Strahlung.

Aus der Abteilung für Geophysik, Meteorologie und Erdmagnetismus:

Viktor F. Hess (Wien), Über Beobachtungen der durchdringenden Strahlung bei sieben Freiballonfahrten.

on the observation of the penetrating radiation during 7 balloon campaigns

Im Vorjahre habe ich bereits Gelegenheit gehabt, zwei Ballonfahrten zur Erforschung der durchdringenden Strahlung zu unternehmen; über die erste Fahrt wurde

7. Fahrt (7. August 1912).

Ballon: „Böhmen" (1680 cbm Wasserstoff). Führer: Hauptmann W. Hoffory.
Meteorolog. Beobachter: E. Wolf. Luftelektr. Beobachter: V. F. Hess.

hydrogen!

altitude

intensity

		Mittlere Höhe		Beobachtete Strahlung					
				Apparat 1	Apparat 2	Apparat 3		Temp.	Relat. Feucht. Proz.
		absolut	relativ m	q_1	q_2	q_3	reduz. q_3		
1	15h 15—16h 15	156	0	17,3	12,9	—	—	—	—
2	16h 15—17h 15	156	0	15,9	11,0	18,4	18,4	1½ Tag vor dem Aufstiege (in Wien)	
3	17h 15—18h 15	156	0	15,8	11,2	17,5	17,5		
4		1700	1400	15,8	14,4			+6,4°	60
		2750	2500	17 3	1			+1,4°	41
		3850	3600	19,8	1			−6,8°	64
7		4800	4700	40,7	31,			−9,8°	40
		(4400-	5350)				—		
8	10h 45—11h 15	4400	4200	28,1	22,7	—	—	—	—
9	11h 15—11h 45	1300	1200	(9,7)	11,5	—	—	—	—
10	11h 45—12h 10	250	150	11,9	10,7	—	—	+16,0°	68
11	12h 25—13h 12	140	0	15,0	11,6	—	—	(nach der Landung in Pieskow, Brandenburg)	

wurde.

Elektrometers gesetzter Zinkstift von 20 cm

Aus der Abteilung für Geophysik, Meteorologie und Erdmagnetismus:

Viktor F. Hess (Wien), Über Beobachtungen der durchdringenden Strahlung bei sieben

radiation with high

V.F. Hess in 1936–37, on the occasion of Nobel prize.

Nobel Prize 1936

der Atmosphäre zurückzuführen.

Die Ergebnisse der vorliegenden Beobachtungen scheinen am ehesten durch die Annahme erklärt werden zu können, daß eine Strahlung von sehr hoher Durchdringungskraft von oben her in unsere Atmosphäre eindringt, und auch noch in deren untersten Schichten einen Teil der in geschlossenen Gefäßen beobachteten Ionisation hervorruft. Die Intensität dieser Strahlung scheint zeitlichen Schwankungen unterworfen zu sein, welche bei einstündigen Ablesungsintervallen noch erkennbar sind. Da ich im Ballon weder bei Nacht noch bei einer Sonnenfinsternis eine Verringerung der Strahlung fand, so kann man wohl kaum die Sonne als Ursache dieser hypothetischen Strahlung ansehen, wenigstens solange man nur an eine direkte γ-Strahlung mit geradliniger Fortpflanzung denkt.

Daß die Zunahme der Strahlung erst jenseits 3000 m so stark merklich wird, ist nicht

1931-34 A.H. Compton 12 expeditions → ~100 locations

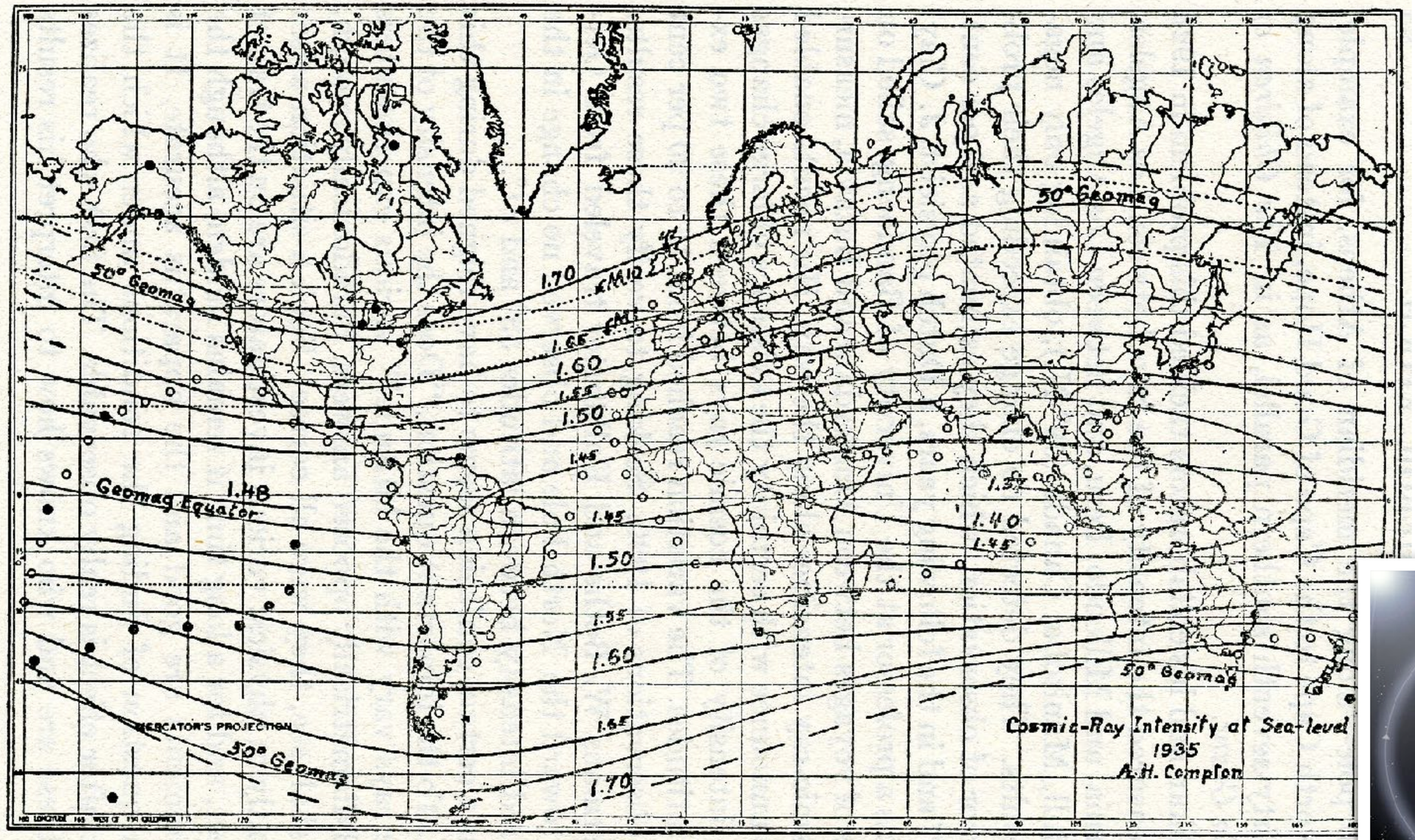

FIG. 6.—Compton's world map of isocosms. Note the parallelism of these lines of equal cosmic-ray intensity and the dot curves of geomagnetic latitude (50° N. and S.).

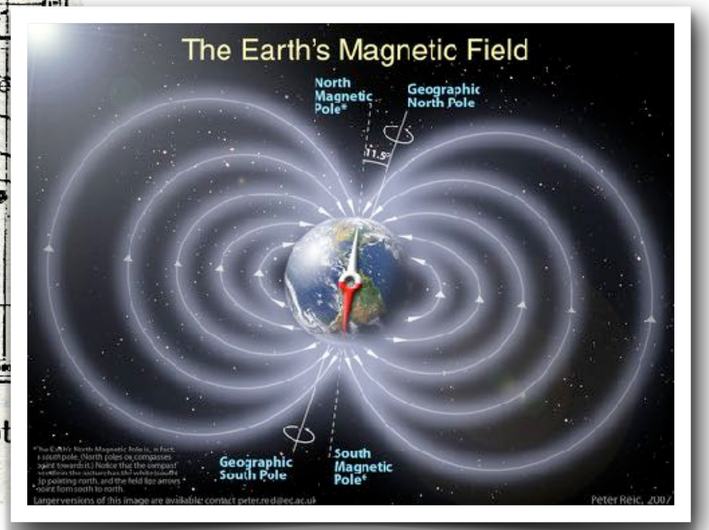

cosmic rays are charged particles

End 1940s plastic balloons

Fig. 1. Inflation of balloon of polyethylene just after dawn. The balloon has a total length of about 120 ft. and most of the fabric is on the ground. Such a balloon can in favourable conditions give level flight at about 90,000 ft. for many hours with a load of 40 kg.

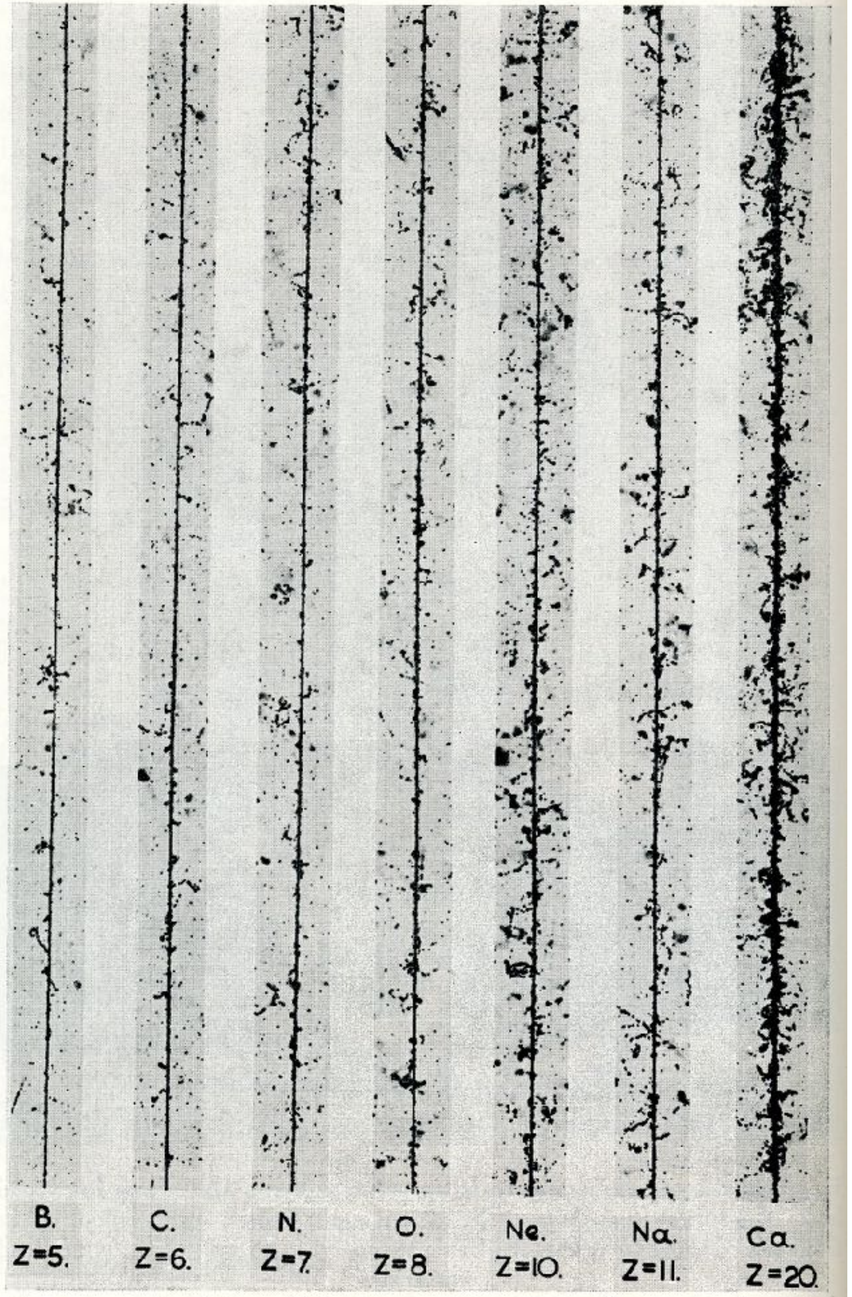

Fig. 2. Examples of the tracks in photographic emulsions of primary nuclei of the cosmic radiation moving at relativistic velocities.

1941 protons (M. Schein)

1948 heavy nuclei (Brandt & Peters)

Detectors for direct measurements of Cosmic Rays above the atmosphere

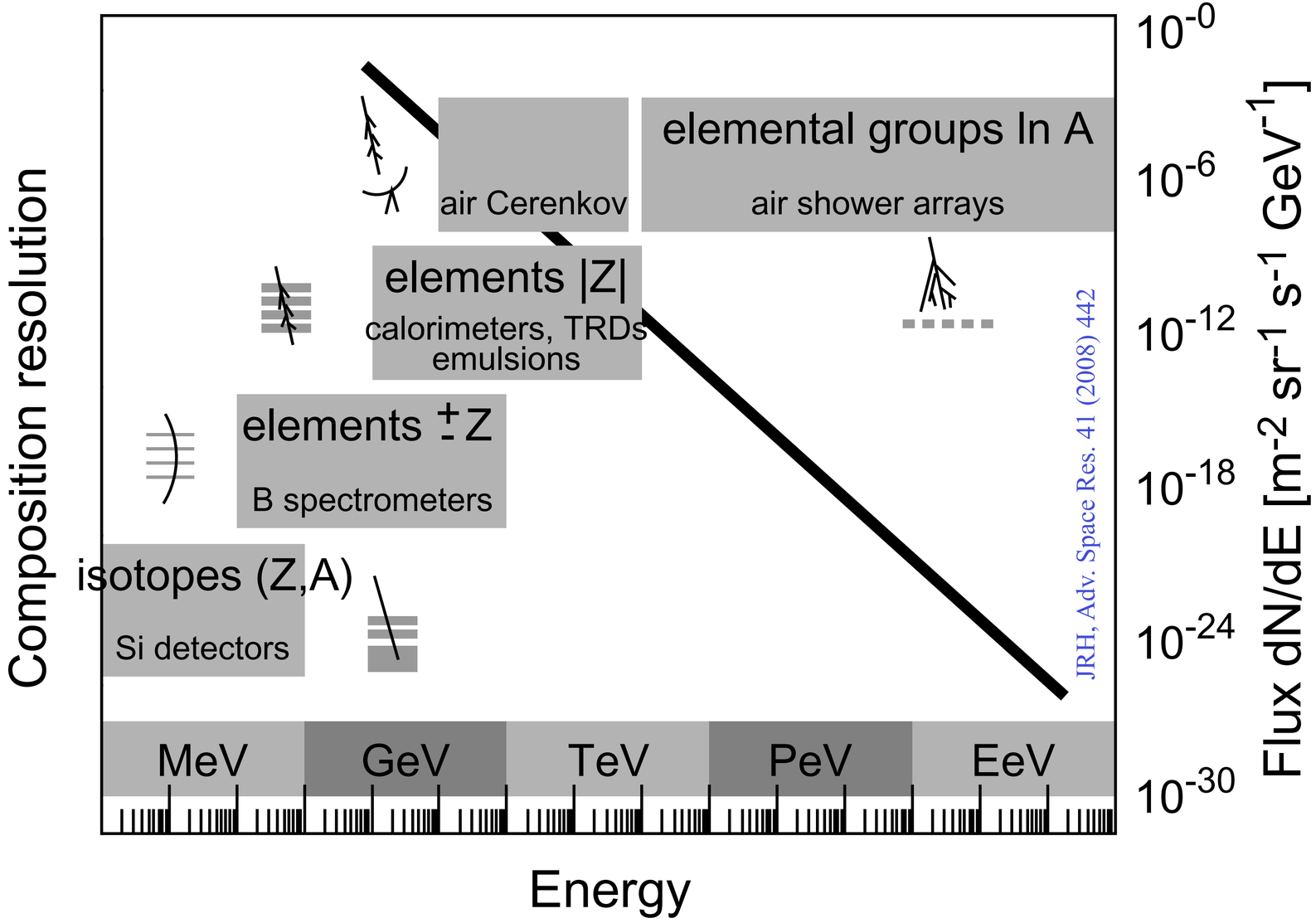

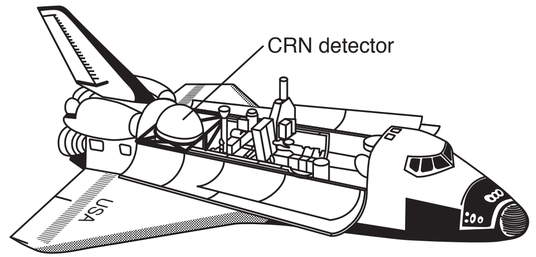

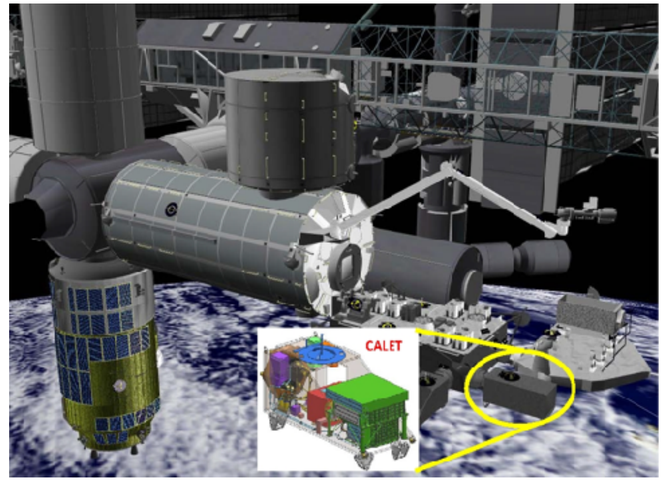

TRACER: Energy spectra for individual elements

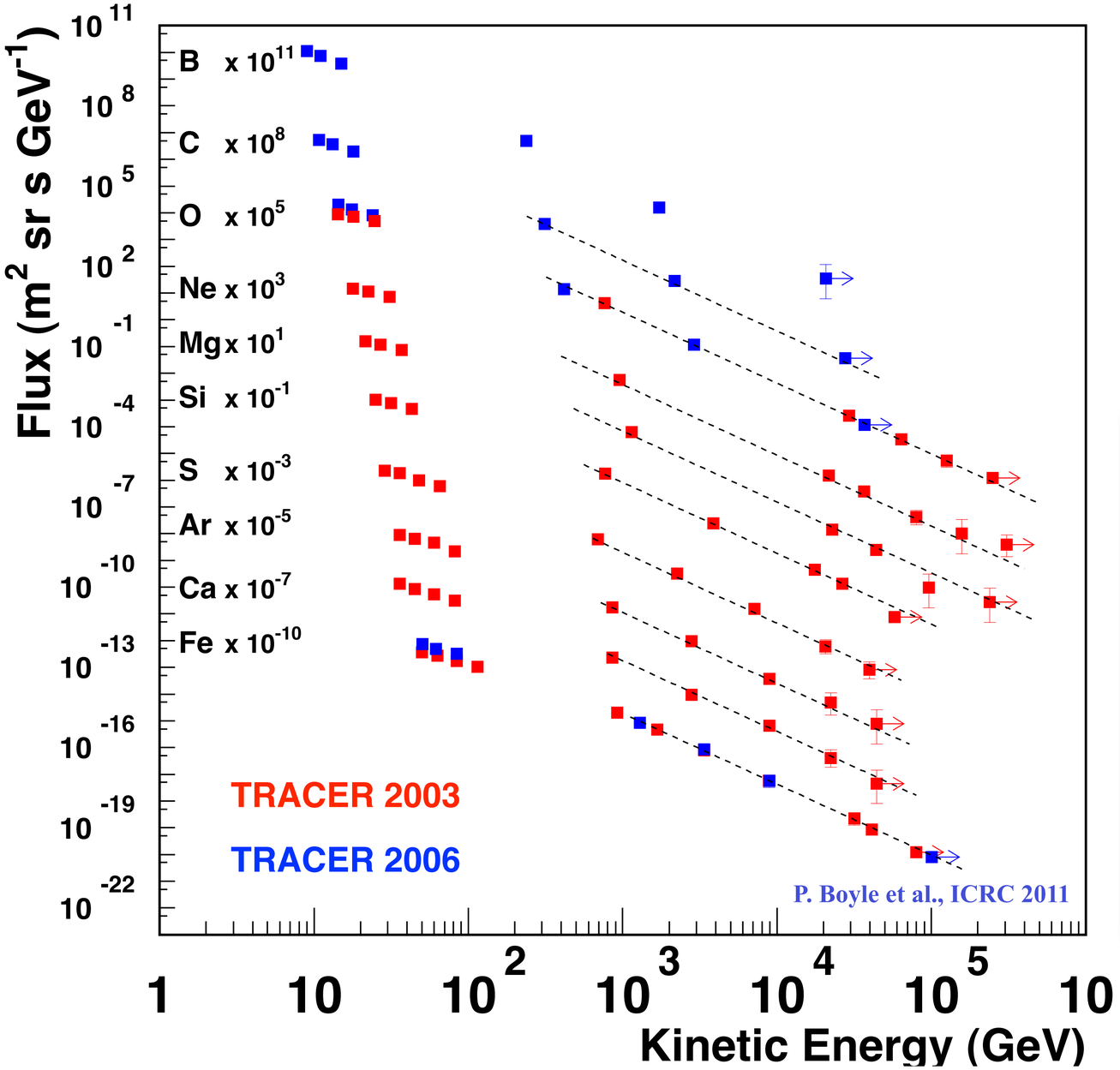

A. Obermeier et al., ApJ 752 (2012) 69

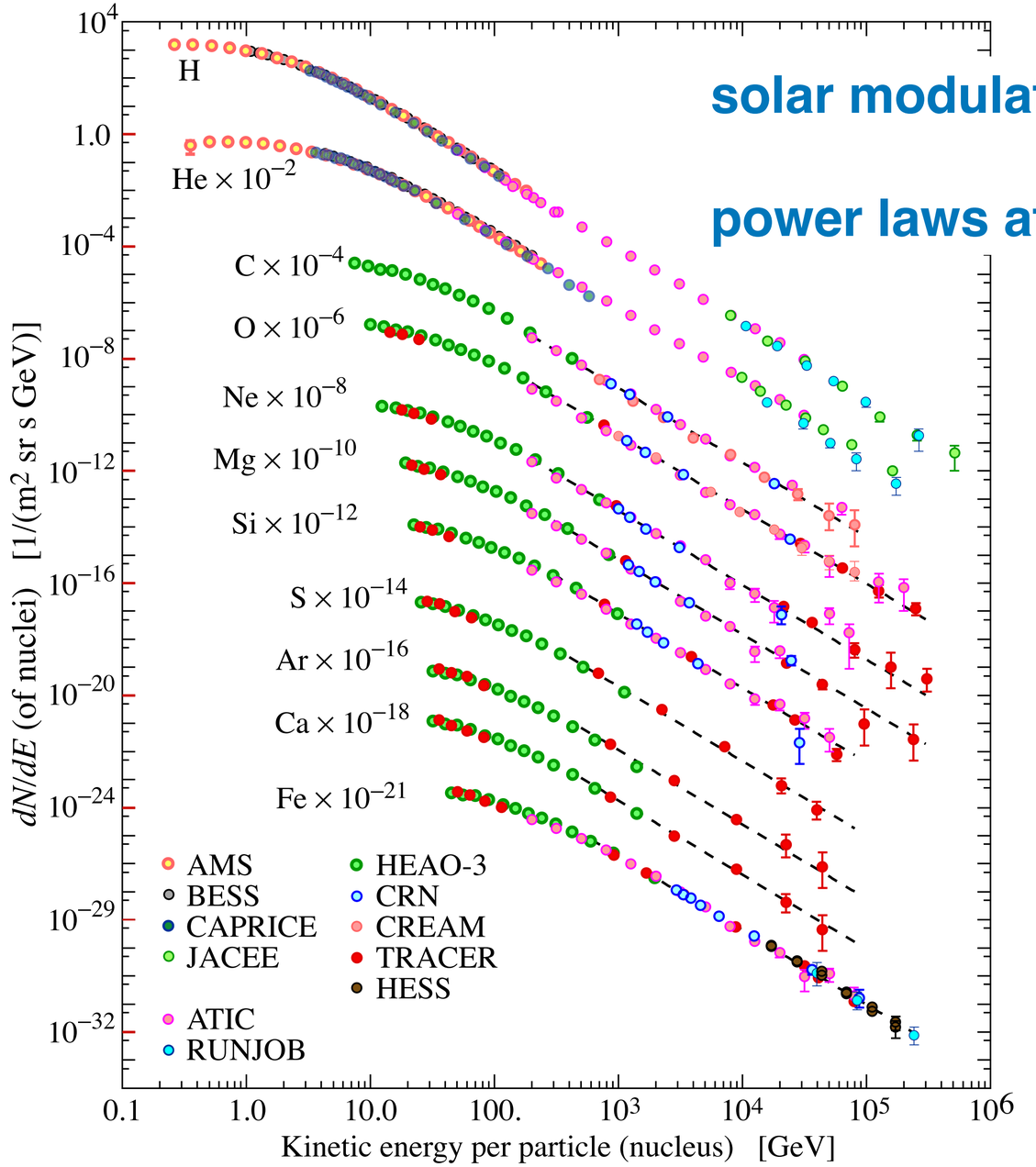

solar modulation at low energies

power laws at high energies

$$\frac{dN}{dE} \propto E^{\gamma}$$

Figure 24.1: Major components of the primary cosmic radiation from Refs. [1–12 The figure was created by P. Boyle and D. Muller. Color version at end of book.

Properties of Cosmic Rays E<10^{14} eV

most important properties:

$$\frac{dN}{dE} \propto E^{\gamma} \quad \gamma \approx -2.7$$

1. **energy spectra are power laws**
   --> non-thermal origin $\left(\frac{dN}{dE} \propto e^{-\kappa E}\right)$

2. **below ~10 GV energy spectra deviate from power laws**
   --> solar modulation, charged particles of extra-solar origin (galactic origin) drift against the solar wind towards Earth/solar system

   magnetic rigidity $R = \frac{p \cdot c}{Z \cdot e}$

3. **in <u>first approximation</u> all elements exhibit about the same slope**
   spectral index $\gamma \approx -2.7$

Galactic Cosmic Rays and the Heliosphere

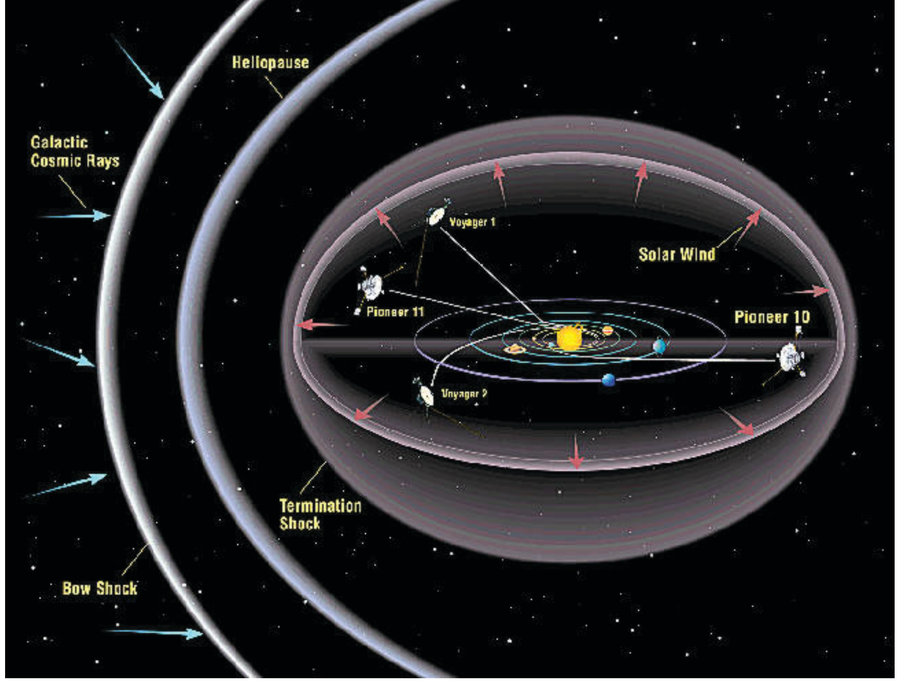

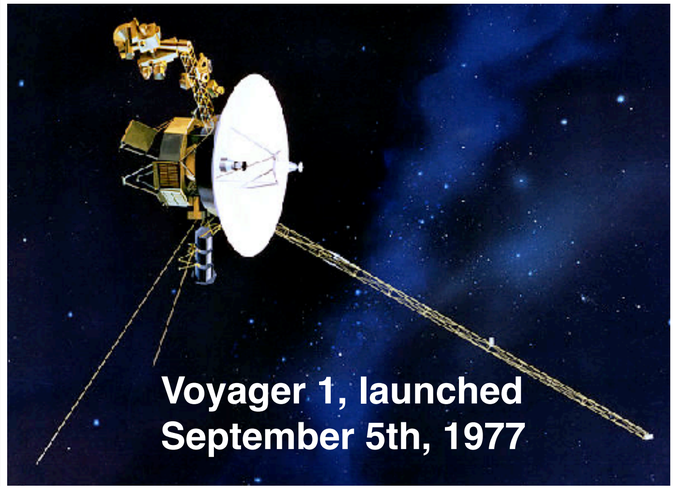

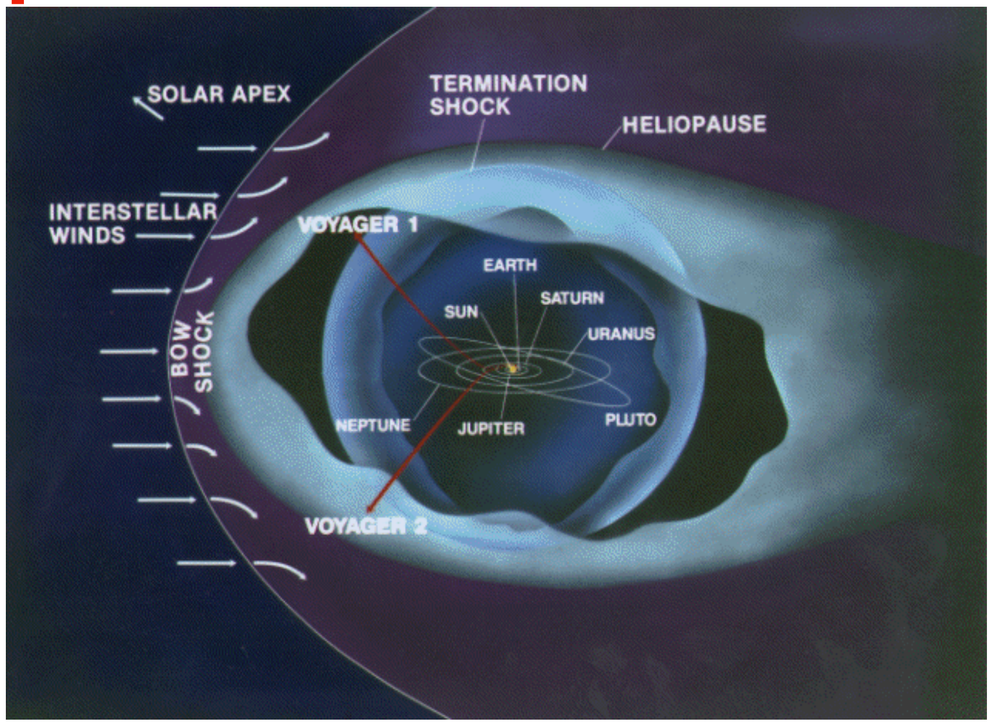

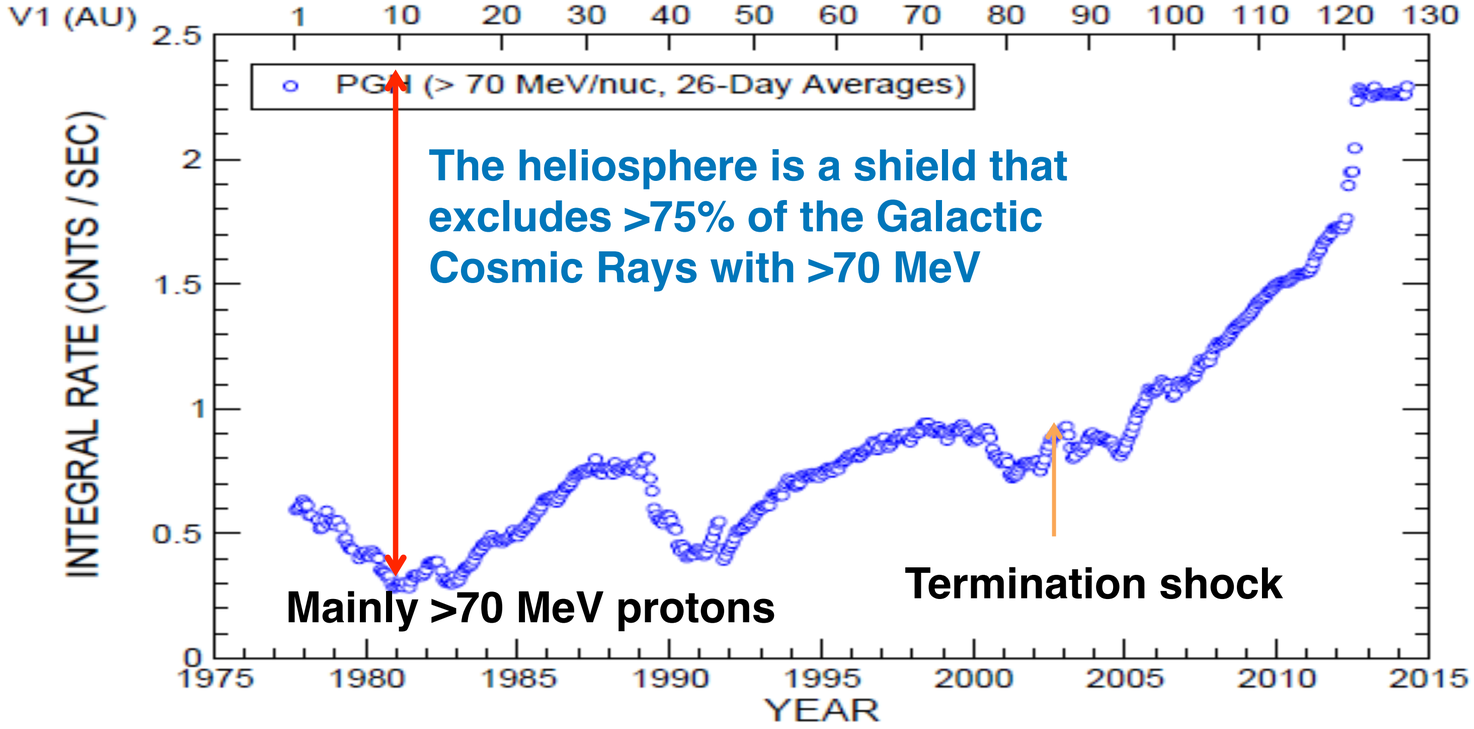

passage through termination shock ended
Voyager 1: 94 AU, December 2004
Voyager 2: 84 AU, August 2007

January 2025: Voyager 1: 166 AU from Sun
Voyager 2: 138 AU from Sun

$$\Delta T = cd \approx 23 \text{ h}$$

Relative abundance of elements at Earth

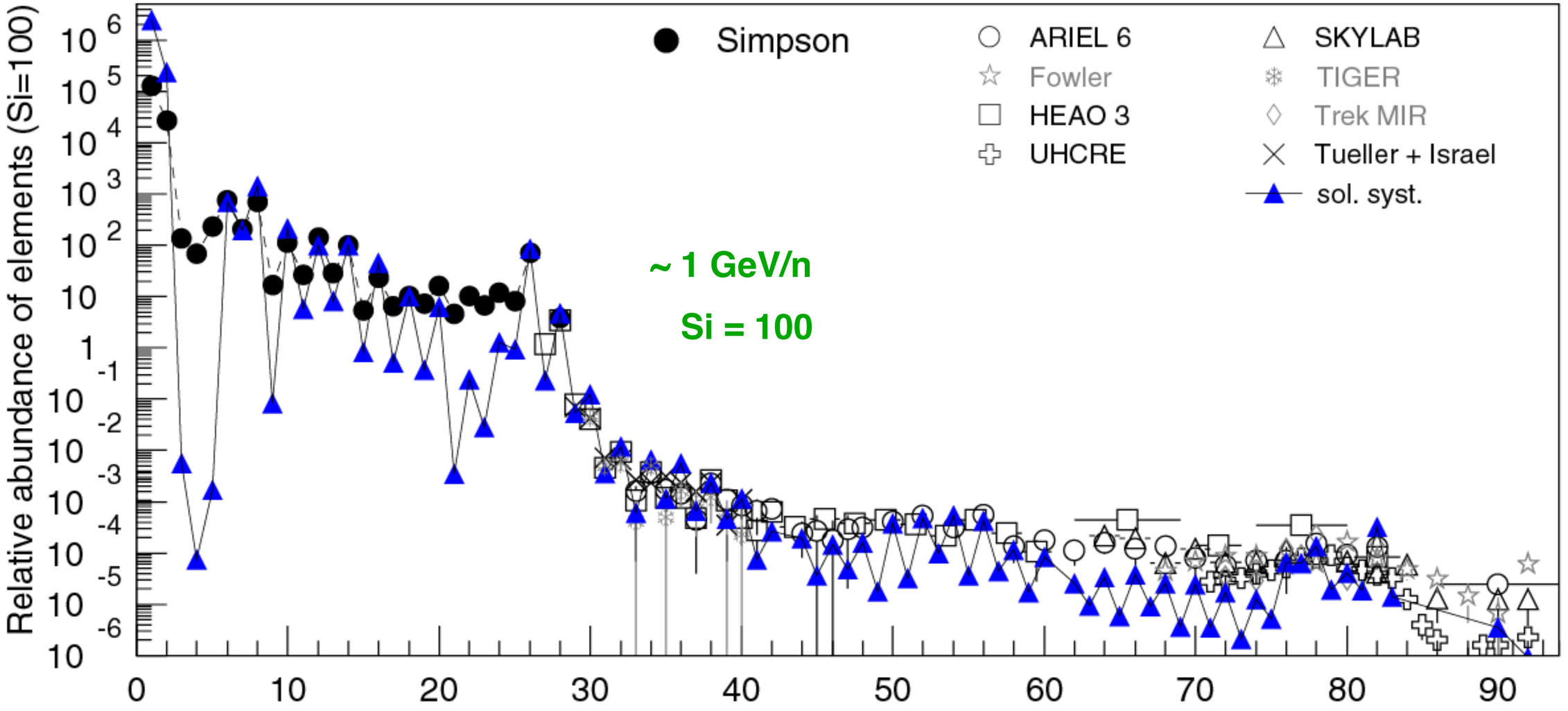

—> Cosmic rays are „regular matter“,
accelerated to extremely high energies

JRH, Adv. Space Res. 41 (2008) 442

elemental composition of cosmic rays

~89% p
9% He
1% heavy nuclei
} ~1 GeV/n

~1% electrons/positrons
<0.1% gamma rays

some remarks:
1. even-odd effect
--> due to high binding energy of ee-nuclei

2. elements Li, Be, B are more abundant in CRs than in solar system
--> propagation in Galaxy

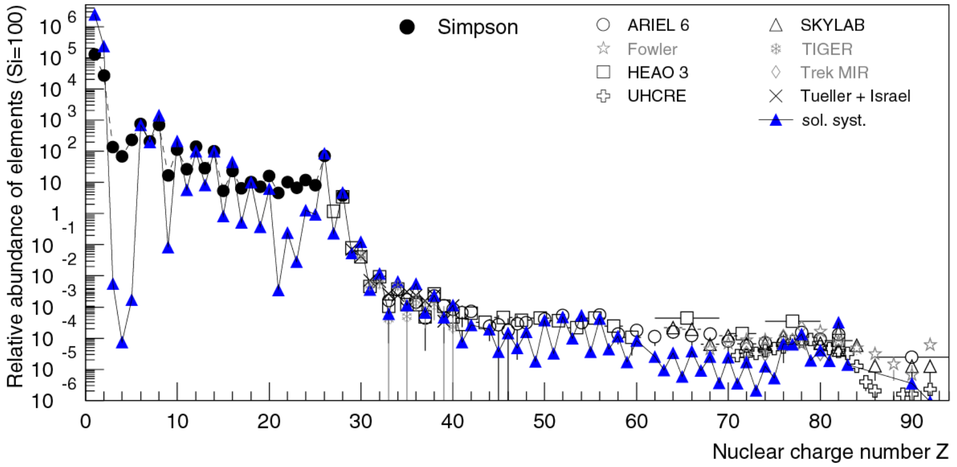

3. same effect for sub-Fe elements (~Ca - Fe)

4. p + He are less abundant in CRs as compared to solar system

electrons(+positrons): ~1% of nuclear cosmic rays

energy spectrum is steeper

$$\frac{dN}{dE} \propto E_e^{-3.3}$$

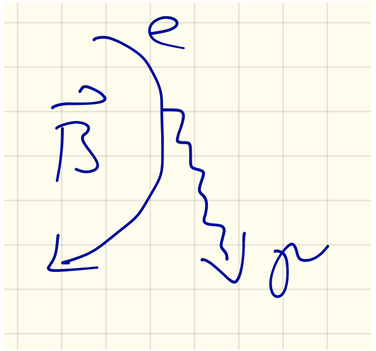

reason:
losses through synchrotron radiation at high energies

For an ensemble of electrons that are scattered randomly in all directions one could calculate the energy loss averaged over all pitch angles, which is

$$\left\langle -\frac{dE}{dt} \right\rangle = \frac{4}{3}\sigma_T c \gamma^2 U_B \qquad (2.27)$$

for relativistic electrons with $\beta \simeq 1$. Expressed in particle physics units the average energy loss becomes

$$-\frac{dE}{dt} = 3.79 \times 10^{-6} \left(\frac{B}{\text{gauss}}\right)^2 \left(\frac{E_e}{\text{GeV}}\right)^2 \text{GeV/s} \; . \qquad (2.28)$$

also inverse Compton scattering at radiation fields and bremsstrahlung on ISM

PAMELA Results: Electrons

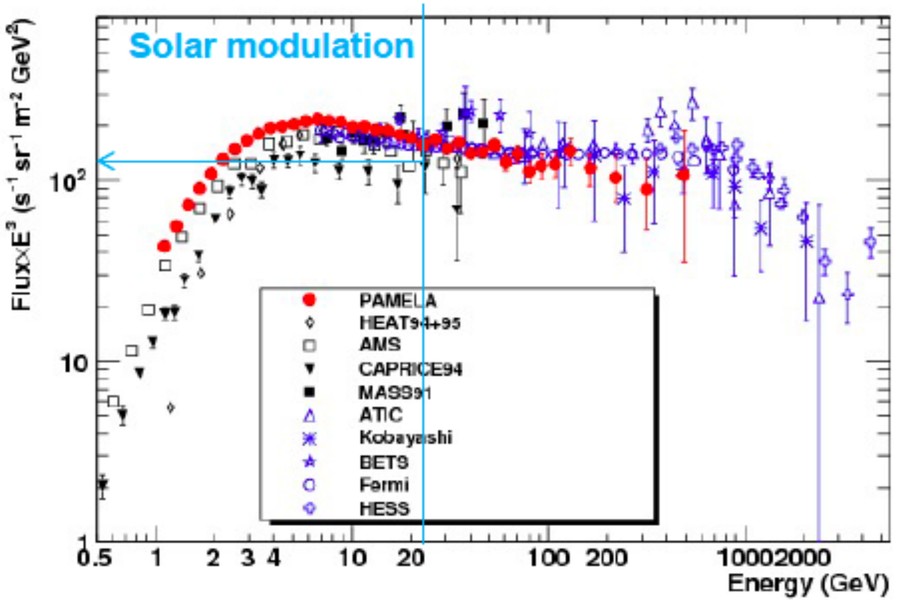

- PAMELA electron spectrum (published data to 625 GeV)
- AMS-02 electrons to 700 GeV

O. Adriani et al., PRL 106, 201101

Study of low energy data (affected by solar modulation)

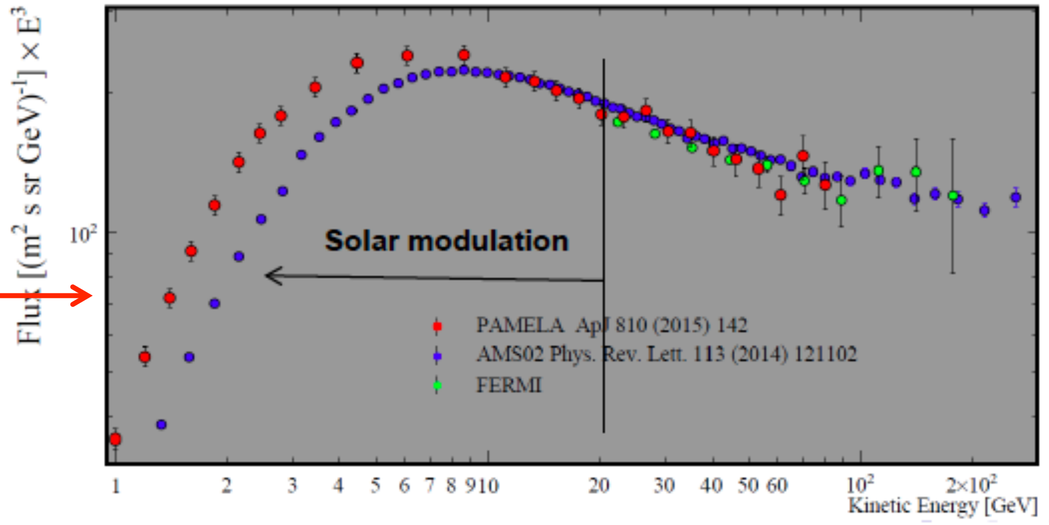

O. Adriani et al., ApJ 810 (2015) 142

Editors' Suggestion | Featured in Physics

High-Statistics Measurement of the Cosmic-Ray Electron Spectrum with H.E.S.S.

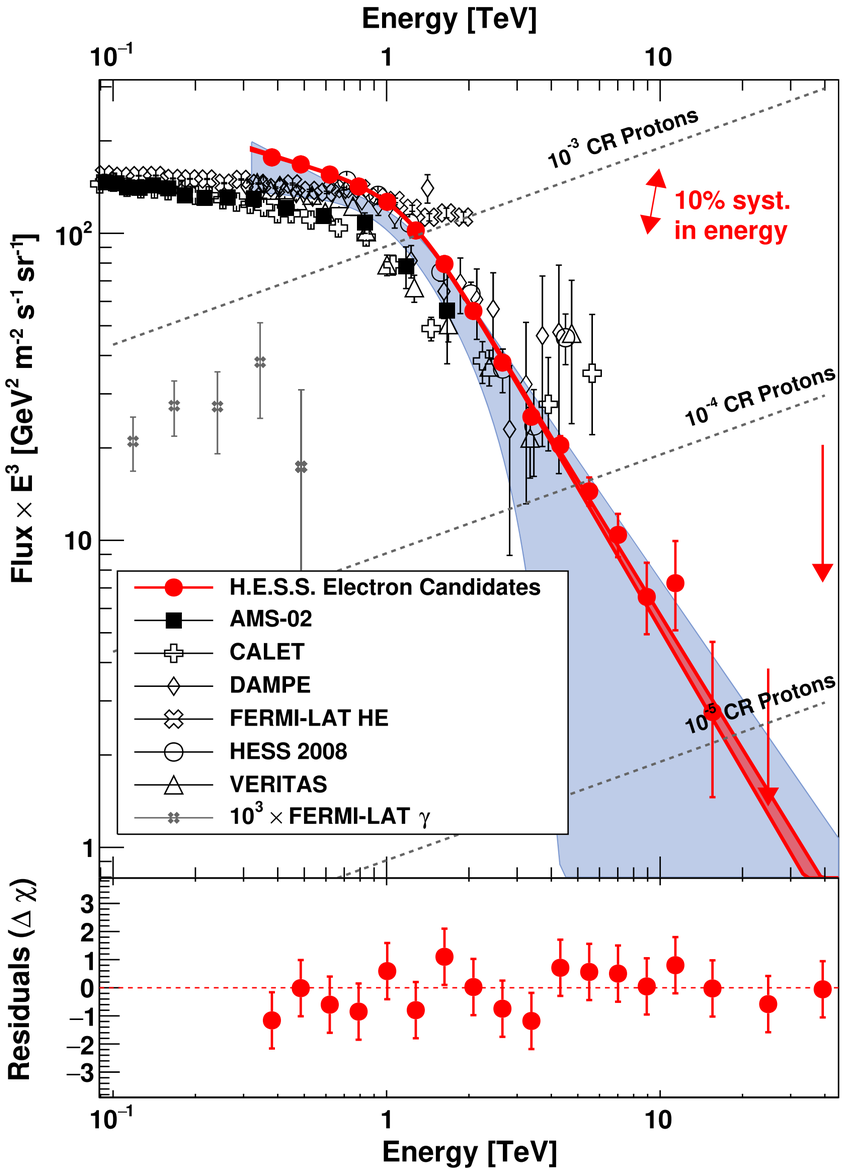

FIG. 3. Filled red circle data points: spectrum of CRe candidate events measured by H.E.S.S. The dataset still contains a residual background from CRn and therefore places an upper limit on the true CRe flux. The dark red band indicates the broken-power-law fit to the data [Eq. (1)], with the width of the band corresponding to statistical errors. The light blue band denotes the estimated range of the true CRe flux, considering the CRn contamination as well as the statistical errors and systematic errors. Separately shown is the systematic error on the global energy scale, which also impacts the normalization of $E^3F(E)$, as visualized by the red arrow. Included are CRe measurements by AMS-02 [25], *Fermi*-LAT [27], CALET [29], DAMPE [28], VERITAS [23], and previous H.E.S.S. measurements [20,21]. Also shown is the CR proton flux based on AMS-02 [37] and DAMPE [38] data (scaled down by $10^{-3} - 10^{-5}$) and the *Fermi*-LAT diffuse extragalactic γ-ray flux [34] (scaled up by 10^3). The bottom panel shows the residuals expressed in $\Delta\chi = (\phi_i - \phi(E))/\sigma_i$ where ϕ_i and σ_i are, respectively, the flux measured in bin i and its statistical uncertainty, and $\phi(E)$ is the expected flux from Eq. (1).

electrons are primary particles
positrons most likely produced in by electrons and nuclei during propagation

PAMELA: first unambiguous evidence of the rise of the positron fraction above 10 GeV

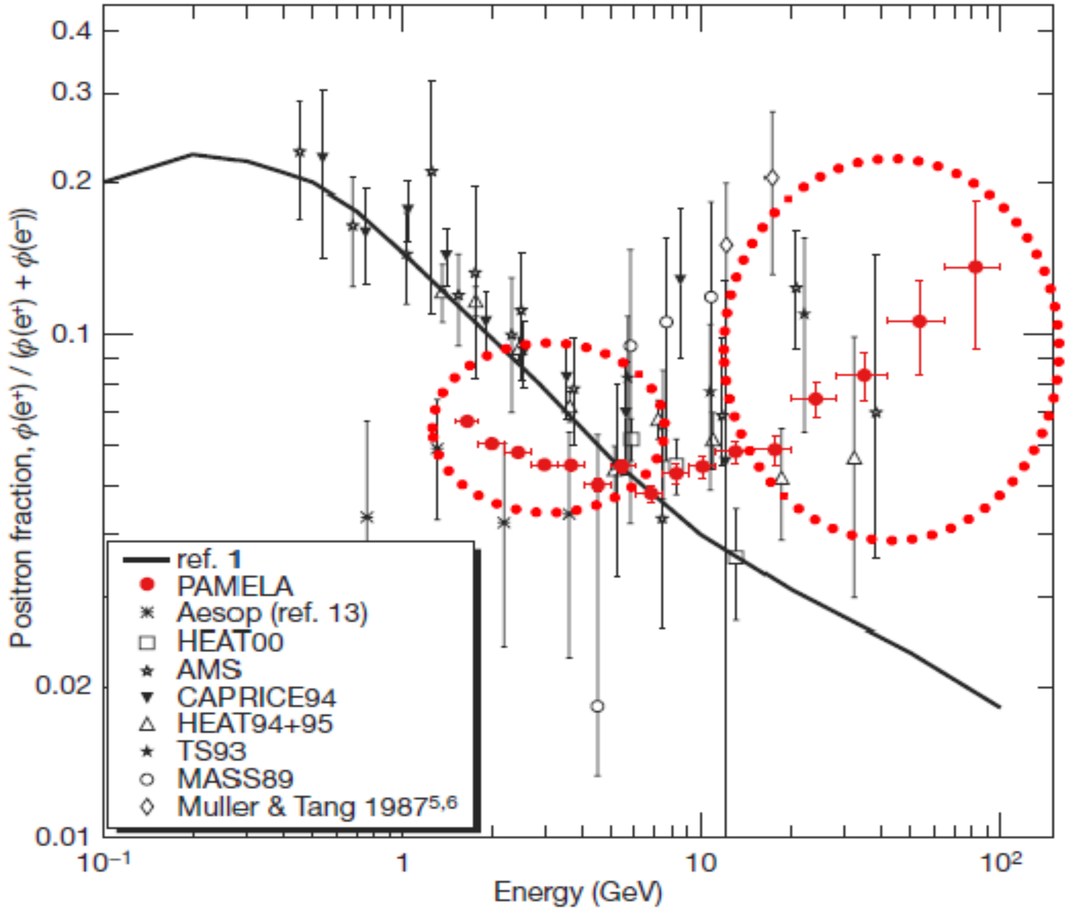

nature International weekly journal of science
Vol 458|2 April 2009|doi:10.1038/nature07942 nature

August 2009

LETTERS

An anomalous positron abundance in cosmic rays with energies 1.5–100 GeV

O. Adriani[1,2], G. C. Barbarino[3,4], G. A. Bazilevskaya[5], R. Bellotti[6,7], M. Boezio[8], E. A. Bogomolov[9], L. Bonechi[1,2], M. Bongi[2], V. Bonvicini[8], S. Bottai[2], A. Bruno[6,7], F. Cafagna[7], D. Campana[4], P. Carlson[10], M. Casolino[11], G. Castellini[12], M. P. De Pascale[11,13], G. De Rosa[4], N. De Simone[11,13], V. Di Felice[11,13], A. M. Galper[14], L. Grishantseva[14], P. Hofverberg[10], S. V. Koldashov[14], S. Y. Krutkov[9], A. N. Kvashnin[5], A. Leonov[14], V. Malvezzi[11], L. Marcelli[11], W. Menn[15], V. V. Mikhailov[14], E. Mocchiutti[8], S. Orsi[13,11], G. Osteria[4], P. Papini[2], M. Pearce[10], P. Picozza[11,13], M. Ricci[17], S. B. Ricciarini[2], M. Simon[15], R. Sparvoli[11,13], P. Spillantini[1,2], Y. I. Stozhkov[5], A. Vacchi[8], E. Vannuccini[2], G. Vasilyev[9], S. A. Voronov[14], Y. T. Yurkin[14], G. Zampa[8], N. Zampa[8] & V. G. Zverev[14]

Citations: 1338

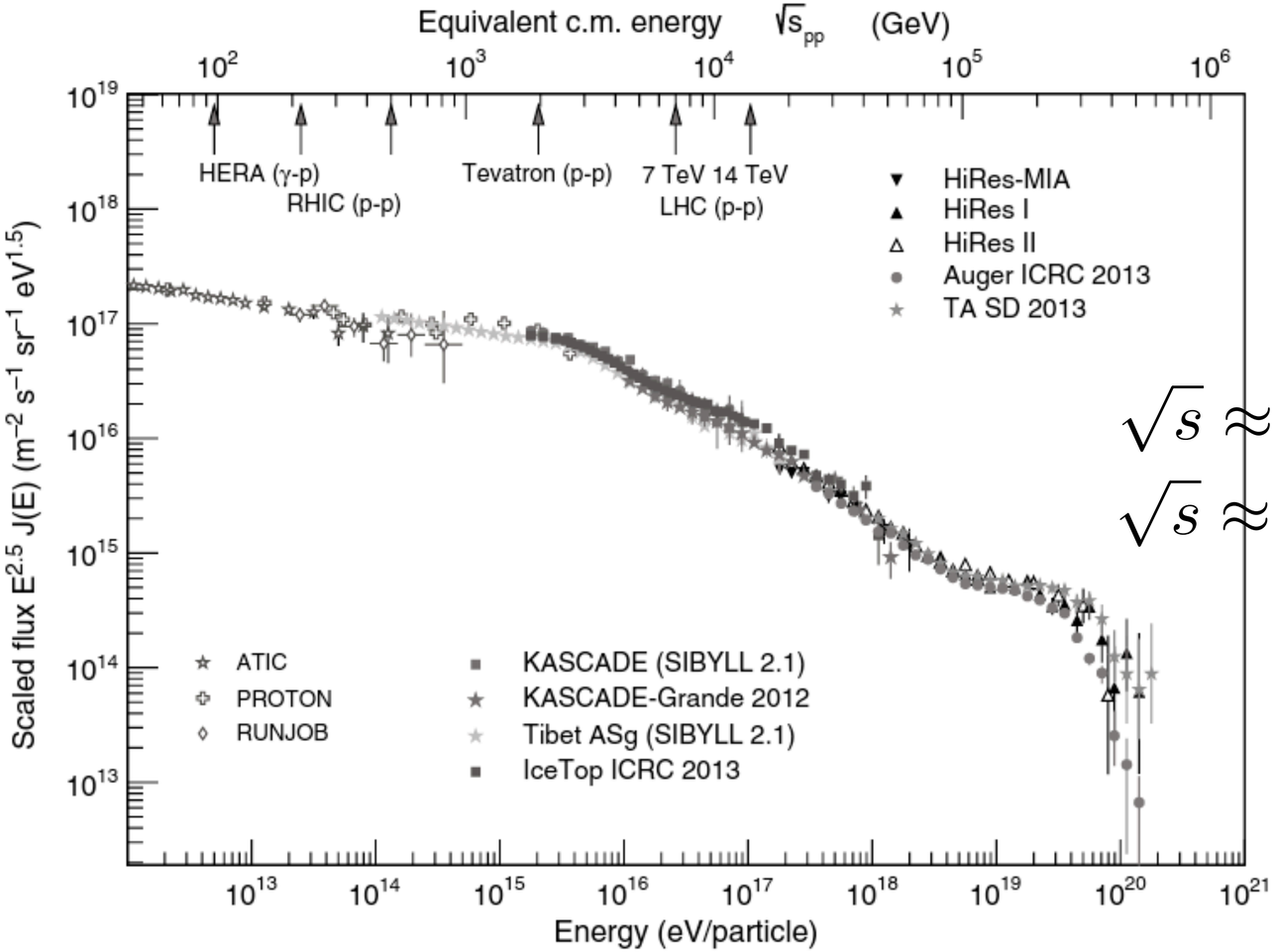

$\sqrt{s} \approx 430$ TeV **p**

$\sqrt{s} \approx 57$ TeV **Fe**

Figure 4.2 All-particle flux of cosmic rays scaled by $E^{2.5}$ (from [33], updated). The x axis at the top shows the equivalent nucleon–nucleon c.m. energy of the interaction of protons of the cosmic ray flux with a nucleon of the air. The energies reached by different colliders are marked by arrows. Fixed target experiments have maximum beam energies of, for example, 350 GeV (NA49, NA61 at CERN) and 800 GeV (SELEX at Tevatron), which is below the lowest energy shown here. The LHC collider was the first accelerator that allowed the study of interactions at energies above the knee in the cosmic ray spectrum.

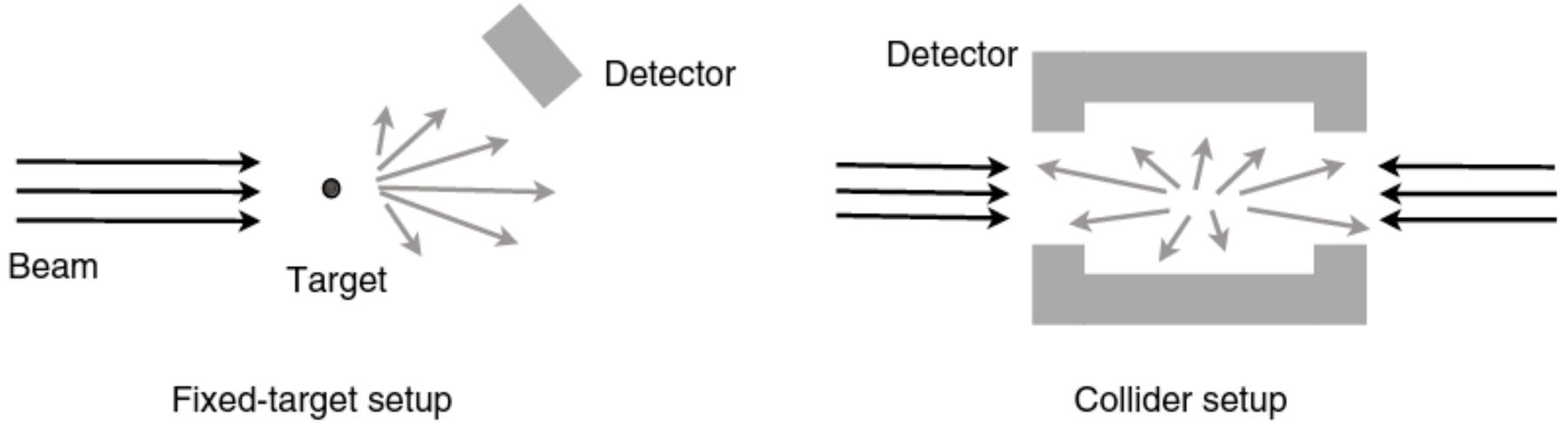

Figure 4.1 Fixed-target and collider setups for measuring particle production at accelerators. The particle detectors are indicated in gray and might provide tracking (of charged particles) and calorimetry. The energies of the two beams of collider experiments are typically the same except if different particles are accelerated such as electrons and protons or protons and nuclei.

$$E_{\mathrm{cm}} = E_a^\star + E_b^\star.$$ **center of mass energy**

$$s = (p_a^\star + p_b^\star)^2 = (p_a + p_b)^2 = E_{\mathrm{cm}}^2.$$ **Mandelstam variable (Lorentz invariant)**

$$E_{\mathrm{cm}} = \sqrt{s} = \left(2E_a m_b + m_a^2 + m_b^2\right)^{1/2} \approx \sqrt{2E_a m_b}.$$

energy in fixed traget exp.
only proportional sqrt(s)

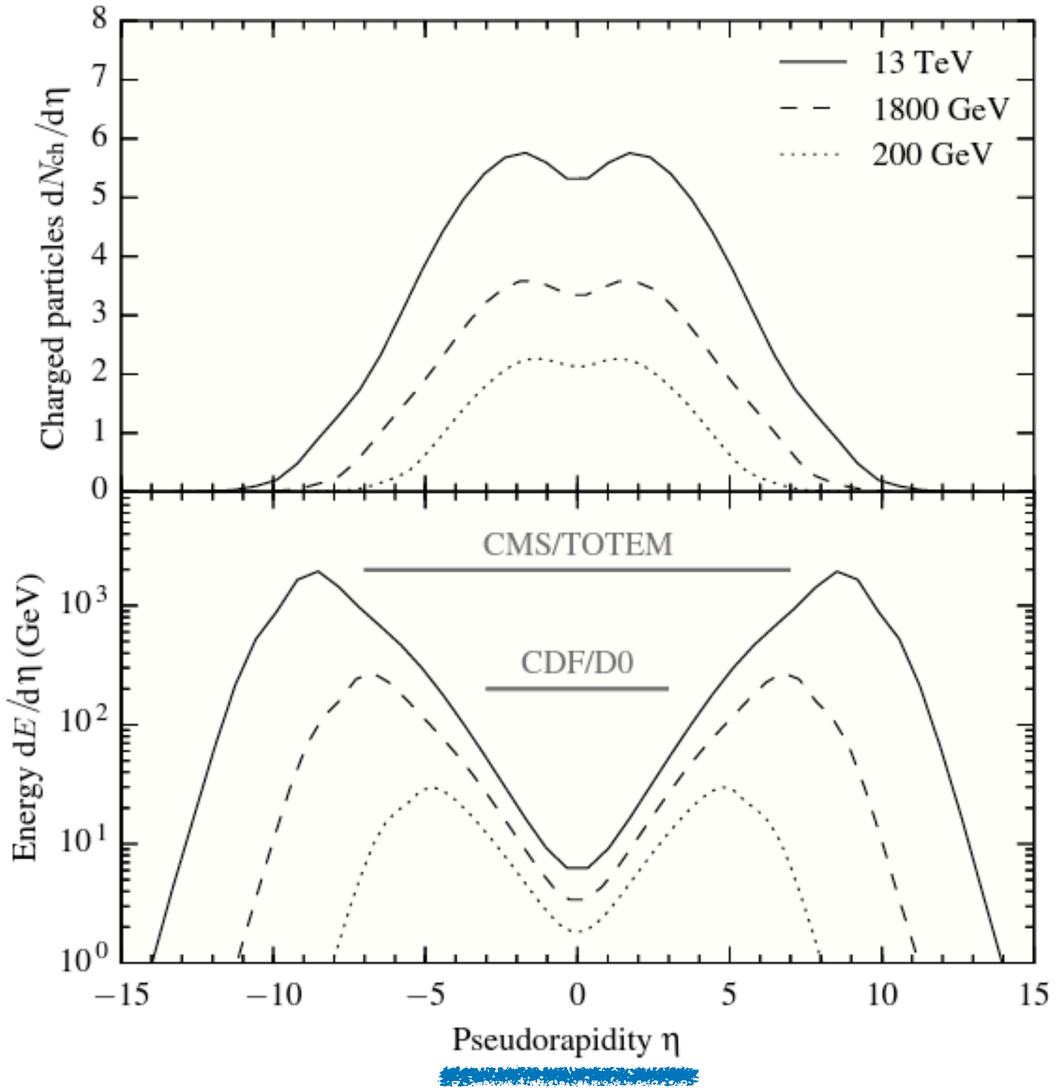

Figure 4.5 Phase space coverage of multi-purpose detectors at high-energy colliders. Shown are the charged particle multiplicity and the total energy of the final state particles as function of pseudorapidity for different c.m. energies. The coverage in pseudorapidity of the CMS detector extended by TOTEM for forward tracking is shown as an example for LHC ($\sqrt{s} = 13\,\text{TeV}$) and that of the CDF and D0 detectors for the Tevatron collider ($\sqrt{s} = 1.8\,\text{TeV}$).

$$\eta = \frac{1}{2} \ln \frac{|p| + p_\parallel}{|p| - p_\parallel} = -\ln \tan \frac{\theta}{2}. \tag{4.14}$$

Here θ is the polar angle of the particle with respect to the beam axis. Pseudorapidity and rapidity of massless particles are identical.

CALIBRATION OF HADRON INTERACTION MODELS AT LHC

p-p 450 GeV + 450 GeV → $E_{lab} \sim 4 \cdot 10^{14}$ eV
p-p 3.5 TeV + 3.5 TeV → $E_{lab} \sim 3 \cdot 10^{16}$ eV
p-p 6.5 TeV + 6.5 TeV → $E_{lab} \sim 9 \cdot 10^{16}$ eV

- Total cross section ↔ TOTEM, ATLAS, CMS
- Multiplicity ↔ Central detectors
- Inelasticity/Secondary spectra ↔ Forward calorimeters (**LHCf**, ZDCs)

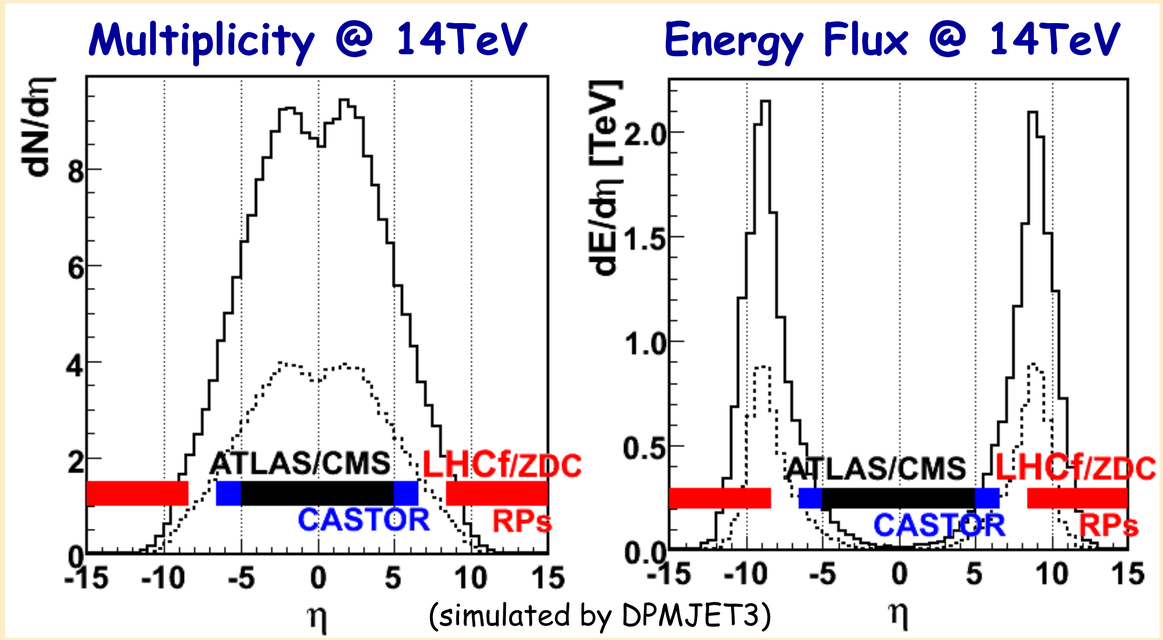

LHCf EXPERIMENTAL SET-UP

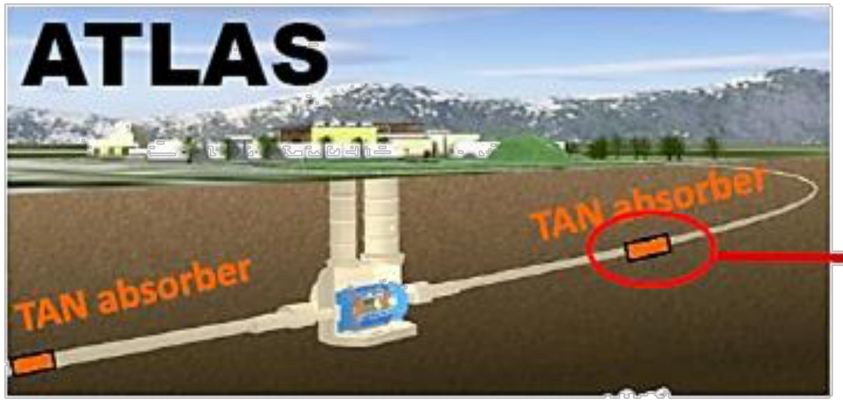

Detectors are located inside the TAN absorber for neutral particles

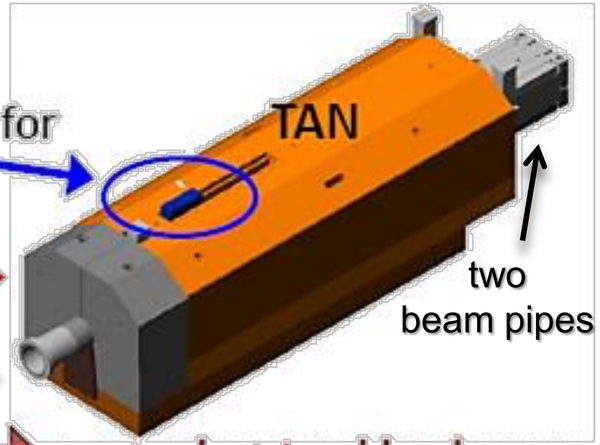

The LHCf detectors measure energy and impact point of γ and n → e.m. calo + tracking layers

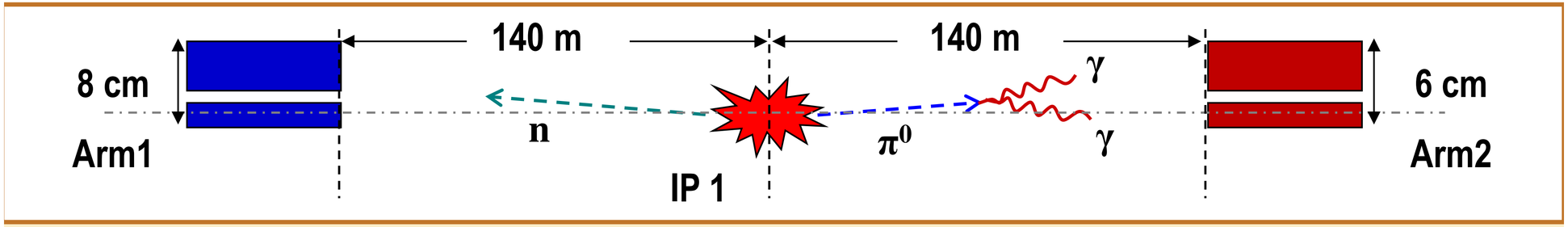

Two independent detectors on both sides of IP1

- ✓ Redundancy
- ✓ Background rejection (esp. beam-gas)

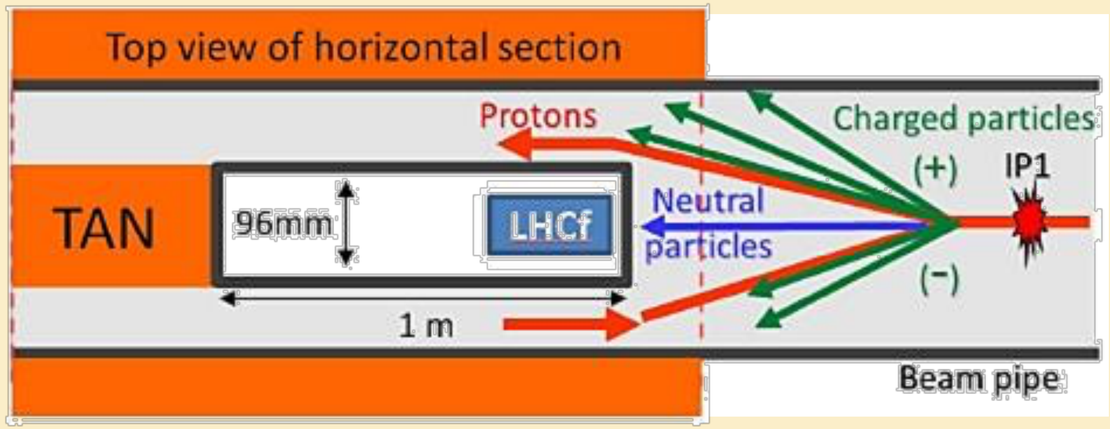

Total and elastic cross sections

It is still not possible to calculate total and elastic cross sections of hadrons within QCD. Measurements at accelerators have to be combined with phenomenological models to obtain a description of cross sections over the energy range of importance for cosmic ray physics. In addition, at the highest energies, measurements of air showers provide constraints on cross sections.

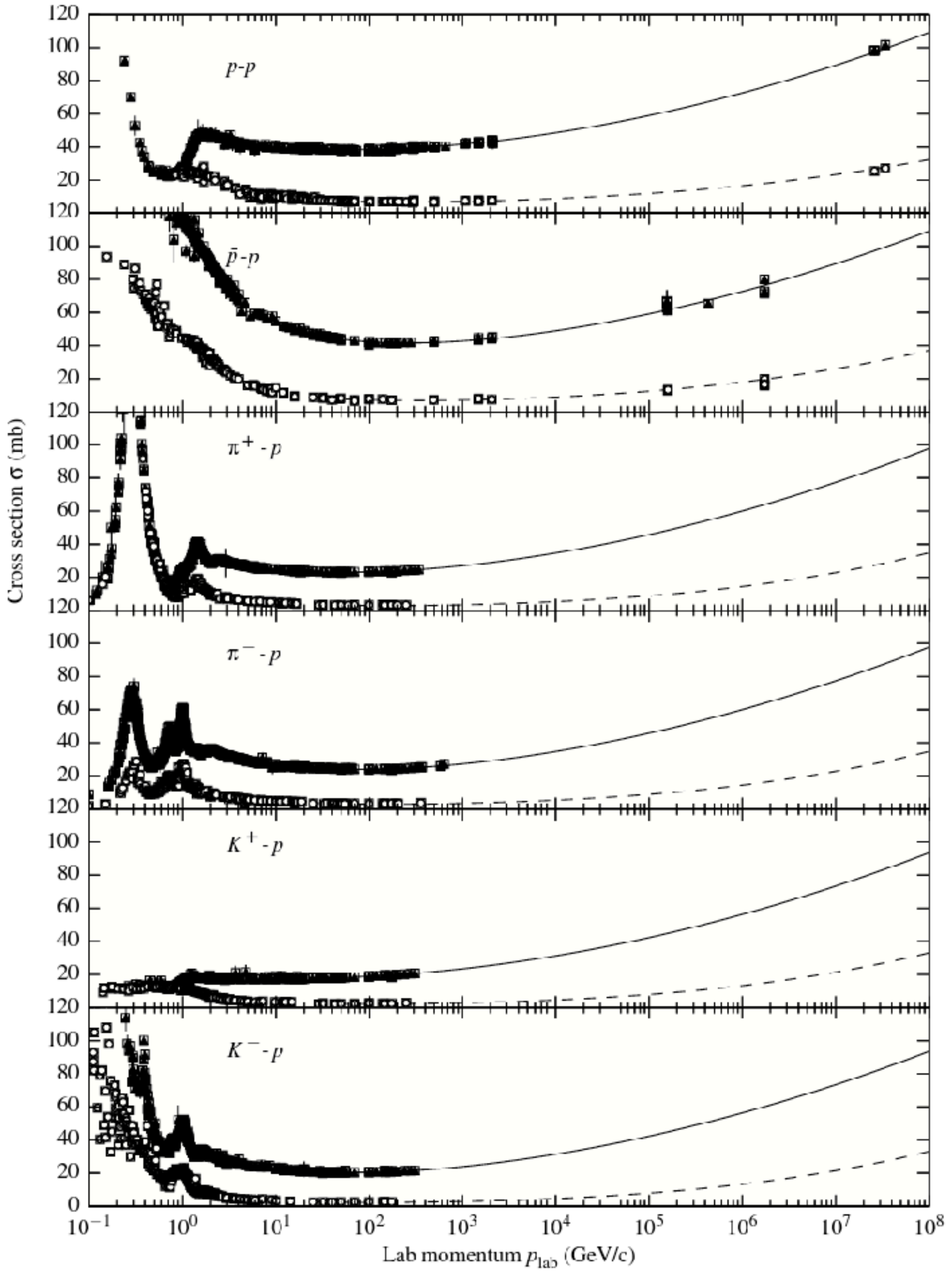

Figure 4.6 Overview of total (solid symbols) and elastic (open symbols) cross sections. The data are from the PDG compilation [10] and the curves show the 2014 fit of the PDG with a universal $\ln^2 s$ increase at high energy; see also [124].

above ~10 GeV only weak (logarithmic) dependence on energy

Extensive Air Shower

Proton 10^{15} eV:
on ground
10^6 particles
80% photons
18% electr./positr.
1.7% muons
0.3% hadrons

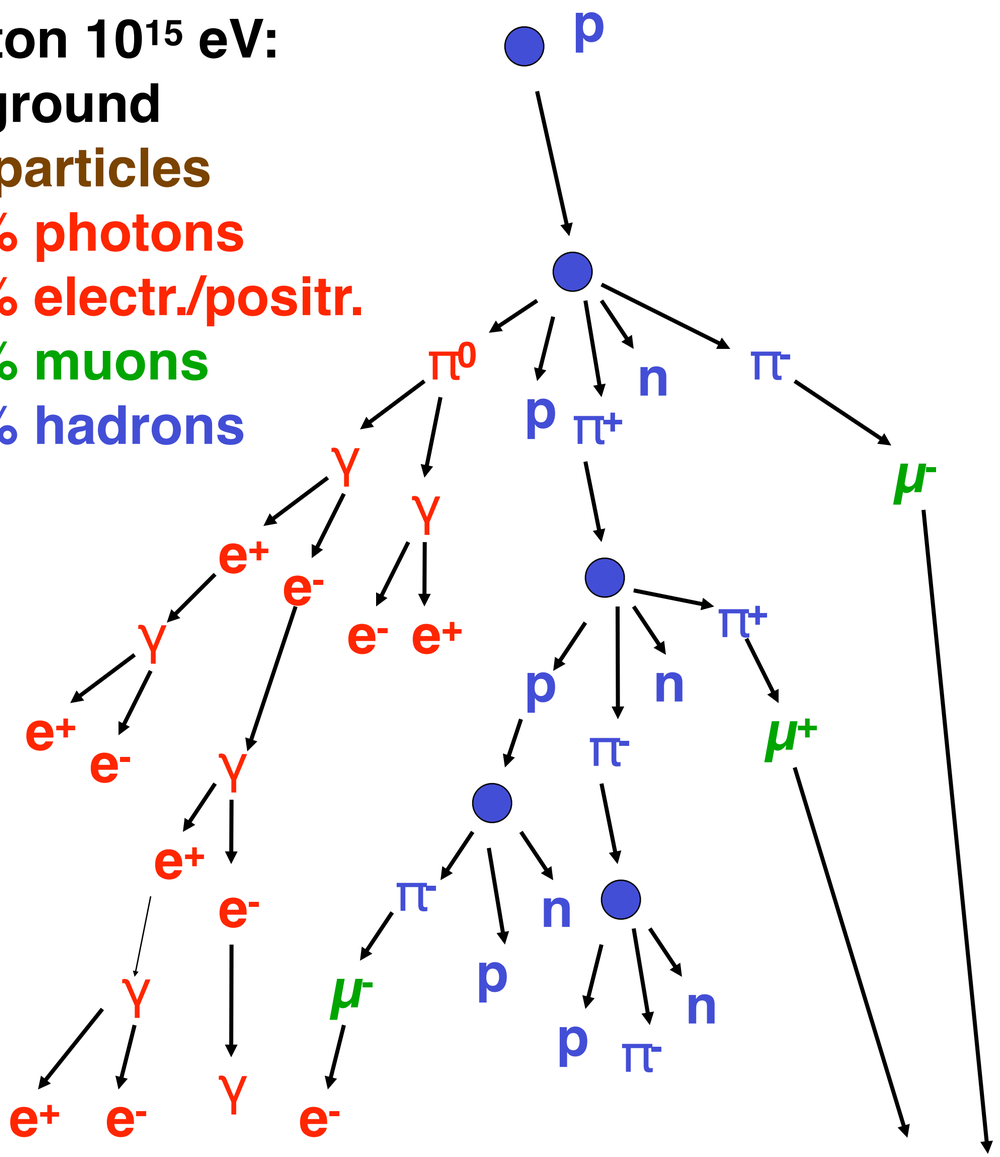

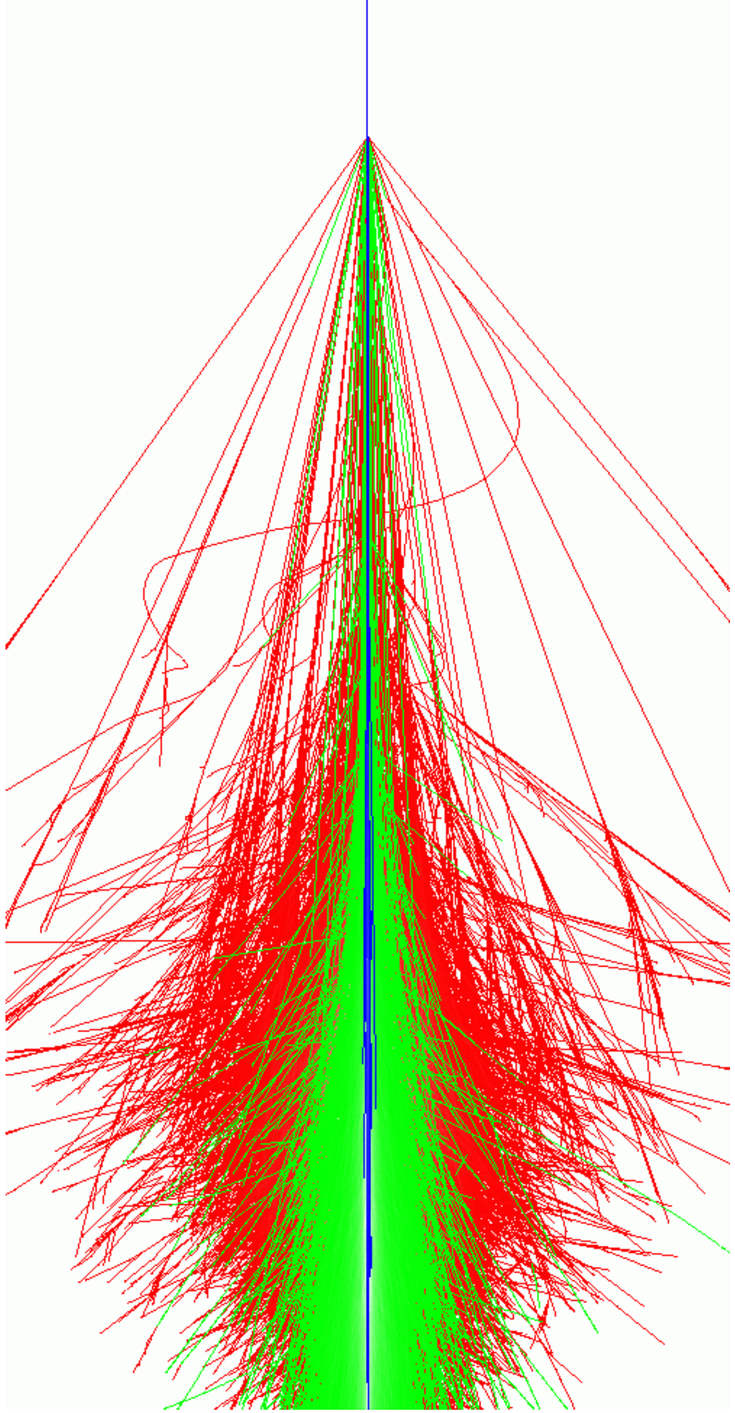

electromagnetic **hadronic** **muonic**
shower component

examples of showers with same (total) energy

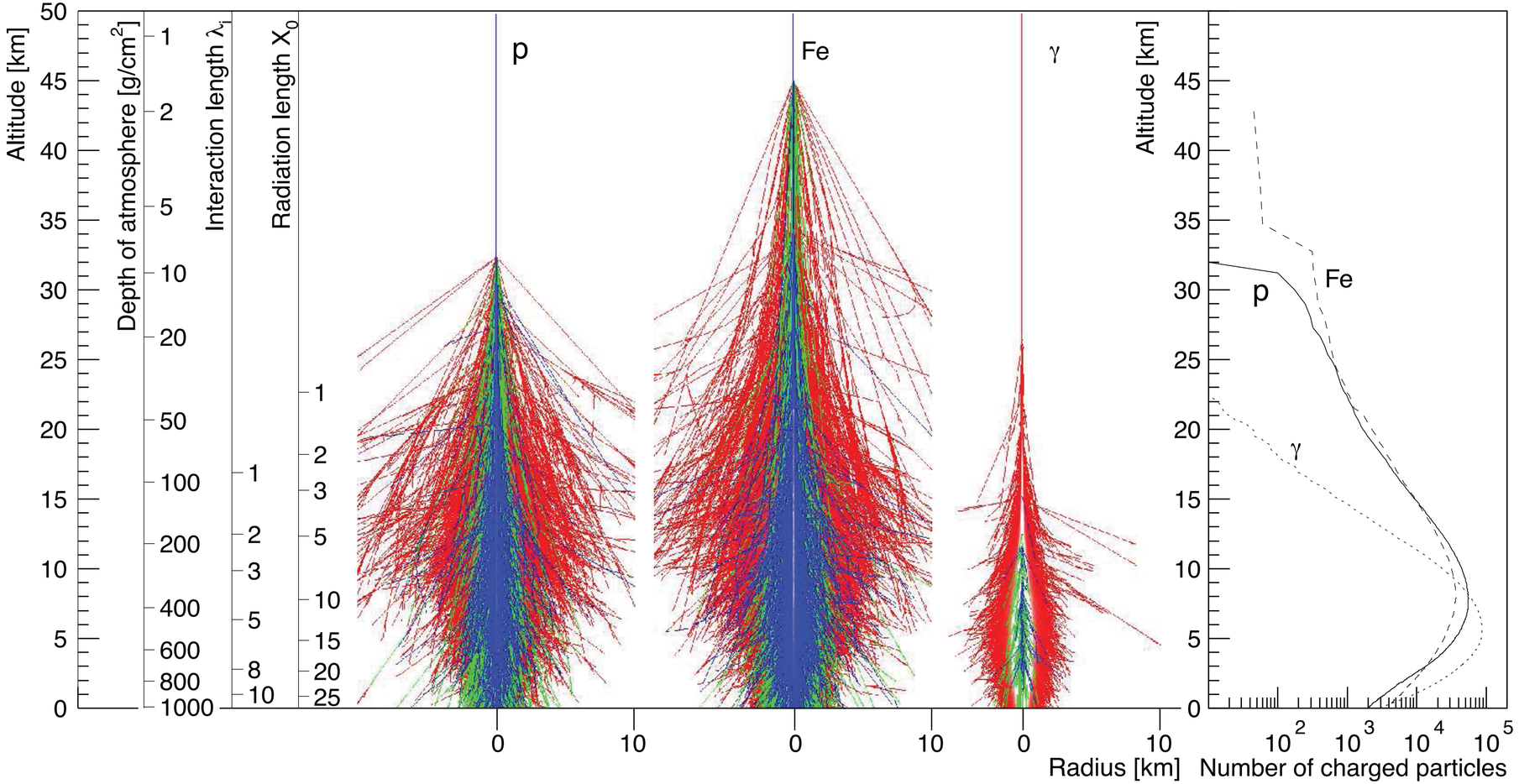

16.1 Basic features of air showers

At each hadronic interaction, slightly more than a third of the energy goes into the electromagnetic component. Since most hadrons re-interact, most of the primary energy eventually finds its way into the electromagnetic component. In addition, because of the rapid multiplication of electromagnetic cascades, electrons and positrons are the most numerous charged particles in cosmic ray air showers. Thus, most of the shower energy is eventually dissipated by ionization losses of the electrons and positrons. It is correct to think of the atmosphere as a calorimeter to be sampled by the air shower detector. Apart from the small fraction, $F(E_0)$, of energy lost to neutrinos, the primary energy, E_0 is given by the *track length integral*,

$$(1 - F) \times E_0 \sim \alpha \times \int_0^\infty \mathrm{d}X \, N(X), \tag{16.1}$$

where $N(X)$ is the number of charged particles in the shower at depth X (measured along the shower axis) and α is the energy loss per unit path length in the atmosphere averaged over all electron energies ($\alpha \approx 2.5\,\mathrm{MeV}/(\mathrm{g/cm}^2)$). In practice the track length integral must be extrapolated beyond the slant depth at the ground to account for energy remaining in the shower when it reaches the surface.

Energy measurement - calorimeter

hadron calorimeter

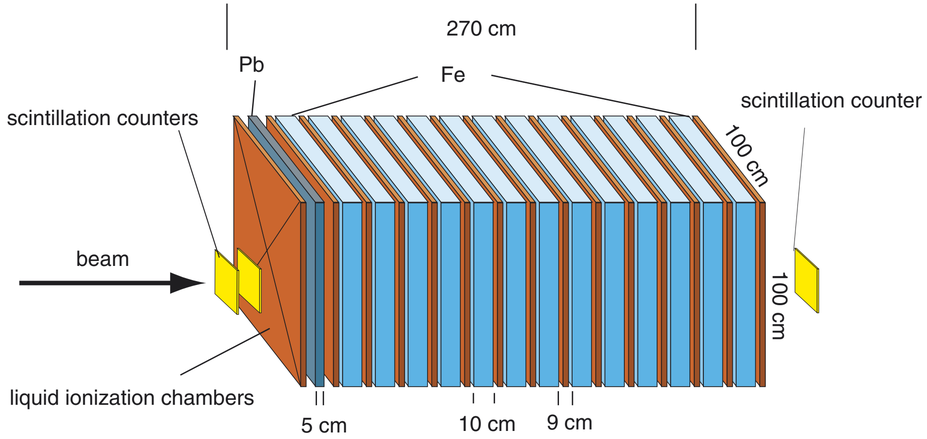

longitudinal shower development

S. Plewnia et al. / Nuclear Instruments and Methods in Physics Research A 566 (2006) 422–432

Fig. 2. Schematic view of the sampling calorimeter.

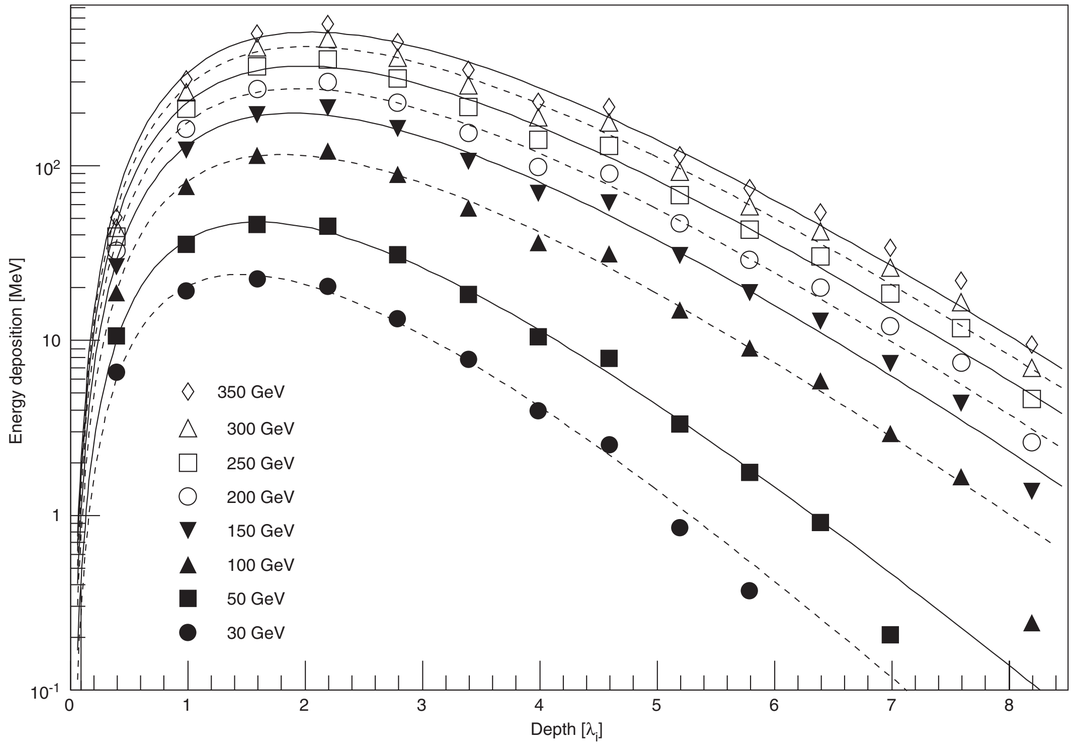

Fig. 13. Measured energy deposition as function of depth in the calorimeter for hadrons with energies from 30 to 350 GeV. The lines represent fits according to Eq. (7).

sampling calorimeter
alternating layers of absorber material and detectors

energy resolution

$$\frac{\sigma(e)}{E} = A + B\frac{1}{\sqrt{E}}$$

$$E_{\mathrm{dep}}(t) = A \cdot t^{B} \cdot \exp(-t/C)$$

Energy measurement - calorimeter

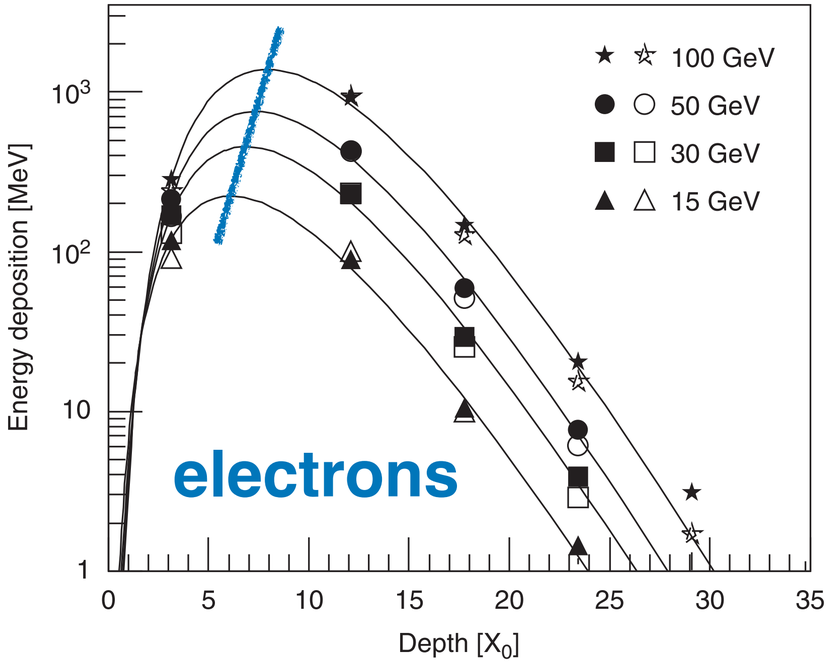

Fig. 16. Energy deposition as function of depth in the calorimeter for electrons. Shown are measurements (filled symbols) and results of simulations (open symbols). The lines represent fits to the measurements according to Eq. (7).

The data points have been fitted using the approach

$$E_{\mathrm{dep}}(t) = A \cdot t^{B} \cdot \exp(-t/C) \qquad (7)$$

originally introduced for electromagnetic cascades [28]. The absorber depth t is measured in interaction lengths λ_i or radiation lengths X_0 for hadrons and electrons, respectively. B characterizes the growth of the cascade before the maximum and C the exponential decrease at large depths.

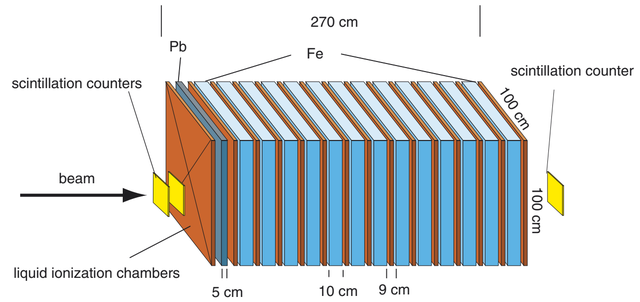

Fig. 2. Schematic view of the sampling calorimeter.

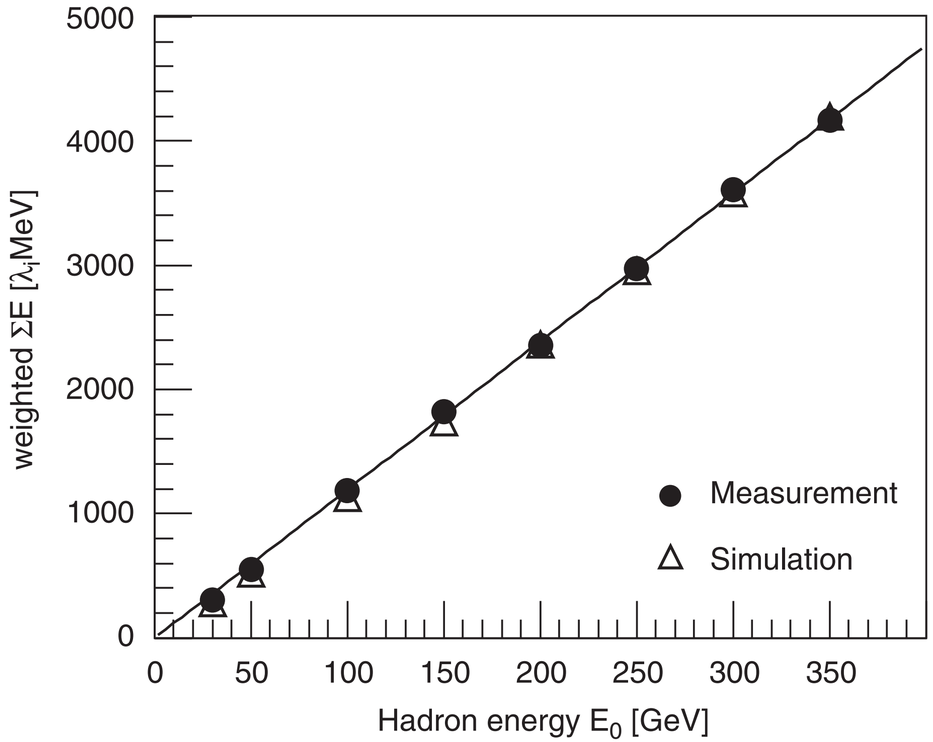

Fig. 17. Energy sum in the calorimeter as function of the incident hadron energy. The energy in each layer is weighted with the amount of absorber in front of the layer.

The number of low-energy ($1 - 10\,\mathrm{GeV}$) muons increases as the shower develops then reaches a plateau because muons rarely interact. The attenuation of the muon component due to muon decay and energy loss is relatively slow. In contrast, the number of electrons and positrons declines rapidly after maximum because radiation and pair production subdivides the energy down to the critical energy ($E_c \sim 80\,\mathrm{MeV}$ – see 5.3) after which electrons lose their remaining energy to ionization quickly. These basic features of longitudinal development of showers are illustrated in the right panel of Figure 16.1.

The left panel of Figure 16.1 shows the lateral distributions of the different components. Secondary hadrons are produced at a typical, almost energy-independent transverse momentum of $p_\perp \sim 350 - 400\,\mathrm{MeV}$, leading to a large angle of low-energy hadrons relative to the shower axis. In contrast, most of the EM particles are in the cascades initiated by high-energy π^0 nearly parallel to the hadronic core. Their lateral spread comes mainly from multiple Coulomb scattering.[1] Thus the lateral distribution of muons is wider than that of EM particles because they are mainly produced in the decay of low-energy pions [505, 506]. For the same reason, hadronic interactions at low energy ($E \lesssim 200\,\mathrm{GeV}$) largely determine the total muon yield [507, 508]. In round numbers the muons make up of order $\sim 10\%$ of the charged particles. In the EM component, the γ-rays outnumber the $e^\pm$ by a factor of ~ 10.

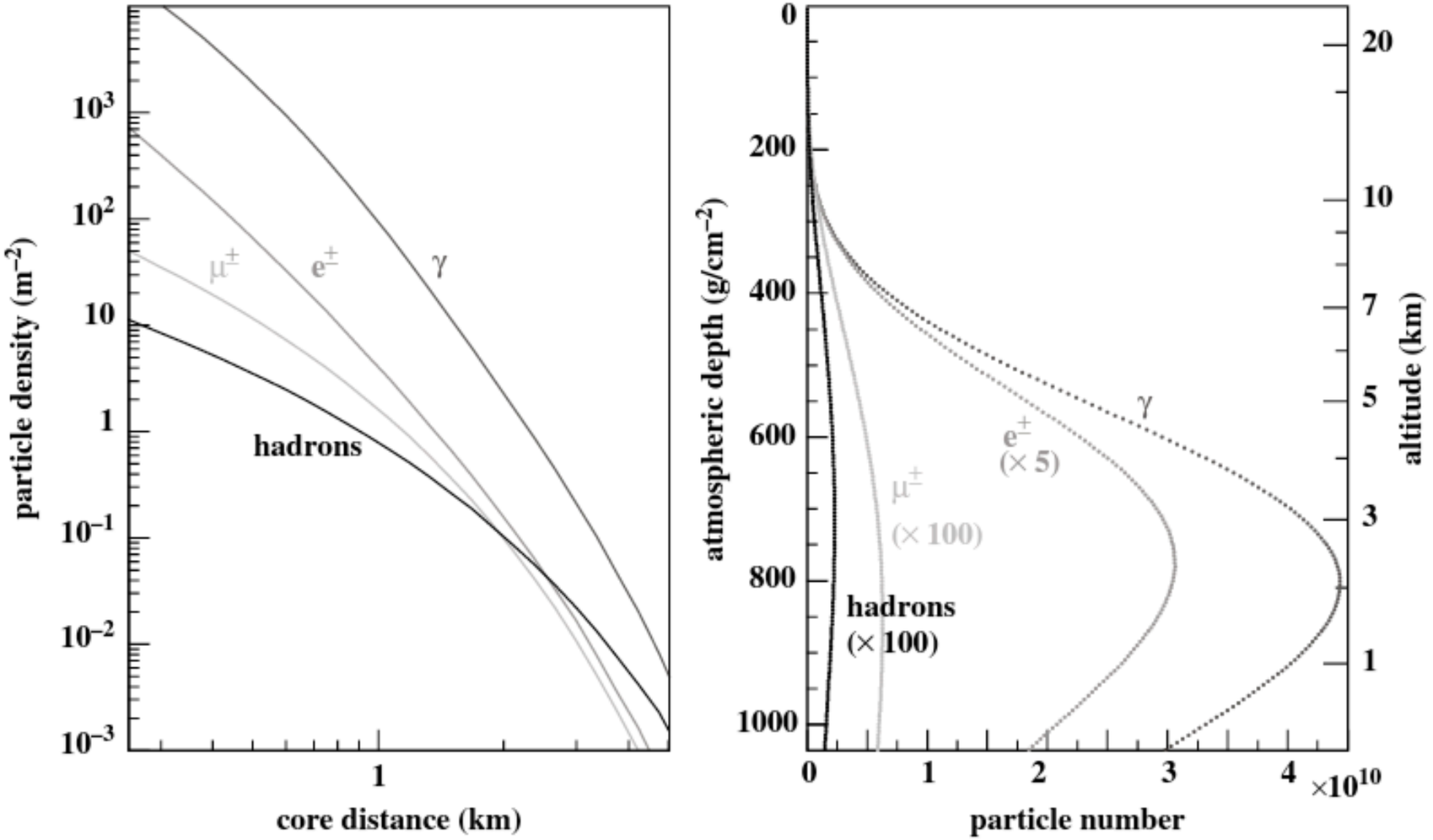

Figure 16.1 Average lateral and longitudinal shower profiles for vertical, proton-induced showers at 10^{19} eV. The lateral distribution of the particles at ground is calculated for 870 g/cm^2, the depth of the Auger Observatory. The energy thresholds of the simulation were 0.25 MeV for γ, $e^{\pm}$ and 0.1 GeV for muons and hadrons (from [33]).

A Matthews Heitler Model – Electromagnetic Cascades

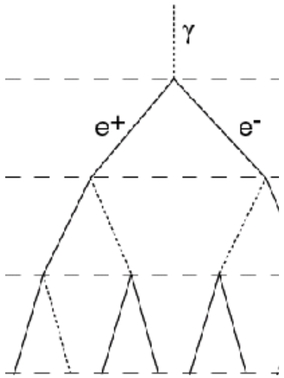

pair production $\gamma \rightarrow e^+ + e^-$

bremsstrahlung $e \rightarrow e + \gamma$

splitting length $d = X_0 \ln 2$

radiation length $X_0 = 36.7$ g/cm²

ELSEVIER

Available online at www.sciencedirect.com
SCIENCE DIRECT®

Astroparticle Physics 22 (2005) 387–397

Astroparticle Physics

www.elsevier.com/locate/astropart

A Heitler model of extensive air showers

J. Matthews *

Department of Physics and Astronomy, Louisiana State University, Baton Rouge, LA 70803, USA
Department of Physics, Southern University, Baton Rouge, LA 70813, USA

Received 8 August 2004; received in revised form 3 September 2004; accepted 13 September 2004
Available online 26 October 2004

after *n* splitting lengths: $x = nX_0 \ln 2$ **and** $N = 2^n = \exp\left(\frac{x}{X_0}\right)$

energy per particle $E = E_0/N$ **critical energy** $E_c^e = 85\ \mathrm{MeV}$

number of particles at shower maximum

$$N_{max} = 2^{n_c} = \frac{E_0}{E_c^e} \qquad n_c = \frac{\ln\left(\frac{E_0}{E_c^e}\right)}{\ln 2}$$

J. Matthews, Astrop. Phys. 22 (2005) 387 JRH, Mod. Phys. Lett. A 22 (2007) 1533

A Matthews Heitler Model – Electromagnetic Cascades

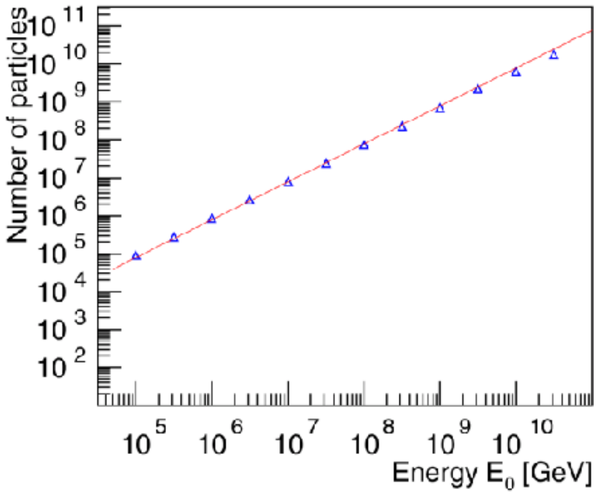

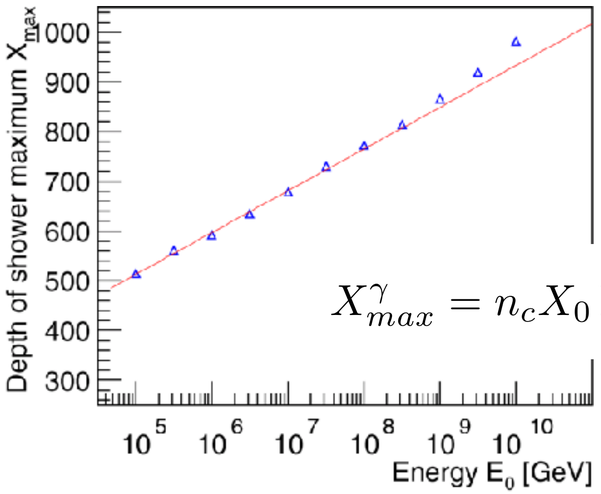

J. Matthews, Astrop. Phys. 22 (2005) 387

number of electrons at shower maximum

$$N_e^{max} = \frac{E_0}{g E_c^e} \approx 9.0 \cdot 10^5 \frac{E_0}{\mathrm{PeV}} \quad g \approx 13$$

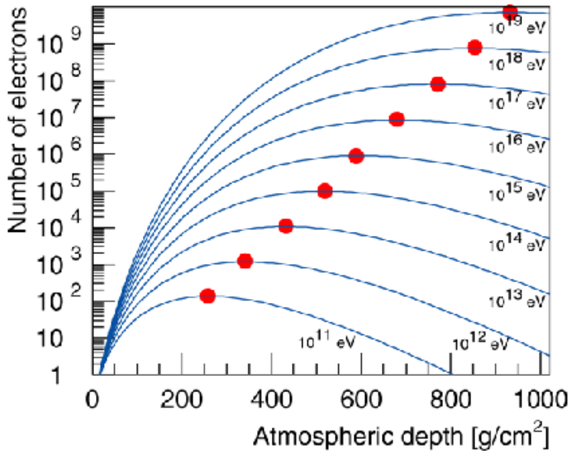

depth of shower maximum

$$X_{max}^{\gamma} = n_c X_0 \ln 2 = X_0 \ln\left(\frac{E_0}{E_c^e}\right) \approx 597 \frac{\mathrm{g}}{\mathrm{cm}^2} + 84 \frac{\mathrm{g}}{\mathrm{cm}^2} \lg\left(\frac{E_0}{\mathrm{PeV}}\right)$$

JRH, Mod. Phys. Lett. A 22 (2007) 1533

A Matthews Heitler Model – Hadronic Cascades

J. Matthews, Astrop. Phys. 22 (2005) 387

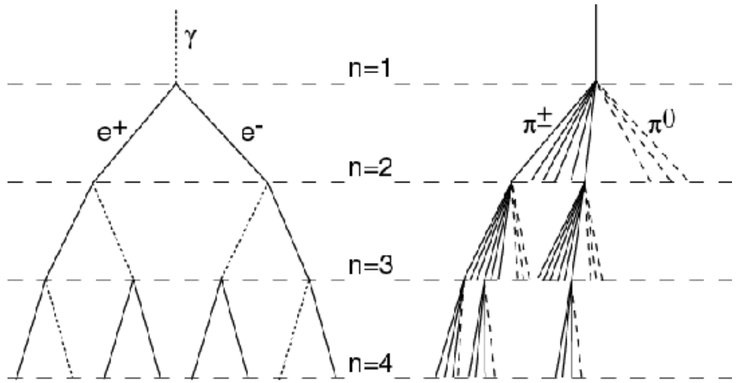

hadronic interaction π+A → π^0 + π^+ + π^-

interaction length $\lambda_I^{\pi\text{-air}}$~120 g/cm^2

π → hadronic interaction
→ decay

„critical energy“ E_c^{π}~20 GeV

in each interaction 3/2N_{ch} particles: N_{ch} π^{+-} and ½ N_{ch} π^0 N_{ch} ~ 10

after *n* interactions $N_\pi = (N_{ch})^n$ $E_\pi = \frac{E_0}{\left(\frac{3}{2}N_{ch}\right)^n}$

after n_c interactions E_π=E_c^{π}: $n_c = \frac{\ln E_0/E_c^\pi}{\ln \frac{3}{2}N_{ch}} = 0.85 \lg\left(\frac{E_0}{E_c^\pi}\right)$

superposition model
particle (E_0,A) → A proton showers with energy E_0/A

JRH, Mod. Phys. Lett. A 22 (2007) 1533

A Matthews Heitler Model – N_μ and N_e

Number of muons at shower maximum

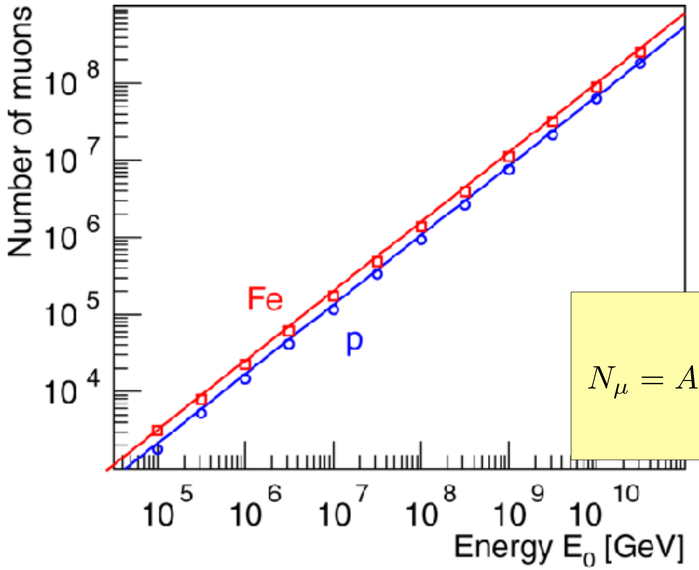

$$N_\mu = N_\pi = (N_{ch})^{n_c}$$

$$\ln N_\mu = n_c \ln N_{ch} = \beta \ln \left(\frac{E_0}{E_c^\pi} \right)$$

$$N_\mu = A \left(\frac{E_0}{A E_c^\pi} \right)^\beta = \left(\frac{E_0}{E_c^\pi} \right)^\beta A^{1-\beta} \approx 1.7 \cdot 10^4 \cdot A^{0.10} \left(\frac{E_0}{1\ \mathrm{PeV}} \right)^{0.90}$$

Number of electrons at shower maximum

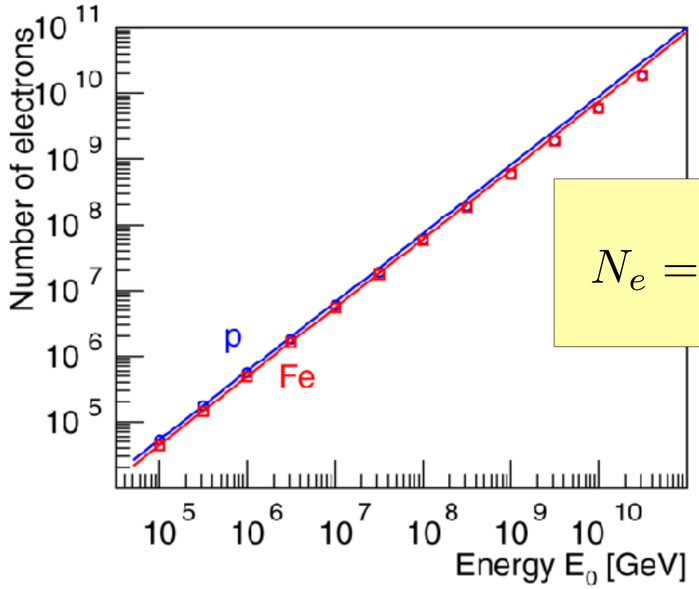

$$\frac{E_{em}}{E_0} = \frac{E_0 - N_\mu E_c^\pi}{E_0} = 1 - \left(\frac{E_0}{A E_c^\pi} \right)^{\beta - 1}$$

$$N_e = \frac{E_{em}}{g E_c^e} \approx 6 \cdot 10^5 \cdot A^{-0.046} \left(\frac{E_0}{1\ \mathrm{PeV}} \right)^{1.046}$$

J. Matthews, Astrop. Phys. 22 (2005) 387

JRH, Mod. Phys. Lett. A 22 (2007) 1533

A Matthews Heitler Model – N_μ vs. N_e

N_e-N_μ plane

$$N_\mu|_{A=const} \approx 0.18 A^{0.14} N_e^{0.86}$$

$$N_\mu|_{E_0=const} \approx 5.77 \cdot 10^{16} \left(\frac{E_0}{1\ \mathrm{PeV}}\right) N_e^{-2.17}$$

N_e-N_μ ratio

$$\frac{N_e}{N_\mu} \approx 35.1 \cdot \left(\frac{E_0}{A \cdot 1\ \mathrm{PeV}}\right)^{0.15}$$

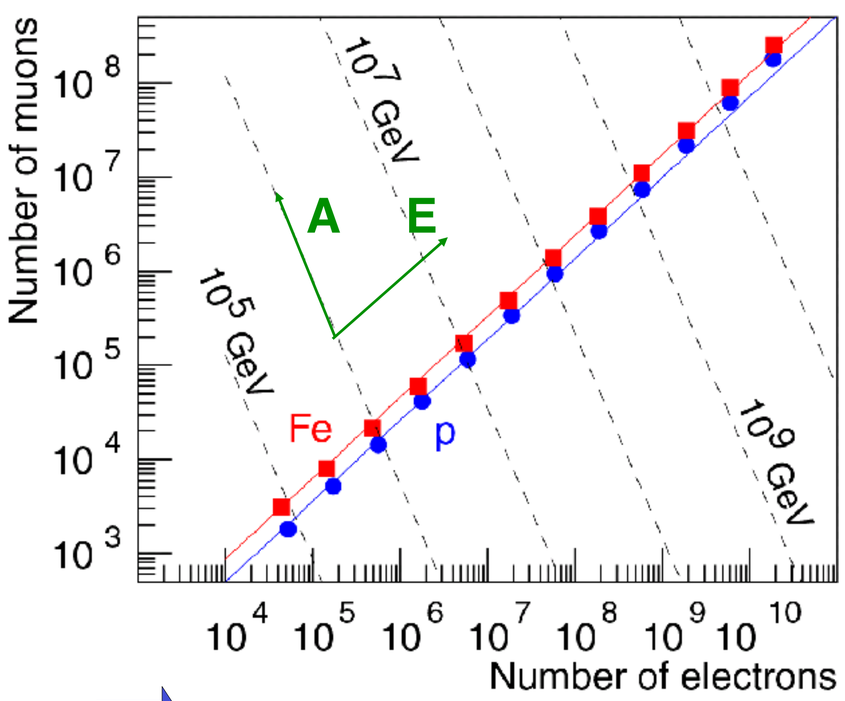

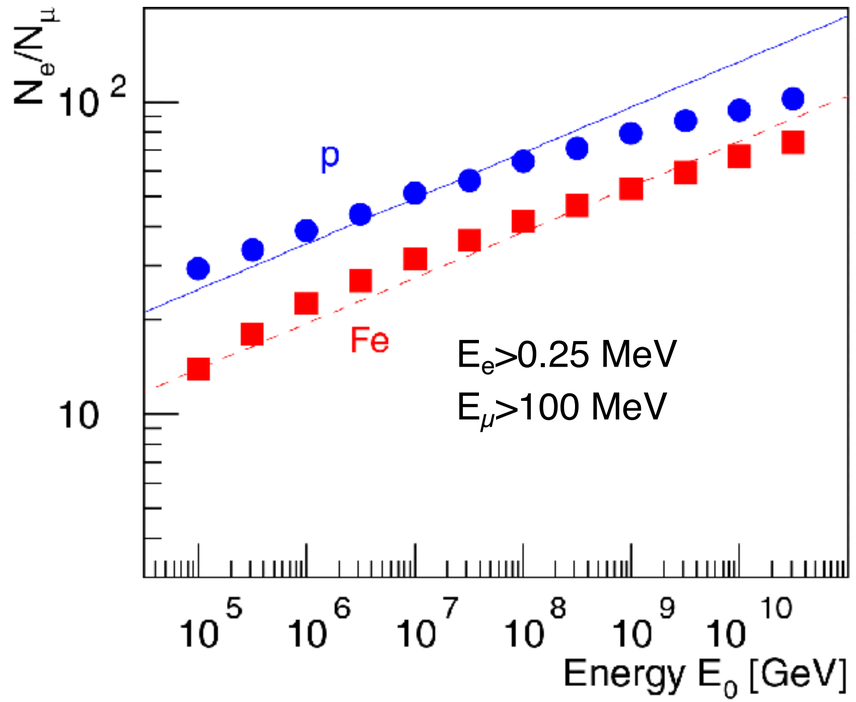

➡ estimator for mass *A* of primary particle

JRH, Mod. Phys. Lett. A 22 (2007) 1533

A Heitler Model – X_{max}

$$X^p_{max} = \lambda_i^{p-air} \ln 2 + X_0 \ln\left(\frac{\kappa E_0}{3 N_{ch} E_c^e}\right)$$

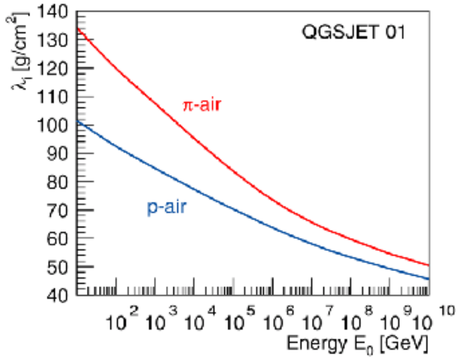

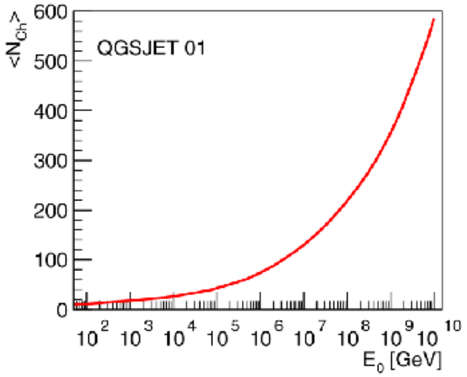

proton air interaction length $\lambda_i^{p-air} = \xi + \zeta \lg \frac{E_0}{\mathrm{PeV}}$ ζ=-4.88 g/cm²

multiplicity of charged particles produced in π-N interactions $N_{ch} = N_0 \left(\frac{E_0}{\mathrm{PeV}}\right)^{\eta}$ η=0.13

$$X^p_{max} = \xi \ln 2 - X_0 \left(\frac{3 N_0 E_c^e}{\kappa \cdot \mathrm{PeV}}\right) + \Lambda^p \lg\left(\frac{E_0}{\mathrm{PeV}}\right)$$

elongation rate

e/m shower $\Lambda^{\gamma} = X_0 \ln 10 \approx 84.4 \mathrm{g/cm}^2$

proton shower

$\Lambda^p = X_0 \ln 10 - \eta X_0 \ln 10 + \zeta \ln 2 \approx 70 \mathrm{g/cm}^2$

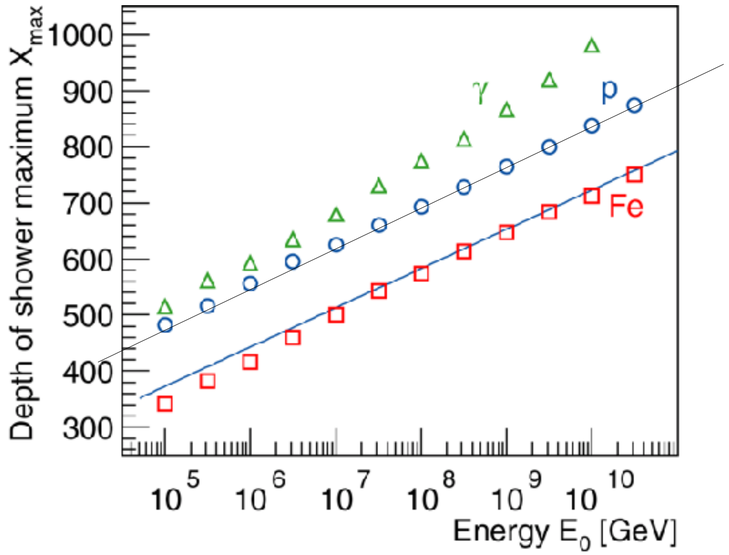

X_{max} for heavy nuclei

$$X^A_{max} = X^p_{max} - X_0 \ln A$$

➡ **estimator for mass *A* of primary particle**

J. Matthews, Astrop. Phys. 22 (2005) 387

JRH, Mod. Phys. Lett. A 22 (2007) 1533

A Matthews Heitler Model – mass resolution in EAS measurements

depth of shower maximum

$$X^{A}_{max} = X^{p}_{max} - X_0 \ln A$$

radiation length X_0=36.7 g/cm²

typical uncertainty

$$\Delta X_{max} \approx 20 \text{ g/cm}^2$$

expected mass resolution

$$\Delta \ln A \approx 0.8 - 1$$

electron-muon ratio

$$\lg(N_e/N_\mu) = C - 0.065 \ln A.$$

$$\Delta \frac{N_e}{N_\mu} \approx 16\% - 20\%$$

4 to 5 mass groups
p, He, CNO, (Si), Fe

JRH, Nucl. Instr. and Meth. A 588 (2008) 181

JRH, Mod. Phys. Lett. A 22 (2007) 1533

KArlsruhe Shower Core and Array DEtector

Simultaneous measurement of
electromagnetic,
muonic,
hadronic
shower components

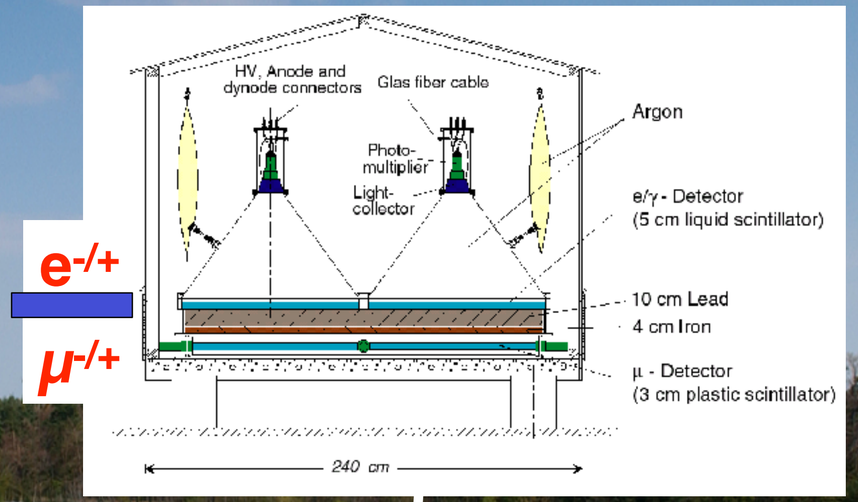

$e^{-/+}$

$\mu^{-/+}$

200 m

200 m

T. Antoni et al, Nucl. Instr. & Meth. A 513 (2004) 490

Event reconstruction in the scintillator array

electromagnetic component

shower core	$\Delta r = 2.5 – 5.5$ m
shower direction	$\Delta\alpha = 0.5° – 1.2°$
shower size	$\Delta N_e/N_e = 6 – 12$ %

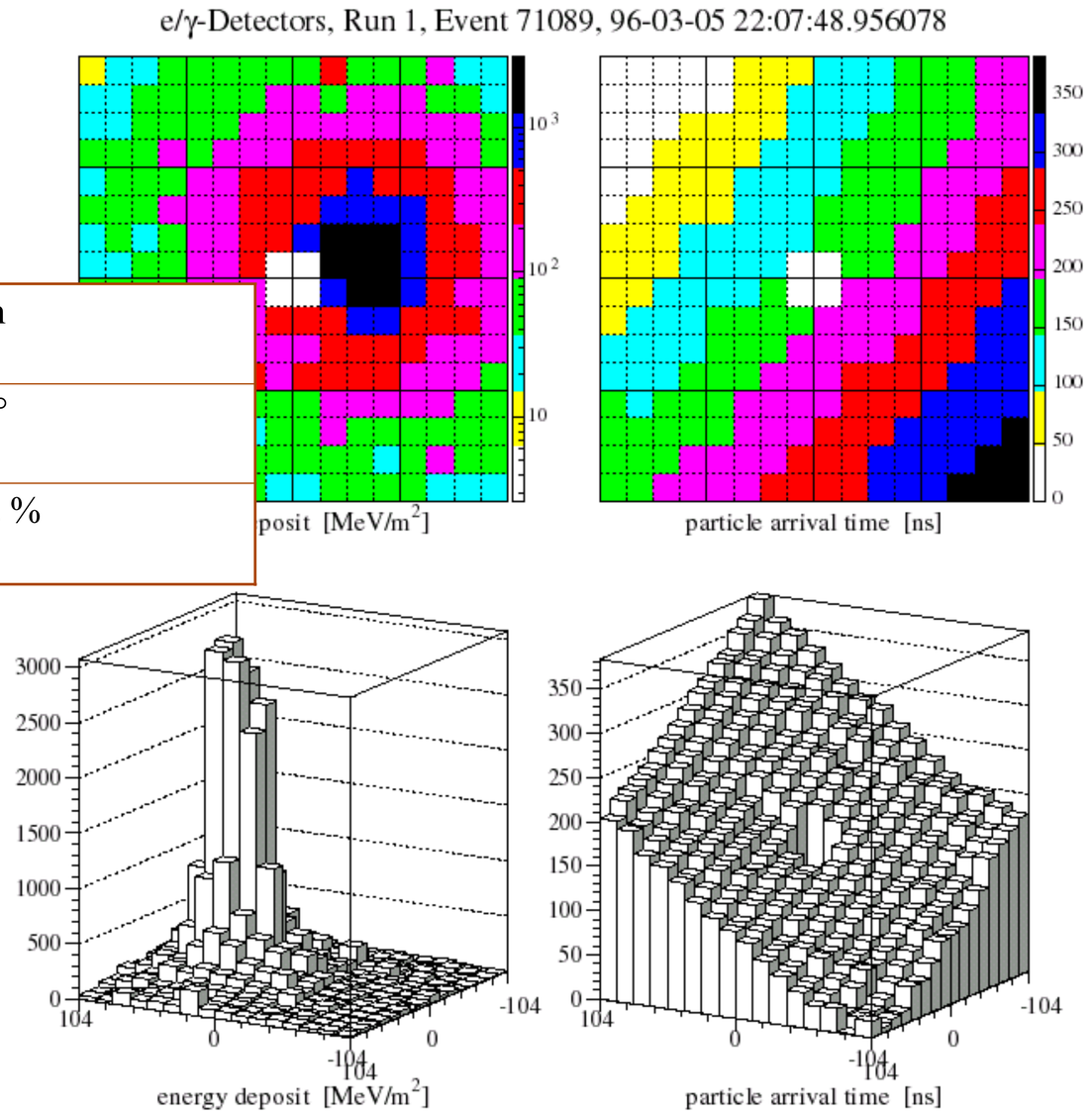

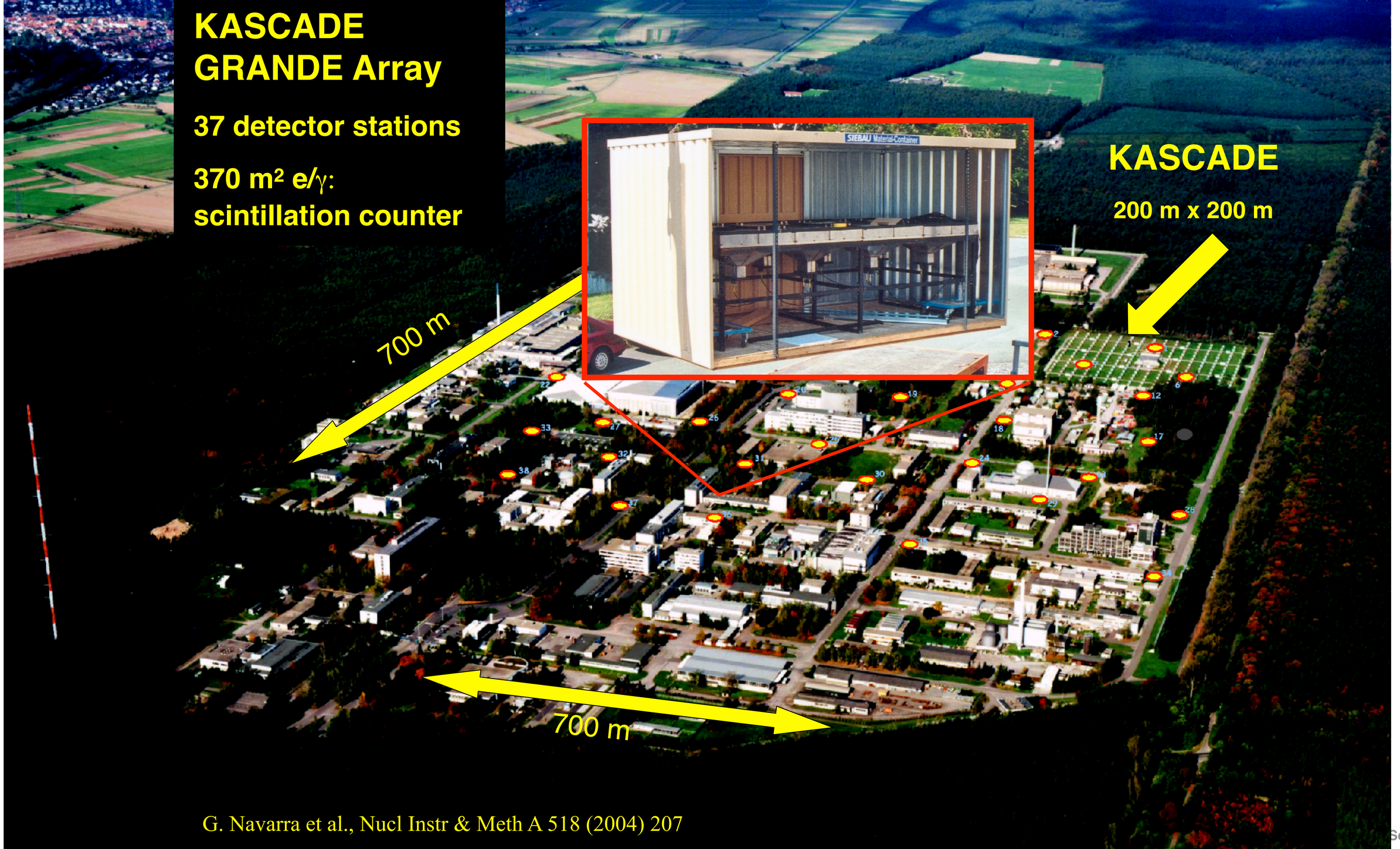

G. Navarra et al., Nucl Instr & Meth A 518 (2004) 207

KASCADE-Grande – Lateral distributions

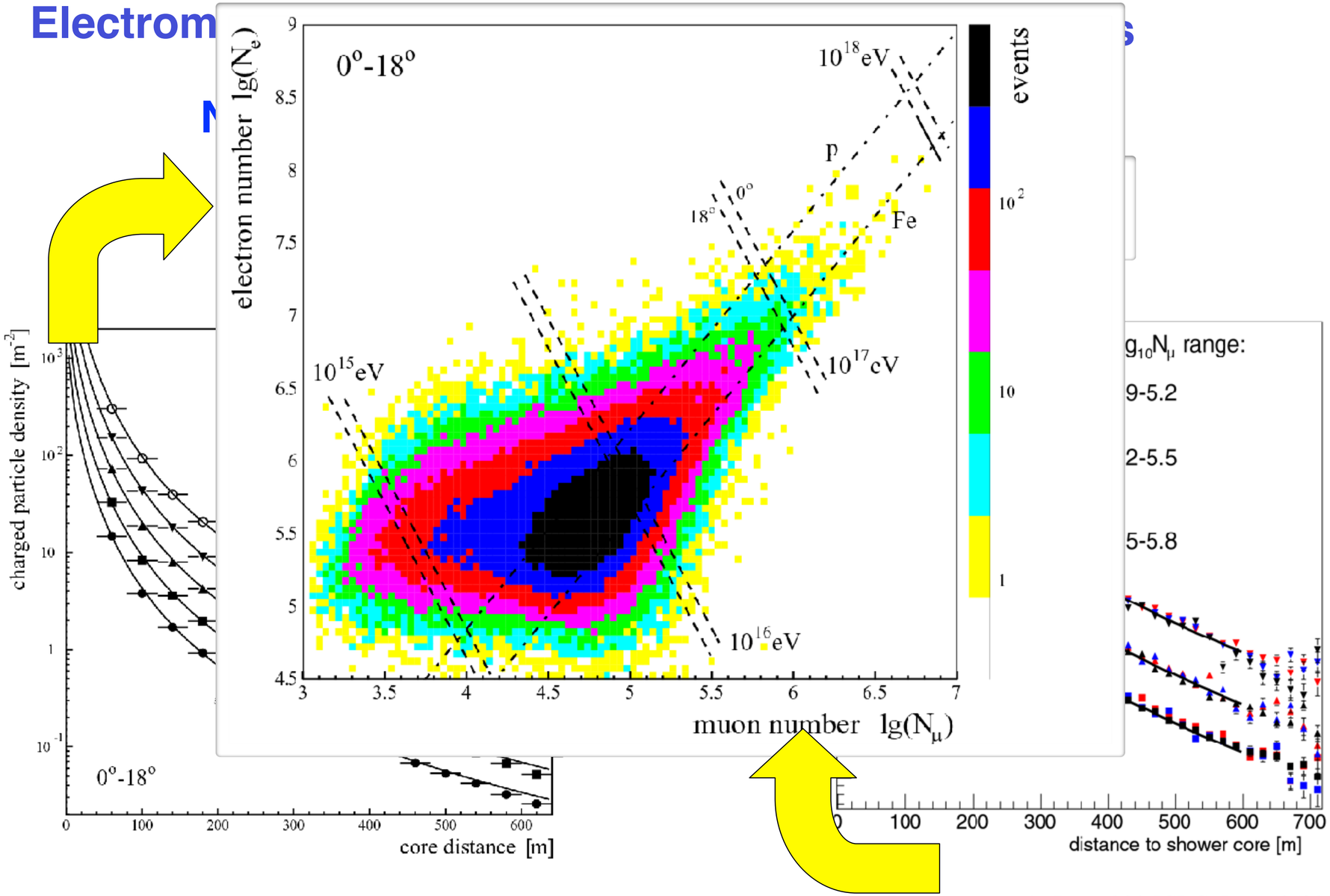

R. Glasstetter et al., Proc. 29th ICRC, Pune 6 (2005) 293

J. v. Buren et al., Proc. 29th ICRC, Pune 6 (2005) 301

KASCADE: Energy spectra for elemental groups

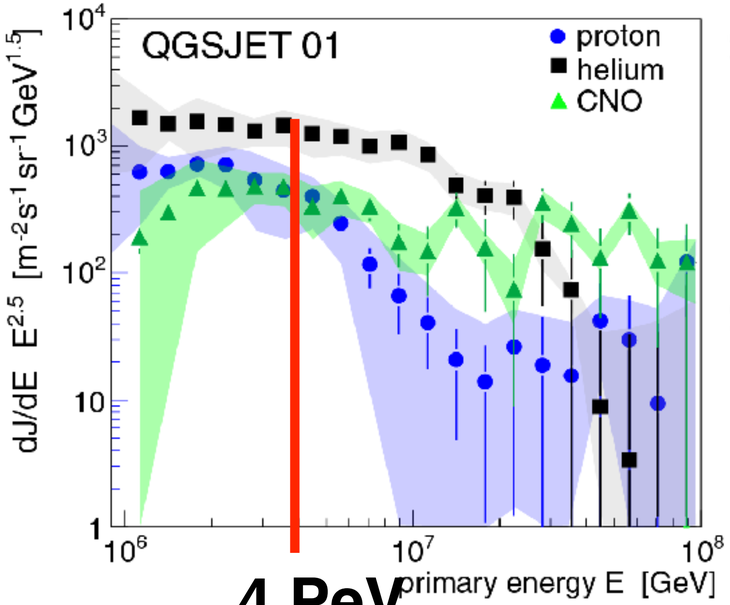

4 PeV

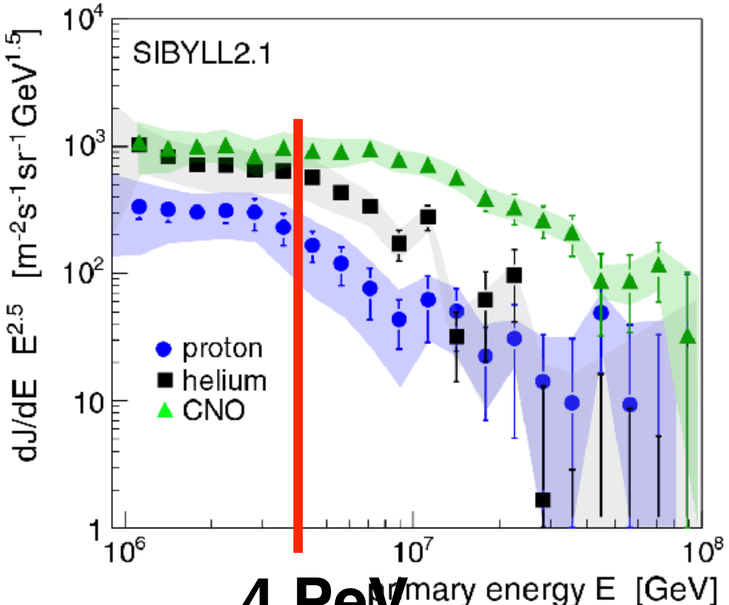

4 PeV

Knee caused by cut-off for light elements

Astrophysical interpretation limited by description of interactions in the atmosphere

T. Antoni et al., Astropart. Phys. 24 (2005) 1

Test of hadronic interaction models

QGSJET 01

Number of hadrons vs. number of muons

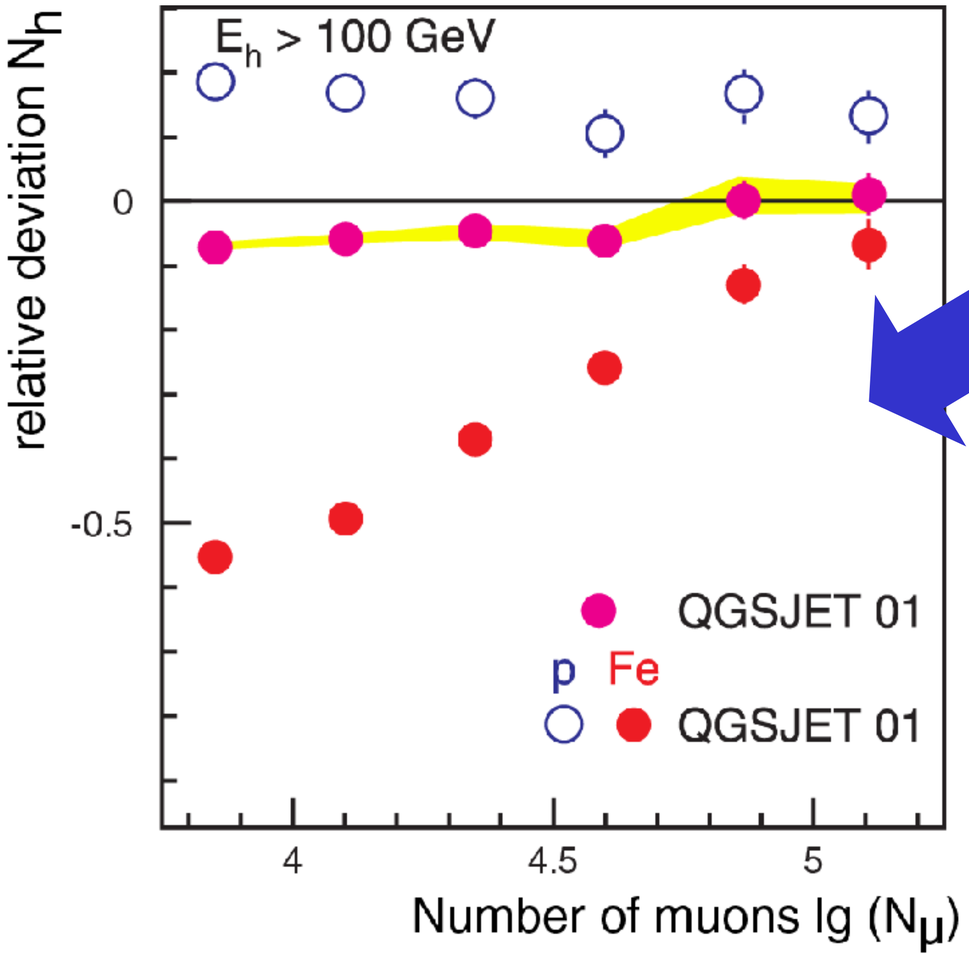

inconsistencies on 10% level

N_e-N_μ analysis

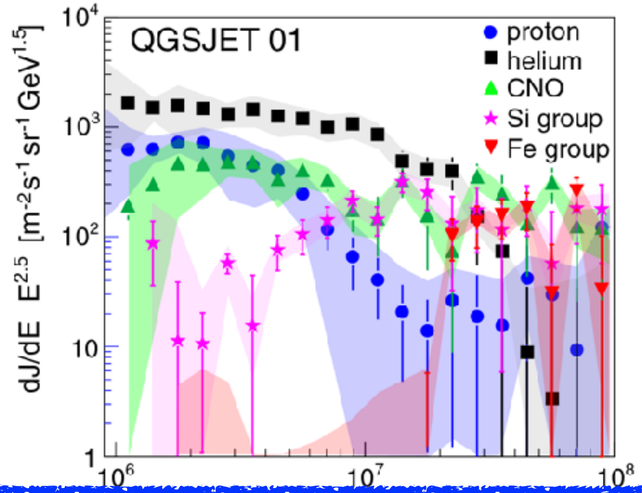

in literature:

ideas that knee is caused by new interactions in atmosphere

—> energy is carried away by „invisible channels"

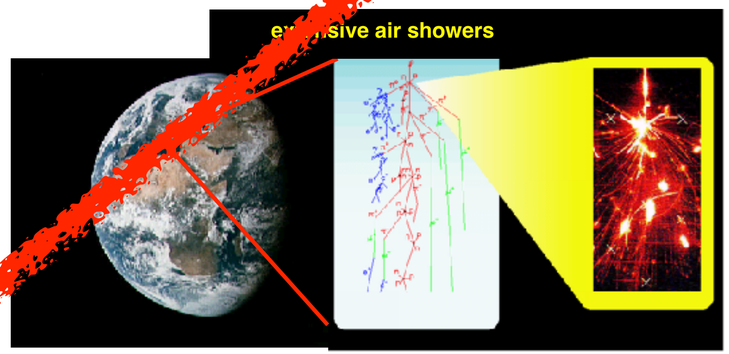

J. Milke et al, Proc. 29th Int. Cosmic Ray Conference Pune 6 (2005) 125

ELSEVIER

Nuclear Physics B (Proc. Suppl.) 75A (1999) 238–240

NUCLEAR PHYSICS B
PROCEEDINGS
SUPPLEMENTS

Electron, muon and hadron size spectra of EAS in the "knee" region

R. Glasstetter[a] and J.R. Hörandel[a] for the KASCADE Collaboration*

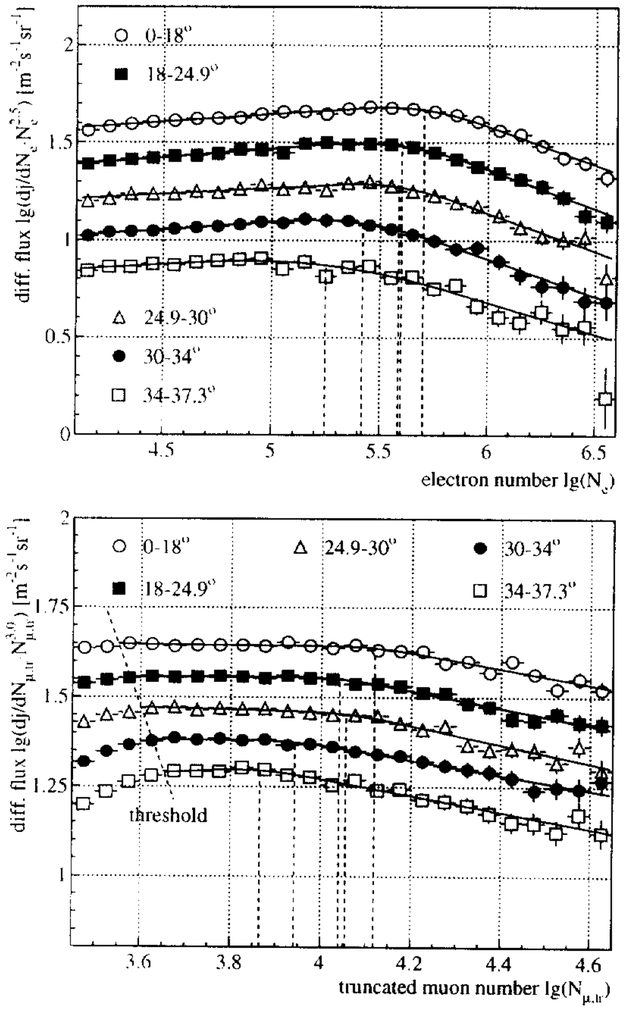

Figure 1. Electromagnetic (top) and muonic (bottom) shower size spectra for different zenith angle bins.

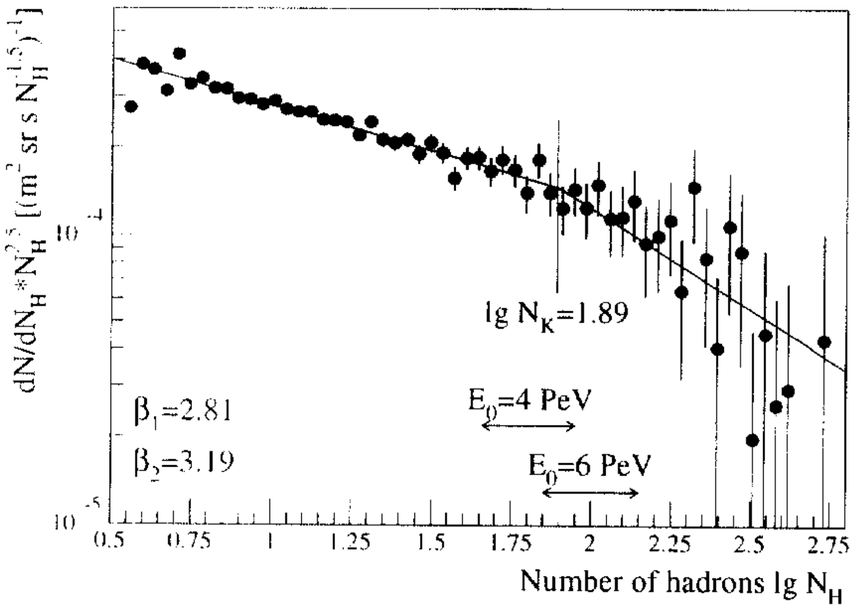

Figure 3. Hadronic shower size spectrum.

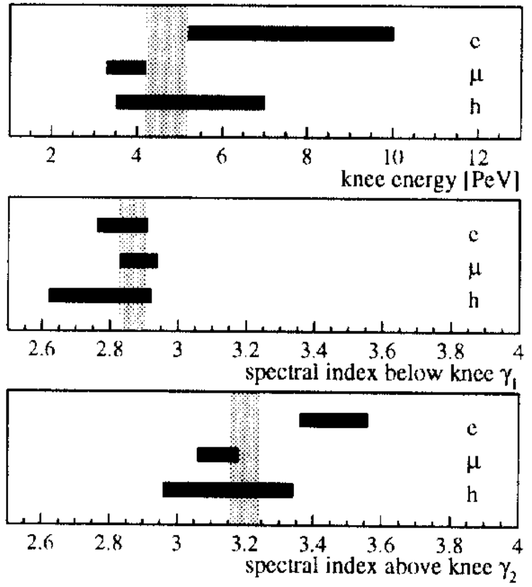

Figure 4. Knee position and spectral indices.

knee observed in all components, electromagnetic, muonic, and hadronic!

KASCADE-Grande

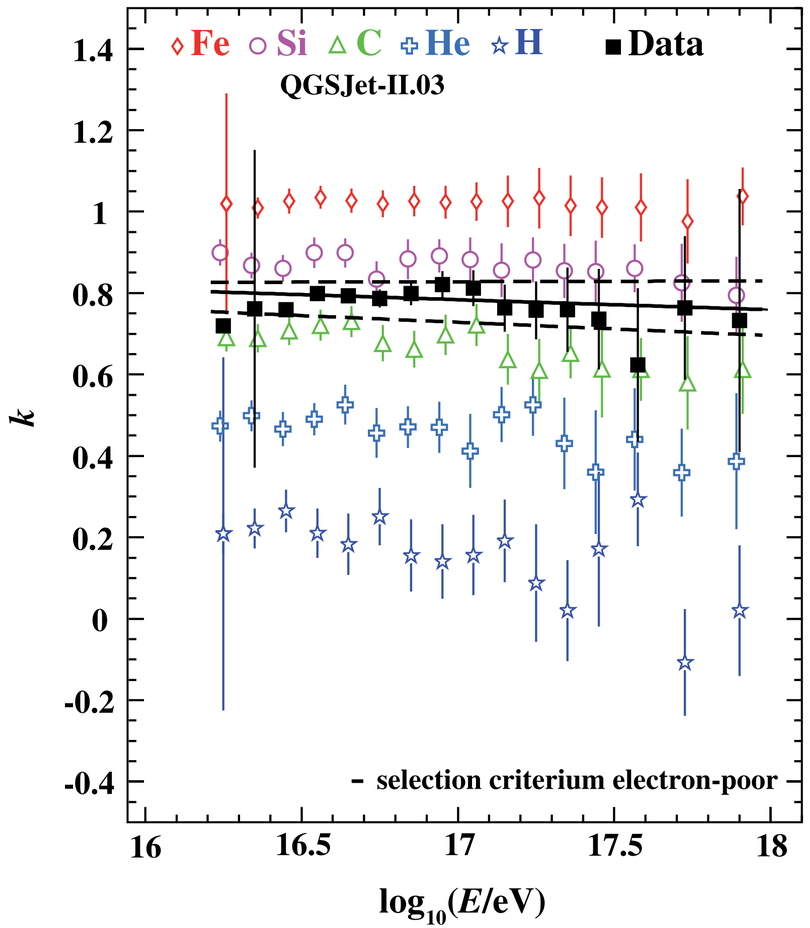

$$k = \frac{\log_{10}(N_{\rm ch}/N_\mu) - \log_{10}(N_{\rm ch}/N_\mu)_{\rm H}}{\log_{10}(N_{\rm ch}/N_\mu)_{\rm Fe} - \log_{10}(N_{\rm ch}/N_\mu)_{\rm H}},$$

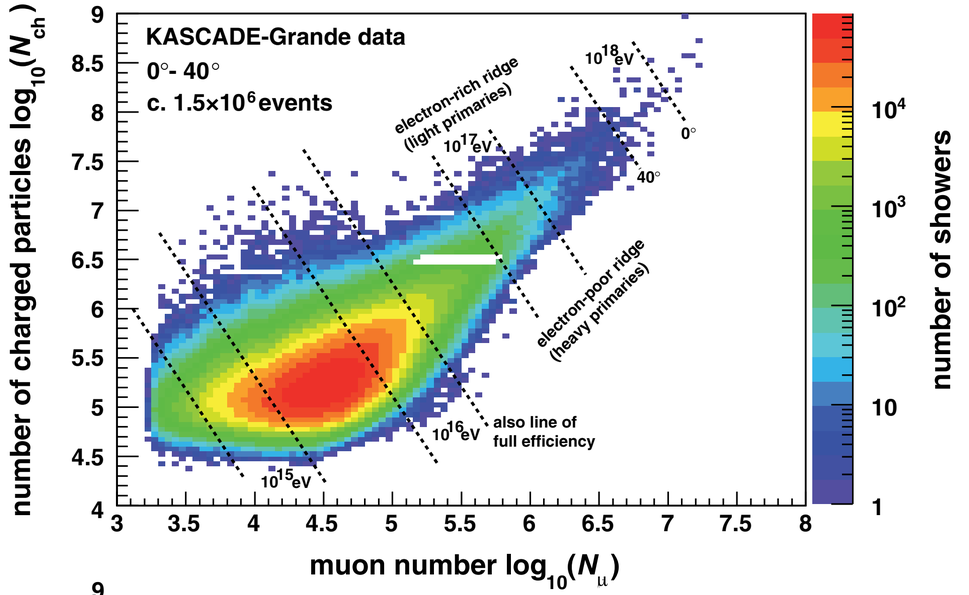

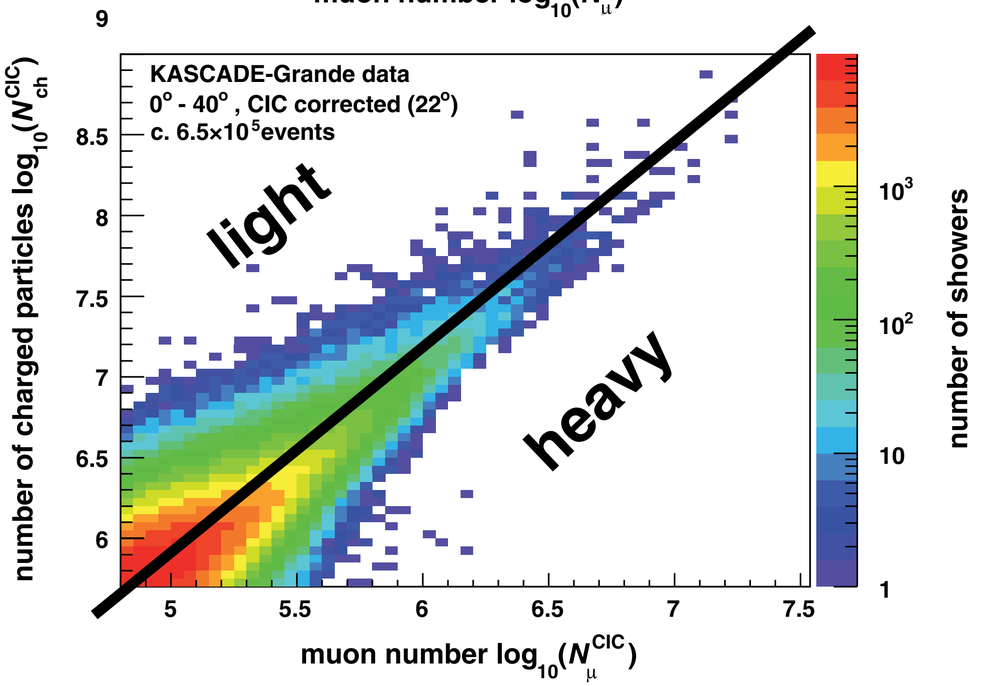

W.D. Apel et al., PRL 107 (2011) 171104

KASCADE-Grande

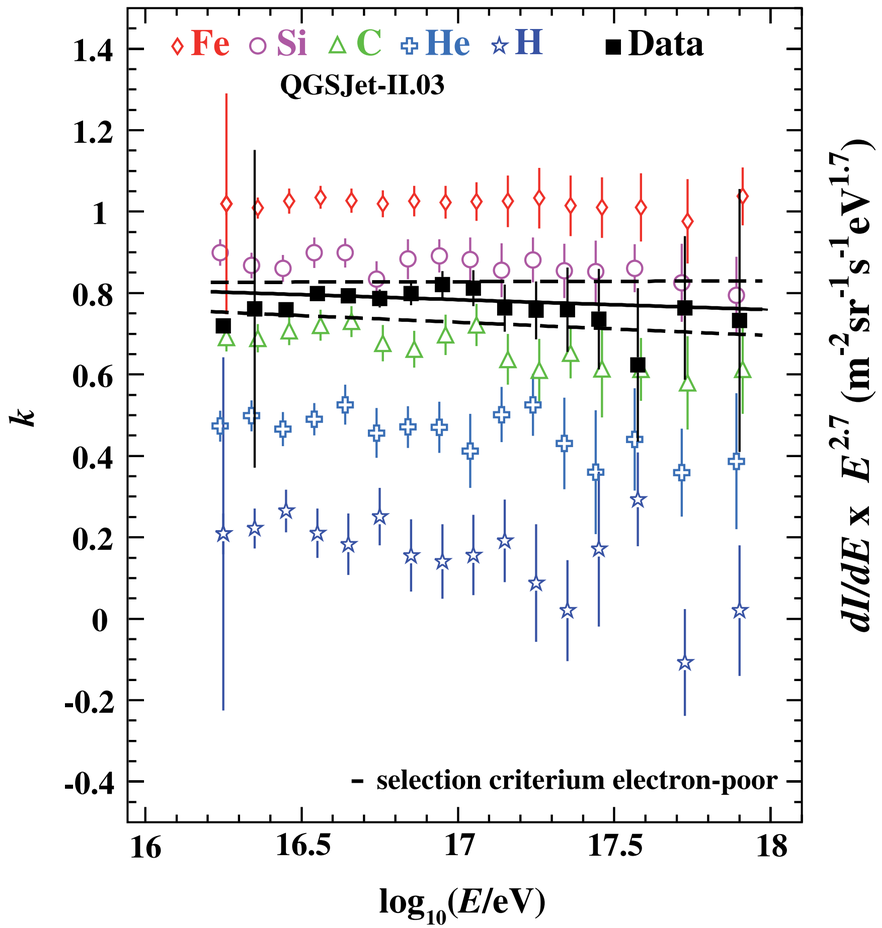

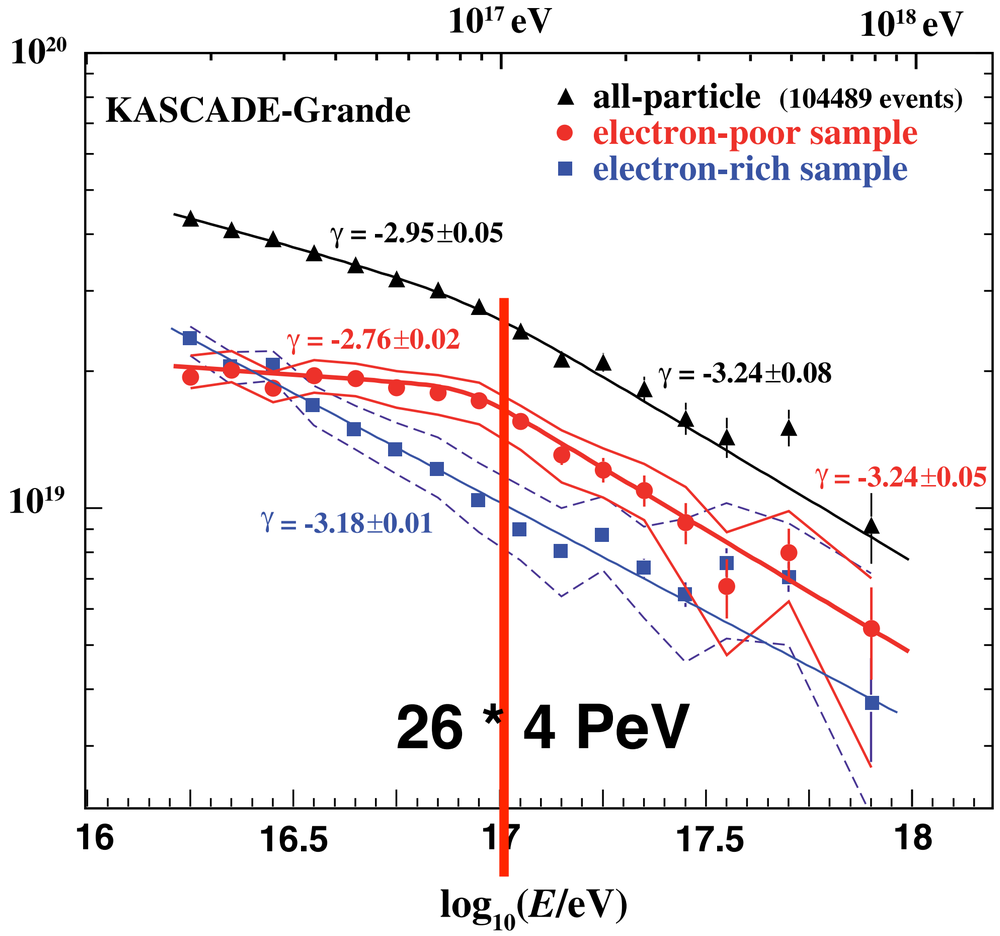

$$k = \frac{\log_{10}(N_{\mathrm{ch}}/N_{\mu}) - \log_{10}(N_{\mathrm{ch}}/N_{\mu})_{\mathrm{H}}}{\log_{10}(N_{\mathrm{ch}}/N_{\mu})_{\mathrm{Fe}} - \log_{10}(N_{\mathrm{ch}}/N_{\mu})_{\mathrm{H}}},$$

W.D. Apel et al., PRL 107 (2011) 171104

Ice Cube - Ice Top

e/m (+μ)

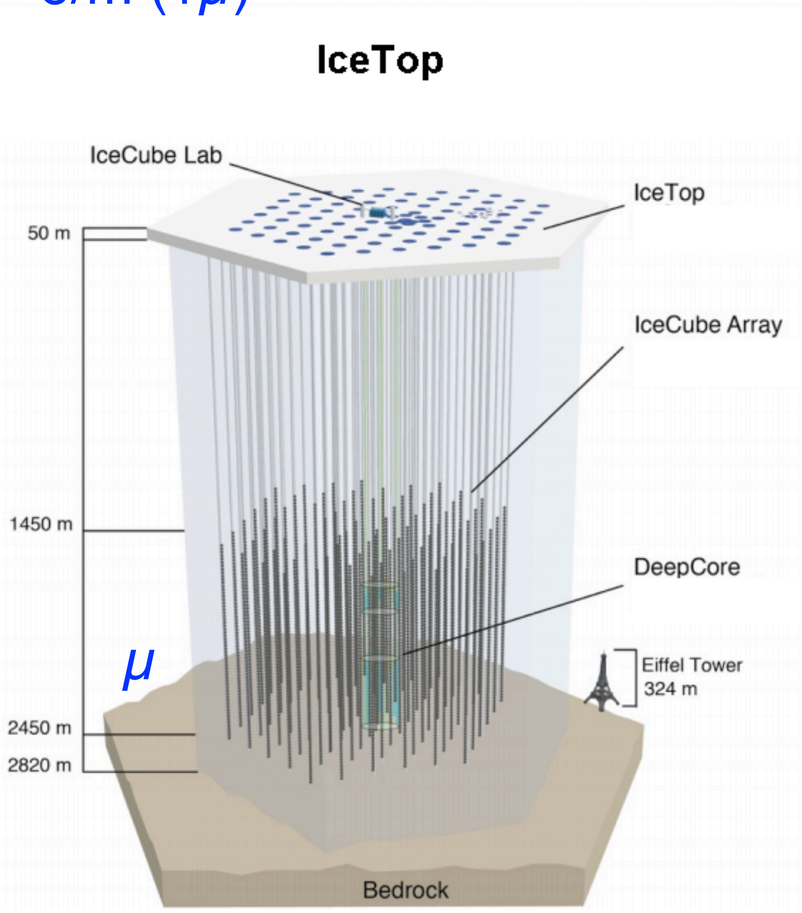

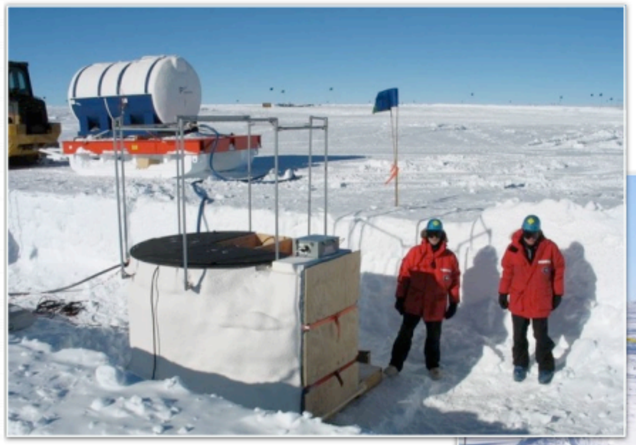

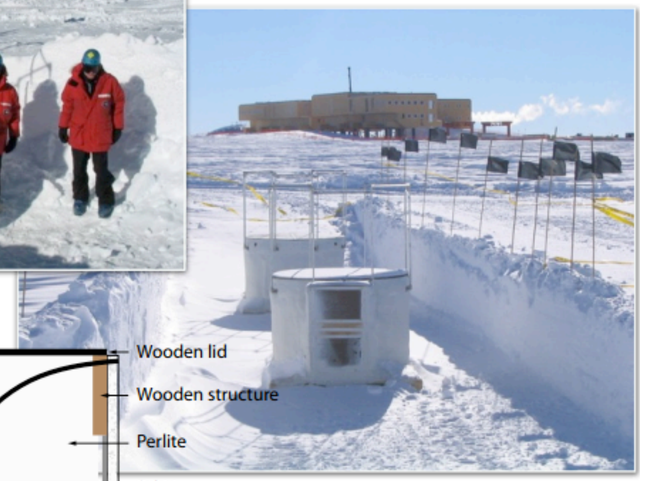

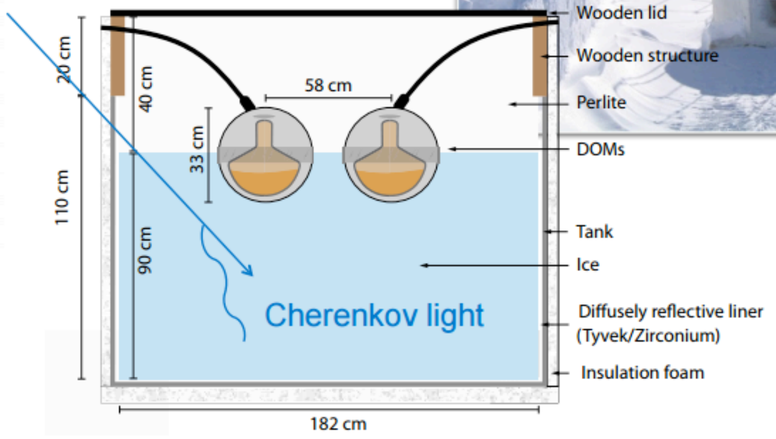

Cosmic ray spectrum and composition from PeV to EeV using 3 years of data from IceTop and IceCube

Ice Cube - Ice Top

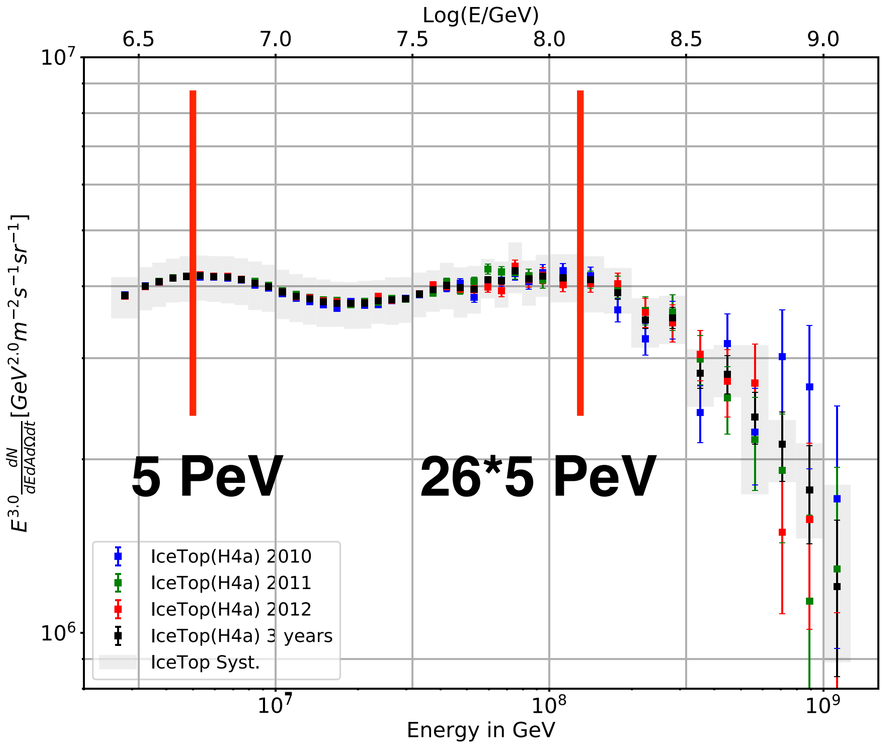

FIG. 9. All-particle energy spectrum from the IceTop-alone analysis from each of the 3 years and the 3 years together.

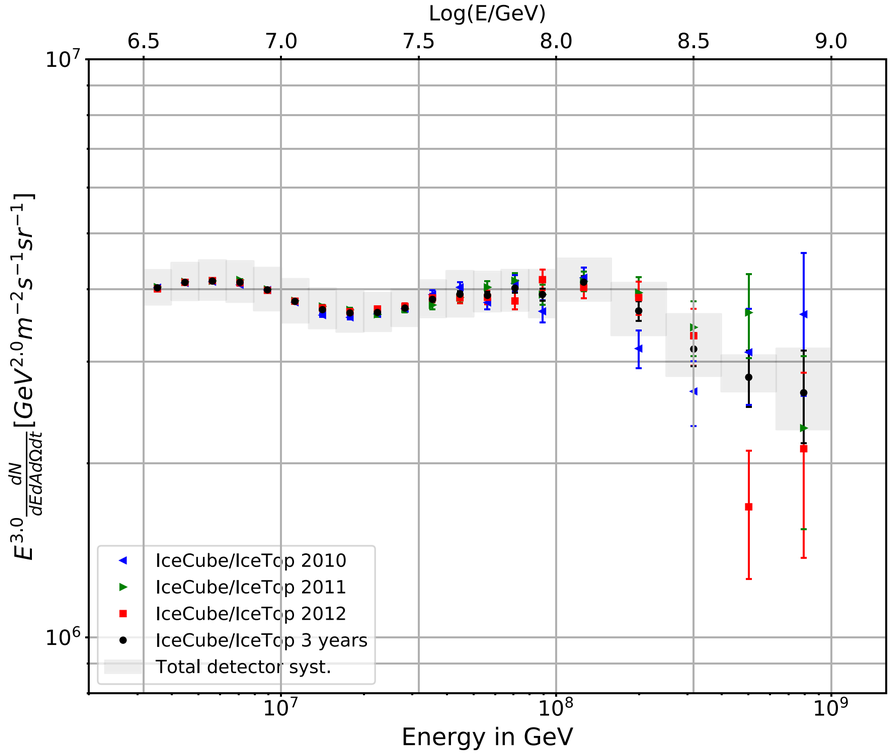

FIG. 12. All-particle energy spectrum from the coincident analysis from each of the 3 years analyzed individually compared to the combined result. The gray band represents the total detector uncertainty from both the IceTop and InIce arrays, as discussed in Sec. IV B.

Ice Top only

combined

M. G. Aartsen et al., PRD 100 (2019) 082002

Cosmic ray spectrum and composition from PeV to EeV using 3 years of data from IceTop and IceCube

Ice Cube - Ice Top

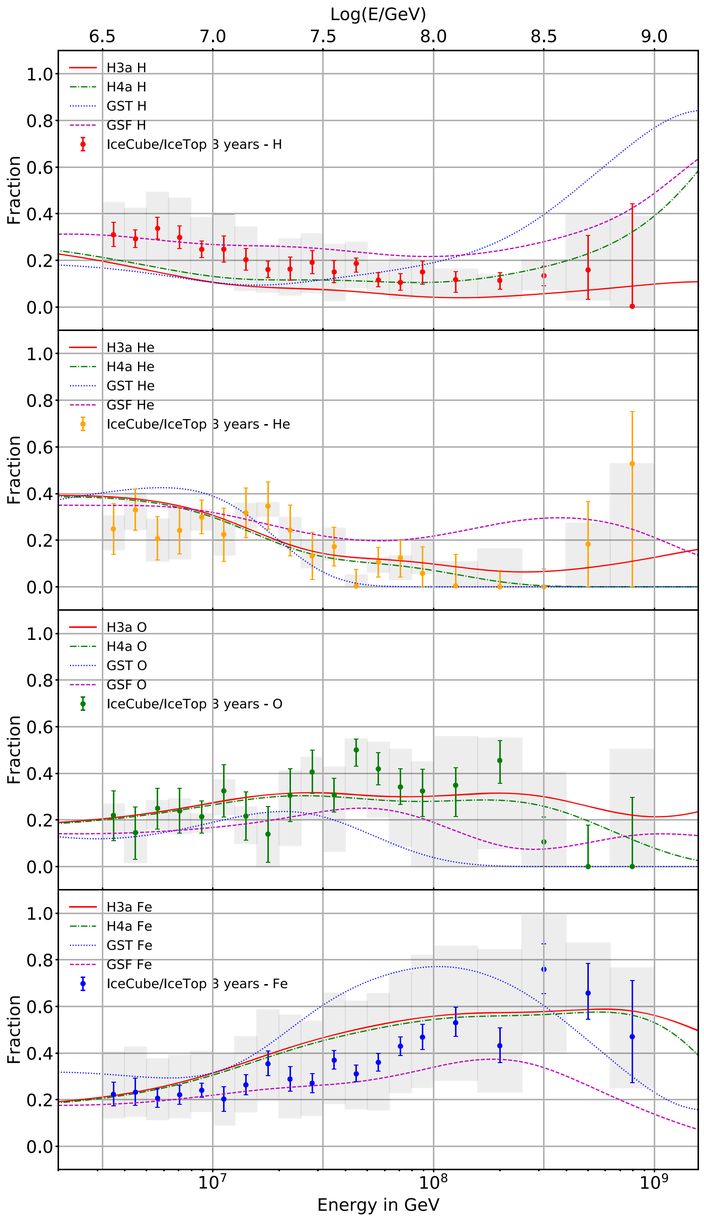

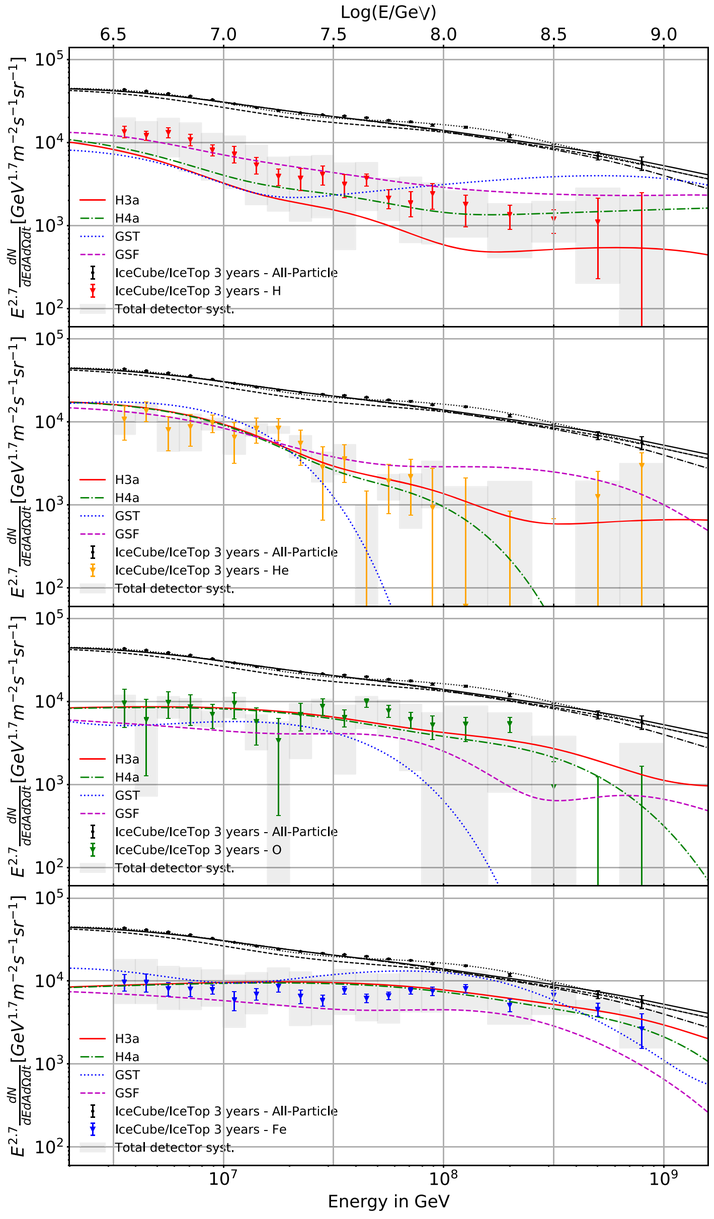

p

He

CNO

Fe

M. G. Aartsen et al., PRD 100 (2019) 082002

Cosmic-ray energy spectrum

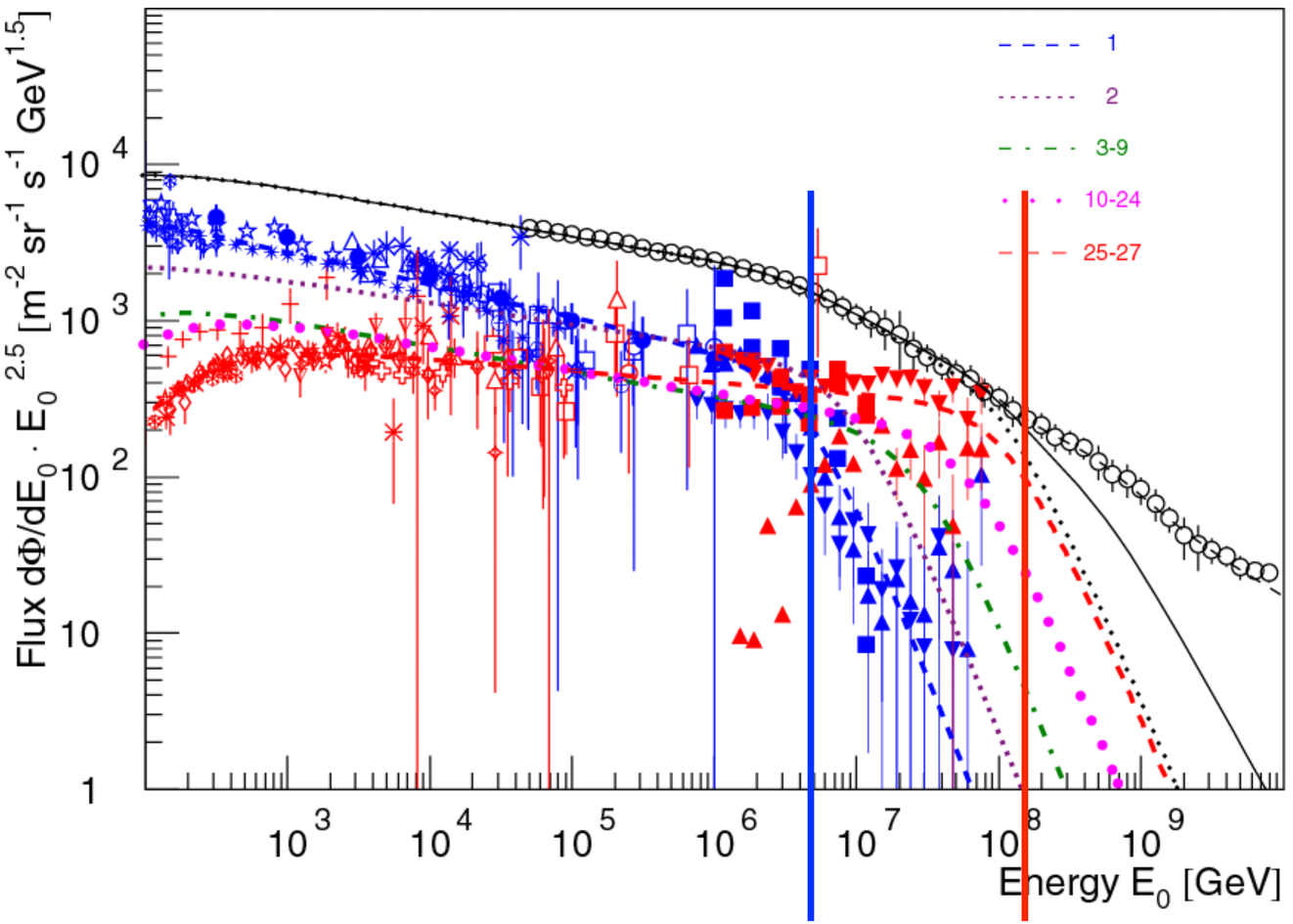

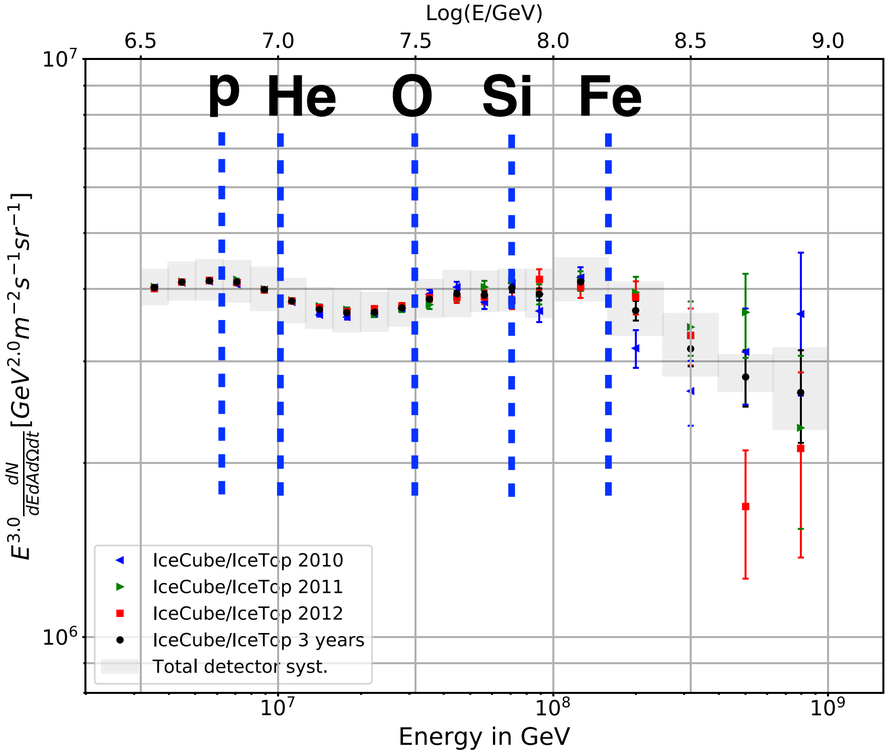

JRH, Astropart. Phys. 19 (2003) 193

TALE (TA low-energy extension)

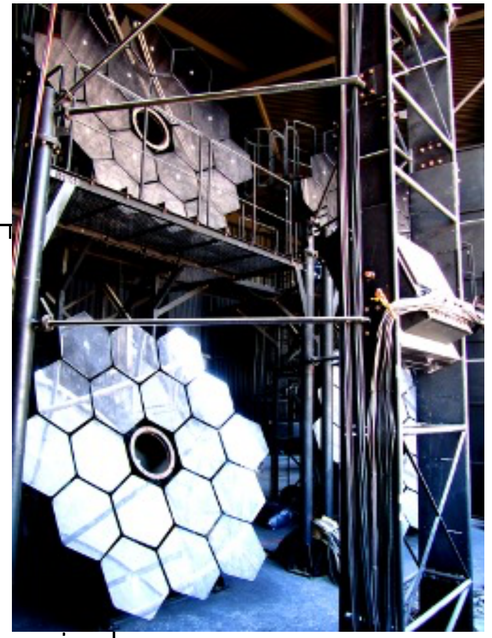

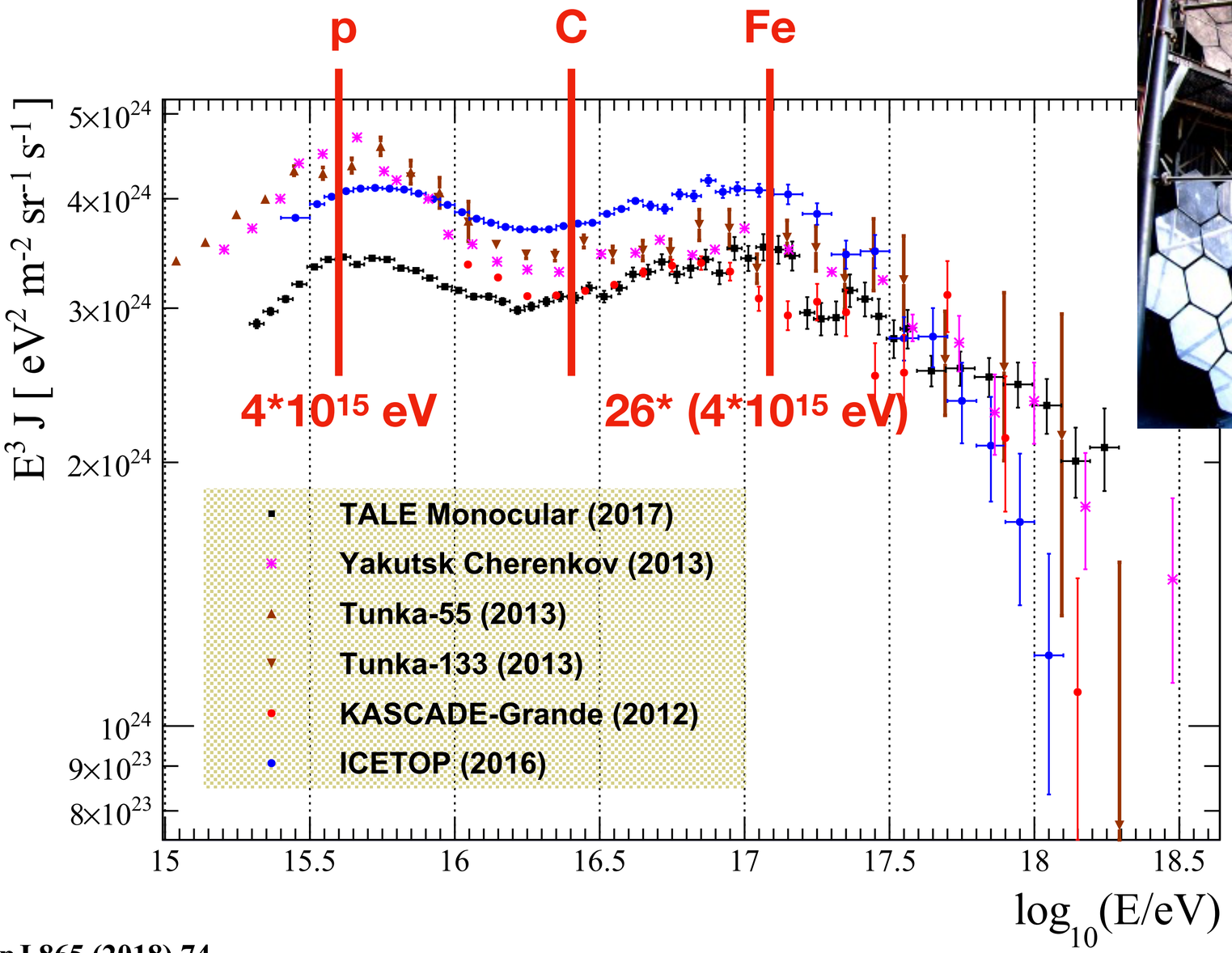

R.U. Abbasi et al., ApJ 865 (2018) 74

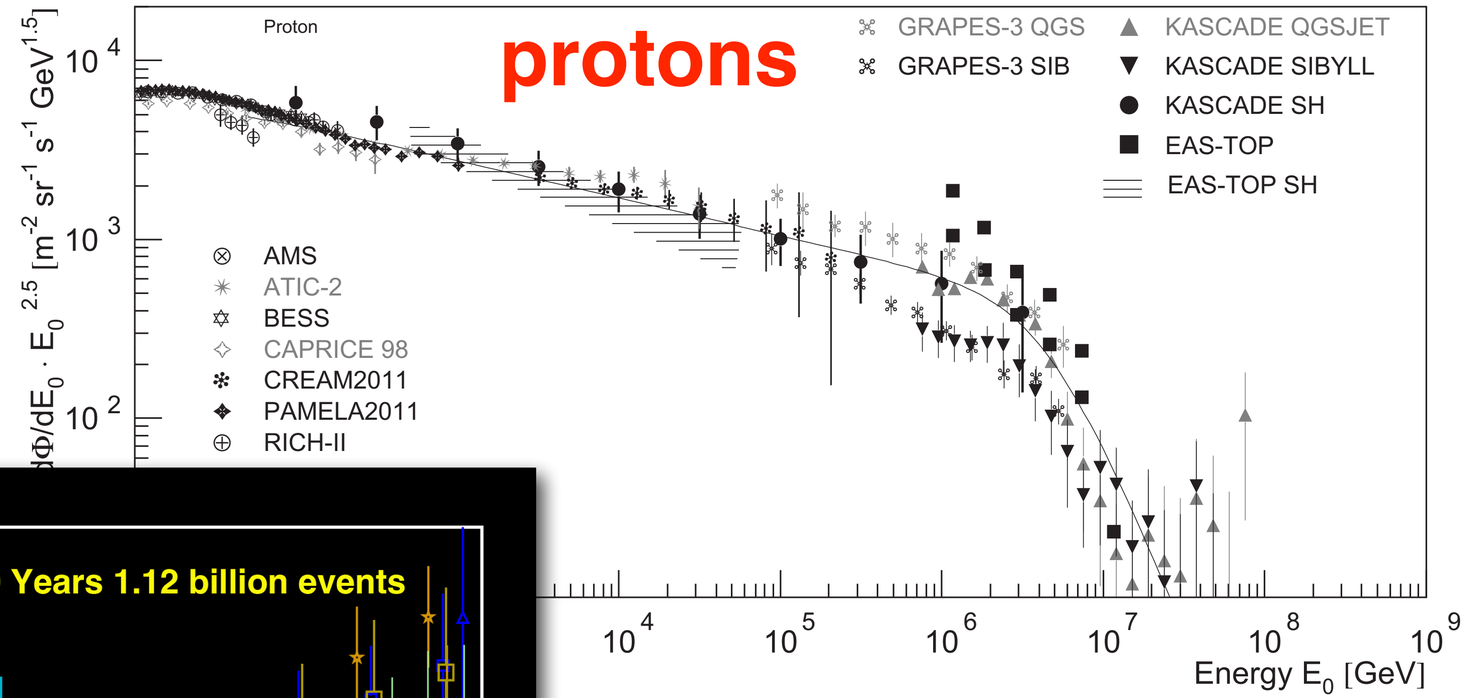

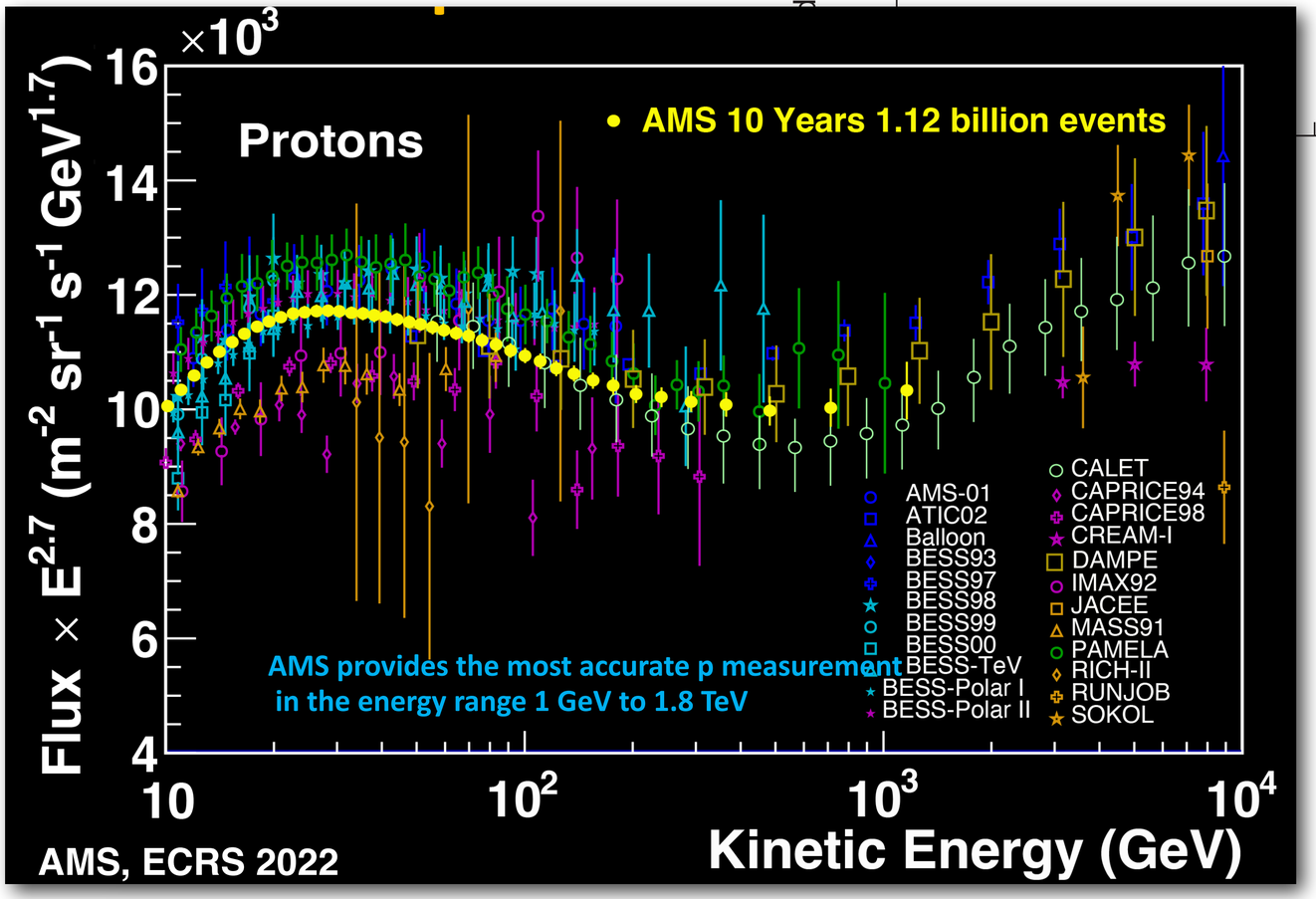

JRH, AIP Conf. Proc. 1516 (2013) 185

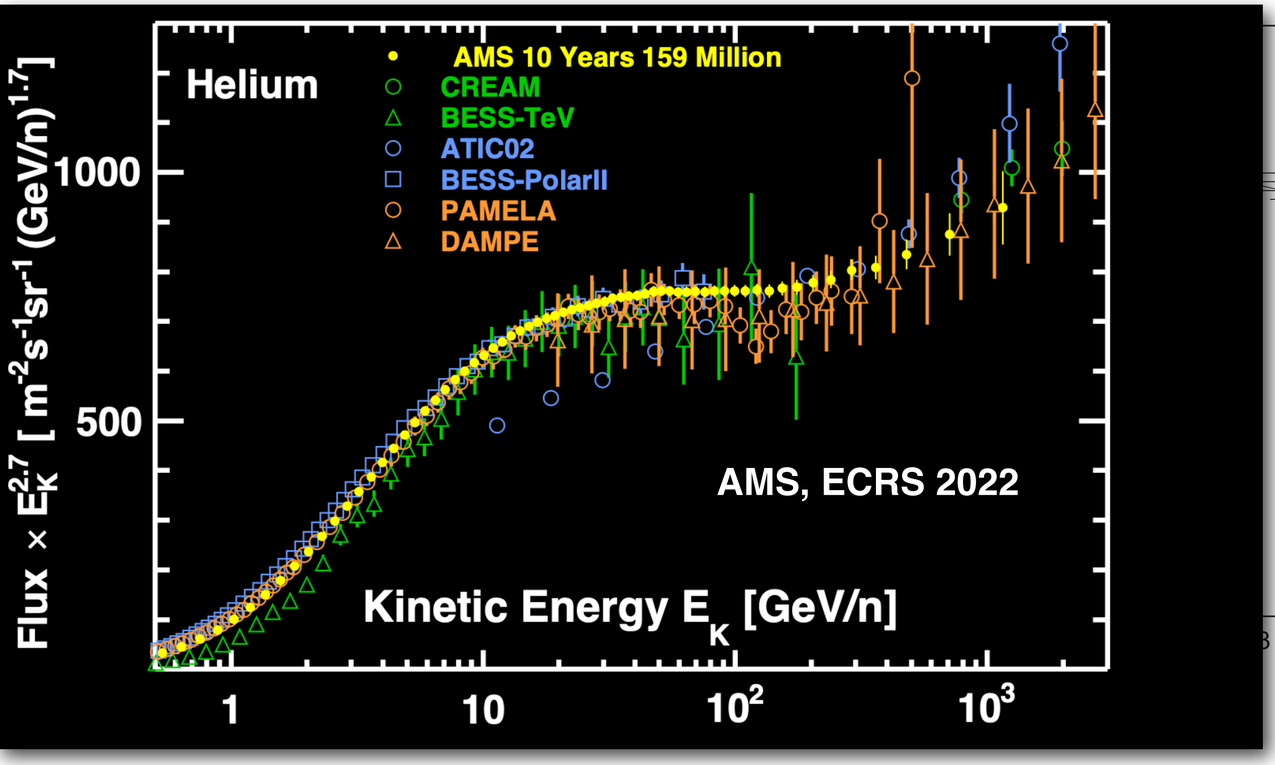

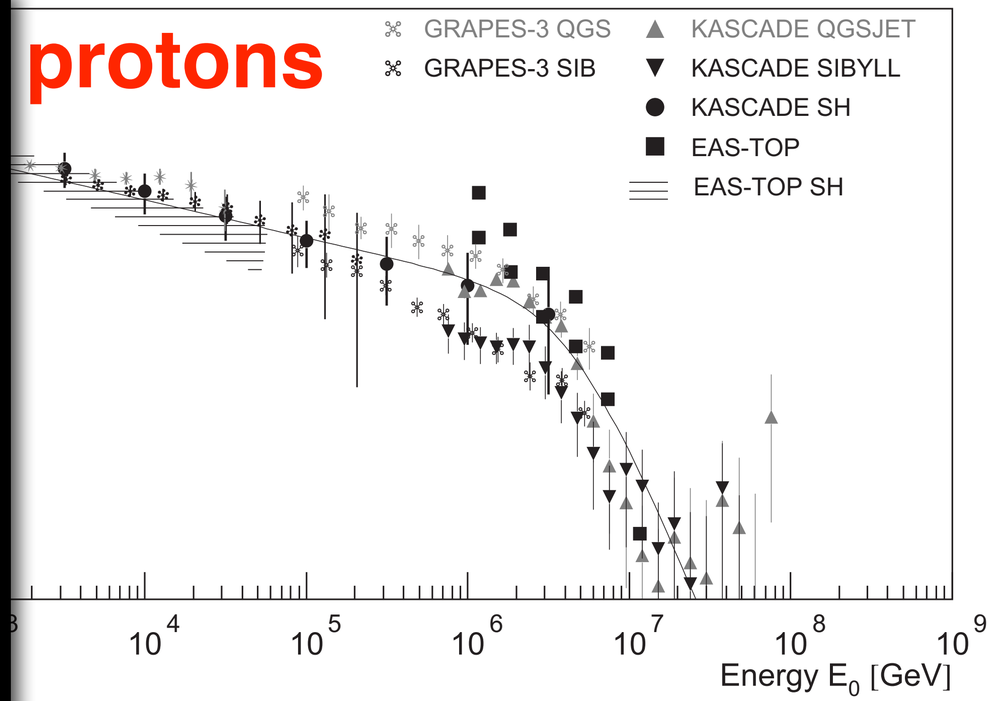

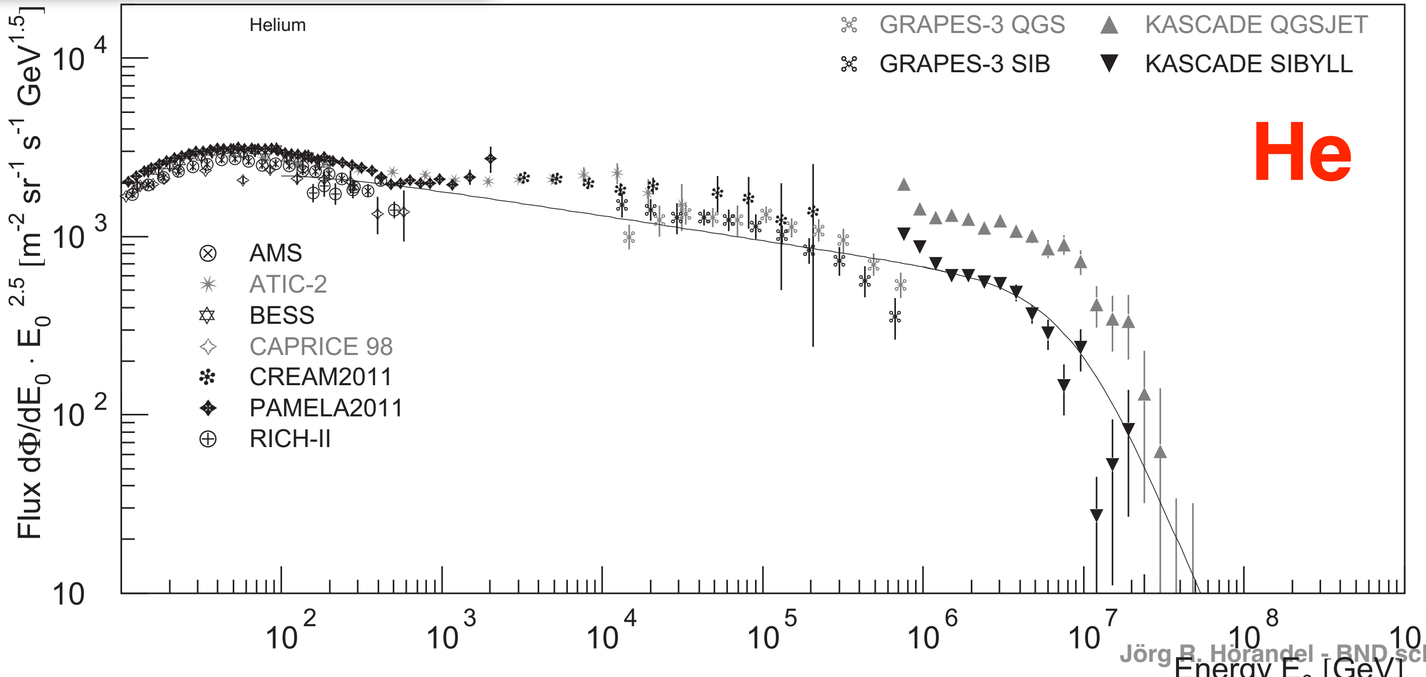

JRH, AIP Conf. Proc. 1516 (2013) 185

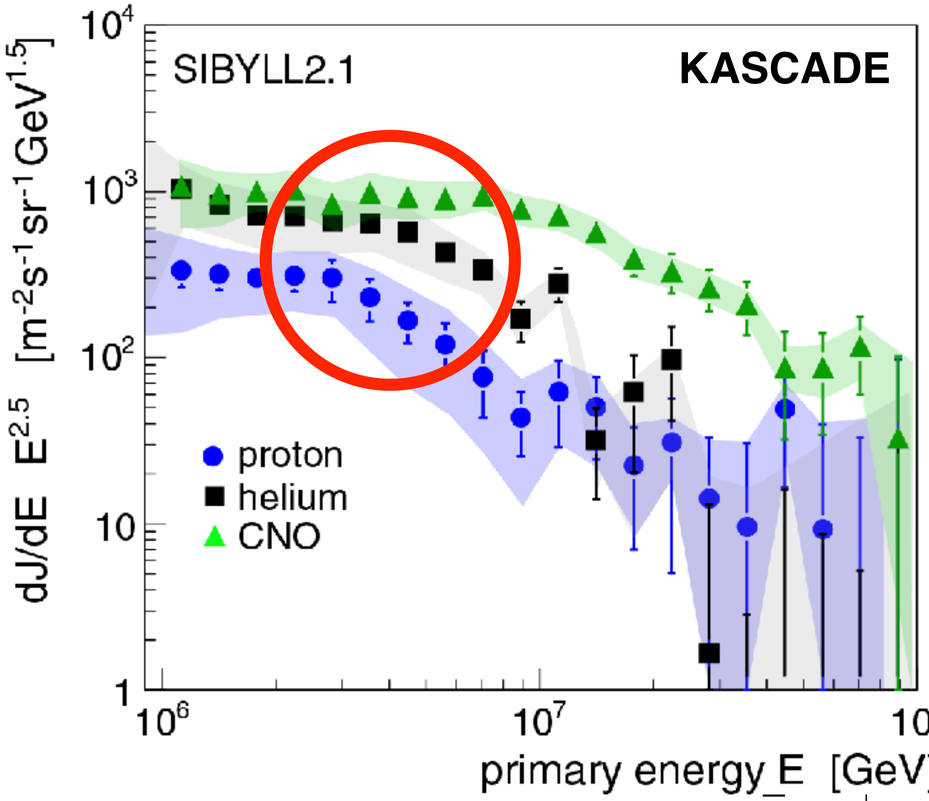

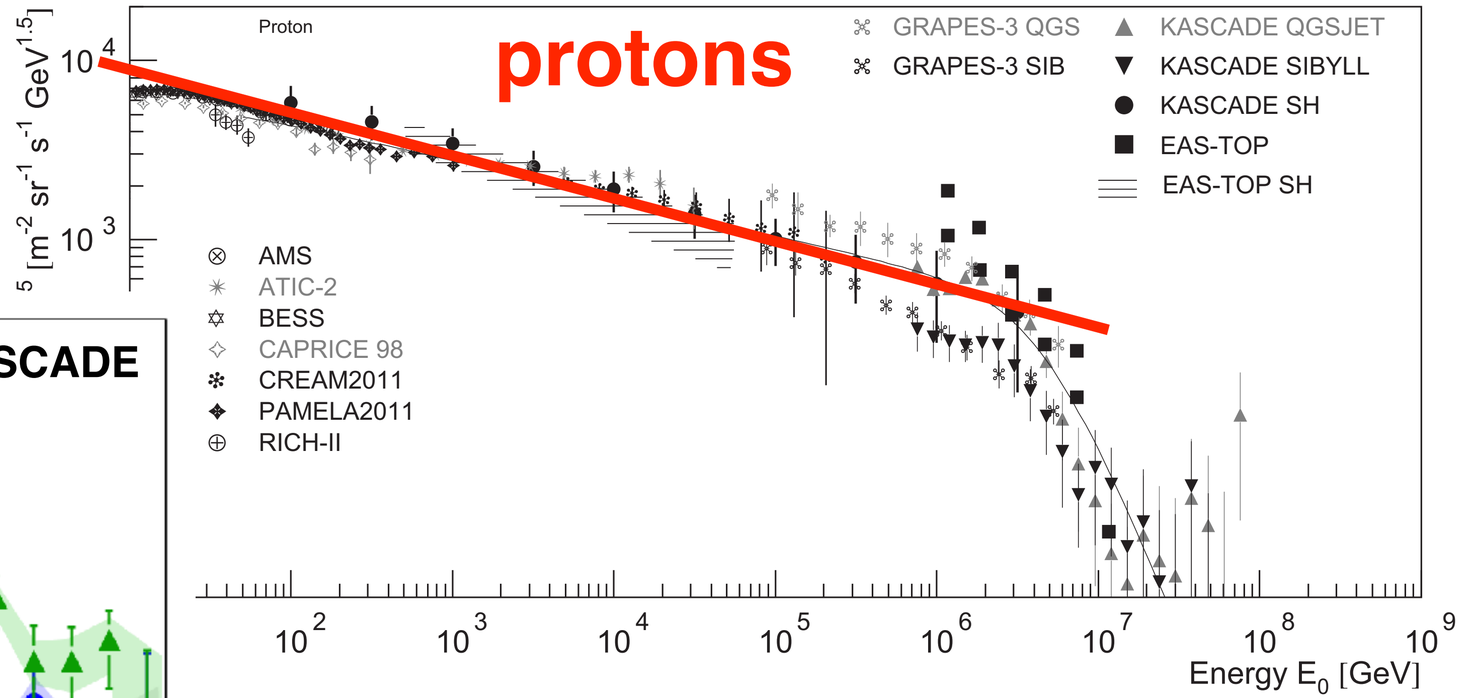

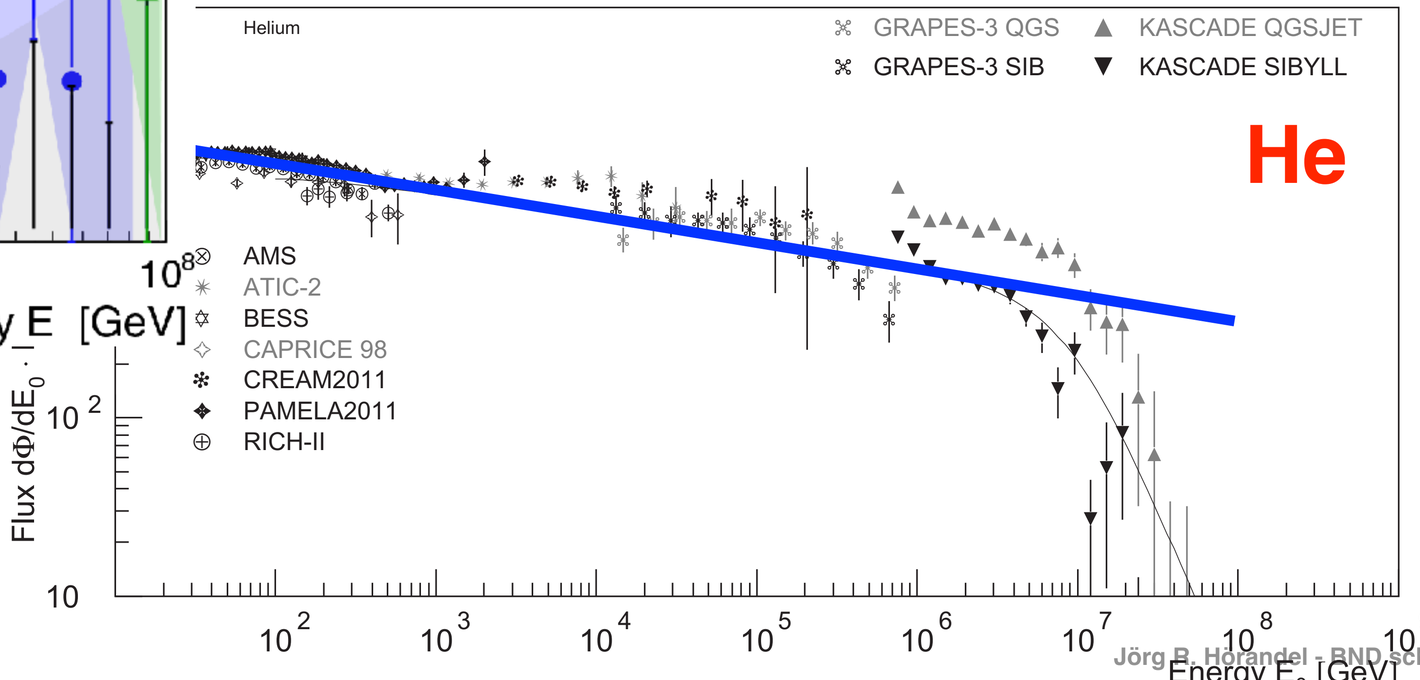

JRH, AIP Conf. Proc. 1516 (2013) 185

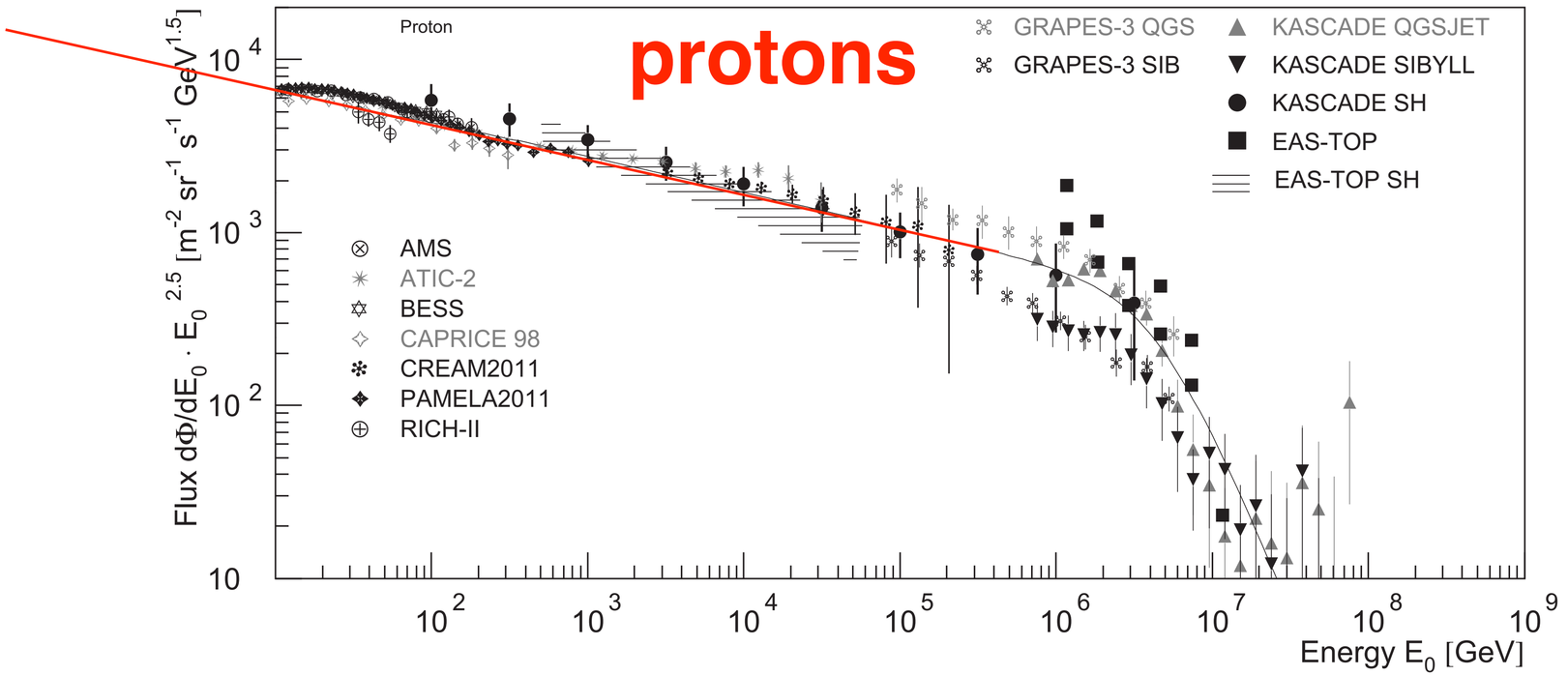

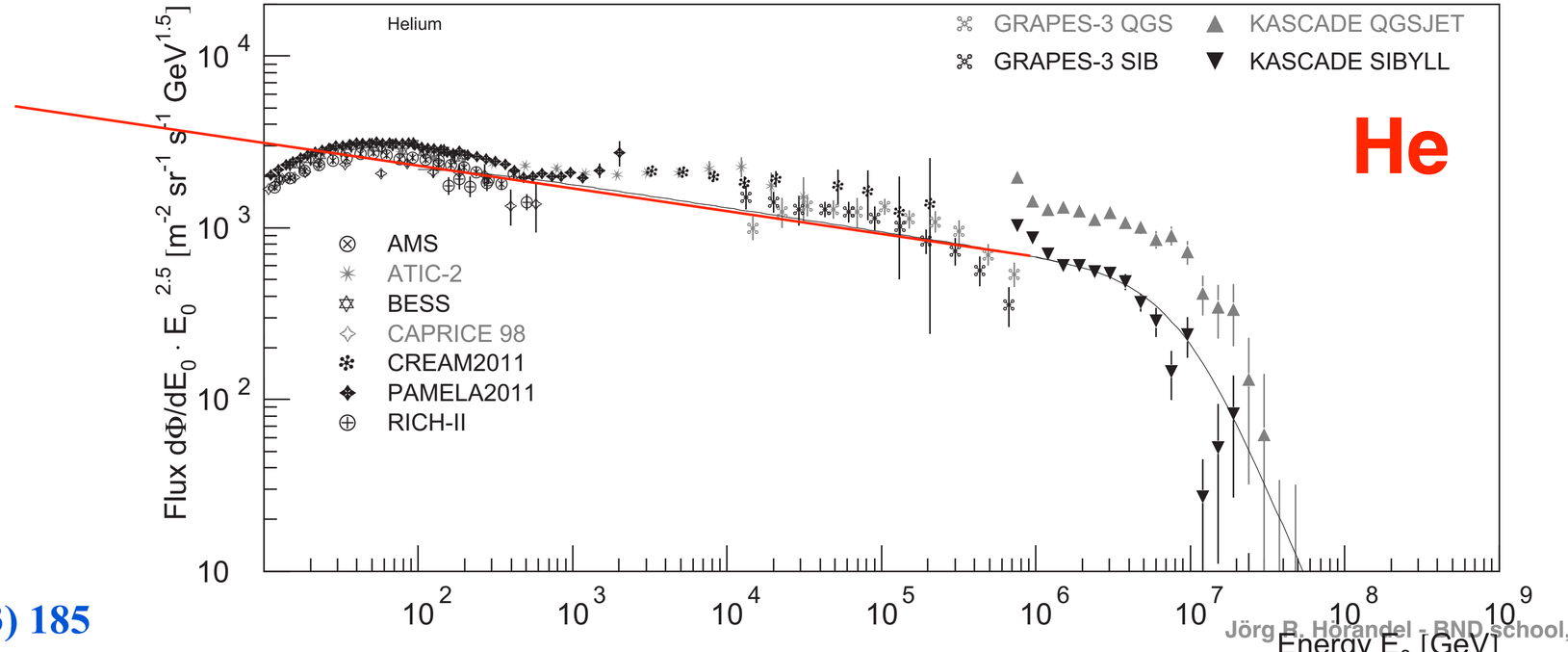

JRH, AIP Conf. Proc. 1516 (2013) 185

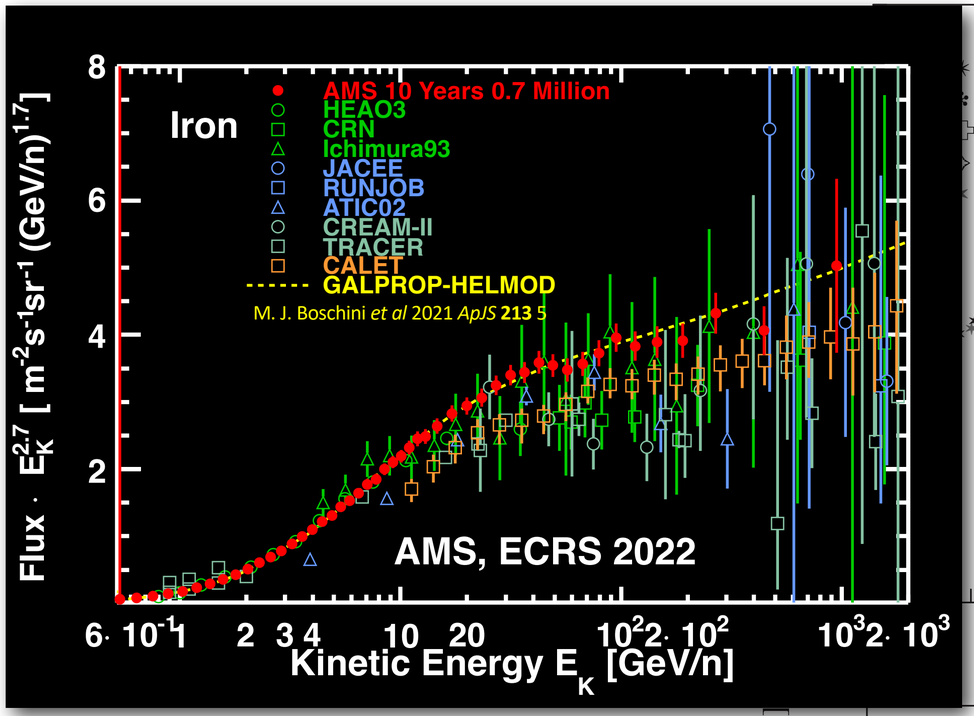

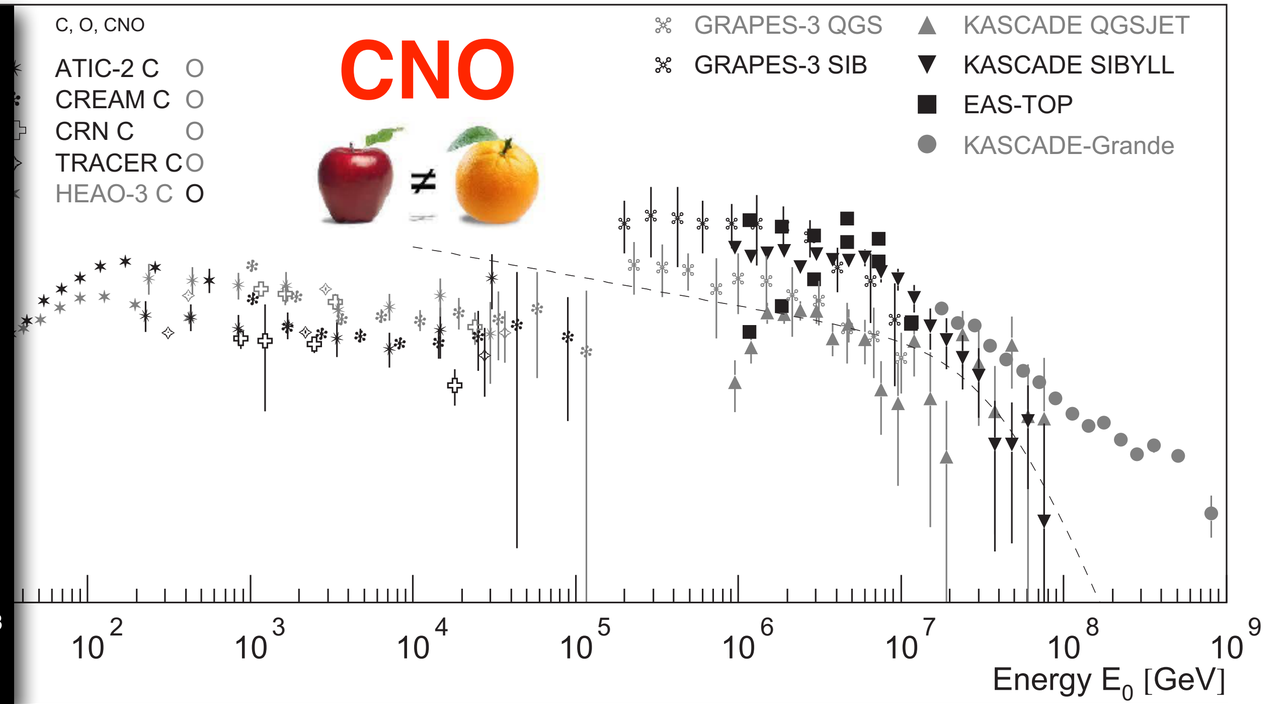

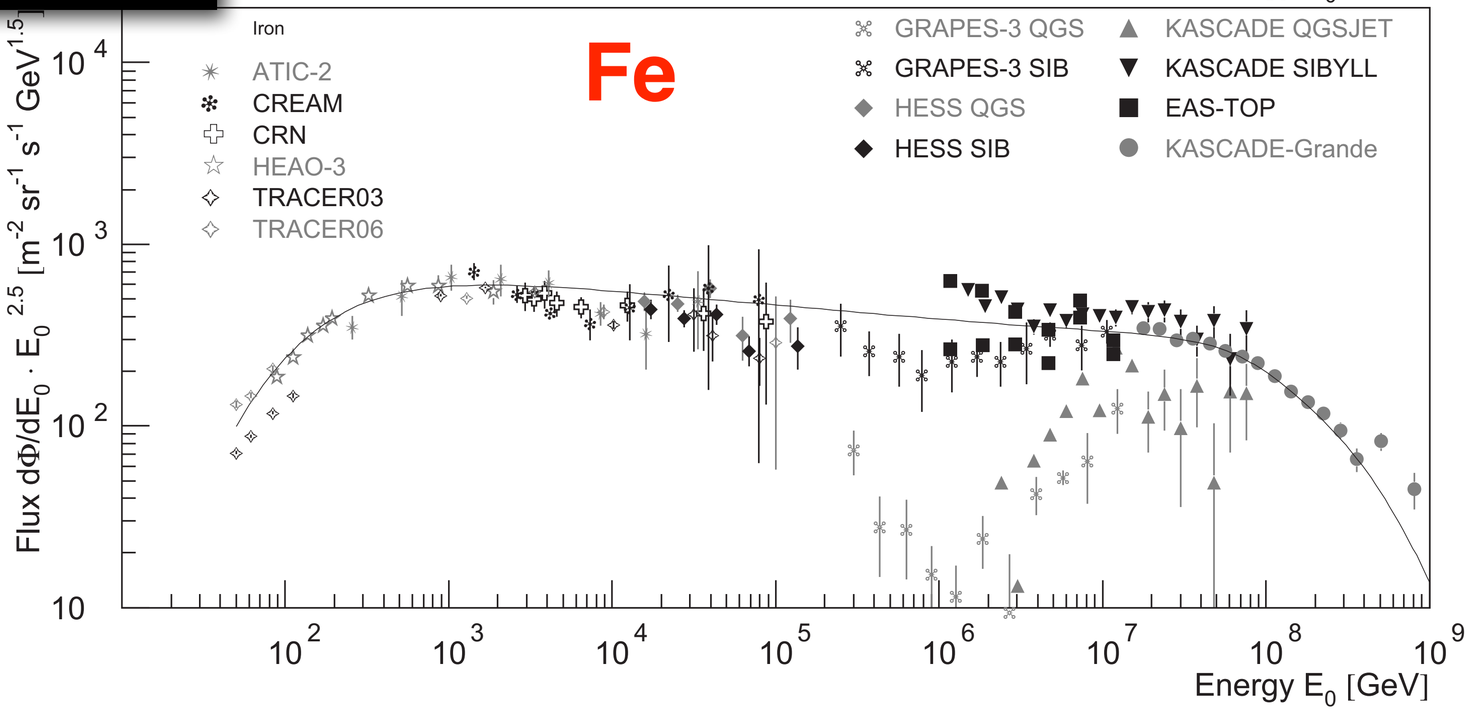

JRH, AIP Conf. Proc. 1516 (2013) 185

Galactic cosmic rays

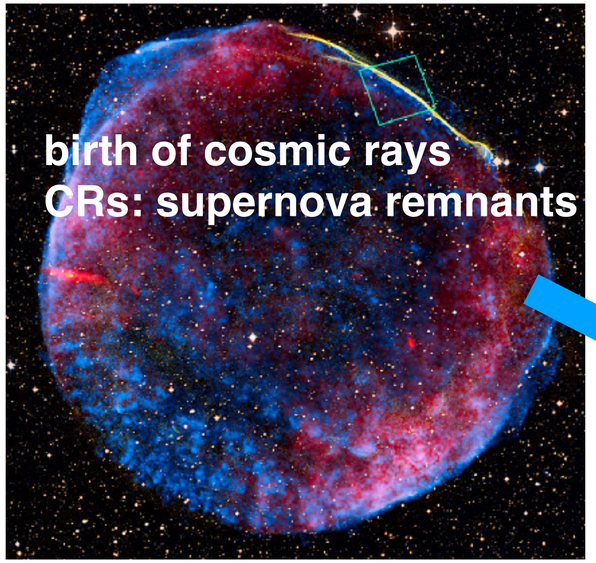

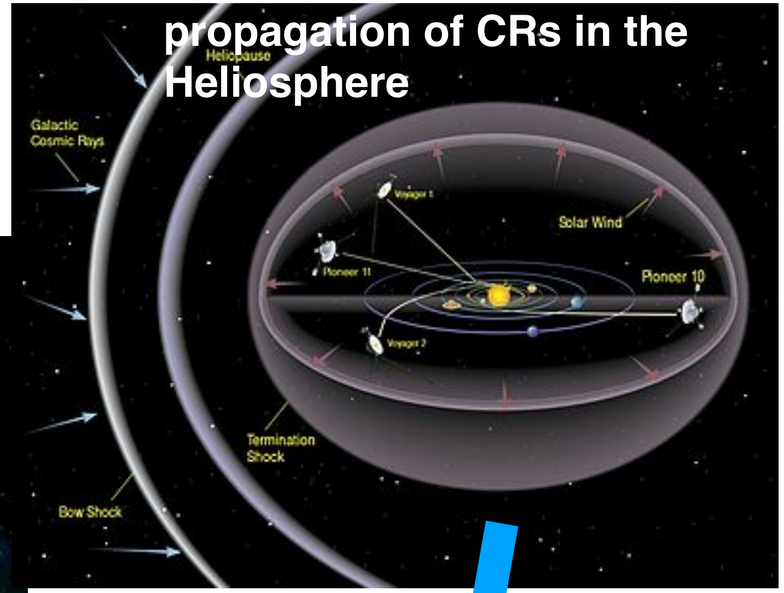

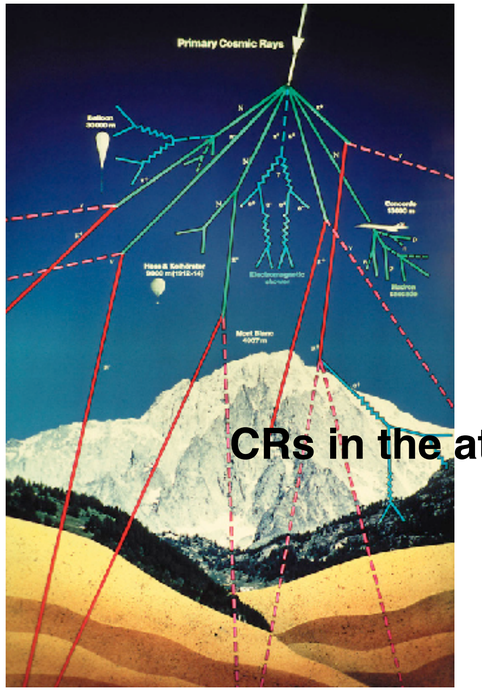

CRs at the top of the atmosphere

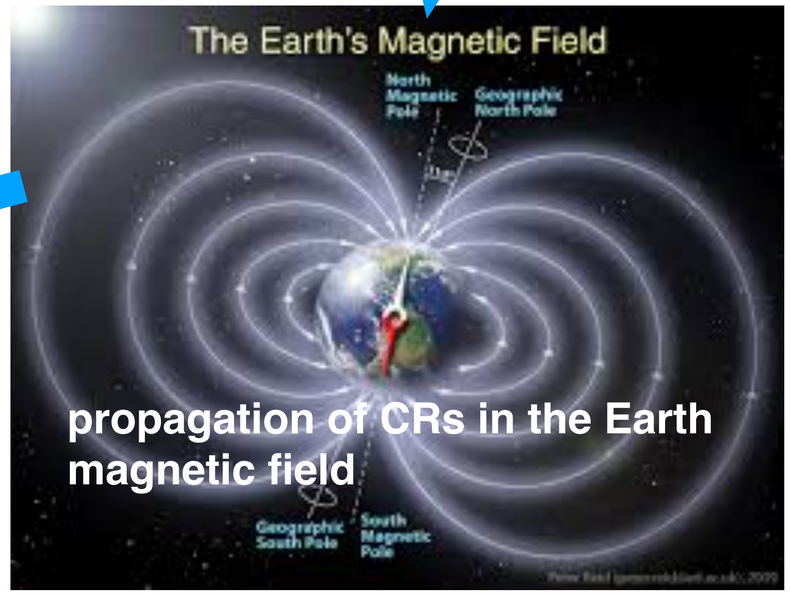

Transport equation for cosmic rays in the Galaxy

diffusion

energy loss (Bethe Bloch)

loss through interactions with ISM (spallation)

loss through radioactive decay

$$\frac{\partial N_i}{\partial t} = \nabla(D_i \nabla N_i) - \frac{\partial}{\partial E}(b_i N_i) - n\nu\sigma_i N_i - \frac{N_i}{\gamma\tau_i} + Q_i + \sum_{j>i} n\nu\sigma_{ij} N_j + \sum_{j>i} \frac{N_j}{\gamma_j \tau_{ij}}$$

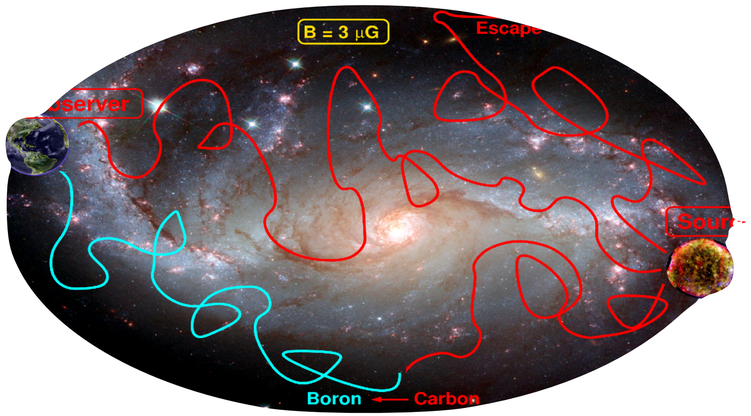

source term

production through spallation of heavy nuclei

production through decay of heavy nuclei

Transport equation for cosmic

diffusion

energy loss (Bethe Bloch)

loss through interactions with ISM (spallation)

loss through radi

$$\frac{\partial N_i}{\partial t} = \nabla(D_i \nabla N_i) - \frac{\partial}{\partial E}(b_i N_i) - n\nu\sigma_i N_i - \frac{N_i}{\gamma\tau_i} + Q_i + \sum_{j>i} n\nu\sigma_{ij} N_j + \sum_{j>i} \frac{N_j}{\gamma_j \tau_{ij}}$$

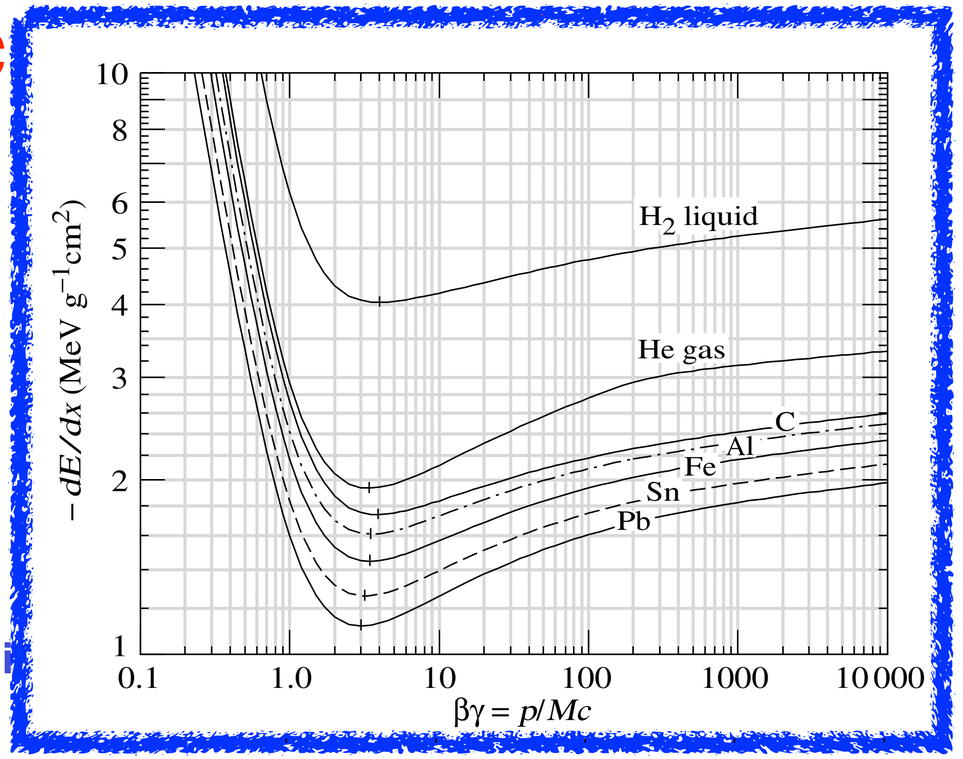

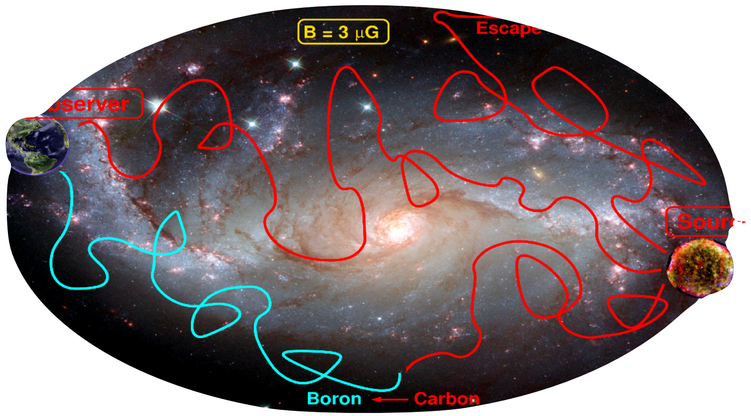

source term

production through spallation of heavy nuclei

production through decay of heavy nuclei

Transport equation for cosmic rays in the Galaxy

diffusion

energy loss (Bethe Bloch)

loss through interactions with ISM (spallation)

loss through radioactive decay

$$\frac{\partial N_i}{\partial t} = \nabla(D_i \nabla N_i) - \frac{\partial}{\partial E}(b_i N_i) - n\nu\sigma_i N_i - \frac{N_i}{\gamma\tau_i} + Q_i + \sum_{j>i} n\nu\sigma_{ij} N_j + \sum_{j>i} \frac{N_j}{\gamma_j \tau_{ij}}$$

source term

production through spallation of heavy nuclei

production through decay of heavy nuclei

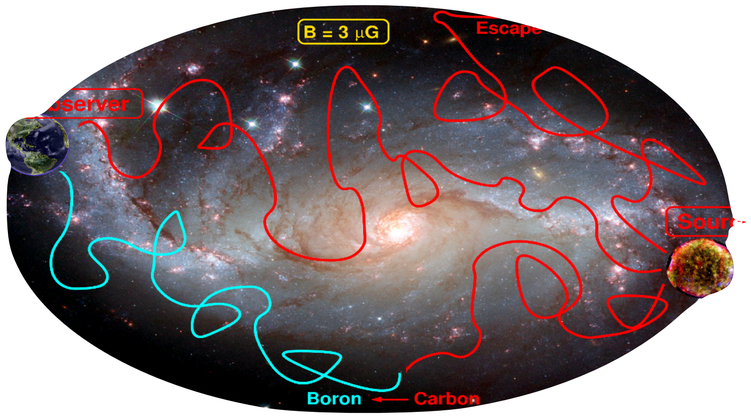

Acceleration of cosmic rays

kinetic energy of SNR is converted to cosmic rays

volume of Galactic disc $\pi\,(15\ \mathrm{kpc})^2(500\ \mathrm{pc}) \sim 10^{67}\ \mathrm{cm}^3$

energy density of cosmic rays $0.5\ \mathrm{eV/cm}^3.$ $t_{GD} = 10^7$ years

we will discuss later measurements of this quantity

power of cosmic rays:

$$L_{CR} = \frac{v_{GD} \times \rho_E}{t_{GD}} \simeq 3 \times 10^{40}\ \mathrm{erg/s}.$$

Three supernova remnants of mass $10 M_\odot$ expanding with velocity of 5×10^8 cm/s per century would produce 3×10^{42} erg/s. Thus an acceleration efficiency of only 1% would supply the energy content of the cosmic rays in the galactic disk.

—> SNR are attractive candidates for cosmic-ray acceleration

On the Origin of the Cosmic Radiation

ENRICO FERMI
Institute for Nuclear Studies, University of Chicago, Chicago, Illinois
(Received January 3, 1949)

A theory of the origin of cosmic radiation is proposed according to which cosmic rays are originated and accelerated primarily in the interstellar space of the galaxy by collisions against moving magnetic fields. One of the features of the theory is that it yields naturally an inverse power law for the spectral distribution of the cosmic rays. The chief difficulty is that it fails to explain in a straightforward way the heavy nuclei observed in the primary radiation.

I. INTRODUCTION

IN recent discussions on the origin of the cosmic radiation E. Teller[1] has advocated the view that cosmic rays are of solar origin and are kept relatively near the sun by the action of magnetic fields. These views are amplified by Alfvén, Richtmyer, and Teller.[2] The argument against the conventional view that cosmic radiation may extend at least to all the galactic space is the very large amount of energy that should be present in form of cosmic radiation if it were to extend to such a huge space. Indeed, if this were the case, the mechanism of acceleration of the cosmic radiation should be extremely efficient.

I propose in the present note to discuss a hypothesis on the origin of cosmic rays which attempts to meet in part this objection, and according to which cosmic rays originate and are accelerated primarily in the interstellar space, although they

where H is the intensity of the magnetic field and ρ is the density of the interstellar matter.

One finds according to the present theory that a particle that is projected into the interstellar medium with energy above a certain injection threshold gains energy by collisions against the moving irregularities of the interstellar magnetic field. The rate of gain is very slow but appears capable of building up the energy to the maximum values observed. Indeed one finds quite naturally an inverse power law for the energy spectrum of the protons. The experimentally observed exponent of this law appears to be well within the range of the possibilities.

The present theory is incomplete because no satisfactory injection mechanism is proposed except for protons which apparently can be regenerated at least in part in the collision processes of the cosmic radiation itself with the diffuse interstellar matter.

1st order Fermi acceleration

1977: Effective acceleration in connection with strong shocks if plasma moves with supersonic velocity through ISM.
Such conditions can be found in supernova explosions.

Shock waves are a general phenomenon if particles or plasma clouds move at supersonic velocities

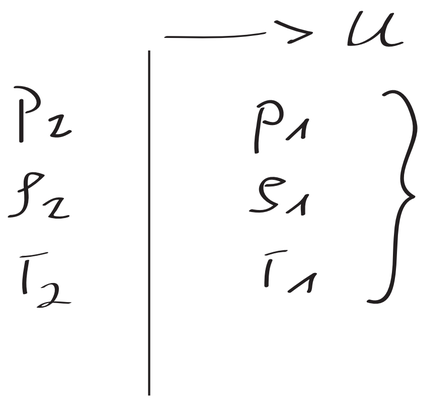

U **supersonic**

resting gas

shock front

examples of ideal shocks:

- **interplanetary shock against the solar wind or**
- **bow shock of solar system**

supersonic shock

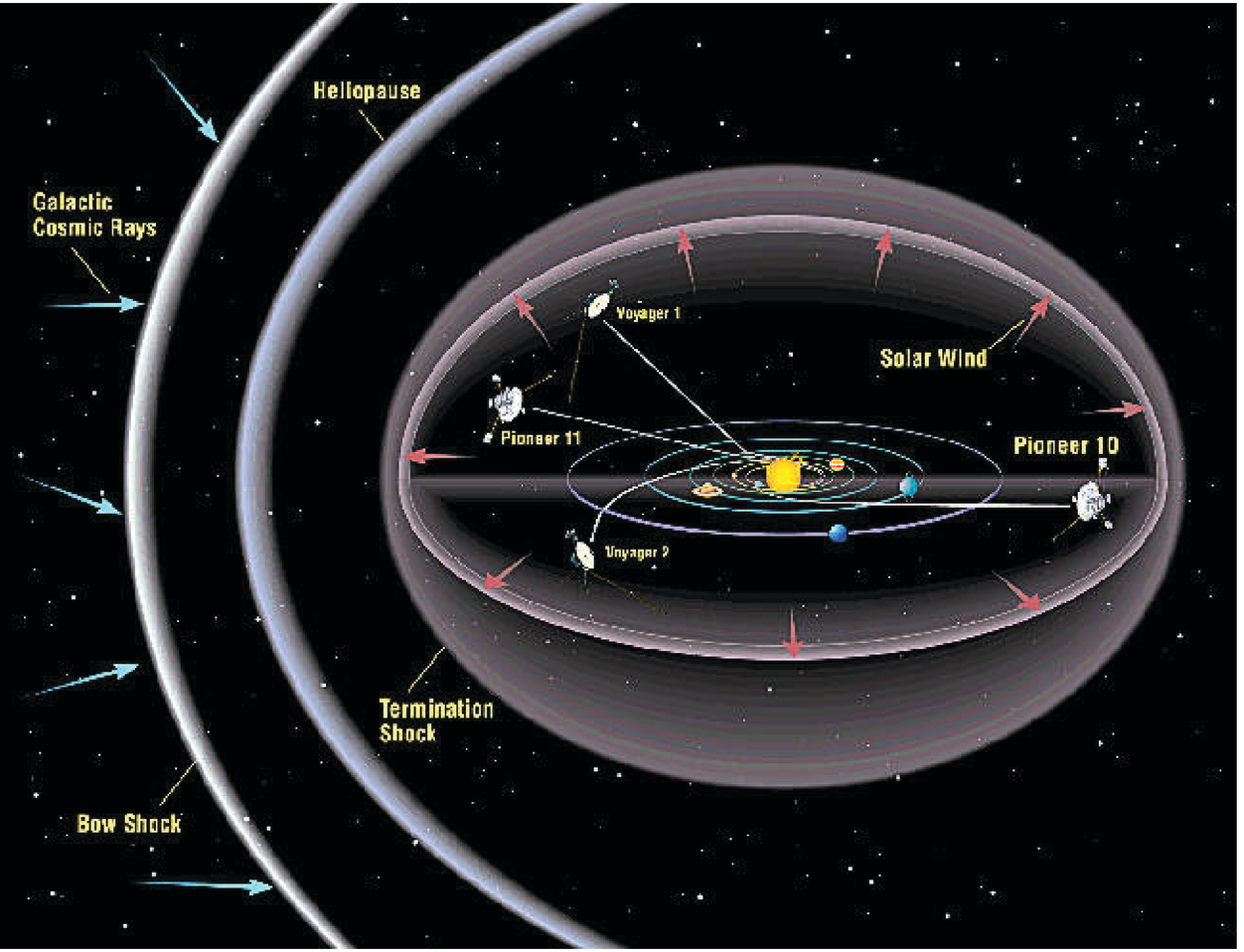

bow shock of solar system

structure of Earth's magnetosphere

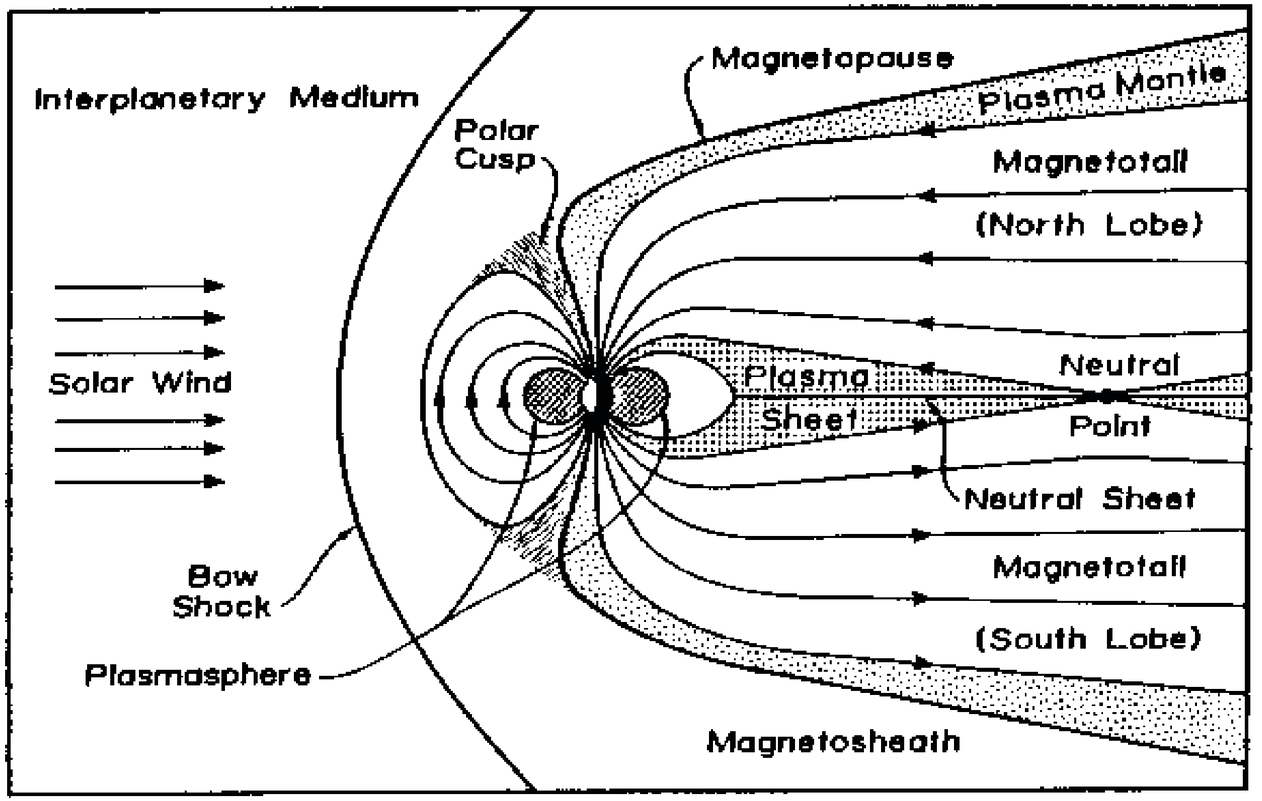

shock acceleration

1st order Fermi acceleration

a) rest system of the un-shocked ISM

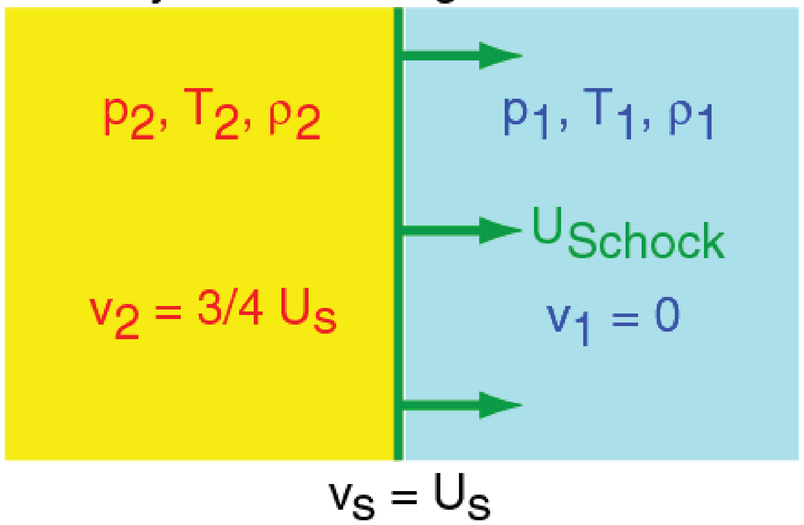

b) rest system of the un-shocked ISM

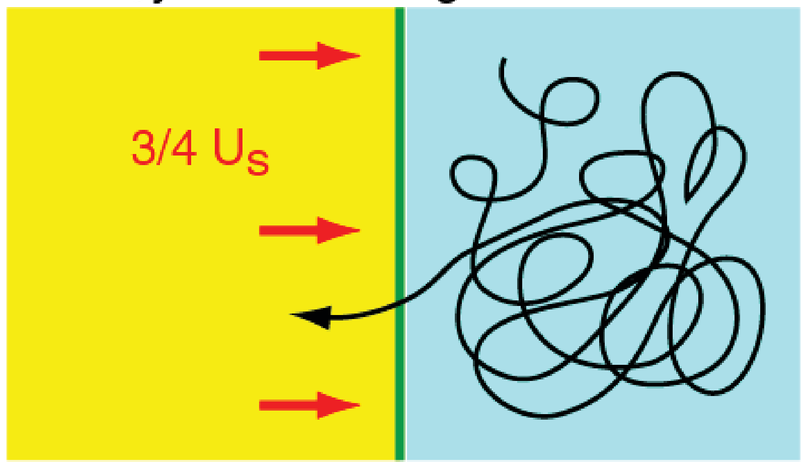

c) rest system of shock

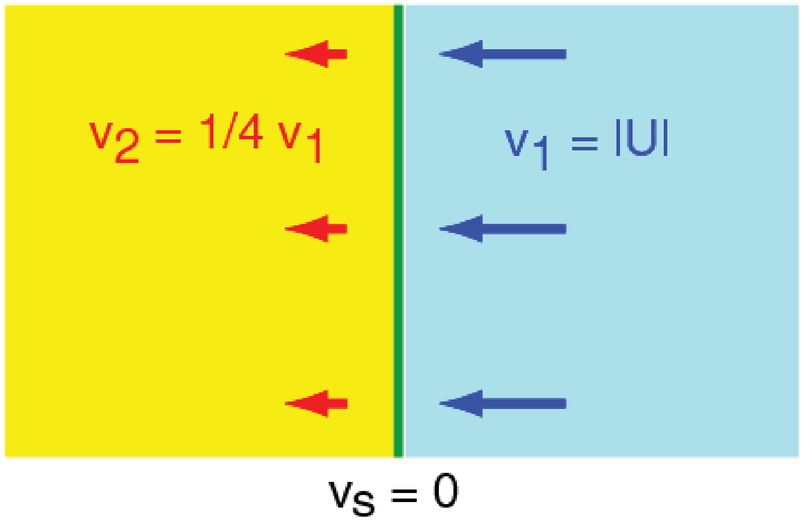

d) rest system of shocked ISM

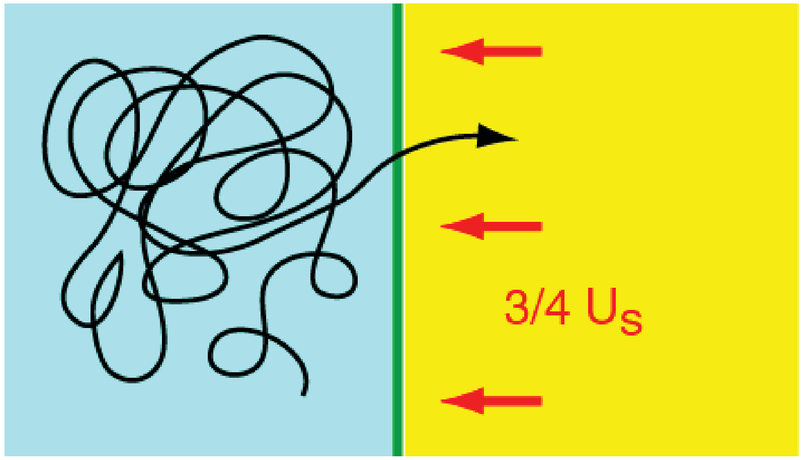

Axford, Blanford, Ostriker 1977 ff

acceleration mechanism:

1) particles in the ISM before the shock

2) shock front passes particles
   plasma cloud moves $\frac{3}{4}U_s$

   energy gain $\frac{\Delta E}{E} \propto \frac{U_s}{c}$

3) isotropized particles stay close to the shock and again move towards the shock front

   --> energy gain $\frac{\Delta E}{E} \propto \frac{U_s}{c}$

4) going back to 2)

remarks:

1) fully symmetric before and after the shock

2) on average, only head-on collisions

3) process is very fast
particles stay in vicinity of shock front
and are accelerated at each encounter $\propto \frac{U_s}{c}$

at some point the particles escape,
because their energy is too high to
be reflected by the B fields

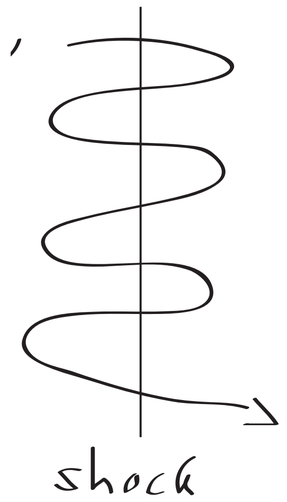

Particle acceleration at astrophysical shocks

β^2 (second-order (Fermi) acceleration).

this mechanism is much faster than original Fermi acceleration
—> 1st order Fermi acceleration, proportional to β

Shock acceleration gives a definite prediction for the spectral index γ of the power law spectrum of the accelerated particles. For a large plane shock the rate of shock encounters is the projection of the isotropic cosmic ray flux of density ρ_{CR} onto the plane front of the shock, which is $c\rho_{CR}/4$. The rate of escaping the shock through convection downstream away (which is the only way of leaving a plane shock of infinite length) is the product of the same cosmic ray density times the convection velocity u_2. The escape probability is the ratio of the escape rate to the encounter rate

$$P_{esc} = \frac{\rho_{CR} u_2}{c\rho_{CR}/4} = \frac{4u_2}{c}.$$

1st order Fermi acceleration gives prediction for spectral index

$$\gamma = \frac{P_{esc}}{\xi} = \frac{4u_2}{c} \times \frac{3c}{4(u_1 - u_2)} = \frac{3}{u_1/u_2 - 1} \sim 1$$

integral flux ~E^{-1}
—> diff. flux ~E^{-2}

SNR shock waves with v~10^9 cm/s and sound speed of ISM 10^6 cm/s

Sources of Cosmic Rays

Galactic sources

Supernovae

We have seen already that Supernovae produce enough energy.
And shock fronts are observable at SNRs.

expansion velocity of shock front up to $20 - 30 \cdot 10^3 \ \frac{\mathrm{km}}{\mathrm{s}}$
(M>>1)

duration up to 100000 a
--> diameter of ~2-3 kpc

Kepler's supernova 1604, d ~ 8 kpc

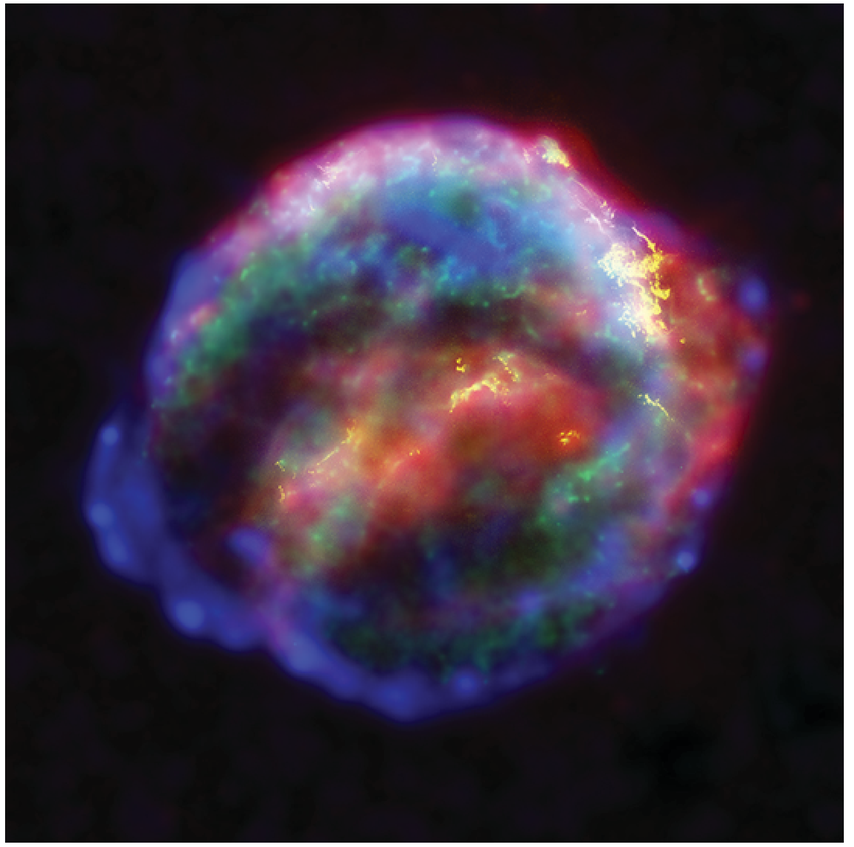

X-ray, Optical & Infrared Composite of Kepler's SNR

Tycho's supernova 1572, d ~ 2.3 kpc
v_S ~ 4600 +/- 400 km/s
E_{kin} ~ 5*10^{50} erg

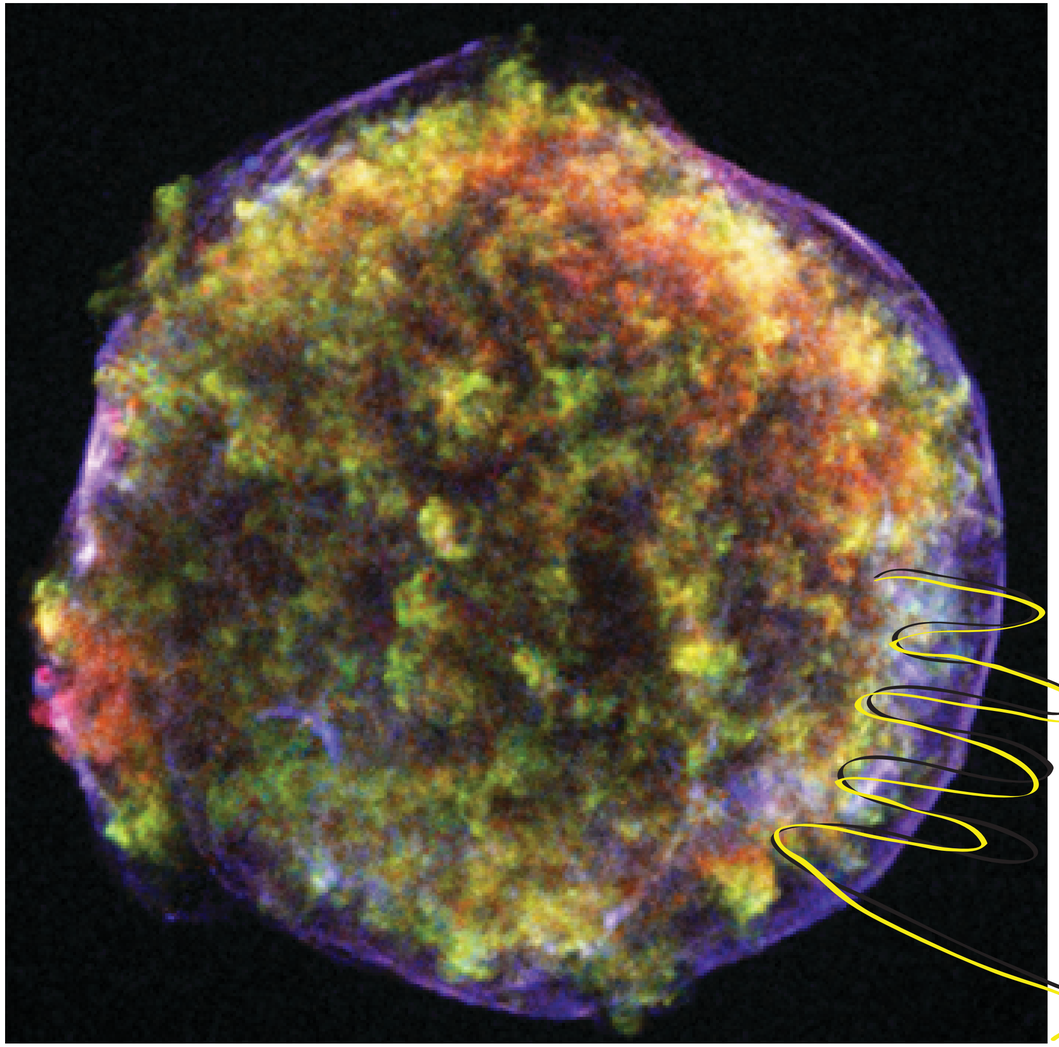

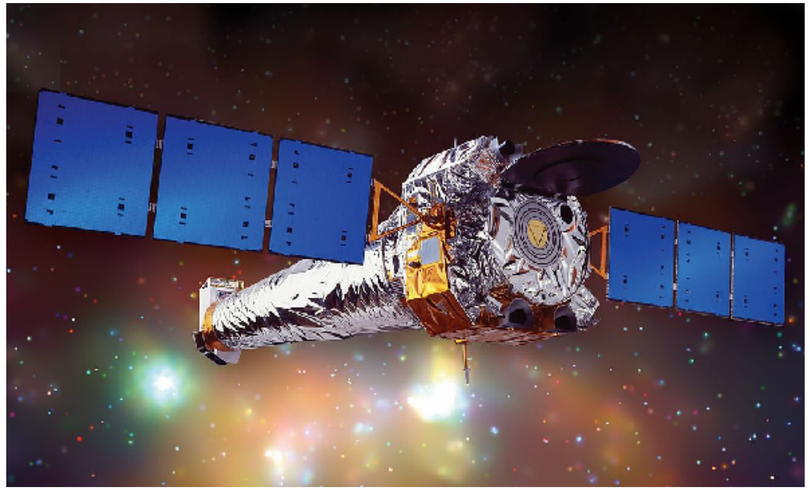

Chandra x-ray image

Particle acceleration at astrophysical shocks

maximum energy of shock acceleration

The maximum energy achievable at supernova remnants is estimated by Lagage & Cesarsky [58]. They show that most of particle acceleration happens before the shock has swept up mass equal to the mass of the ejecta, i.e. when the average density times the volume of the remnant equals the mass of the ejecta.

$$\frac{4}{3}\pi(u_1 t)^3 \rho_{IS} = M_{SR}. \tag{3.24}$$

For $M_{SR} = 10 M_\odot$ and $u_1 = 10^9$ cm/s and interstellar medium with density 1 nucleon per cm^3 the maximum energy is

$$E_{max} = Z \times 2.4 \times 10^5 \text{ GeV}. \tag{3.25}$$

The original number of Lagage & Cesarsky is 3×10^4 GeV since they use an expansion velocity of 5×10^8 cm/s. A higher value is derived for a lower value of the interstellar density. Some more detailed recent calculations [59] derive values close to 5×10^5 GeV.

SN 1006
x-ray image

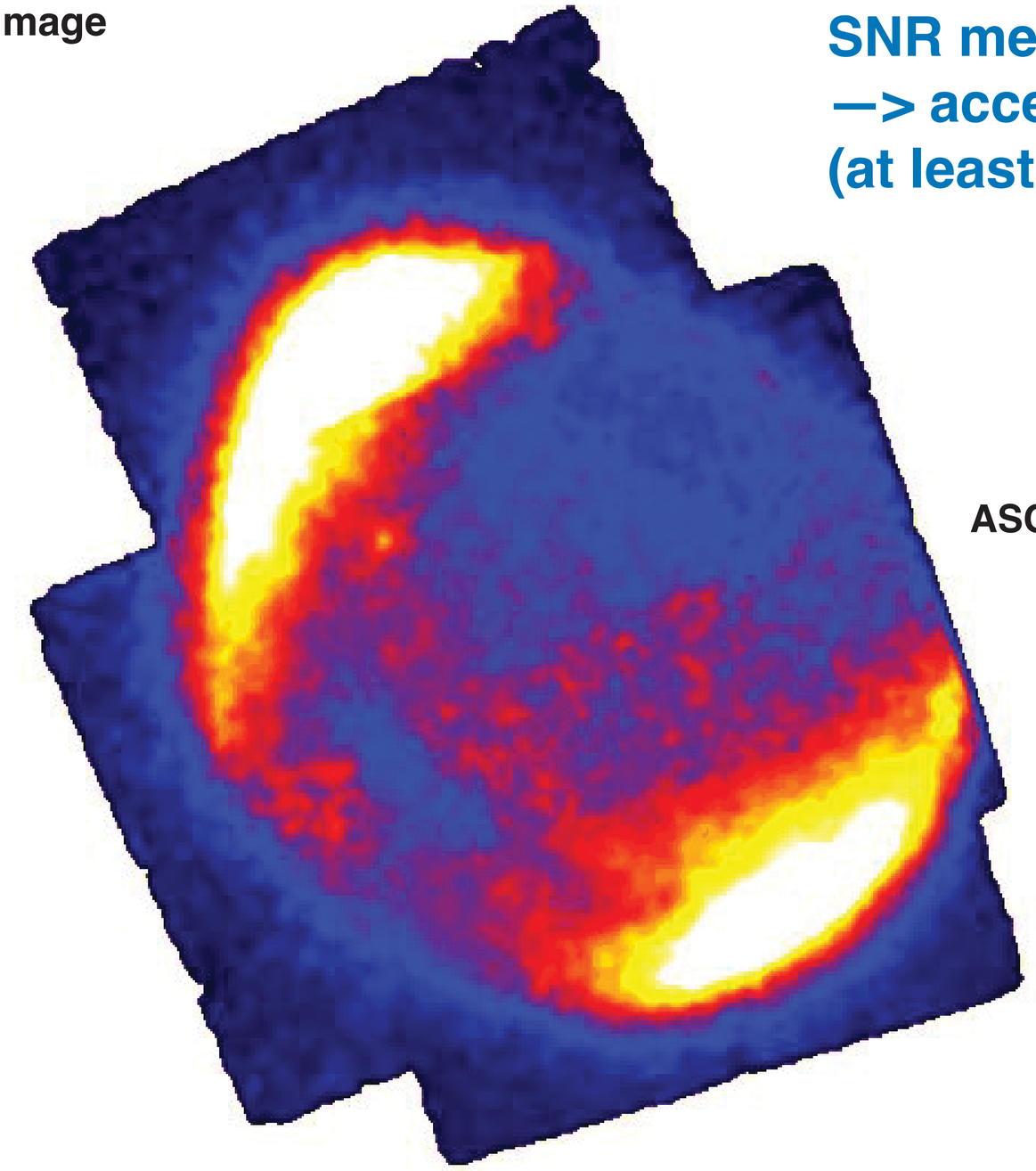

SNR measured in x-rays —> acceleration of particles (at least electrons)

ASCA (Advanced Satellite for Cosmology and Astrophysics)

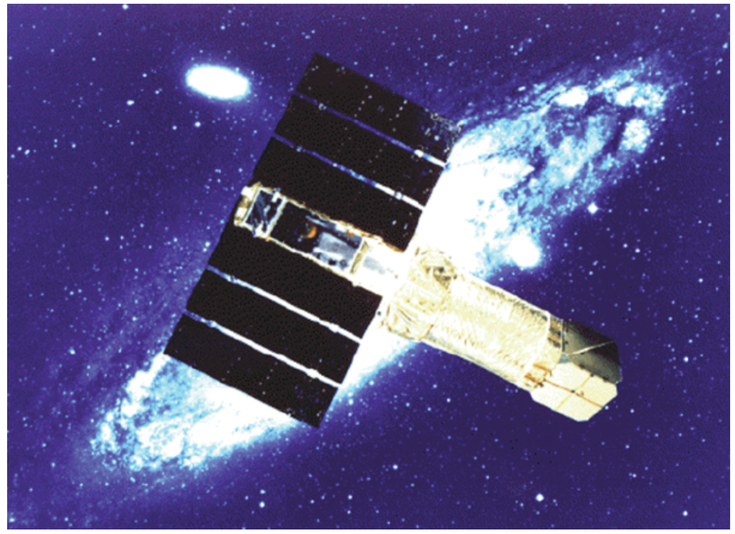

SN emits radiation in x-ray regime
(high plasma temperatures)

emission through synchrotron radiation of electrons

energy loss:

$$-\frac{dE}{dt} \propto \left(\frac{E}{M_0}\right)^4 \propto \gamma^4$$ ***r* fixed**

$$-\frac{dE}{dt} \propto B^2\gamma^2$$ ***r* free**

--> important for electrons (10⁴ compared to protons)

--> confirmation of shock acceleration of particles
(striclty speaking only for electrons)

Acceleration of particles in supernova remnant

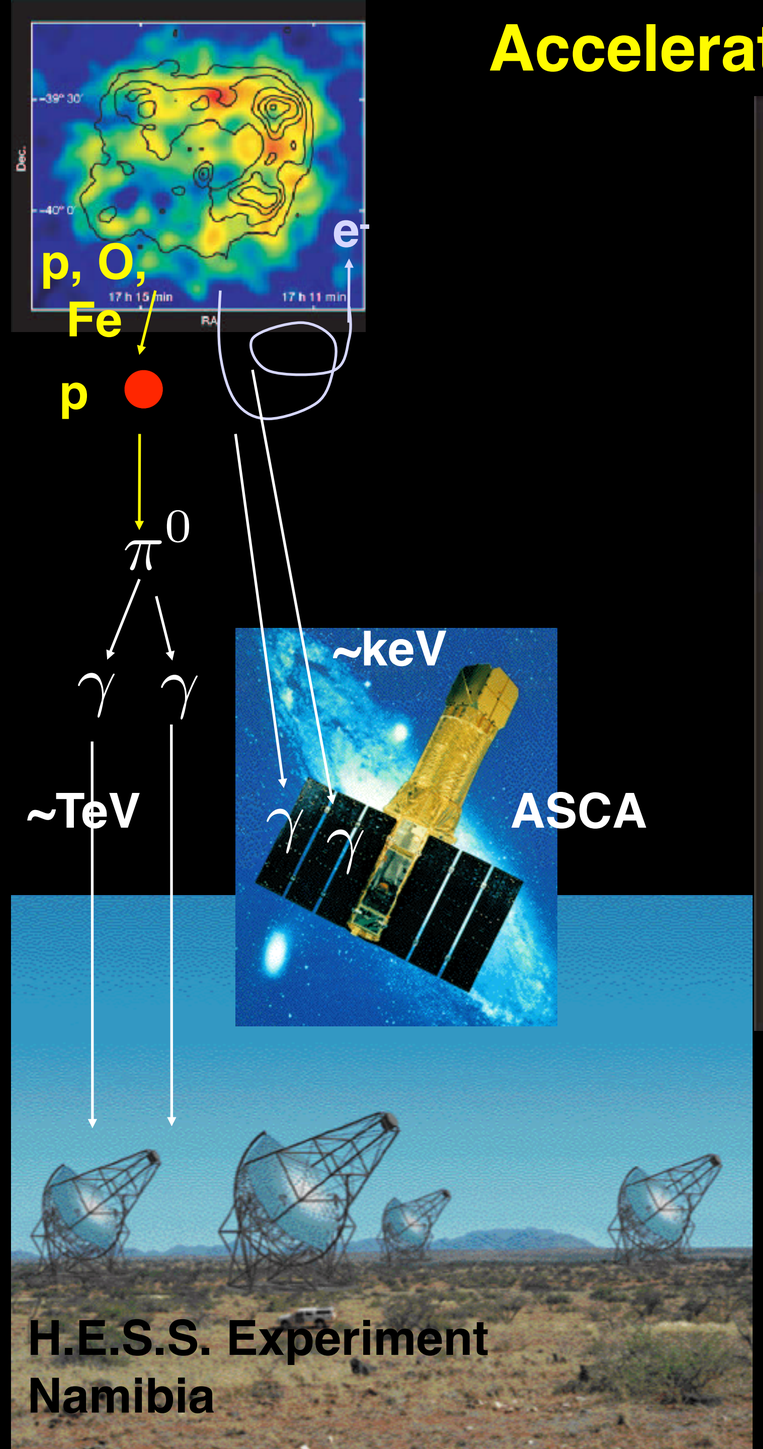

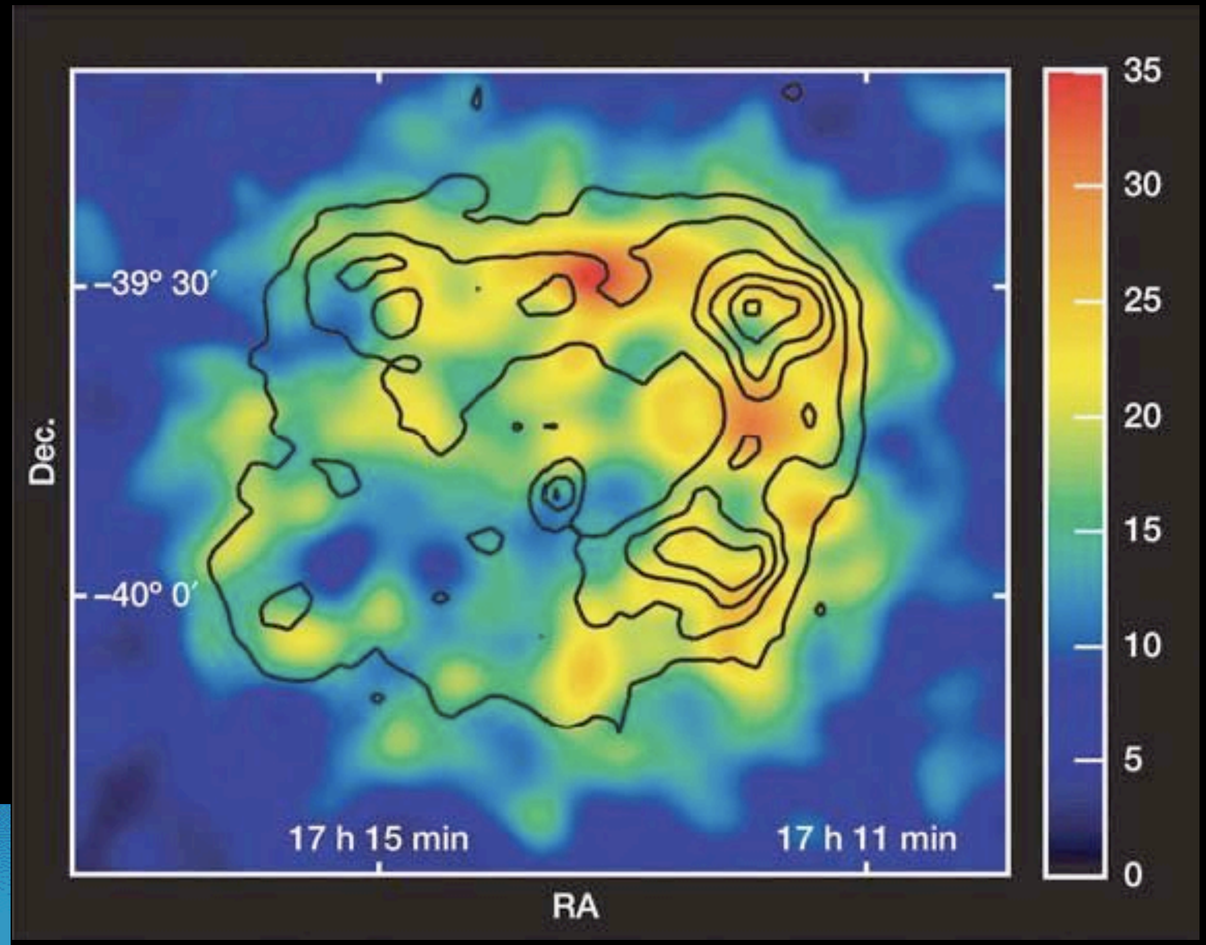

SNR RX J1713.7-3946
H.E.S.S.: TeV-Gamma rays
ASCA: X-rays (keV)

F. Aharonian et al, Nature 432 (2004) 75

H.E.S.S. supernova remnant RXJ 1713

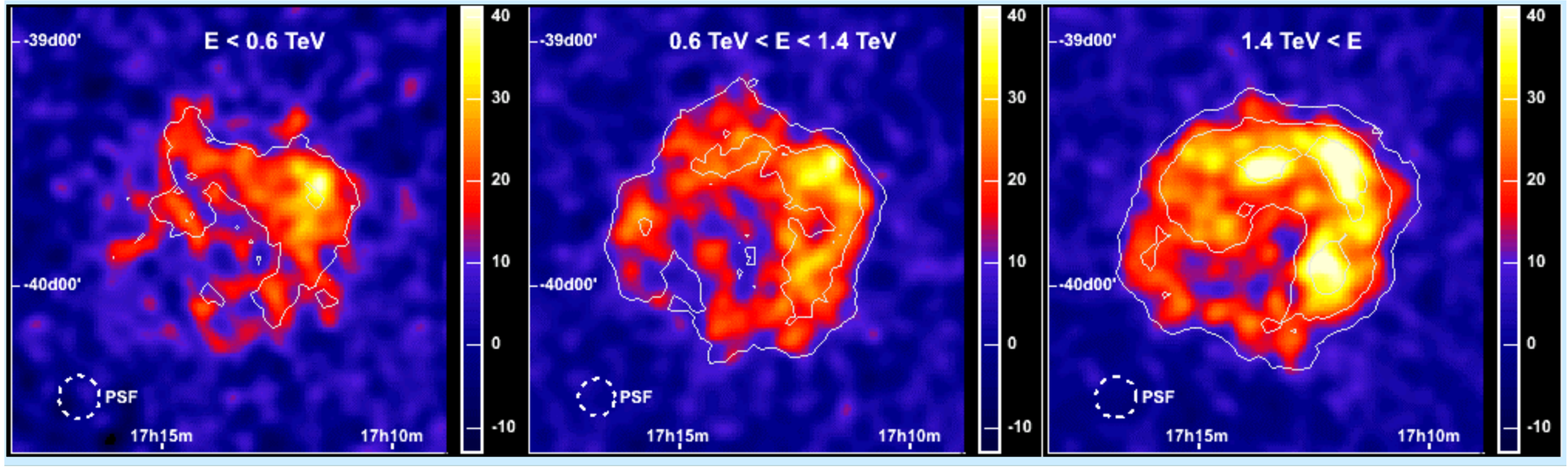

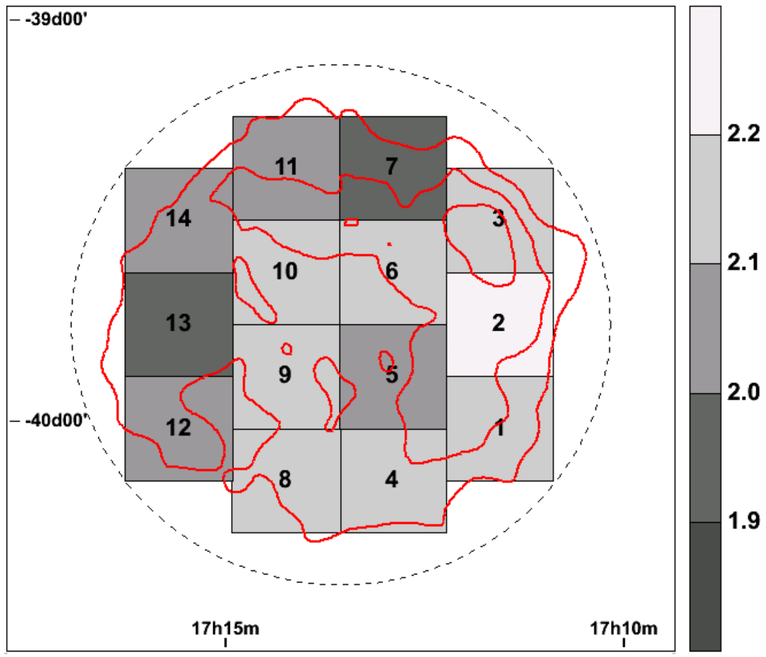

measured in TeV gamma rays

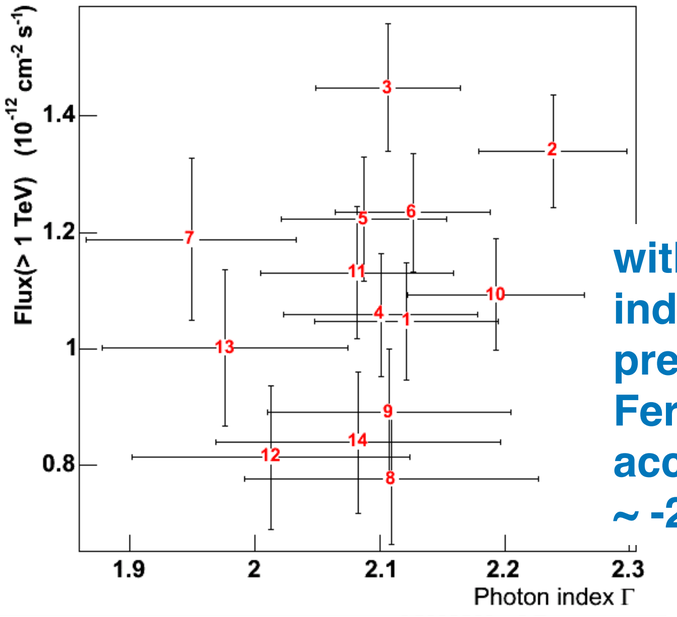

with spectral index as predicted by Fermi acceleration ~ -2.1

2004: H.E.S.S. telescopes observation of SNR RXJ1713

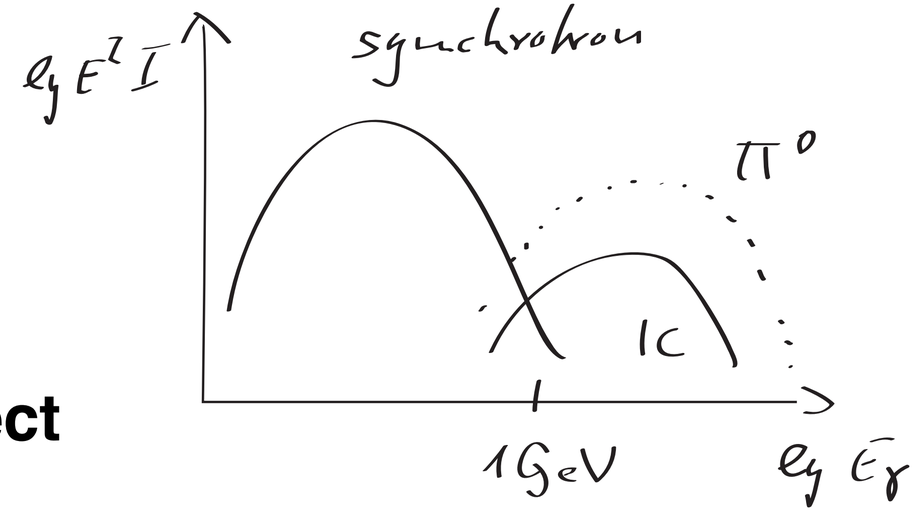

observed spectrum:

- acceleration of electrons: SSC, i.e. inverse Compton effect of γs on TeV electrons

- acceleration of hadrons (nuclei): γs originate from π^0 decay

which process dominates?

Acceleration of hadrons

Accelerated cosmic rays modify the B field at the SNR (self amplification)
--> B field in SNR is (much) larger than in ISM
~100 μG instead of ~3 μG

--> effective production of synchrotron radiation
--> observed flux of x rays and radio can be explained by a moderate electron number density

--> fraction of inverse Compton contribution is relatively small
--> most likely the observed TeV gamma rays are from π^0 decay
--> hint for the acceleration of hadrons in SNR

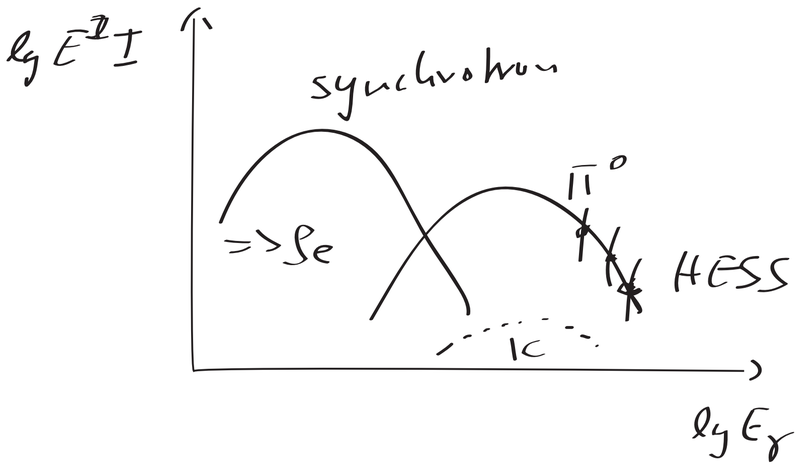

H. Völk & E.G. Berezhko, A&A 451 (2006) 981

The Astrophysical Journal, 790:85 (16pp), 2014 August 1 doi:10.1088/0004-637X/790/2/85

MAGNETIC FIELD AMPLIFICATION IN THE THIN X-RAY RIMS OF SN 1006

Sean M. Ressler[1], Satoru Katsuda[2], Stephen P. Reynolds[3], Knox S. Long[4], Robert Petre[5], Brian J. Williams[5], and P. Frank Winkler[6]

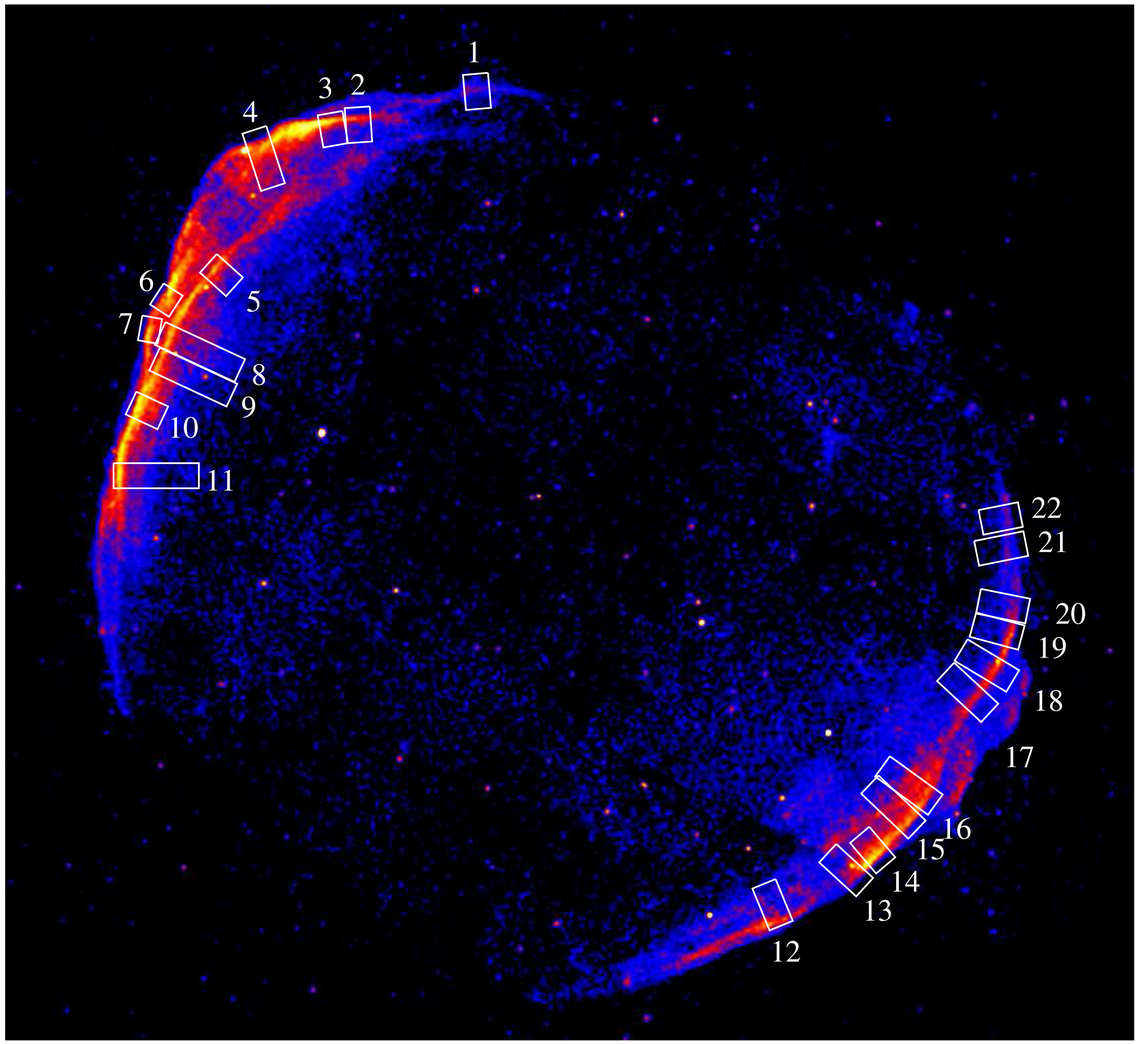

Figure 7. *Chandra* image at 2–7 keV showing the regions where radial profiles were extracted. Filament 1: Regions 1–4 and 6; Filament 2: Regions 5, 7, and 9–11; Filament 3: Regions 12–16; Filament 4: Regions 17–22; Filament 5: Regions 6 and 8.

RX J1713.7-3946

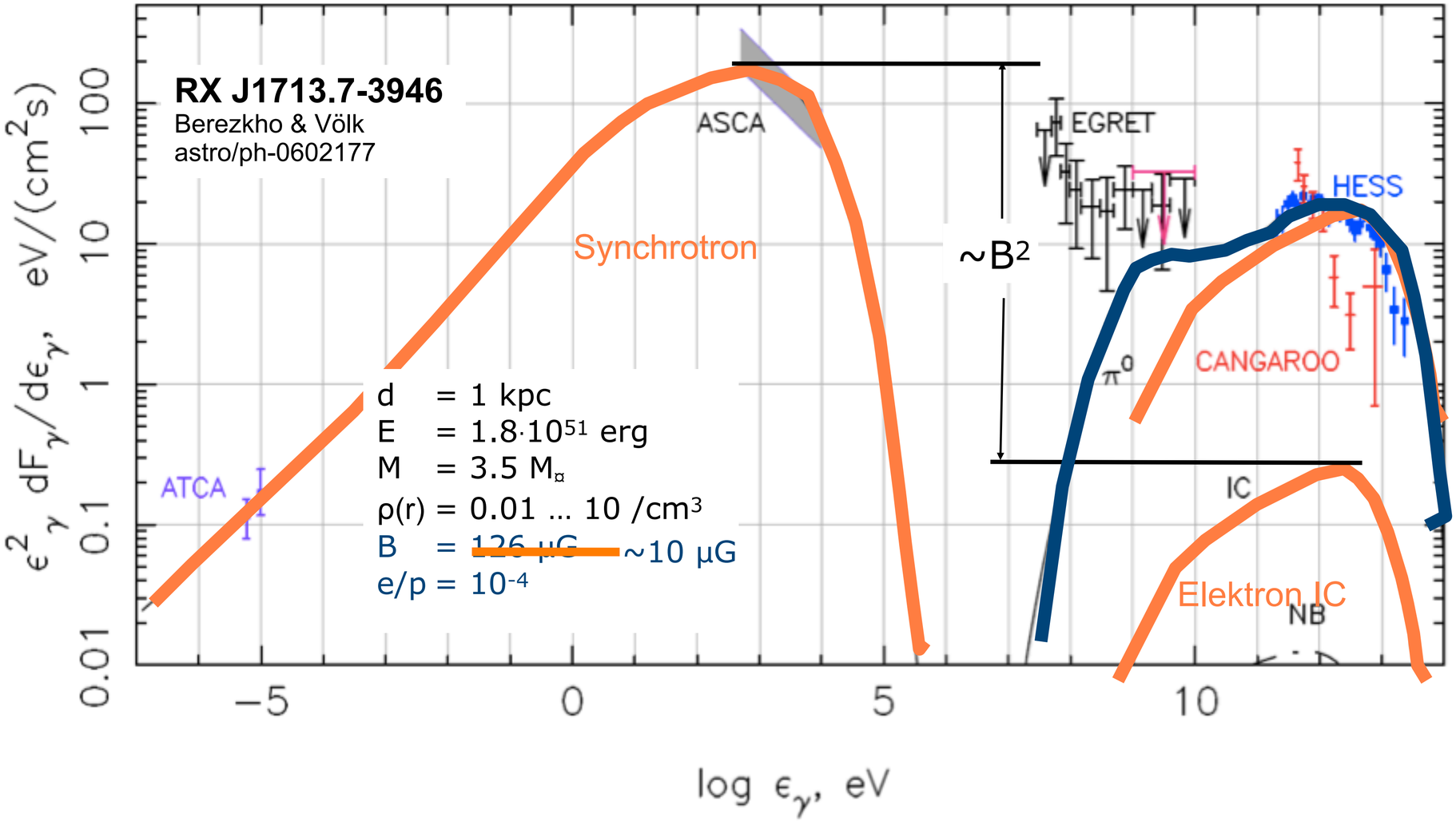

A&A 565, A74 (2014)
DOI: 10.1051/0004-6361/201322685

Astronomy & Astrophysics

The supernova remnant W44: Confirmations and challenges for cosmic-ray acceleration

M. Cardillo[1,2], M. Tavani[1,2,3], A. Giuliani[3,4], S. Yoshiike[5], H. Sano[5], T. Fukuda[5], Y. Fukui[5], G. Castelletti[6], and G. Dubner[6]

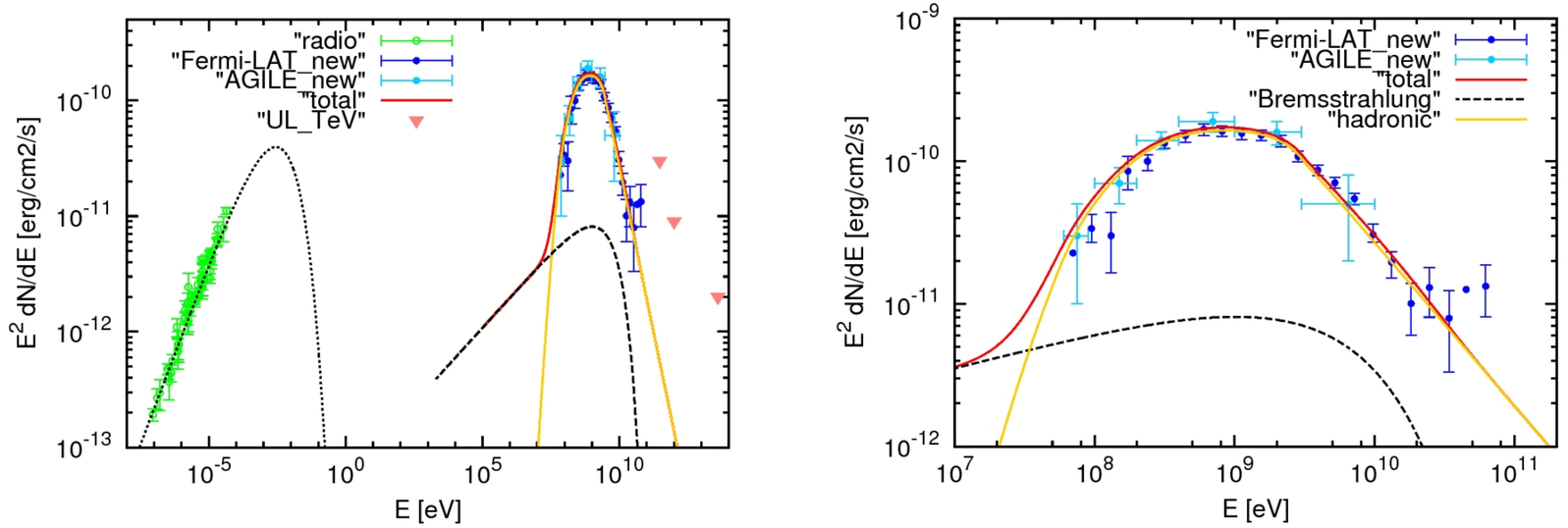

Fig. 4. Our best hadronic model, H3, of the broadband spectrum of the SNR W44 superimposed with radio (data points in green color) and gamma-ray data of Fig. 1 (in blue and cyan color). Proton distribution in Eq. (3) with index $p_1 = 2.2 \pm 0.1$ (for $E < E_{\rm br}$) and $p_2 = 3.2 \pm 0.1$ (for $E > E_{\rm br}$) where $E_{\rm br}^{\rm p} = 20$ GeV. This model is characterized by $B = 210$ μG and $n = 300$ cm^{-3}. The yellow curve shows the neutral pion emission from the accelerated proton distribution discussed in the text. The black curves show the electron contribution by synchrotron (dot) and bremsstrahlung (dashed) emissions; the IC contribution is negligible. The red curve shows the total gamma-ray emission from pion-decay and bremsstrahlung. *Left panel*: SED from radio to gamma-ray band. *Right panel*: only gamma-ray part of the spectrum.

Acceleration of cosmic rays at SNR

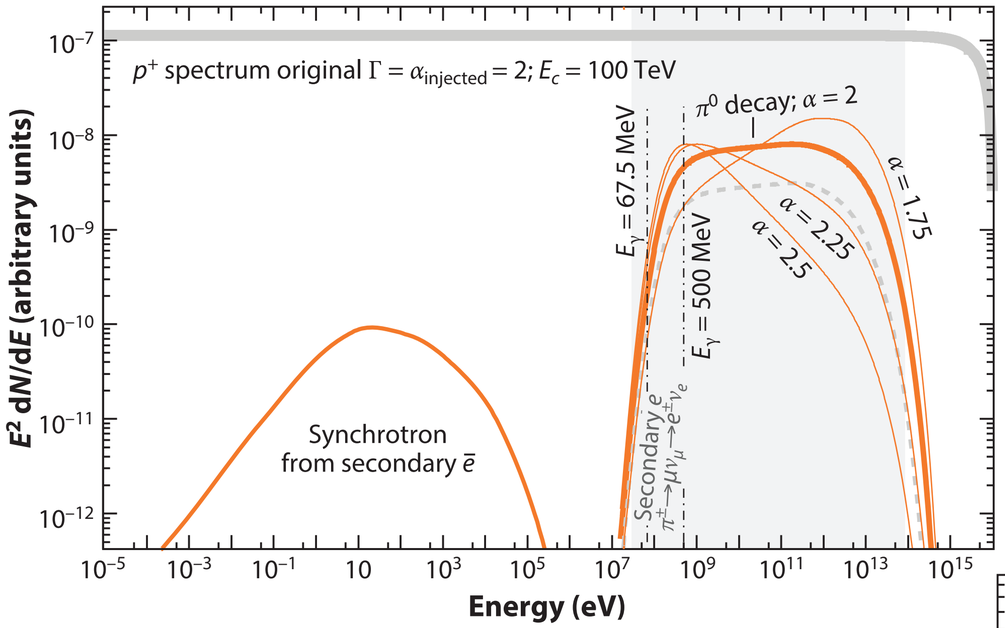

Figure 3

Spectral energy distribution of accelerated protons (power-law index $\alpha_{injected} = 2.0$ and cutoff at 100 TeV) and γ-rays resulting from inelastic collisions with interstellar material. The dominant emission into photons occurs via the decay $\pi^0 \to \gamma\gamma$ (*solid orange curves*). The γ-ray spectrum follows the parent protons' spectrum rather closely in the midenergy range and in the high-energy cutoff region. For all proton indices, the low-energy turnover is a characteristic feature of the pion-decay emission. Also shown is the spectrum of electrons resulting from the inelastic proton–proton interactions via the decay chain $\pi^\pm \to \mu + \nu_\mu \to e^\pm\nu_e$ (*dashed gray curve*). For the synchrotron emission from these so-called secondary electrons, a source with age $t_{age} = 1{,}000$ years and $B = 30$ μG have been assumed. The shaded gray region shows the sensitive range of current γ-ray detectors (*Fermi*-LAT, imaging atmospheric Cherenkov detectors).

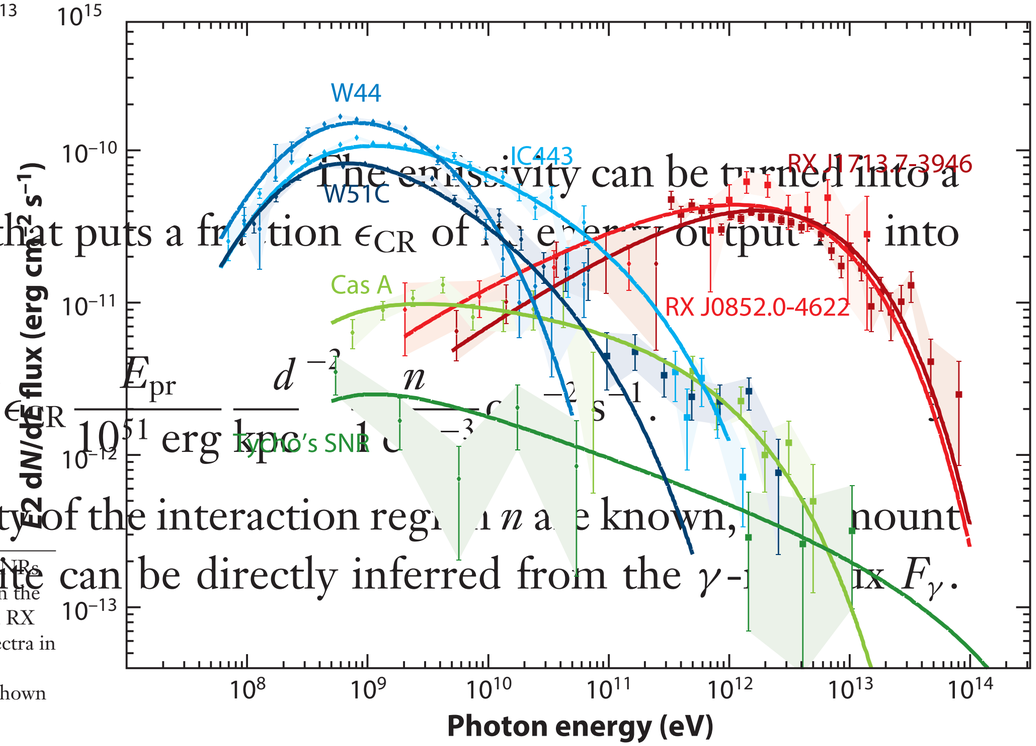

Figure 6

Typical γ-ray energy spectra for several of the most prominent supernova remnants (SNRs). Young SNRs (<1,000 years) are shown in green. These typically show smaller γ-ray fluxes but rather hard spectra in the GeV and TeV bands. The older (but still referred to as young) shell-type SNRs RX J1713.7-3946 and RX J0852.0-4622 (Vela Junior) of ages ~2,000 years are shown in shades of red. These show very hard spectra in the GeV band ($\Gamma = 1.5$) and a peak in the TeV band with an exponential cutoff beyond 10 TeV. The middle-aged SNRs (~20,000 years) interacting with molecular clouds (W44, W51C, and IC443) are shown in blue. Also shown are hadronic fits to the data (*solid lines*).

flux at Earth by an astrophysical accelerator that puts a fraction ϵ_{CR} of the energy output into the acceleration of protons:

$$F_\gamma(>100\,\mathrm{MeV}) = 4.4 \times 10^{-7}\,\epsilon_{CR}\,\frac{E_{pr}}{10^{51}\,\mathrm{erg}}\,\frac{d^{-2}}{1\,\mathrm{kpc}^{-2}}\,\frac{n}{1\,\mathrm{cm}^{-3}}\,\mathrm{cm}^{-2}\,\mathrm{s}^{-1}.$$

In other words, if the distance d and the density n of the interaction region are known, the amount of energy in protons E_{pr} at the interaction site can be directly inferred from the γ-ray flux F_γ.

S. Funk, Ann. Rev. Nucl. Part. Sci. 65 (2015) 245

Ultrahigh-energy photons up to 1.4 petaelectronvolts from 12 γ-ray Galactic sources

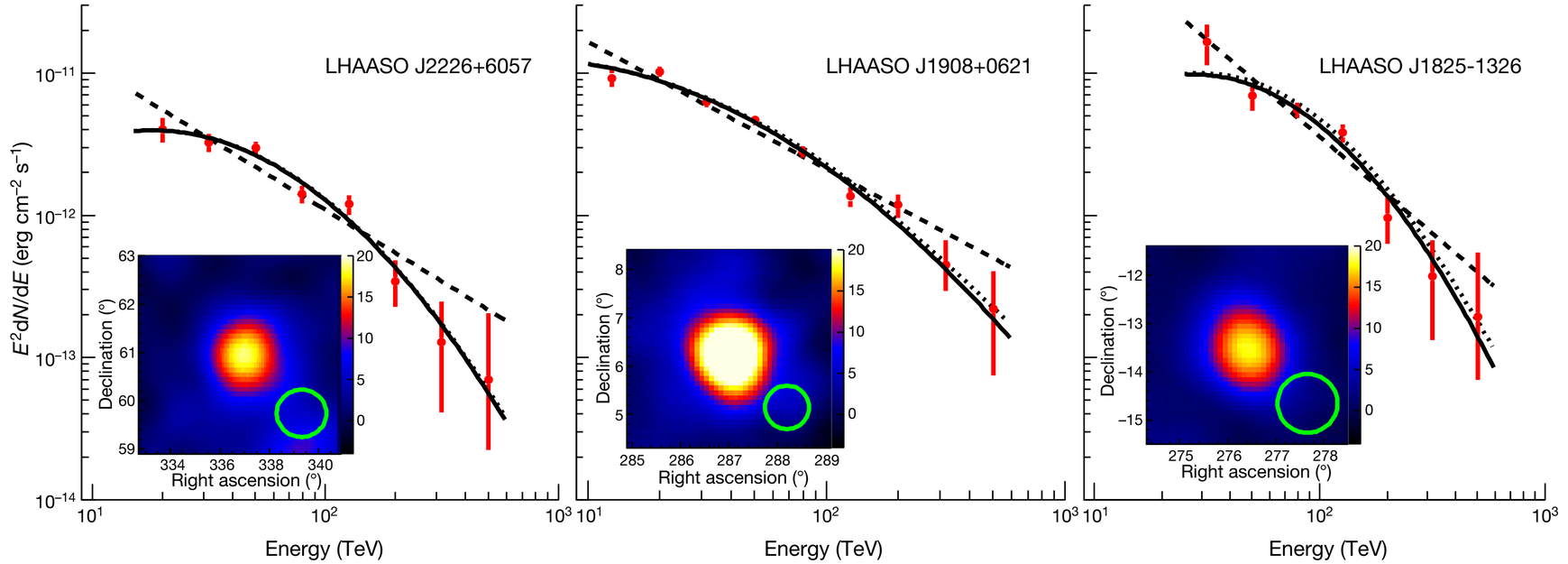

Fig. 1 | Spectral energy distributions and significance maps. a–**c**, Data are shown for LHAASO J2226+6057 (**a**), LHAASO J1908+0621 (**b**), and LHAASO J1825-1326 (**c**). Spectral fits with a log-parabola function (solid lines) in the form of $[E/(10\ \mathrm{TeV})]^{-a-b\log[E/(10\ \mathrm{TeV})]}$ are compared with the power-law fits $E^{-\Gamma}$ for: $a = 1.56$, $b = 0.88$ and $\Gamma = 3.01$ (**a**); $a = 2.27$, $b = 0.46$ and $\Gamma = 2.89$ (**b**); and $a = 0.92$, $b = 1.19$ and $\Gamma = 3.36$ (**c**). The dotted curves correspond to the log-parabola fits corrected for the interstellar γ–γ absorption (see Methods for the radiation fields and Extended Data Fig. 6 for the opacity curves). The comparison of the power-law (PL) model and the log-parabola (LOG) model with the Akaike Information Criterion[20] (AIC) gives: $\mathrm{AIC_{LOG}} = 12.3$ and $\mathrm{AIC_{PL}} = 24.4$ for LHAASO J2226+6057; $\mathrm{AIC_{LOG}} = 15.1$ and $\mathrm{AIC_{PL}} = 30.1$ for LHAASO J1908+0621; and $\mathrm{AIC_{LOG}} = 11.6$ and $\mathrm{AIC_{PL}} = 14.8$ for LHAASO J1825-1326. The insets show the significance maps of the three sources, obtained for γ-rays above 25 TeV. The colour bars show the square root of test statistics (TS), which is equivalent to the significance. The significance ($\sqrt{\mathrm{TS}}$) maps are smoothed with the Gaussian-type point spread function (PSF) of each source. The size of PSFs (68% contamination regions) are shown at the bottom right of each map. We note that the PSFs of the three sources are slightly different owing to different inclination angles. Namely, the 68% contamination angles are 0.49° for LHAASO J2226+6057, 0.45° for LHAASO J1908+0621 and 0.62° for LHAASO J1825-1326. Error bars represent one standard deviation.

The Astrophysical Journal Supplement Series, 271:25 (26pp), 2024 March https://doi.org/10.3847/1538-4365/acfd29

The First LHAASO Catalog of Gamma-Ray Sources

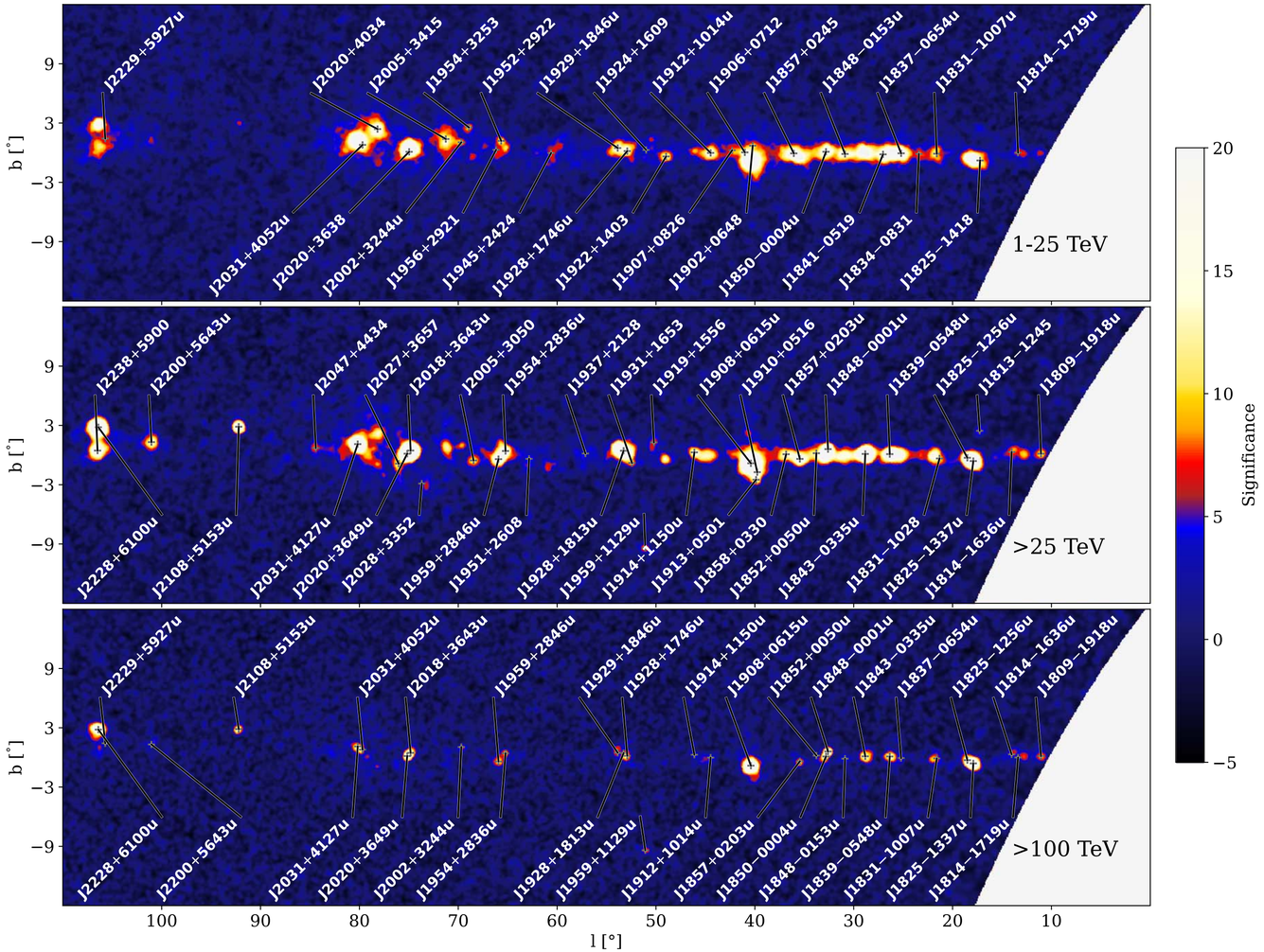

Figure 8. LHAASO significance map within the region $10^\circ \leqslant l \leqslant 115^\circ$, $|b| \leqslant 12^\circ$. Top panel: WCDA (1 TeV $< E <$ 25 TeV) significance map. Middle panel: KM2A ($E >$ 25 TeV) significance map. Bottom panel: KM2A ($E >$ 100 TeV) significance map. In this figure and in the following figure, the LHAASO source are represented by gray crosses and white labels. The LHAASO sources for which the WCDA component has higher significance are plotted in the top panel. The LHAASO sources for which the KM2A component has higher significance are plotted in the middle panel. Meanwhile, UHE sources are shown again in the bottom panel.

NEUTRINO ASTROPHYSICS

Observation of high-energy neutrinos from the Galactic plane

IceCube Collaboration*†

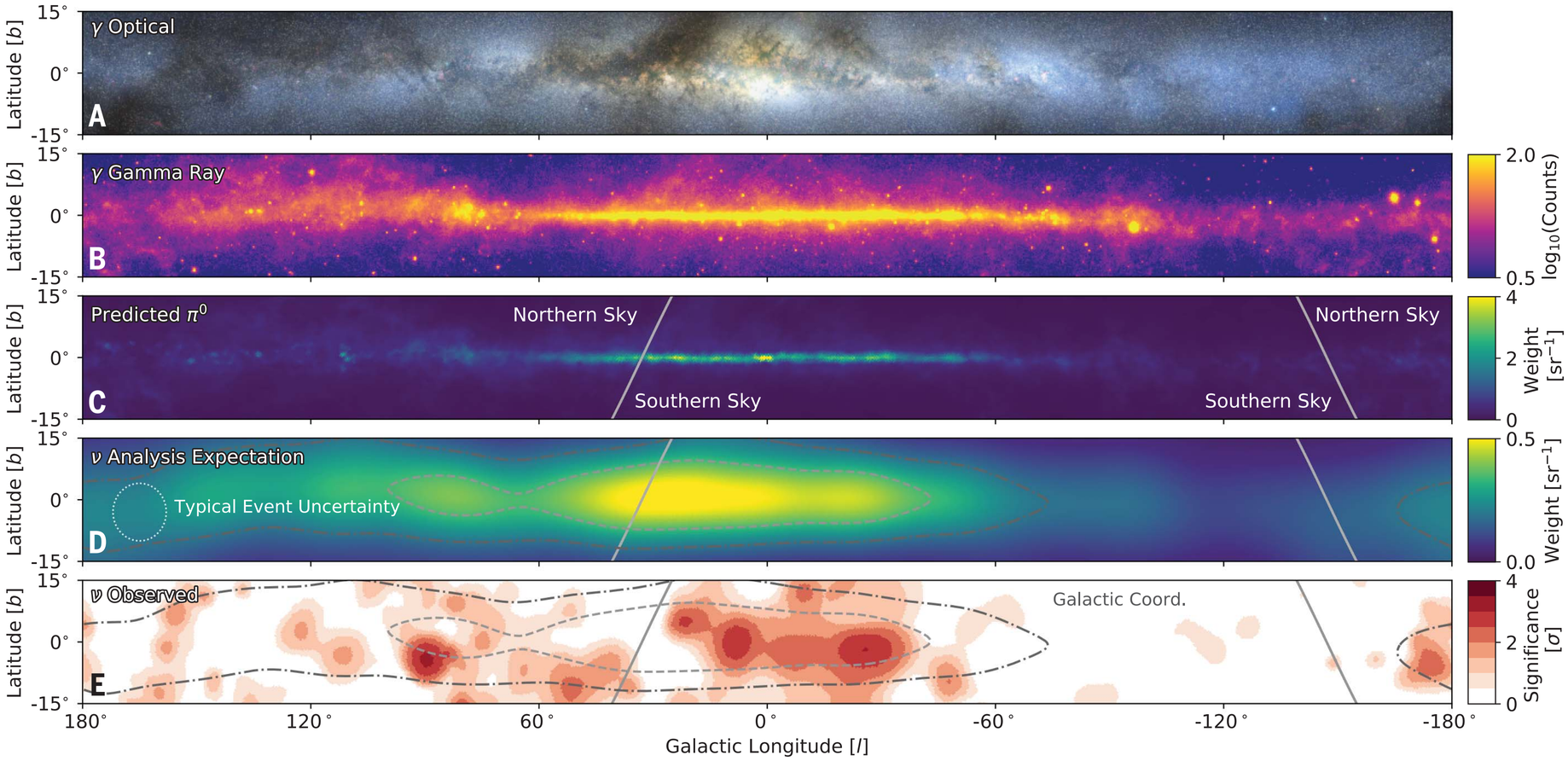

$$\mathrm{CR} + \mathrm{ISM} \rightarrow \pi^{\pm} \rightarrow \nu$$

IceCube Collaboration, *Science* **380**, 1338–1343 (2023) 30 June 2023

general considerations about accelerators

trajectory of particle in B field

centripedal force = Lorentz force

$$m\frac{v^2}{r} = q \cdot v \cdot B \qquad m \cdot v = p \quad \textbf{momentum}$$

$$\frac{p}{r} = Z \cdot e \cdot B$$

$$r_L = \frac{p}{z \cdot e \cdot B} \quad \textbf{Larmor radius}$$

L **dimension of accelerator**

$L > 2\, r_L$

closer look (Hillas 1984): $L > \dfrac{2 r_L}{\beta}$

velocity of scattering centers $\beta = \dfrac{v}{c}$

A.M. Hillas, Ann. Rev. Astron. Astrophys. 22 (1984) 425

$$L > \frac{2 \cdot p}{z \cdot e \cdot B \cdot \beta}$$

$$B \cdot L > \frac{2 \cdot p}{z \cdot e \cdot \beta}$$ **Hillas criterion**

in astrophyscial units

$$r_L = 1.08 \text{ pc } \frac{E_{15}}{Z \cdot B_{\mu G}}$$

$$B_{\mu G} \cdot L_{pc} > \frac{2 \cdot E_{15}}{Z \cdot \beta}$$ **necessary condition not sufficient**

$$E_{15} < Z \cdot B_{\mu G} \cdot L_{pc} \cdot \frac{\beta}{2}$$

A.M. Hillas, Ann. Rev. Astron. Astrophys. 22 (1984) 425

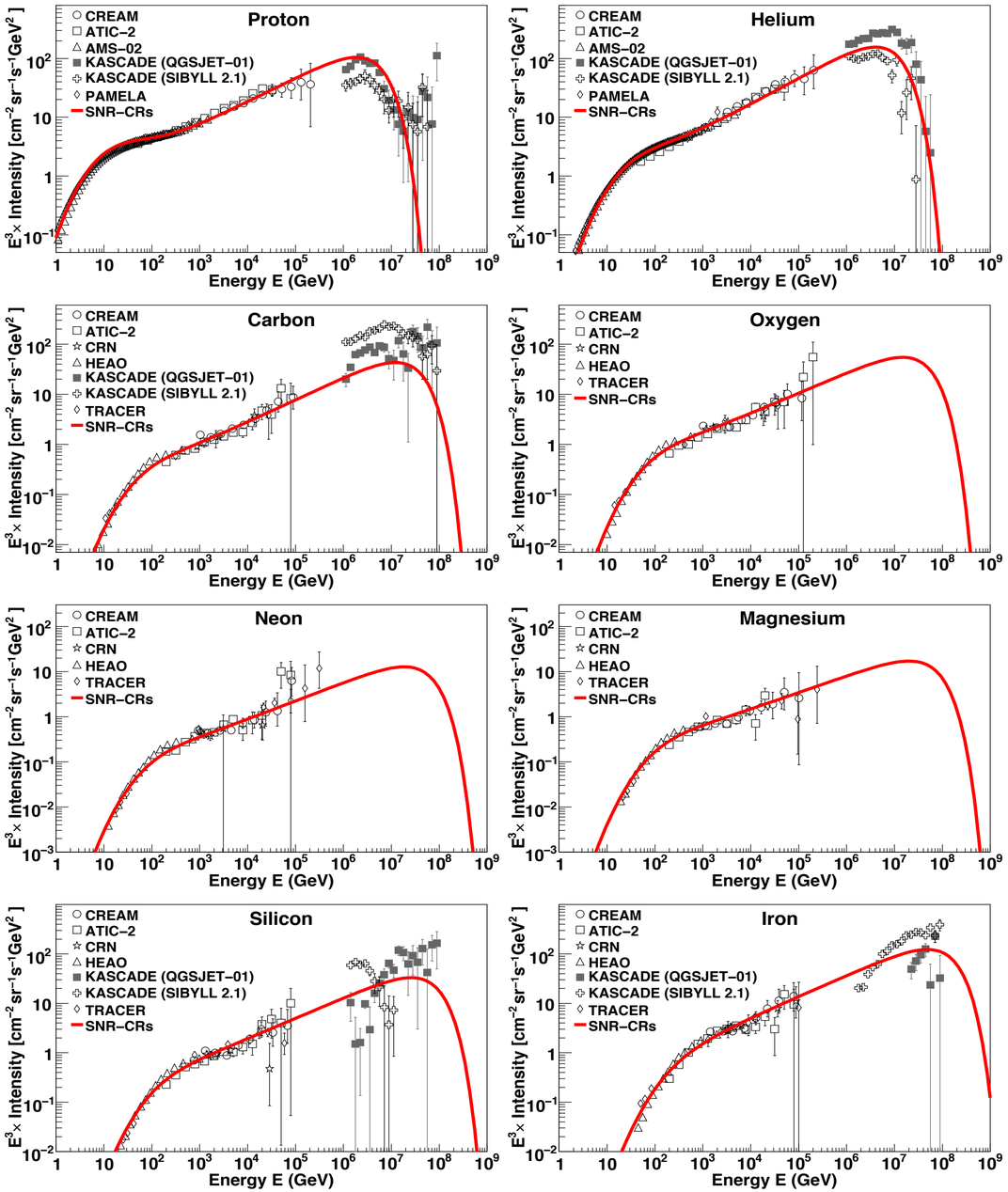

Fig. 1. Energy spectra for different cosmic-ray elements. *Solid line*: Model prediction for the SNR-CRs. *Data*: CREAM (Ahn et al. 2009; Yoon et al. 2011), ATIC-2 (Panov et al. 2007), AMS-02 (Aguilar et al. 2015a,b), PAMELA (Adriani et al. 2011), CRN (Müller et al. 1991; Swordy et al. 1990), HEAO (Engelmann et al. 1990), TRACER (Obermeier et al. 2011), and KASCADE (Antoni et al. 2005). Cosmic-ray source parameters (q, f) used in the calculation are given in Table 1. For the other model parameters (D_0, a, η, s), see text for details.

Contribution of (regular) SNR-CR

$$E_c = Z \cdot 4.5\ 10^6\ \text{GeV}$$

$$Q(p) = AQ_0(Ap)^{-q} \exp\left(-\frac{Ap}{Zp_c}\right),$$

Table 1. Source spectral indices, q, and energy injected per supernova, f, for the different species of cosmic rays used in the calculation of the SNR-CRs spectra shown in Figures 1 and 2.

Particle type	q	f ($\times 10^{49}$ ergs)
Proton	2.24	6.95
Helium	2.21	0.79
Carbon	2.21	2.42×10^{-2}
Oxygen	2.25	2.52×10^{-2}
Neon	2.25	3.78×10^{-3}
Magnesium	2.29	5.17×10^{-3}
Silicon	2.25	5.01×10^{-3}
Iron	2.25	4.95×10^{-3}

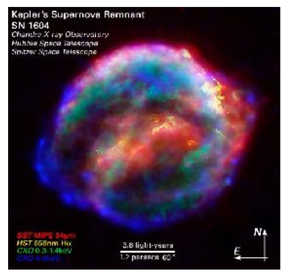

S. Thoudam et al., A&A 595 (2016) A33

Transport equation for cosmic rays in the Galaxy

diffusion

energy loss (Bethe Bloch)

loss through interactions with ISM (spallation)

loss through radioactive decay

$$\frac{\partial N_i}{\partial t} = \nabla(D_i \nabla N_i) - \frac{\partial}{\partial E}(b_i N_i) - n\nu\sigma_i N_i - \frac{N_i}{\gamma\tau_i} + Q_i + \sum_{j>i} n\nu\sigma_{ij} N_j + \sum_{j>i} \frac{N_j}{\gamma_j \tau_{ij}}$$

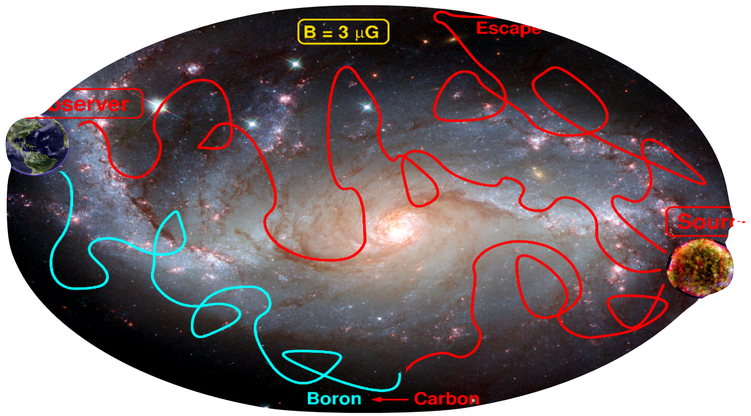

source term

production through spallation of heavy nuclei

production through decay of heavy nuclei

Formation of the chemical composition

Relative abundance of elements at Earth

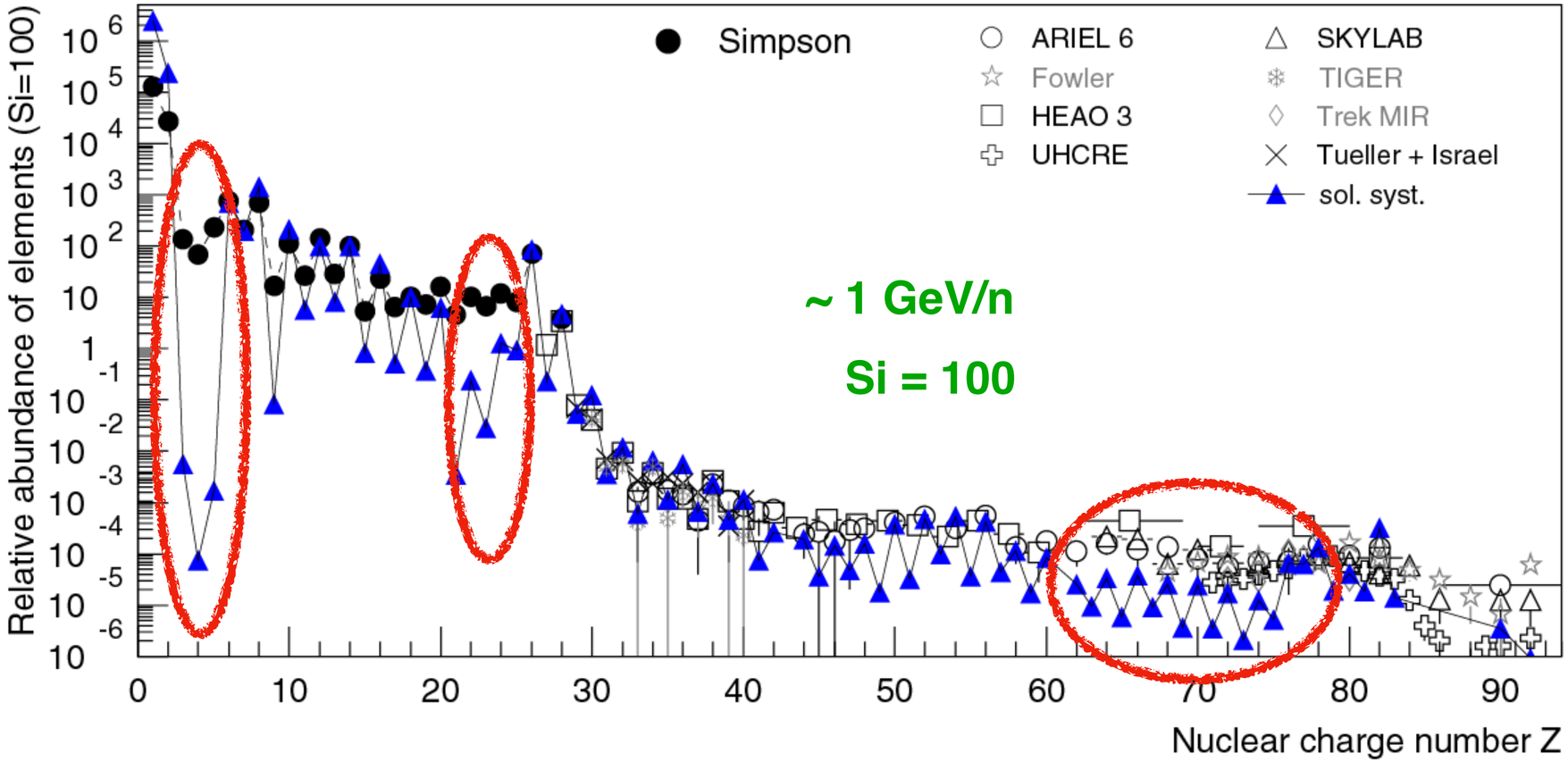

abundance of elements in CRs and solar system mostly similar

but few differences, e.g. Li, Be, B —> important to understand propagation of cosmic rays in Galaxy —> column density of traversed matter

primary cosmic rays generated at source e.g. p, He, Fe
spallation products —> secondary cosmic rays, e.g. Li, Be, B

Leaky box approximation

free propagation of CRs in a closed volume (Galaxy)

energy dependent escape probability $P_{esc}(E)$, constant in time

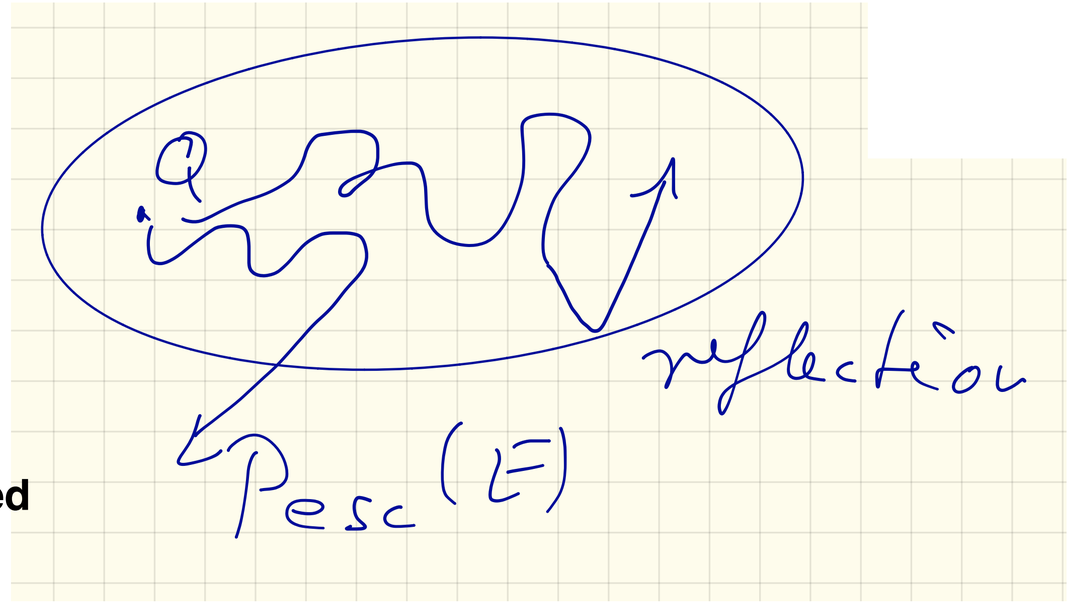

λ_{esc}, **mean amount of matter traversed by CRs in the Galaxy**

$$\lambda_{esc} \equiv \rho_{ISM} \beta c \tau_{esc},$$

τ_{esc} **life time/residence time of CRs in the Galaxy**

simplified transport equation for stable CR nuclei

(neglecting energy loss and gain)

$$\frac{N_j(E)}{\tau_j(E)} = Q_j(E) - \frac{\beta c\, \rho_{ISM}}{\lambda_j(E)} N_j(E) + \frac{\beta c\, \rho_{ISM}}{m} \sum_{i>j} \sigma_{i\to j} N_i(E)\ . \qquad (4.11)$$

The negative term on the right-hand side of the equation describes the number of nuclei of type j lost in propagation because of fragmentation. The positive term sums over all higher mass nuclei that produce j in spallation processes.

Formation of the chemical composition

The observed cosmic ray composition can be understood in terms of the general elemental abundance and the fragmentation cross-sections if all cosmic ray nuclei have the same propagation history [83, 84] and have on the average traversed 5 to 10 g/cm^2 of matter. For ρ_{ISM} of one nucleon per cm^3 this corresponds to escape time $\tau_{esc} = N_A \lambda_{esc}/c \simeq 3$–$6 \times 10^6$ years.

The study of the energy dependence of the secondary to primary ratio establishes the energy dependence of the containment time for cosmic rays in the Galaxy. Using measurements like the one shown in Fig. 4.6 one could fit the energy dependence of λ_{esc} as [82]

$$\lambda_{esc} = 10.8\,\beta \times \left(\frac{4}{R}\right)^{\delta} \text{ g/cm}^2\,, \tag{4.12}$$

where R is the particle rigidity in GV and $\delta \simeq 0.6$ shows the rigidity dependence of the escape length. The formula is valid for rigidities above 4 GV. At lower rigidities the escape length is almost constant at $\lambda_{esc} = 10.8\beta$ g/cm^2.

Pathlength of cosmic rays in Galaxy

TRACER balloon experiment

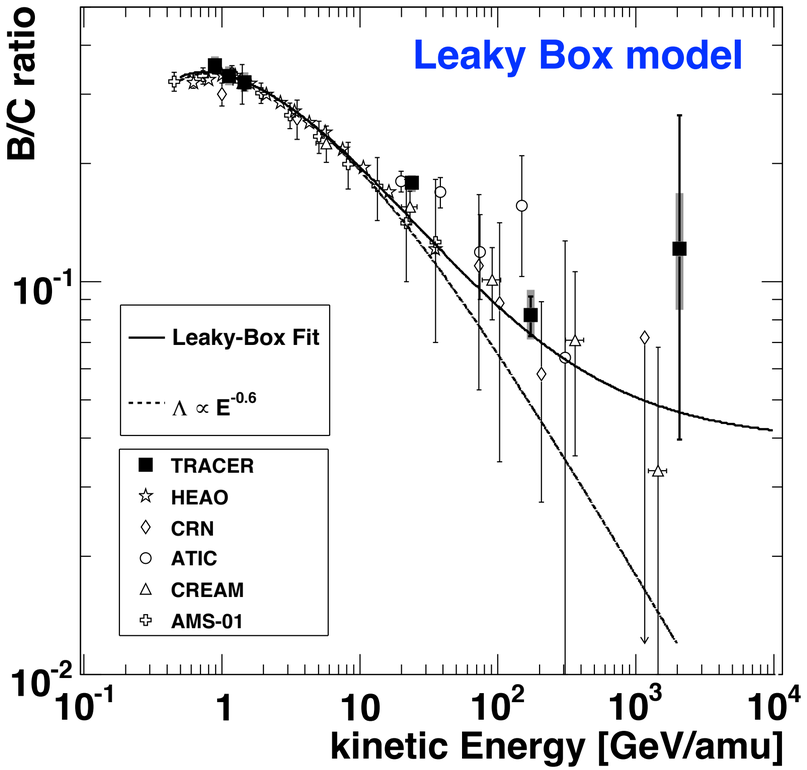

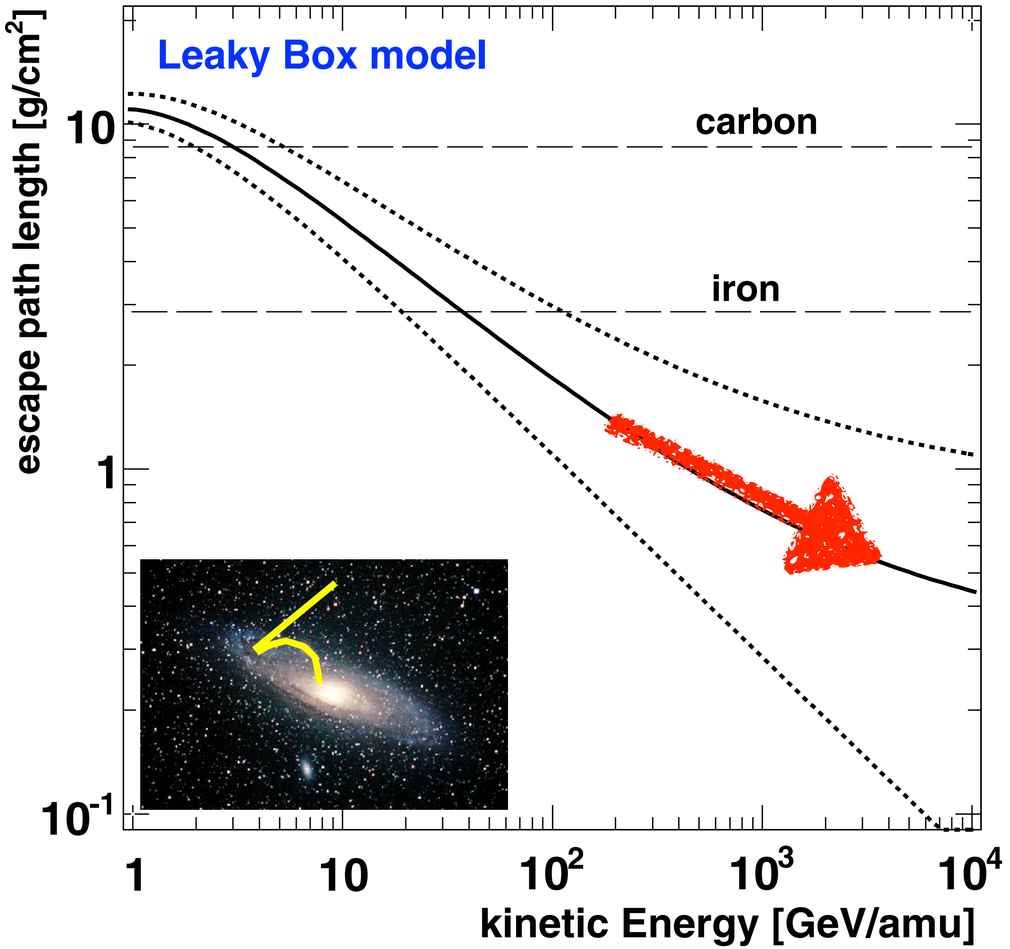

Escape Path Length:

$$\Lambda_{esc}(E) = CE^{-\delta} + \Lambda_0$$

- Propagation index: $\delta = 0.64 \pm 0.02$.
- Residual path length: $\Lambda_0 = 0.7 \pm 0.2$ g/cm^2.

$$\Lambda(R) = \frac{26.7\beta}{(\beta R)^{\delta} + (0.714 \cdot \beta R)^{-1.4}} + \Lambda_0 \text{ g/cm}^2,$$

A. Obermeier et al., ApJ 752 (2012) 69

Science Bulletin 67 (2022) 2162–2166

Contents lists available at ScienceDirect

Science Bulletin

journal homepage: www.elsevier.com/locate/scib

Article

Detection of spectral hardenings in cosmic-ray boron-to-carbon and boron-to-oxygen flux ratios with DAMPE

DAMPE Collaboration [1]

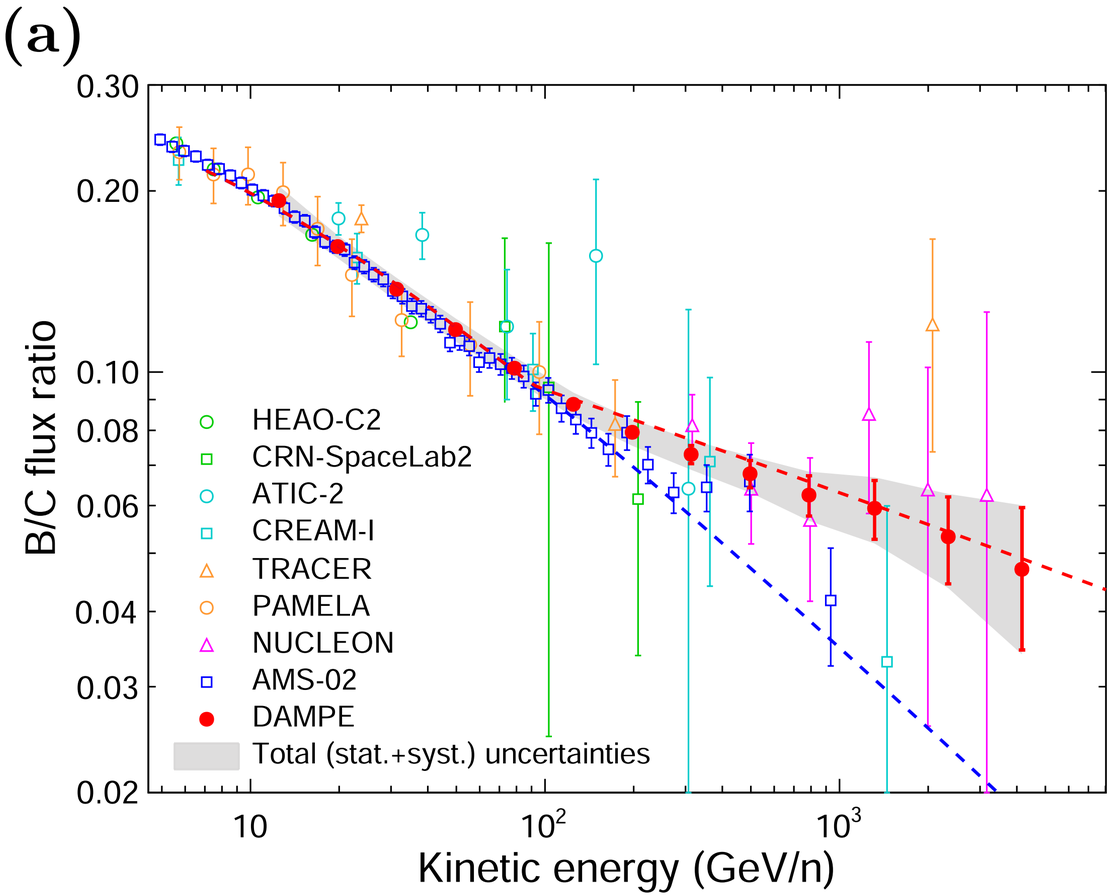

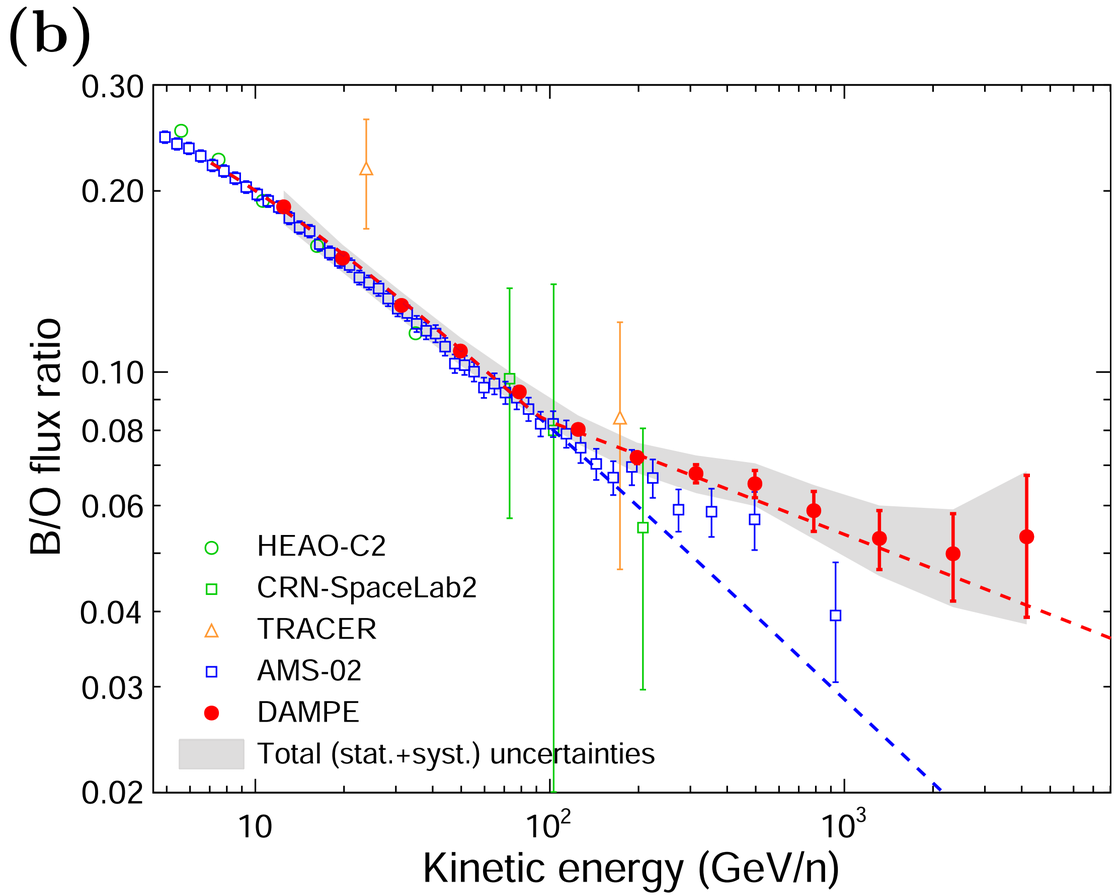

Pathlength vs. interaction length

pathlength in Galaxy $\lambda_{esc} = 5 - 10\ \mathrm{g/cm^2}$

interaction length

nuclear radius $r = r_0 A^{1/3} \qquad r_0 = 1.3 \cdot 10^{-13}\ \mathrm{cm}$

cross section $\sigma_{p-A} = \pi(r_p + r_0 A^{1/3})^2$

ISM: protons $n = 1/\mathrm{cm}^3 \quad \rho = 1.67 \cdot 10^{-24}\ \mathrm{g/cm^3}$

interaction length $\lambda_{p-A} = \dfrac{\rho}{\sigma_{p-A} \cdot n}$

$\lambda_{p-p} = 21\ \mathrm{g/cm^2} \qquad > \lambda_{esc}$

$\lambda_{p-Fe} = 1.6\ \mathrm{g/cm^2} \qquad < \lambda_{esc}$

Shape of energy spectrum

$$\frac{dN}{dE} \propto E_0^{\gamma}$$

at source γ ~ -2.1

at Earth γ ~ -2.6 to -2.7

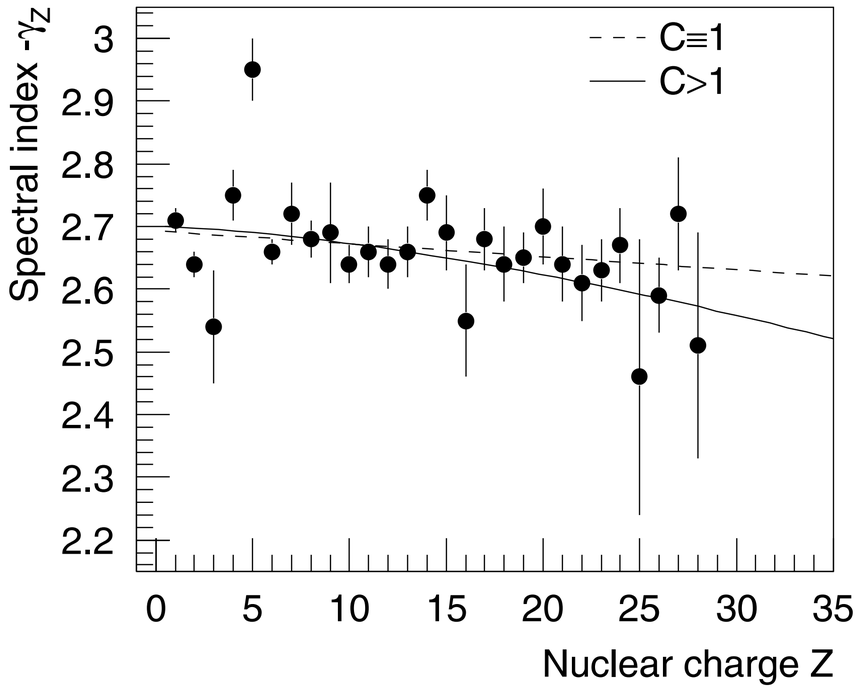

Fig. 5. Spectral index γ_Z versus nuclear charge Z (see Table 1). The solid line represents a three parameter fit according to Eq. (6), the dashed graph a linear fit.

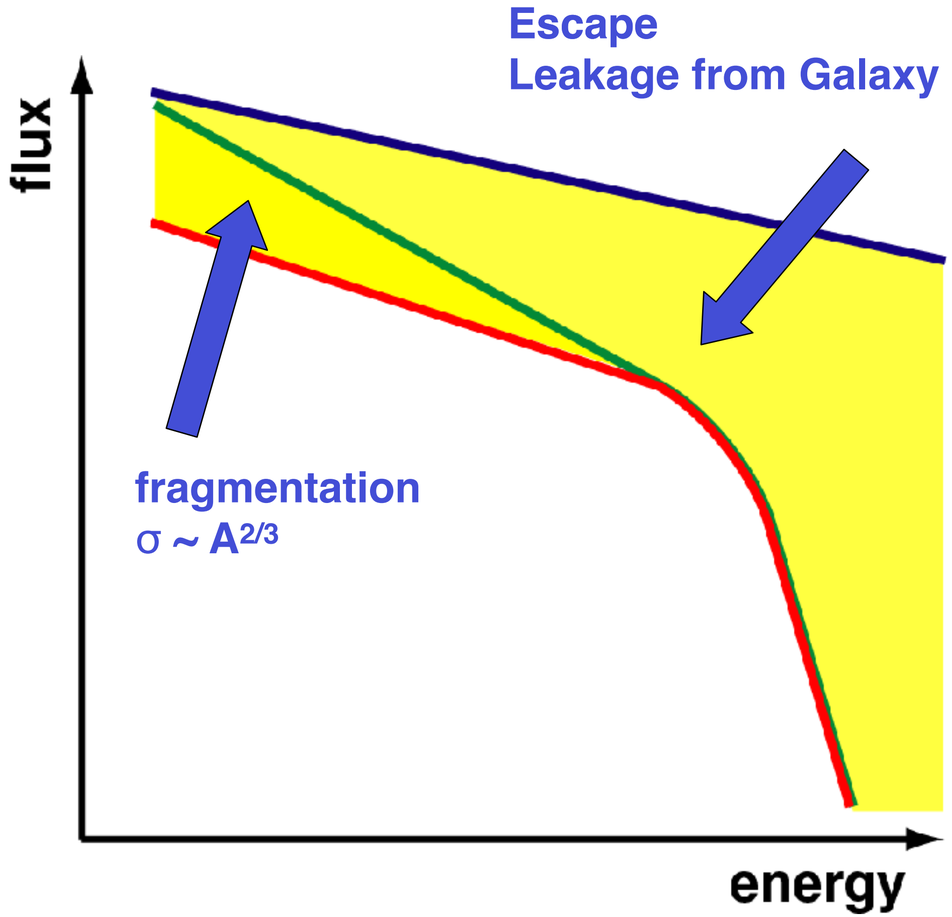

JRH, Astropart. Phys. 19 (2003) 193

Transport equation for cosmic rays in the Galaxy

diffusion

energy loss (Bethe Bloch)

loss through interactions with ISM (spallation)

loss through radioactive decay

$$\frac{\partial N_i}{\partial t} = \nabla(D_i \nabla N_i) - \frac{\partial}{\partial E}(b_i N_i) - n\nu\sigma_i N_i - \frac{N_i}{\gamma\tau_i} + Q_i + \sum_{j>i} n\nu\sigma_{ij} N_j + \sum_{j>i} \frac{N_j}{\gamma_j \tau_{ij}}$$

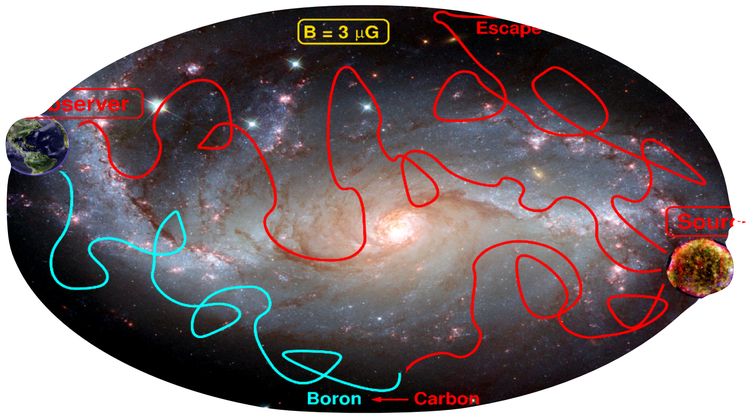

source term

production through spallation of heavy nuclei

production through decay of heavy nuclei

Life time of CRs in Galaxy

In principle the problem of the containment volume could be solved by observations of non-stable secondaries that decay with a half life comparable to the escape time of cosmic rays. To do this one has to put back the decay length in the negative term of (4.11), which becomes

$$\left(\frac{\beta c \rho_{ISM}}{\lambda_j(E)} + \frac{1}{\gamma \tau_j} \right) \times N_j(E) \; .$$

A very suitable isotope is ^{10}Be with a half life of 1.6×10^6 years. The flux of ^{10}Be can be compared with the stable isotopes ^{9}Be and ^{7}Be. The production of the three isotopes depends on the partial production cross-sections and on λ_{esc}. ^{10}Be would decay and its measured flux depends also directly on τ_{esc}. The actual estimate involves folding of the production with the decay of the isotope during propagation in a particular propagation model. The measurements are also very difficult and the results from their analysis are not fully conclusive.

Chart of the nuclides

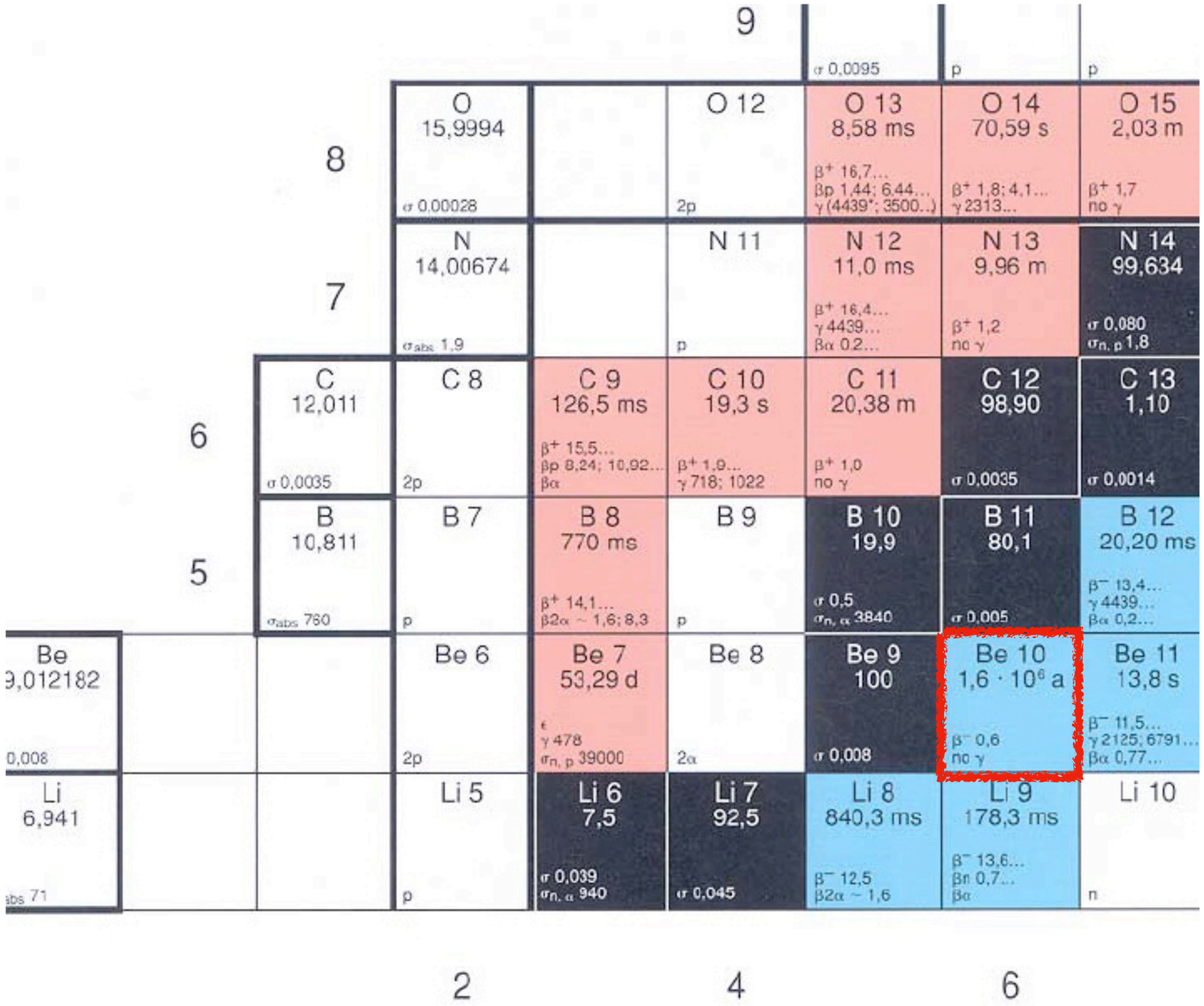

„Age“ of galactic cosmic rays

THE ASTROPHYSICAL JOURNAL, 217:859–877, 1977 November 1

THE AGE OF THE GALACTIC COSMIC RAYS DERIVED FROM THE ABUNDANCE OF ^{10}Be*

M. GARCIA-MUNOZ, G. M. MASON, AND J. A. SIMPSON†
Enrico Fermi Institute, University of Chicago
Received 1977 March 14; accepted 1977 April 21

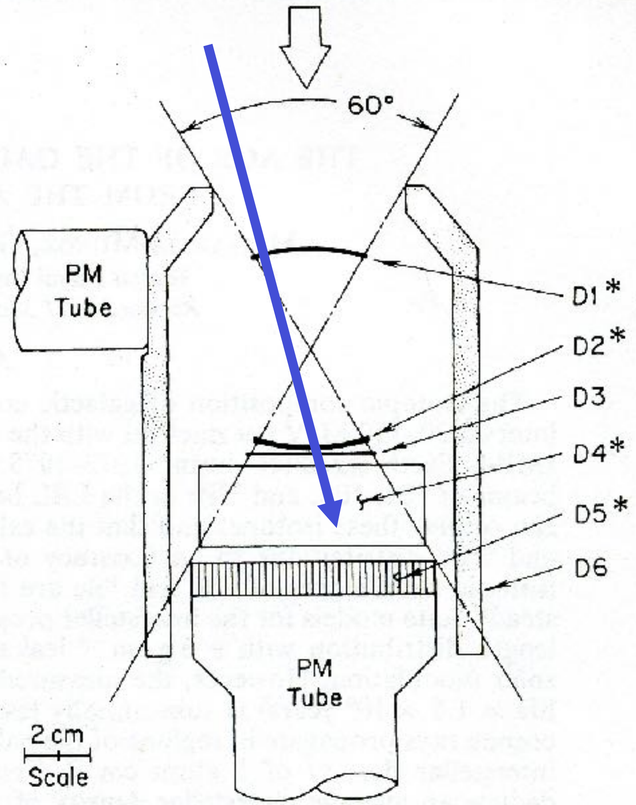

FIG. 1.—Cross section of the IMP-7 and IMP-8 telescopes. D1, D2, and D3 are lithium-drifted silicon detectors of thickness 750, 1450, and 800 μm, respectively. D4 is an 11.5 g cm^{-2} thick CsI (T1) scintillator viewed by four photodiodes. D5 is a sapphire scintillator/Cerenkov radiator of thickness 3.98 g cm^{-2}, and D6 is a plastic scintillation guard counter viewed by a photomultiplier tube. Asterisks denote detectors whose output is pulse-height analyzed.

Residence time in Galaxy

^{10}Be → ^{10}B + e$^-$ (t =2.4 10^6 a)

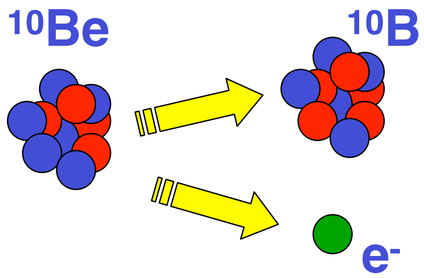

latest measurement from ACE/CRIS experiment:

$$\tau_{esc} = 17 \cdot 10^6 \text{ a}$$

$\Rightarrow \tau_{esc} = 17 \cdot 10^6$ a

from this, we can derive an average density

$$\bar{\rho} = \frac{\lambda_{esc}}{v \cdot \tau_{esc}} = \frac{10\ \mathrm{g/cm^2}}{3 \cdot 10^{10}\ \frac{\mathrm{cm}}{\mathrm{s}} \cdot 17 \cdot 10^6 \cdot 86400 \cdot 365\ \mathrm{s}}$$

$$= 0{,}3\ \mathrm{H\ atom/cm^3}$$

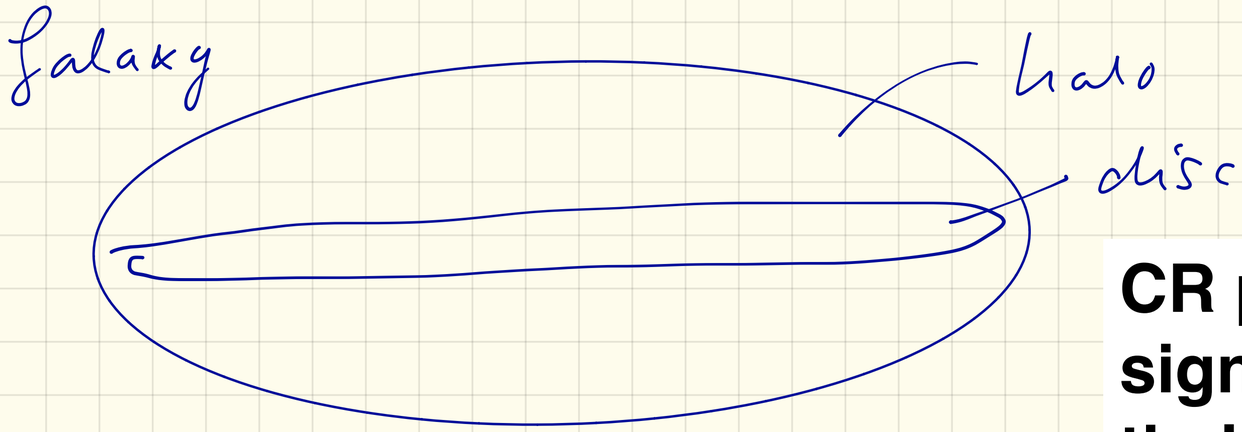

CR particles spend a significant fraction of their residence time in the Galactic halo (lower density)

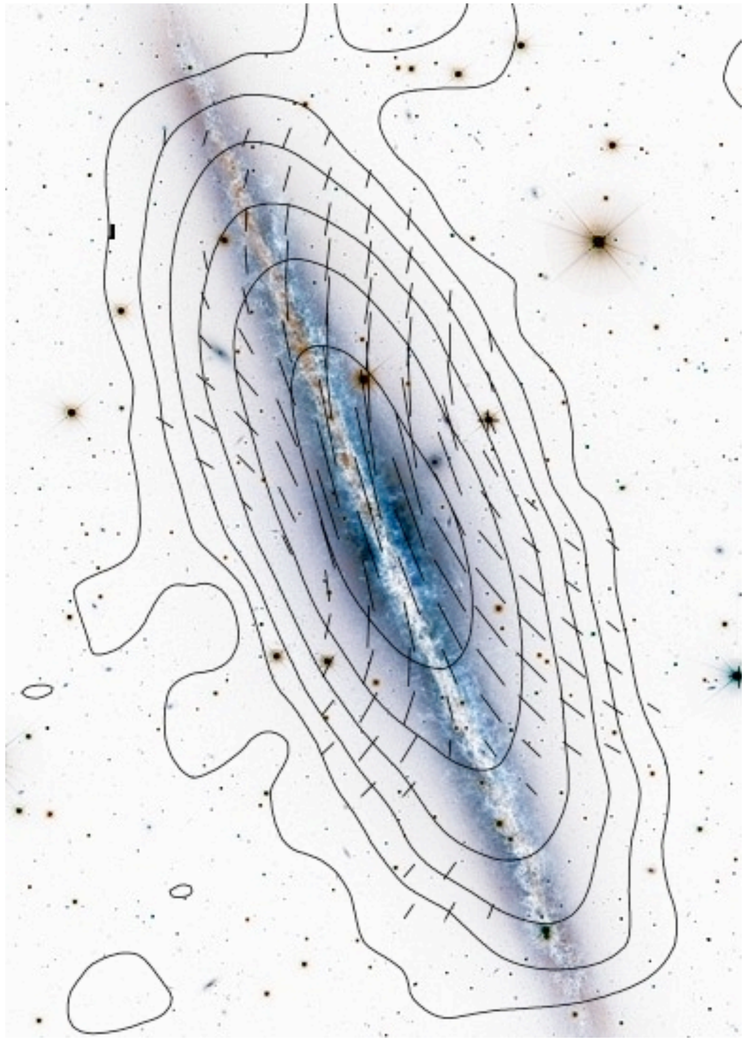

confirmed by observations of diffuse radio emission

synchrotron radiation

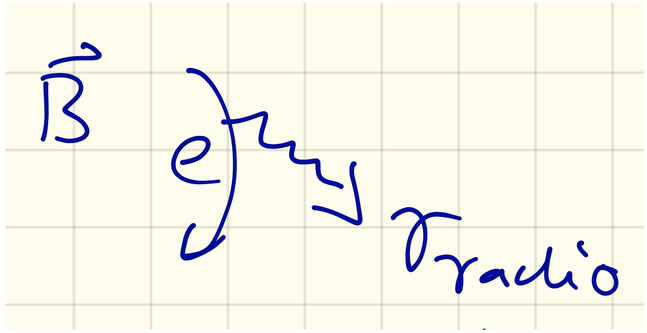

This figure shows the spiral galaxy **NGC 891**, seen almost edge-on, which is believed to be very similar to our Milky Way. It was observed at 8.4 GHz (3.6 cm wavelength) with the Effelsberg 100m telescope. The background optical image is from the CFHT Observatory. The "X-shaped" structure of the magnetic fields indicates the action of a galactic wind. The observed extent of the radio halo is limited by the large energy losses of the cosmic-ray electrons emitting at this wavelength. At lower frequencies (longer wavelengths) the radio waves are emitted by electrons with lower energies for which the energy lossesare smaller, so that larger radio halos are expected.

diffuse radio background of the Milky Way

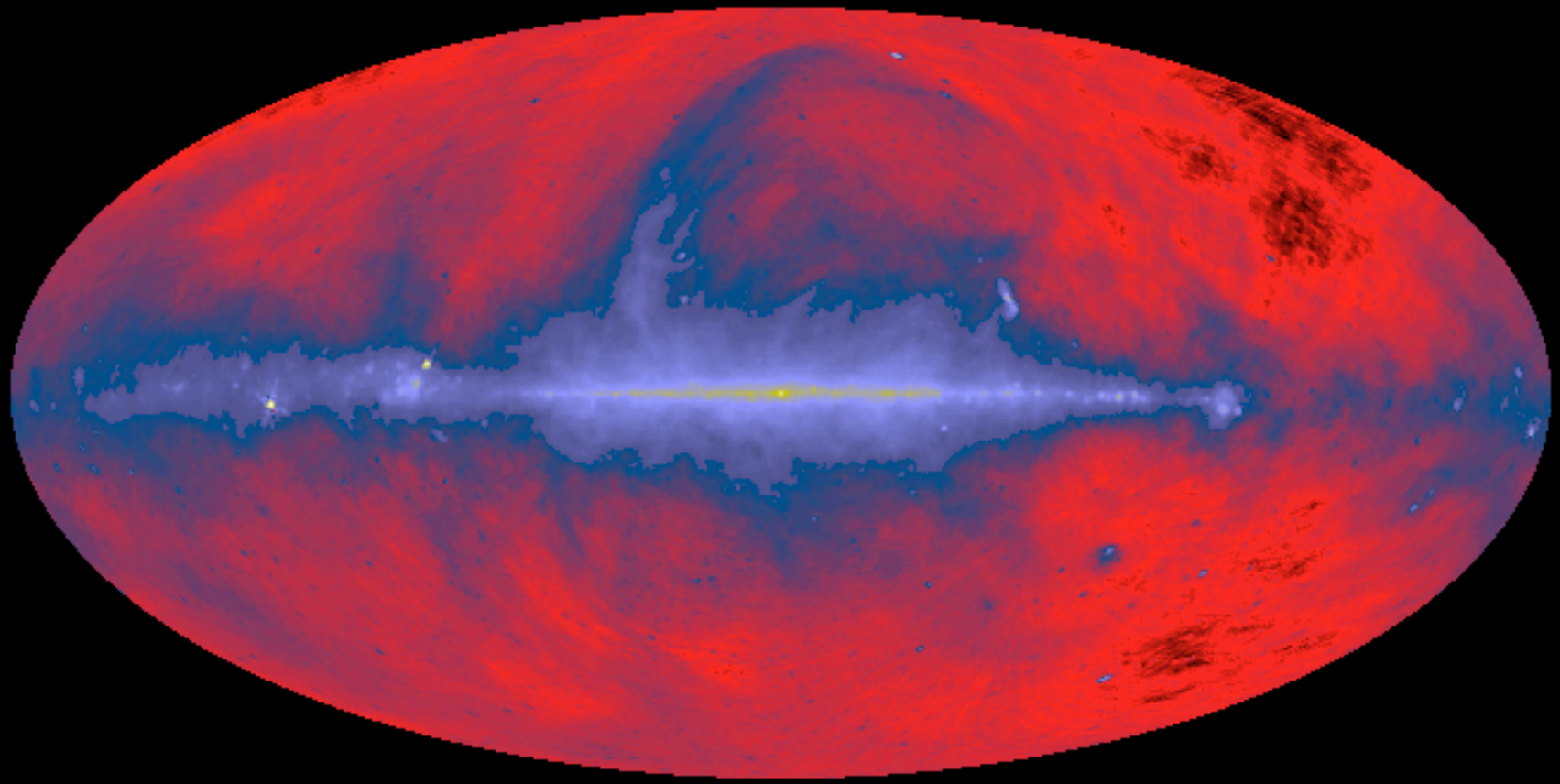

radio wavelengths
synchrotron radiation from electrons in B fields
intensity $\propto B\rho_e$
halo of galaxies are more extended than the visible region
--> confirmation that cosmic rays (electrons)
propagate in the galactic halo

Diffuse Galactic gamma rays

diffuse gamma radiation observed E>100 MeV
origin: $CR + ISM \rightarrow \pi^0 \rightarrow \gamma + \gamma$

--> direct hint that cosmic rays (hadrons) are not a local phenomenon
they propagate in the halo of the Milky Way and they exist in other galaxies

electrons produce gamma rays through *bremsstrahlung* and *inverse Compton interaction* with CMB and with diffuse infrared/optical radiation

The Fermi All Sky Map, showing the diffuse galactic gamma-ray background from the Milky Way.

Courtesy of NASA/DOE/International LAT Team

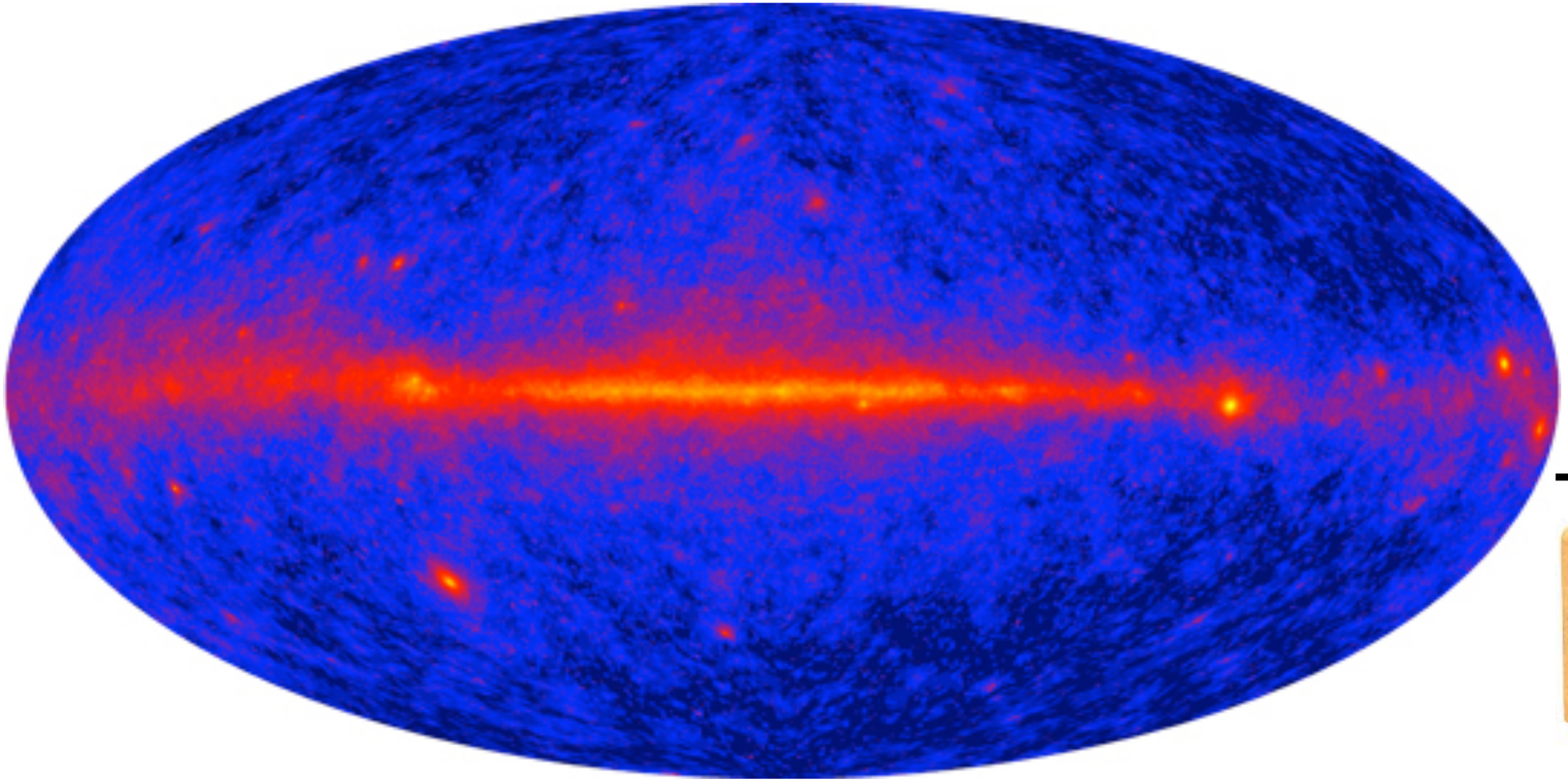

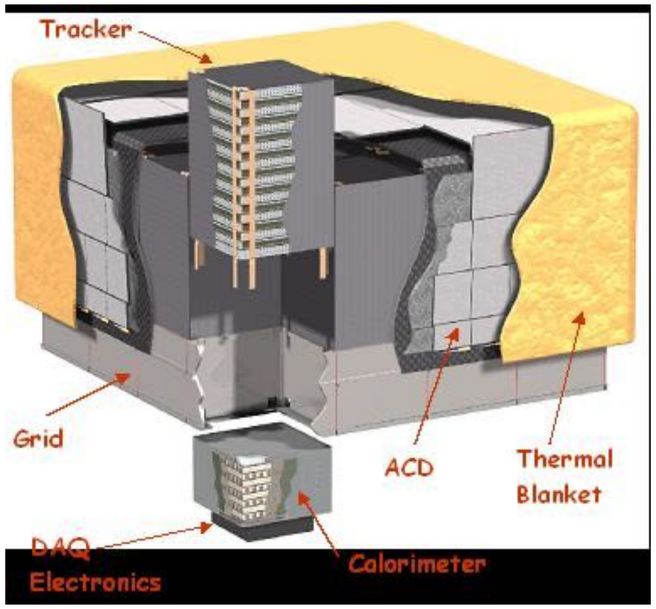

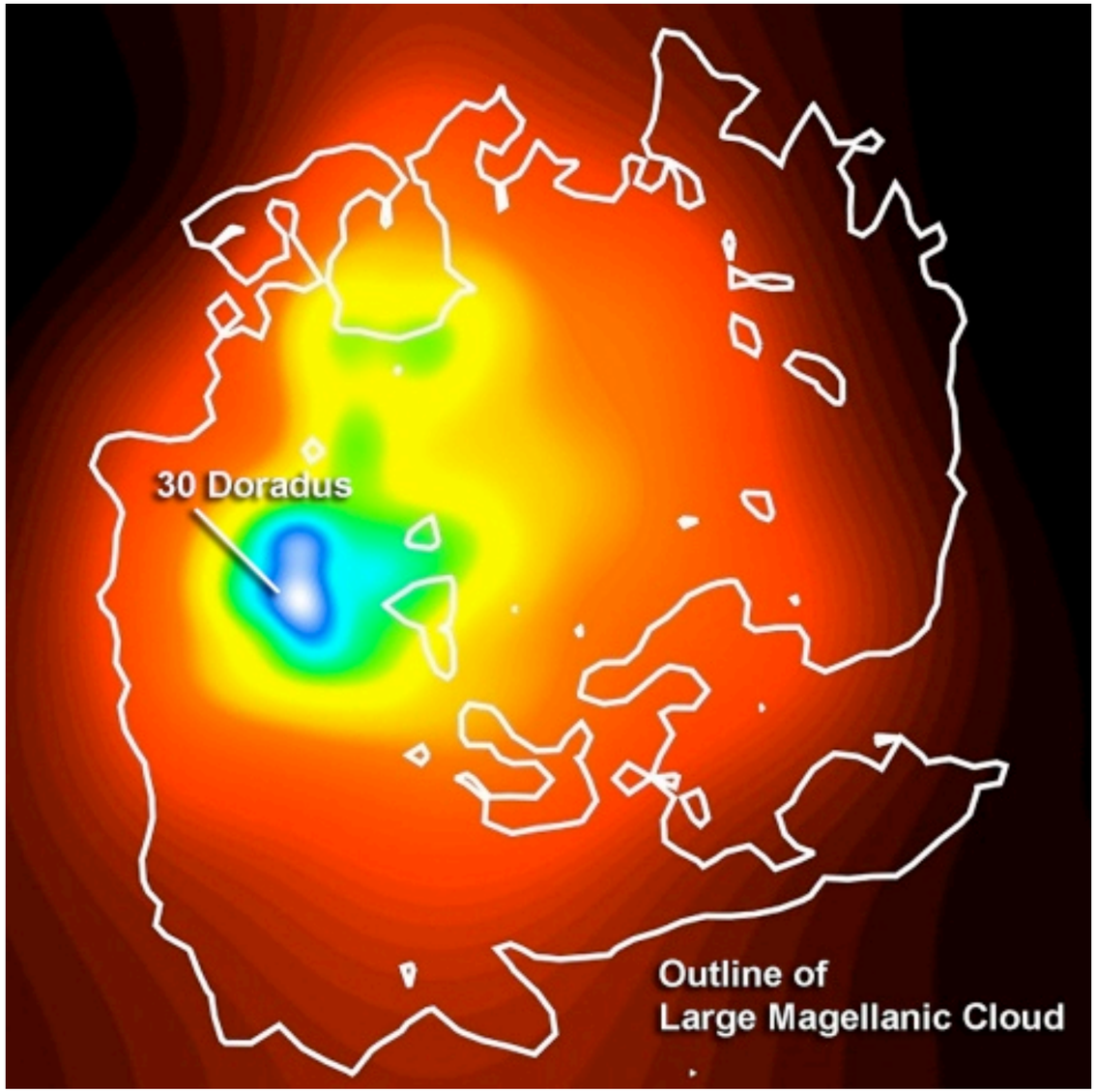

Fermi's Large Area Telescope shows that an intense star-forming region in the Large Magellanic Cloud named 30 Doradus is also a source of diffuse gamma rays. Brighter colors indicate larger numbers of detected gamma rays.

Relative importance of gamma-ray production processes

For this estimate we approximate the total proton spectrum by $N(E_p) \equiv dN/dE_p = a_p E_p^{-\alpha}$ protons GeV^{-1} cm^{-3}. For $E_\gamma \gg m_\pi c^2/2$, the γ-ray source function from π^0 production is

$$Q_{\pi^0}(E_\gamma) \approx n \left(\sigma_{pp}^{inel} \frac{2 Z_{N\pi^0}}{\alpha} \right) \times a_p \, E_\gamma^{-\alpha}, \tag{4.14}$$

where σ_{pp}^{inel} is the inelastic proton–proton cross section, n is the average matter density per cm^3 and $Z_{N\pi}$ is a spectrum-weighted moment of the momentum distribution of pions produced in proton–proton collisions [6]. The spectrum weighted moments give the yield of the process ab from a power law cosmic ray spectrum of integral spectral index γ

$$Z_{ab} \equiv \int_0^1 x_L^\gamma F(x_L) dx_L \ , \tag{4.15}$$

where x_L is the ratio of the energy of the secondary particle b to the primary energy in the Lab system. For $\alpha = 2.0$, 2.4, and 2.7 respectively, $Z_{N\pi^0} \approx 0.16$, 0.066 and 0.035. Thus, for $\alpha = 2.7$, close to the locally measured proton spectrum

$$Q_{\pi^0}(E_\gamma) \approx 2.5 \times 10^{-26} \, a_p \, n \, E_\gamma^{-2.7} \quad \text{photons GeV}^{-1} \text{ s}^{-1} \text{ cm}^{-3} \ , \tag{4.16}$$

where E_γ is in GeV and n is in cm^{-3}.

from protons

Relative importance of gamma-ray production processes

Similarly, we approximate the total electron spectrum by $N(E_e) \equiv dN/dE_e = a_e E_e^{-\alpha}$ electrons $\mathrm{GeV}^{-1}\,\mathrm{cm}^{-3}$. To obtain the bremsstrahlung source function, we assume that after an electron of energy E_e has traveled one radiation length, X_0, it is converted into a photon of energy $E_\gamma = E_e$. Hence,

$$Q_{\mathrm{br}}(E_\gamma) \approx N(E_\gamma) n / X_0. \tag{4.17}$$

Thus, for $\alpha = 2.7$,

$$Q_{\mathrm{br}}(E_\gamma) \approx 1.2 \times 10^{-25} a_e n E_\gamma^{-2.7} \quad \text{photons GeV}^{-1}\ \mathrm{s}^{-1}\ \mathrm{cm}^{-3}\ . \tag{4.18}$$

from electrons (bremsstrahlung)

Relative importance of gamma-ray production processes

For inverse Compton scattering, we approximate the photon energy after scattering by an electron of energy $E_e = \gamma m_e c^2$ by $\gamma^2 \bar{\varepsilon}$ where $\bar{\varepsilon}$ is the mean photon energy of the radiation field under consideration. Provided the Compton scattering is in the Thomson regime ($\gamma\bar{\varepsilon} \ll m_e c^2$) this gives an inverse Compton source function

$$Q_{\rm IC}(E_\gamma) \approx N(\gamma) n_{\rm ph} \sigma_T / 2\gamma\bar{\varepsilon} \,, \tag{4.19}$$

where $N(\gamma)d\gamma = N(E_e)\, dE_e$, and we obtain

$$Q_{\rm IC}(E_\gamma) \approx a_e \frac{(\bar{\varepsilon})^{1/2}}{E_\gamma^{(\alpha-1)/2}} \frac{n_{\rm ph}\sigma_T}{m_e c^2} \,. \tag{4.20}$$

electrons inverse Compton

Relative importance of gamma-ray production processes

For scattering on the microwave background, we use $n_{\rm ph} = 400$ cm^{-3}, $\bar{\varepsilon} = 6.25 \times 10^{-4}$ eV, and obtain for $\alpha = 2.7$

$$Q_{\rm IC}(E_\gamma) \approx 2.1 \times 10^{-24} a_e E_\gamma^{-1.85} \quad \text{photons GeV}^{-1}\ \text{s}^{-1}\ \text{cm}^{-3}\ , \tag{4.21}$$

where E_γ is in GeV. We note that, for an assumed matter density of 1 cm^{-3}, at 1 GeV the inverse Compton scattering contribution is an order of magnitude larger than the bremsstrahlung contribution, and the relative importance of the inverse Compton scattering contribution increases with energy. The bremsstrahlung contribution is higher than that of π^0 by about a factor of five. The π^0 γ-rays can only be important if there are many more protons than there are electrons.

from electrons (inverse Compton scattering on CMB)

More exact gamma-ray yields

previous section: estimates
main inaccuracy: energy spectra for protons and electrons are different in CRs
electrons suffer synchrotron radiation losses and have a steeper spectrum

Bertsch et al. [71] suggest the following spectrum of the galactic electrons (in $\mathrm{cm}^{-2}\,\mathrm{s}^{-1}\,\mathrm{sr}^{-1}\,\mathrm{GeV}^{-1}$)

$$\begin{aligned} dN/dE_e &= 0.019 E_e^{-2.35} && \text{for } E_e < 5 \text{ GeV} \\ &= 0.149 E_e^{-3.30} && \text{for } E_e \geq 5 \text{ GeV} \end{aligned} \qquad (4.22)$$

INCLUSIVE (e^-+e^+) spectrum below 1 TeV (AMS-02, FERMI & PAMELA)

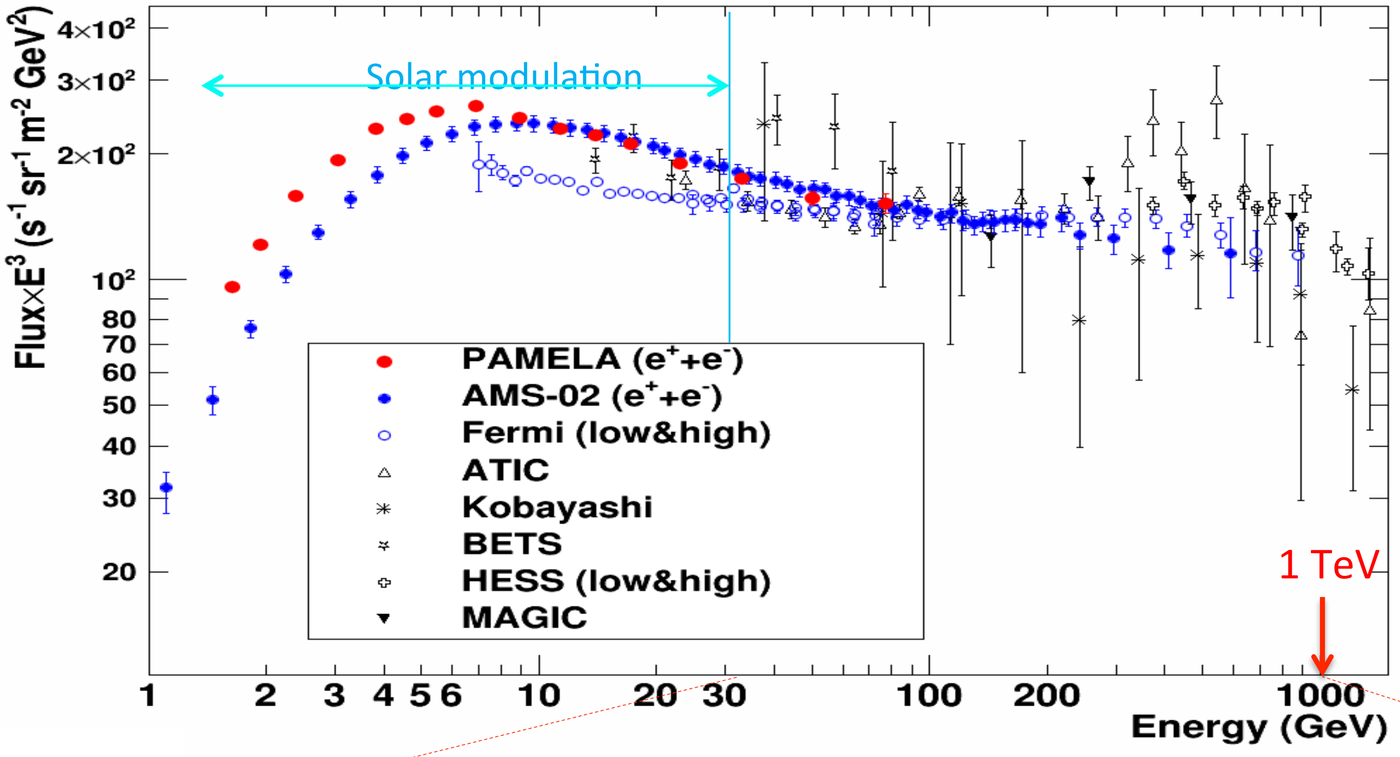

Figure 4.8 shows the source functions of the three processes using the electron spectrum given by (4.23) and a proton spectrum $dN/dE_p = 3.06 E_p^{-2.70}$. The matter density for π^0 and bremsstrahlung is 1 (atom/cm^3) and the microwave background is used as target for the inverse Compton effect. The π^0 yield peaks at $E_\gamma = m_{\pi^0}/2 \simeq 70$ MeV but in Fig. 4.8 the peak appears at higher energy because it is shifted by the E_γ factor. The bremsstrahlung spectrum dominates at lower energies and clearly follows the break in the electron spectrum. The inverse Compton spectrum is indeed very flat ($\sim E_\gamma^{(\alpha+1)/2}$) and approaches the π^0 contribution at $E_\gamma = 10^4$ GeV in spite of the much steeper electron spectrum.

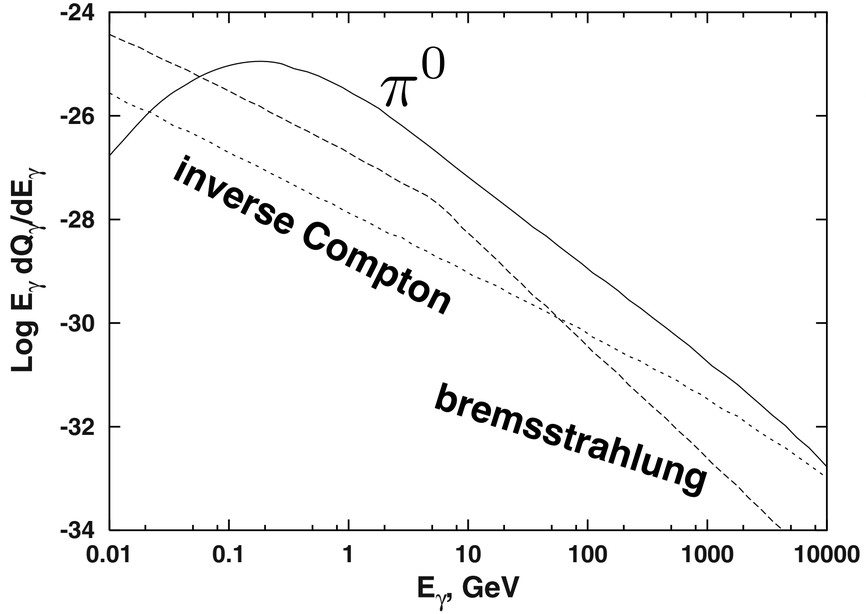

More exact gamma-ray yields as obtained with MC calculations

Fig. 4.8. Yields of the γ-ray production by π^0 (solid line), bremsstrahlung (dashes) and inverse Compton (dots) for the proton and electron spectra described in the text.

Transport equation for cosmic rays in the Galaxy

diffusion

energy loss (Bethe Bloch)

loss through interactions with ISM (spallation)

loss through radioactive decay

$$\frac{\partial N_i}{\partial t} = \nabla(D_i \nabla N_i) - \frac{\partial}{\partial E}(b_i N_i) - n v \sigma_i N_i - \frac{N_i}{\gamma \tau_i} + Q_i + \sum_{j>i} n v \sigma_{ij} N_j + \sum_{j>i} \frac{N_j}{\gamma_j \tau_{ij}}$$

source term

production through spallation of heavy nuclei

production through decay of heavy nuclei

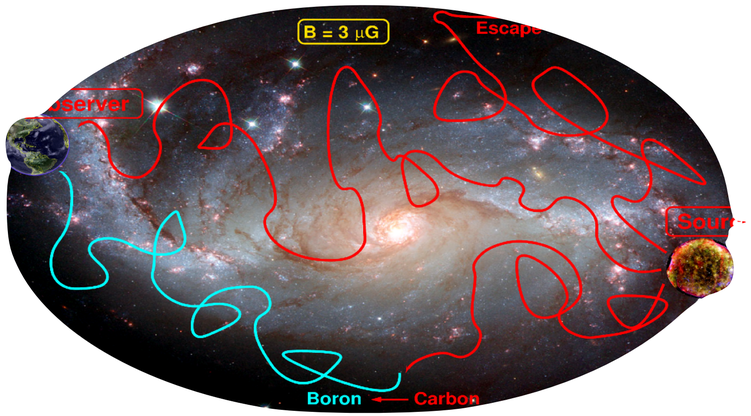

Available online at www.sciencedirect.com
ScienceDirect
Astroparticle Physics 27 (2007) 119–126
Astroparticle Physics
www.elsevier.com/locate/astropart

example of knee due to propagation/leakage from Galaxy

Propagation of super-high-energy cosmic rays in the Galaxy

Jörg R. Hörandel [a,*], Nikolai N. Kalmykov [b], Aleksei V. Timokhin [c]

The steady-state diffusion equation for the cosmic-ray density $N(r)$ is (neglecting nuclear interactions and energy losses)

$$-\nabla_i D_{ij}(r)\nabla_j N(r) = Q(r). \quad (1)$$

$Q(r)$ is the cosmic-ray source term and $D_{ij}(r)$ the diffusion tensor.

Under the assumption of azimuthal symmetry and taking into account the predominance of the toroidal component of the magnetic field, Eq. (1) is presented in cylindrical coordinates as

$$\left[-\frac{1}{r}\frac{\partial}{\partial r}rD_\perp\frac{\partial}{\partial r}-\frac{\partial}{\partial z}D_\perp\frac{\partial}{\partial z}-\frac{\partial}{\partial z}D_A\frac{\partial}{\partial r}+\frac{1}{r}\frac{\partial}{\partial r}rD_A\frac{\partial}{\partial z}\right]N(r,z)=Q(r,z), \quad (2)$$

where $N(r,z)$ is the cosmic-ray density averaged over the large-scale fluctuations with a characteristic scale $L \sim 100$ pc [3]. $D_\perp \propto E^m$ is the diffusion coefficient, where m is much less than one ($m \approx 0.2$), and $D_A \propto E$ the Hall diffusion coefficient. The influence of Hall diffusion becomes predominant at high energies ($>10^{15}$ eV). The sharp

The magnetic field of the Galaxy consists of a large-scale regular and a chaotic, irregular component $\vec{B} = \vec{B}_{\rm reg} + \vec{B}_{\rm irr}$. A purely azimuthal magnetic field was assumed for the regular field

$$B_z = 0, \quad B_r = 0, \quad B_\phi = 1\ \mu\text{G}\exp\left(-\frac{z^2}{z_0^2}-\frac{r^2}{r_0^2}\right),$$

where $z_0 = 5$ kpc and $r_0 = 10$ kpc are constants [3].

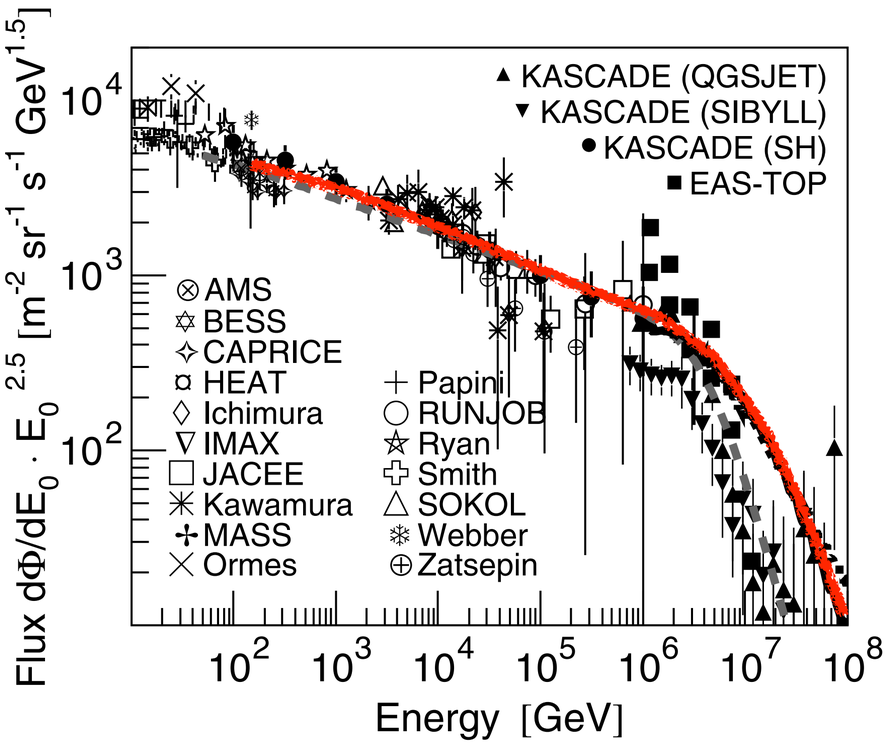

Fig. 7. Proton flux as obtained from various measurements, for references see [28], compared to the spectra shown in Fig. 6 (black lines) and the *poly-gonato* model [26] (grey, dashed line).

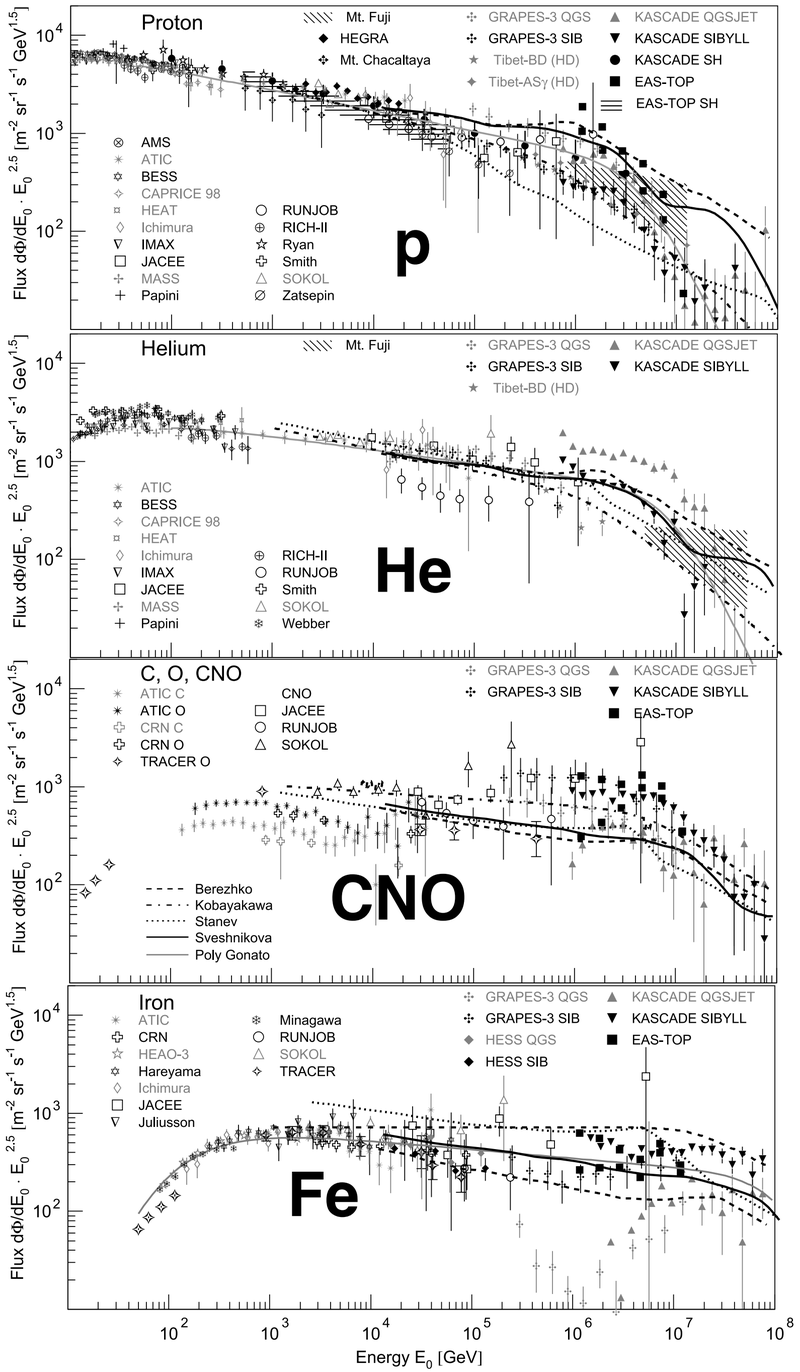

maximum energy

$$E_{max} \propto B \cdot Z$$

$$E_{max} \approx Z \cdot 100\ \mathrm{TeV} \ldots Z \cdot 5\ \mathrm{PeV}$$

JRH, Adv. Space Res. 41 (2008) 442

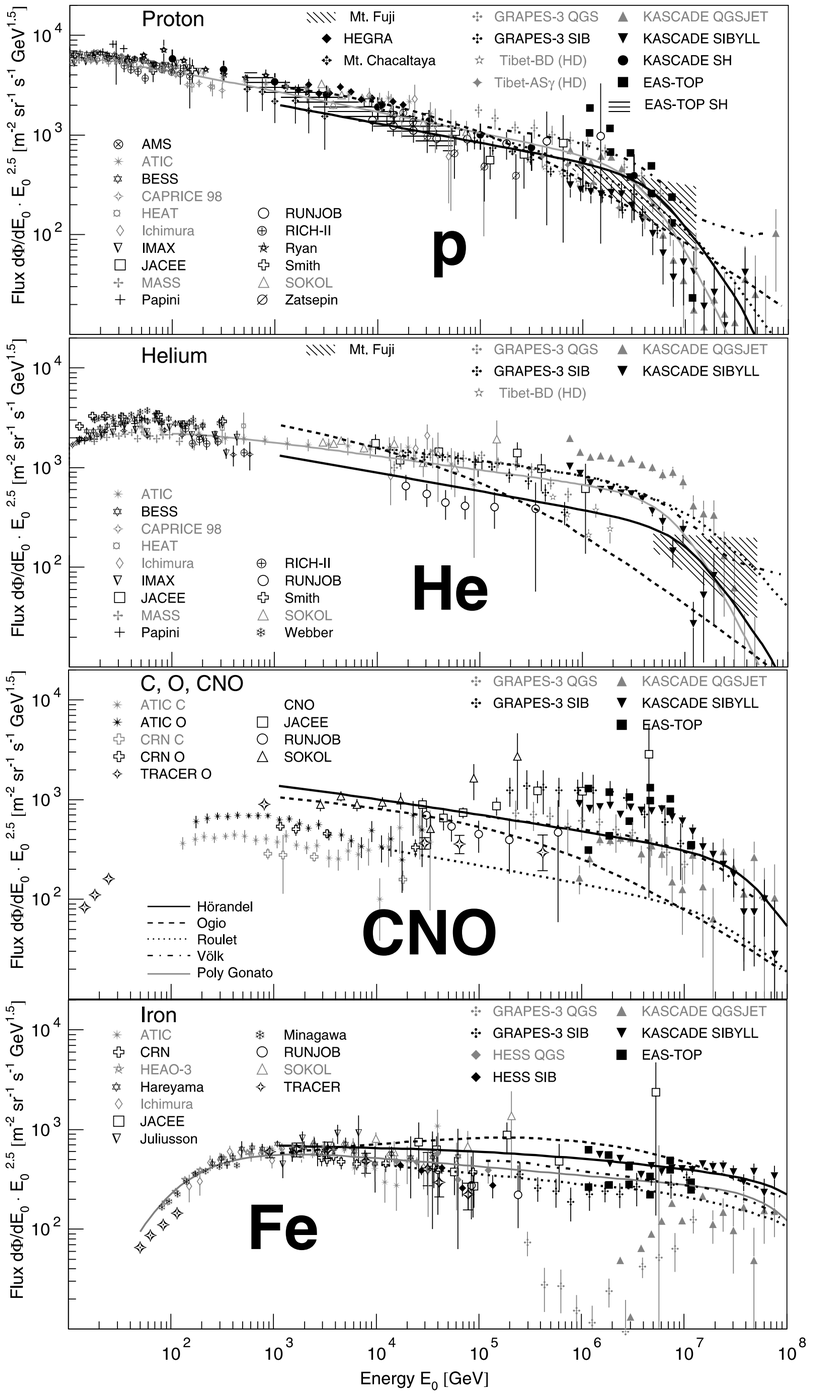

leakage from Galaxy

$$E_k \propto Z$$

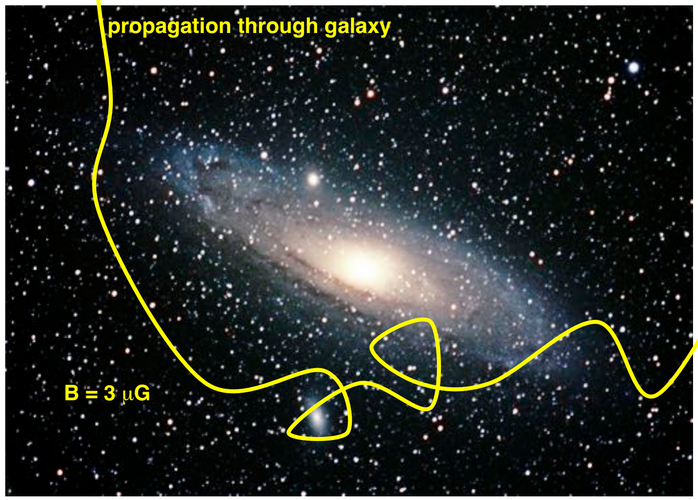

JRH, Adv. Space Res. 41 (2008) 442

Transition to extragalactic CR component

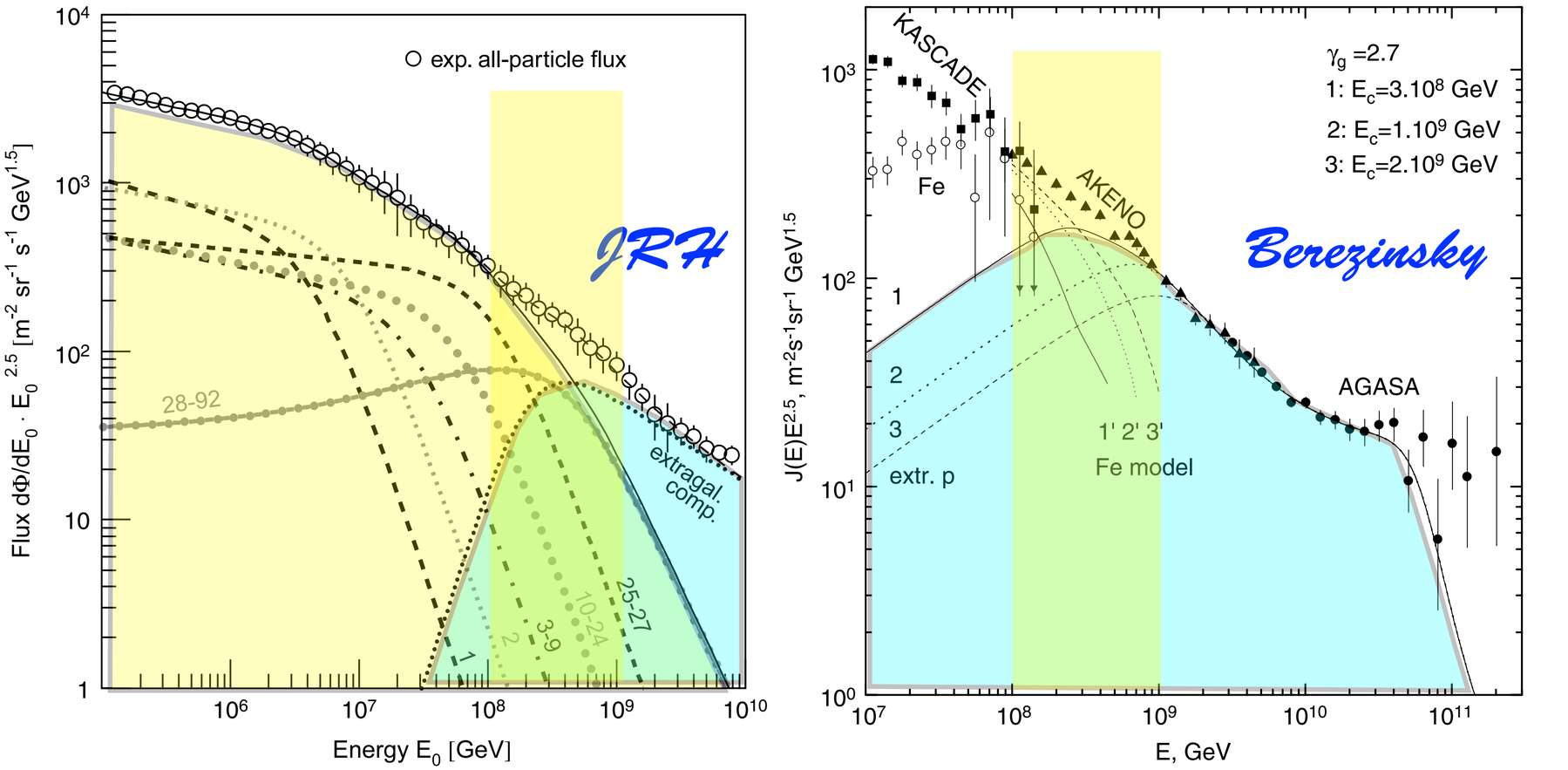

Fig. 26. *Left panel*: Cosmic-ray energy spectra according to the poly-gonato model [2]. The spectra for groups of elements are labeled by their respective nuclear charge numbers. The sum of all elements yields the galactic all-particle spectrum (—) which is compared to the average measured flux. In addition, a hypothetical extragalactic component is shown to account for the observed all-particle flux (- - -). *Right panel*: Transition from galactic to extragalactic cosmic rays according to Berezinsky et al. [451]. Calculated spectra of extragalactic protons (curves 1, 2, 3) and of galactic iron nuclei (curves 1′, 2′, 3′) are compared with the all-particle spectrum from the Akeno and AGASA experiments. KASCADE data are shown as filled squares for the all-particle flux and as open circles for the flux of iron nuclei.

Transition to extragalactic CR component

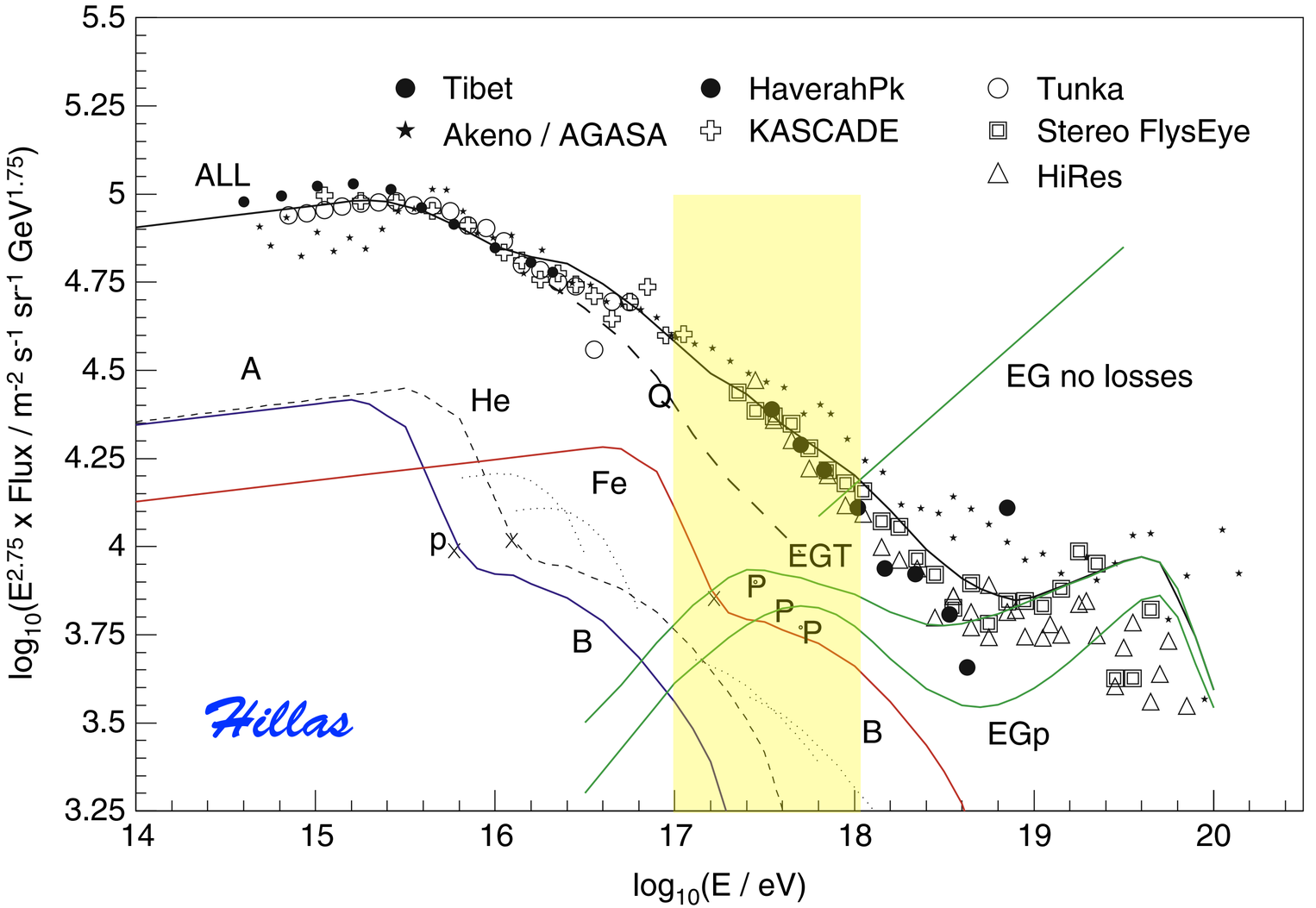

„classical“ supernovae + additional component

M. Hillas, J. Phys. G 31 (2005) R95

Contribution of (regular) SNR-CR to all-particle spectrum

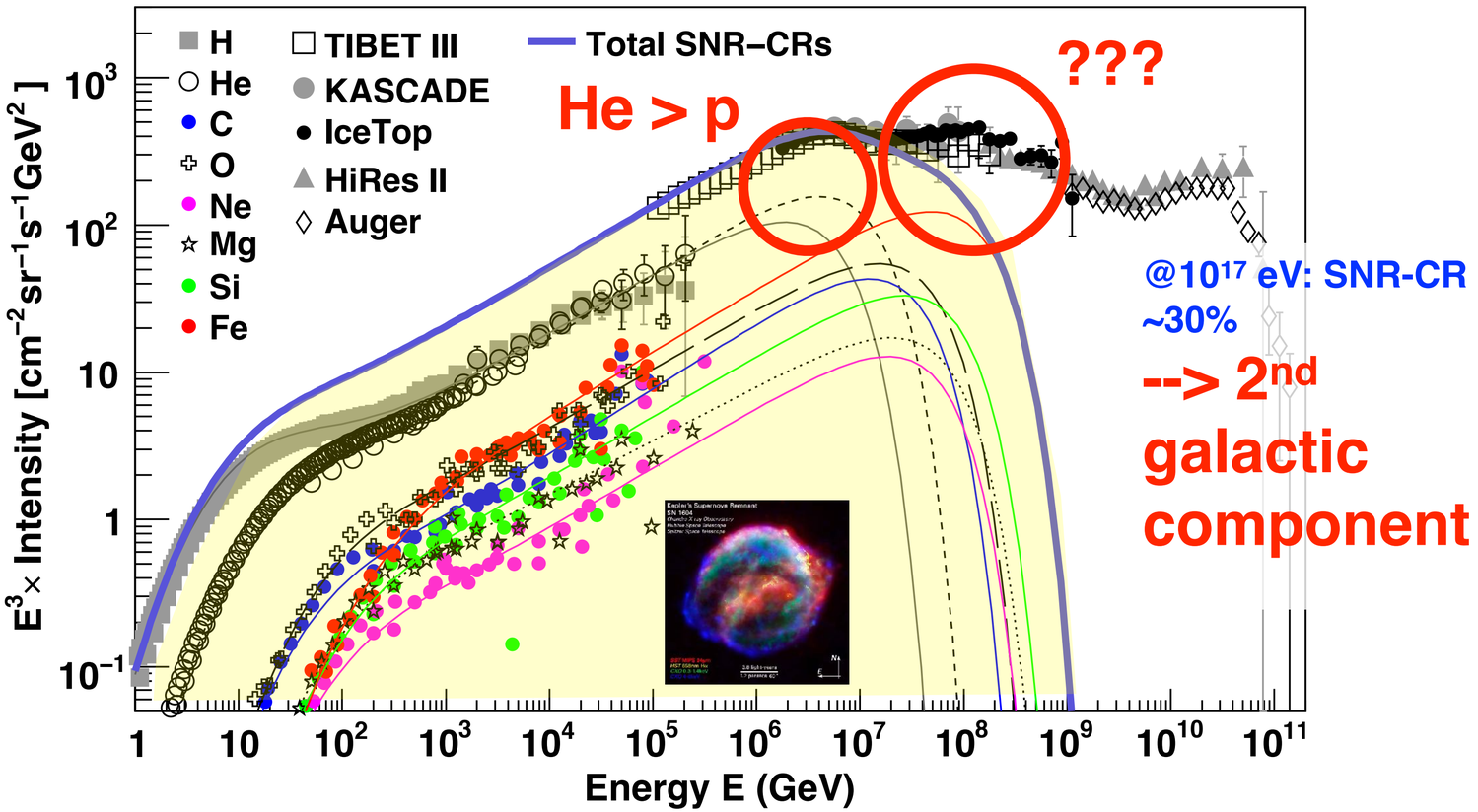

Fig. 2. Contribution of SNR-CRs to the all-particle cosmic-ray spectrum. The thin lines represent spectra for the individual elements, and the thick-solid line represents the total contribution. The calculation assumes an exponential cut-off energy for protons at $E_c = 4.5 \times 10^6$ GeV. Other model parameters, and the low-energy data are the same as in Figure 1. Error bars are shown only for the proton and helium data. High-energy data: KASCADE (Antoni et al. 2005), IceTop (Aartsen et al. 2013), Tibet III (Amenomori et al. 2008), the Pierre Auger Observatory (Schulz et al. 2013), and HiRes II (Abbasi et al. 2009).

~8% of mechanical power of SN --> CRs

S. Thoudam et al., A&A 595 (2016) A33

Combined fit of spectrum and composition data as measured by the Pierre Auger Observatory

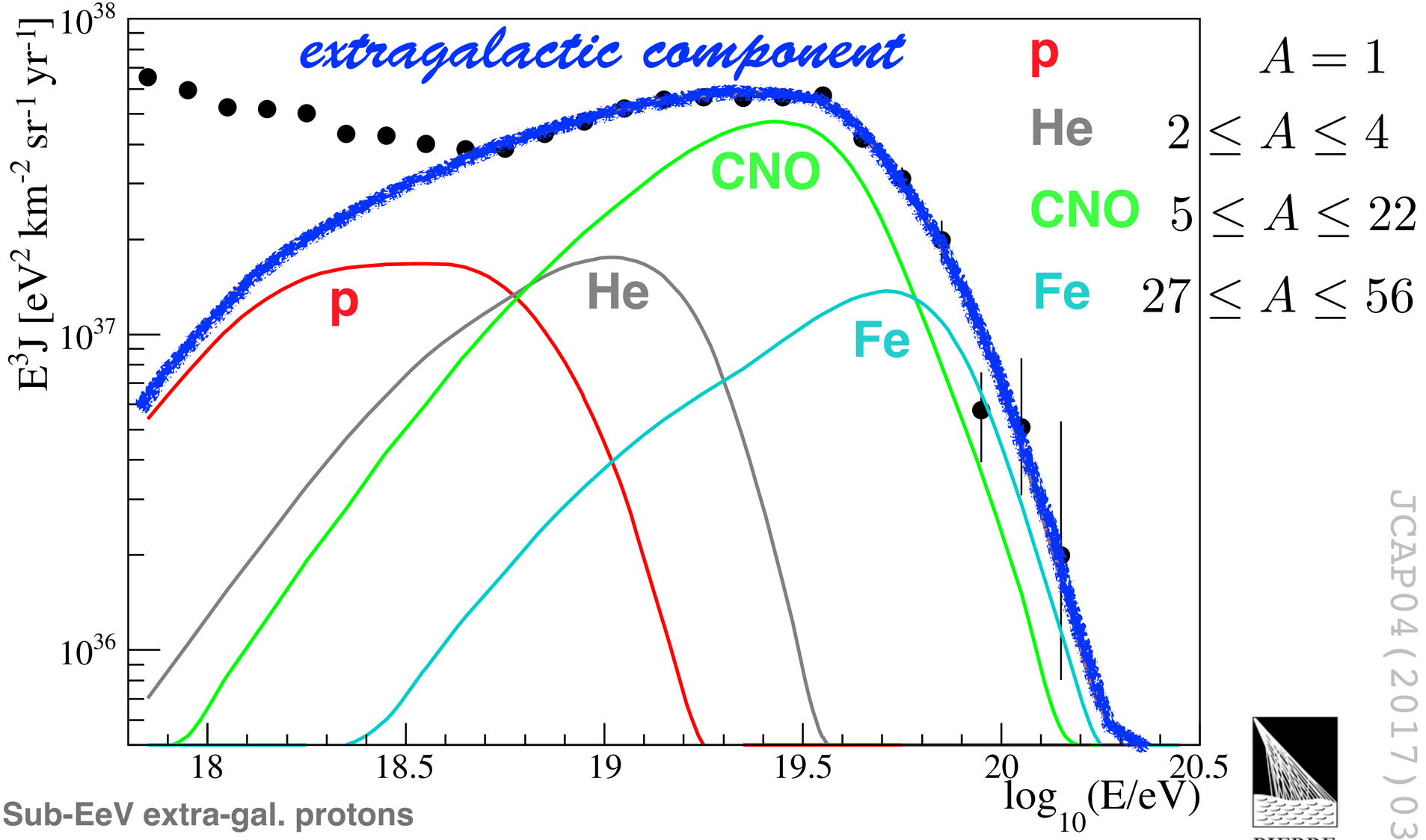

JCAP04(2017)038

Sub-EeV extra-gal. protons from interactions of heavier nuclei

all-particle spectra including 2nd galactic component

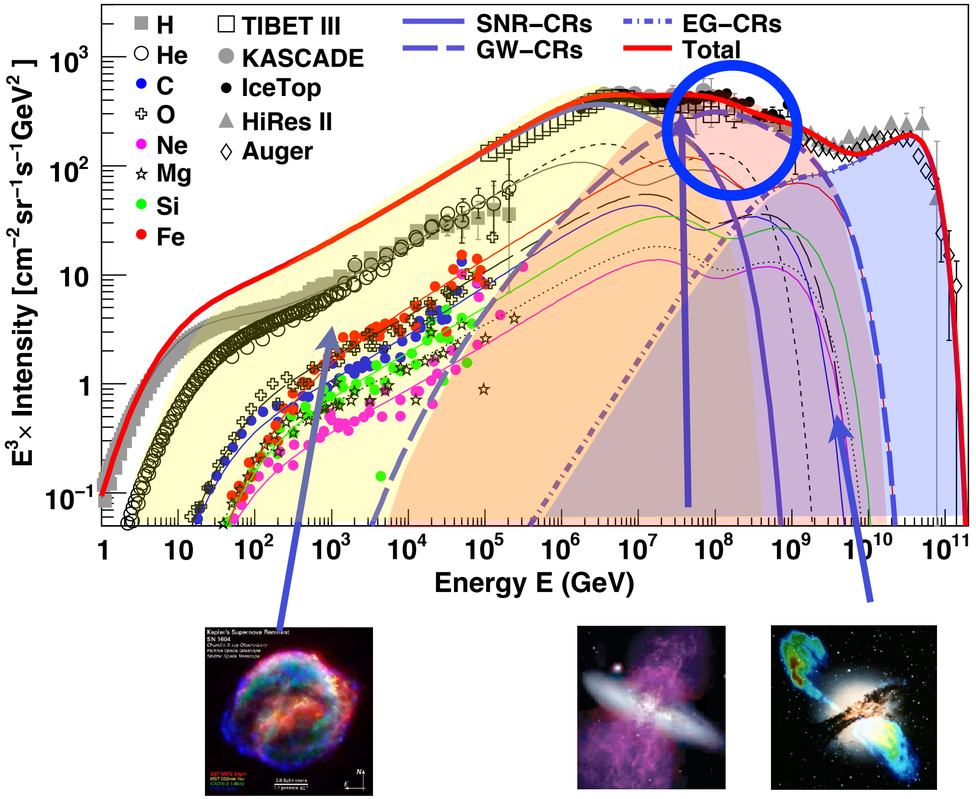

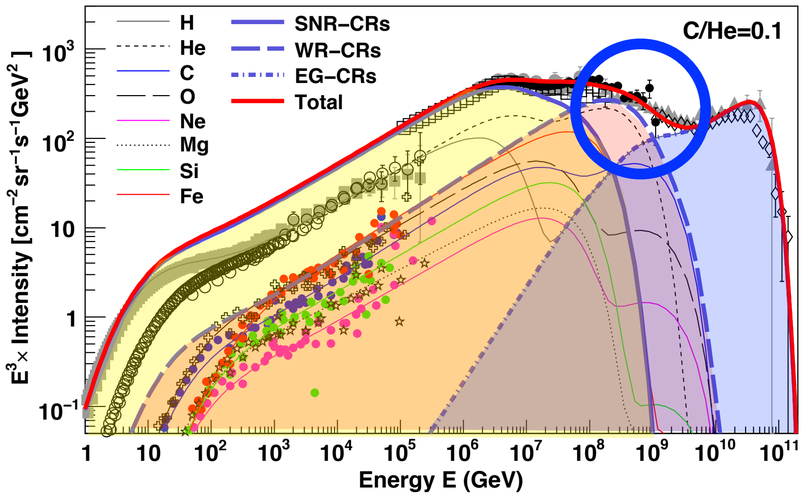

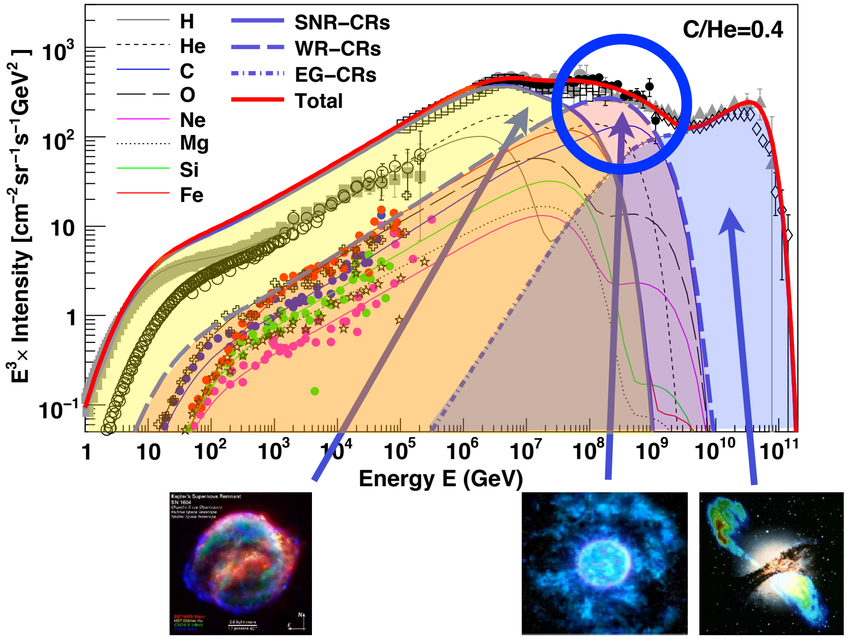

Table 3. Injection energy of SNR-CRs used in the calculation of all-particle spectrum in the WR-CR model (Figure 6).

Particle type	C/He = 0.1 $f(\times 10^{49}$ ergs)	C/He = 0.4 $f(\times 10^{49}$ ergs)
Proton	8.11	8.11
Helium	0.67	0.78
Carbon	2.11×10^{-2}	0.73×10^{-2}
Oxygen	2.94×10^{-2}	2.94×10^{-2}
Neon	4.41×10^{-3}	4.41×10^{-3}
Magnesium	6.03×10^{-3}	6.03×10^{-3}
Silicon	5.84×10^{-3}	5.84×10^{-3}
Iron	5.77×10^{-3}	5.77×10^{-3}

S. Thoudam et al., A&A 595 (2016) A33

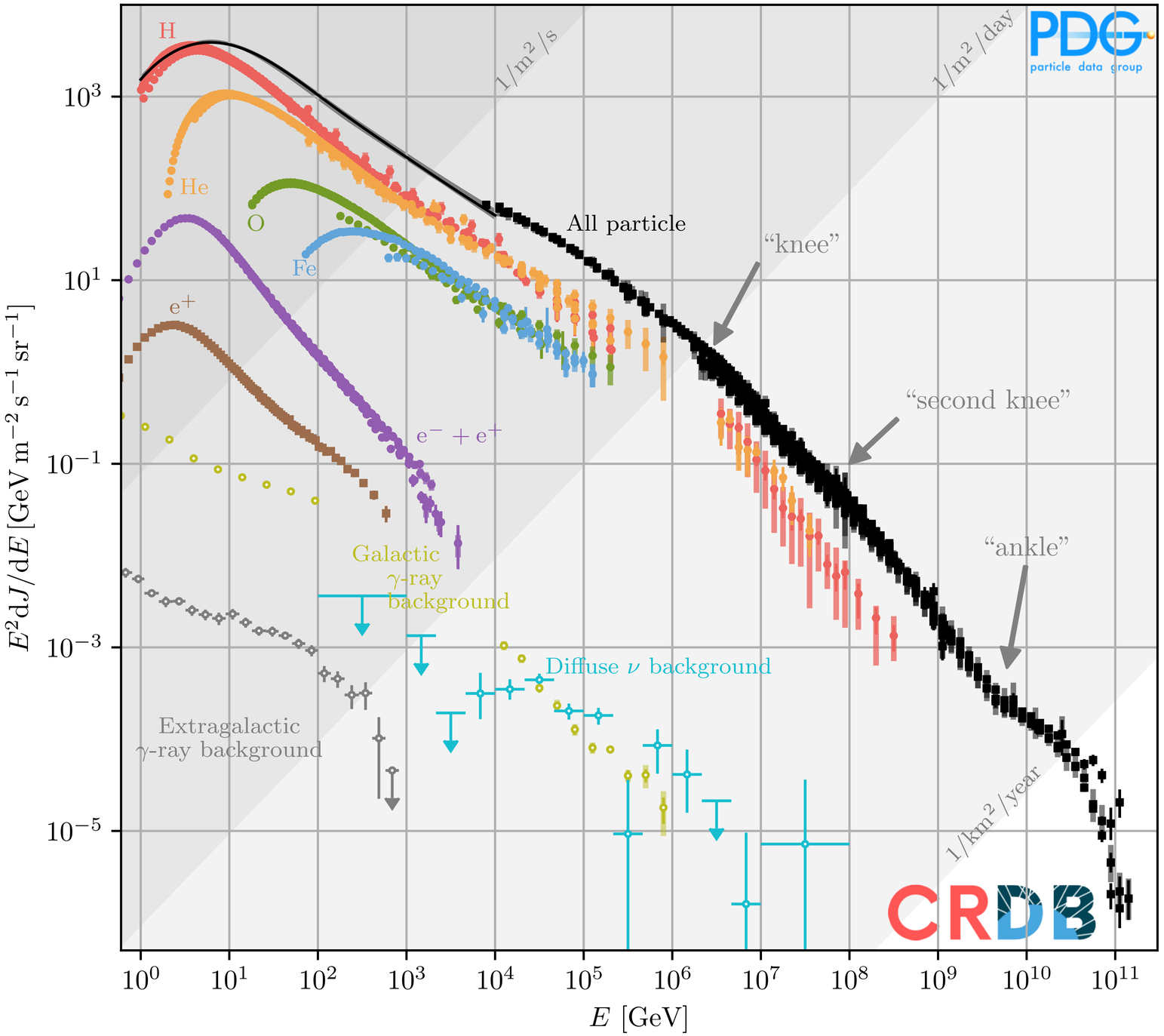

some more details

latest updates - ICRC 2025

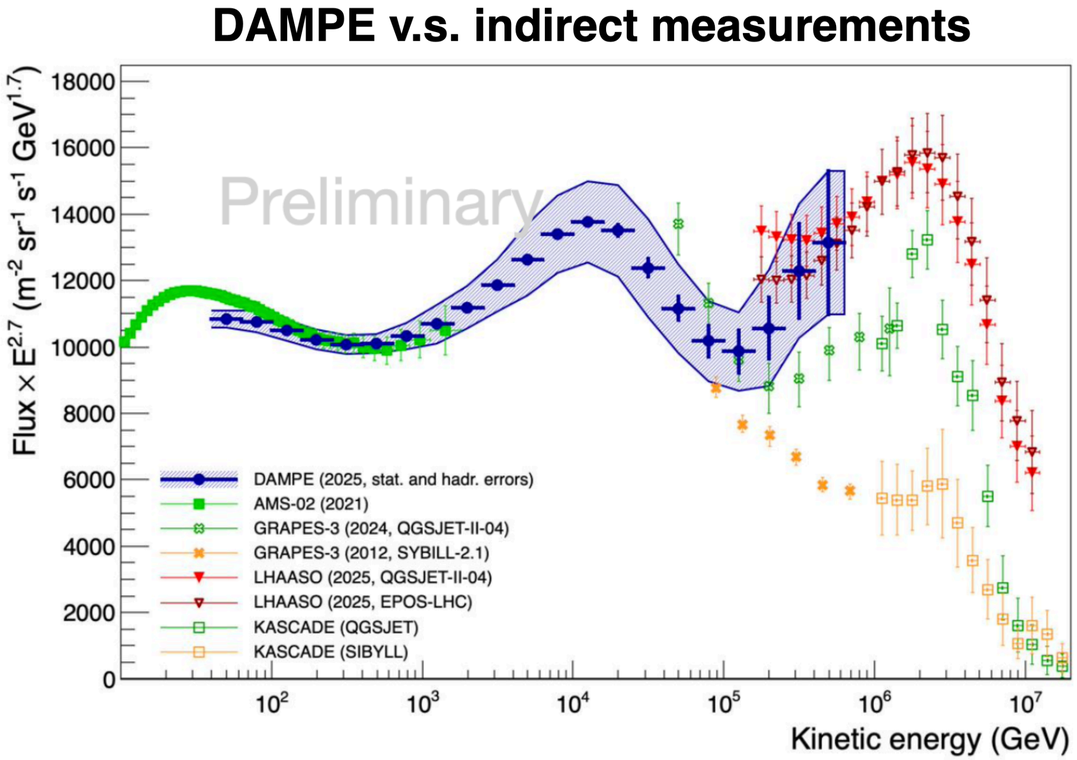

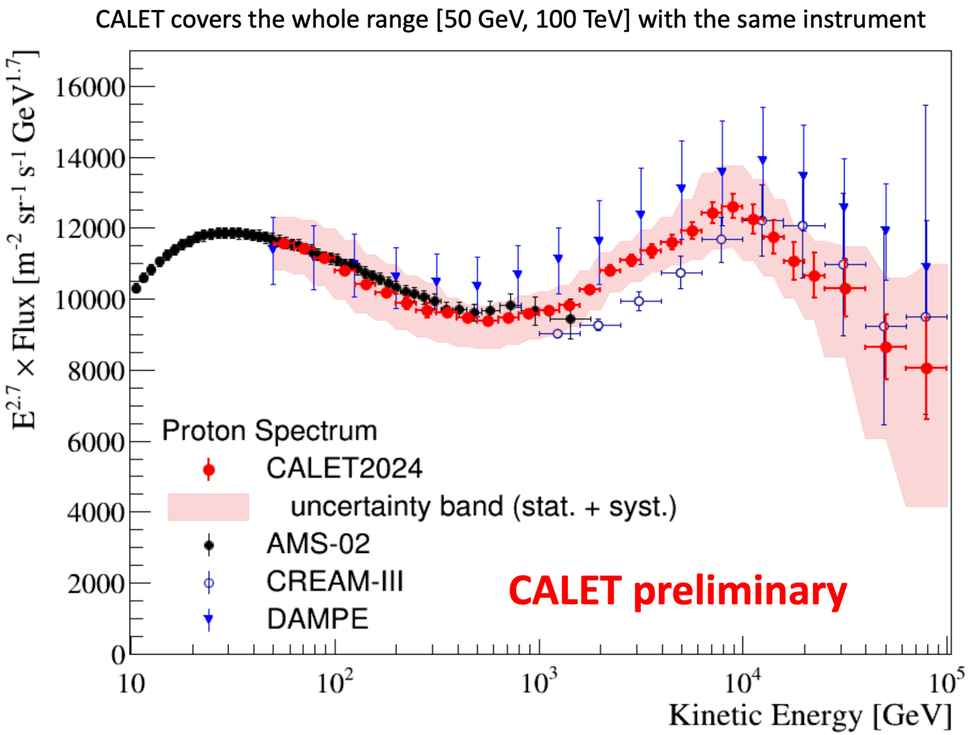

- Presented high-precision spectra of protons from AMS-02, CALET, DAMPE, and ISS-CREAM
- Above $\gtrsim 100$ GeV the proton spectrum clearly departs from a single power law
- Excellent consistency across direct instruments
- Good agreement with ground-based arrays (GRAPES, LHAASO): unique test of HIM and air-shower physics!

latest updates - ICRC 2025

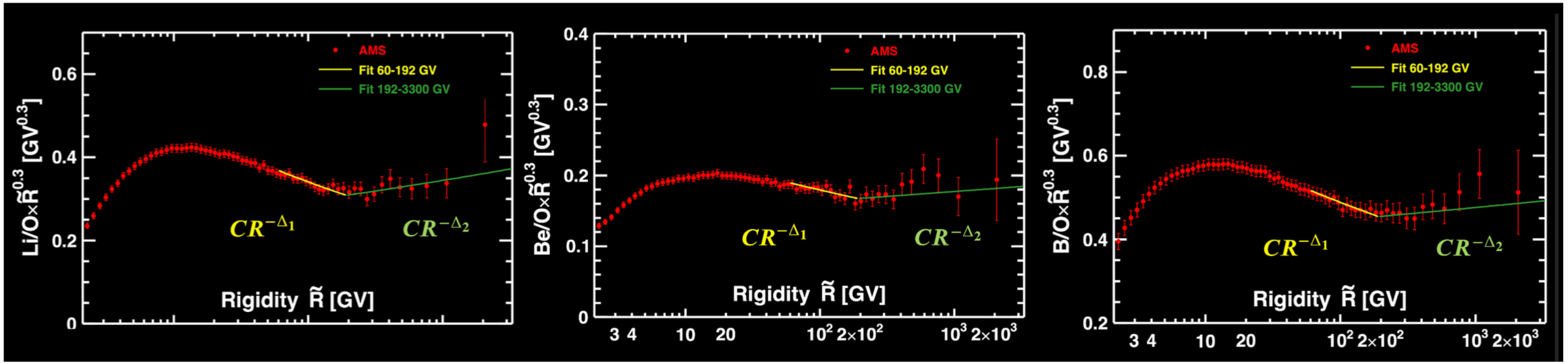

AMS-02: secondary-over-primary ratios

- At about the same rigidity the secondary-to-primary flux ratios exhibit a similar hardening
- Remember:

$$\frac{N_{\text{sec}}}{N_{\text{pri}}}(\mathcal{R}) \propto \frac{H}{D(\mathcal{R})} \propto \text{grammage}$$

- This additional hardening favors the propagation origin of the proton first spectral hardening.

latest updates - ICRC 2025

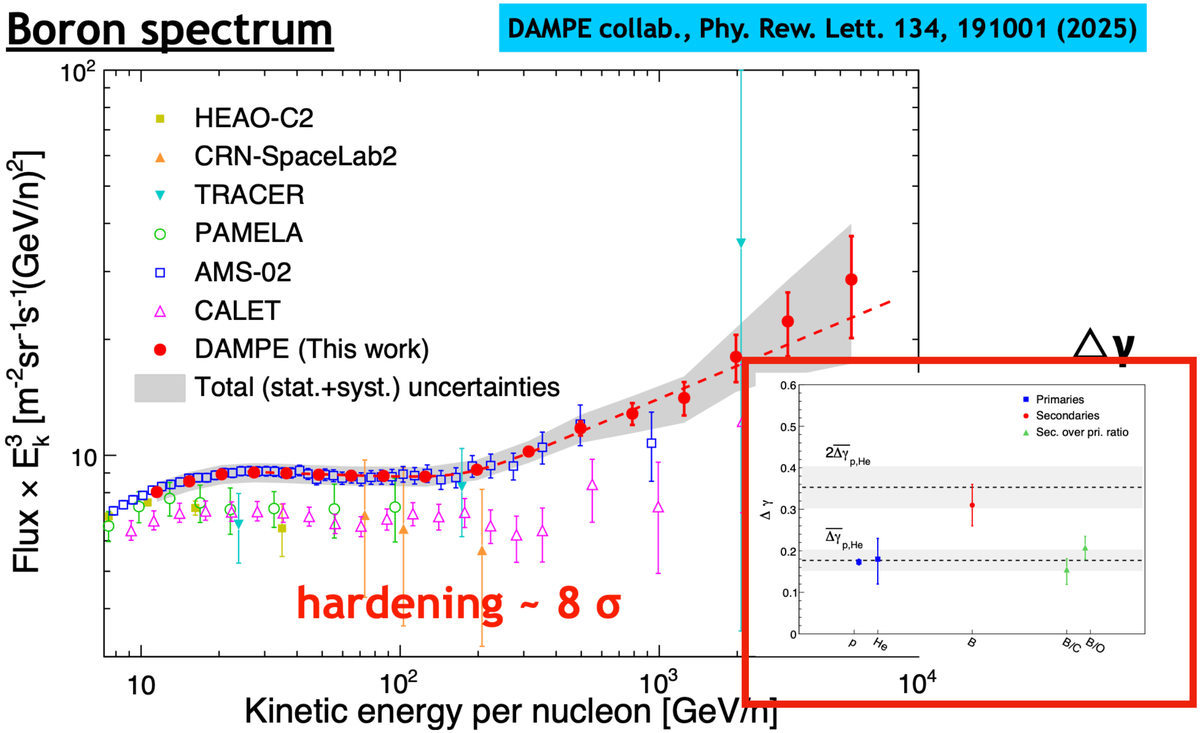

DAMPE: Boron spectrum up to 6 TeV/n

- Increased statistics: DAMPE Boron measurements now extend to ~ 12 TV.
- The Boron spectrum exhibits a highly significant hardening, with

$$\Delta\gamma_{\rm sec} \approx 2\,\Delta\gamma_{\rm pri}$$

Understanding the ∼10 TeV Softening

latest updates - ICRC 2025

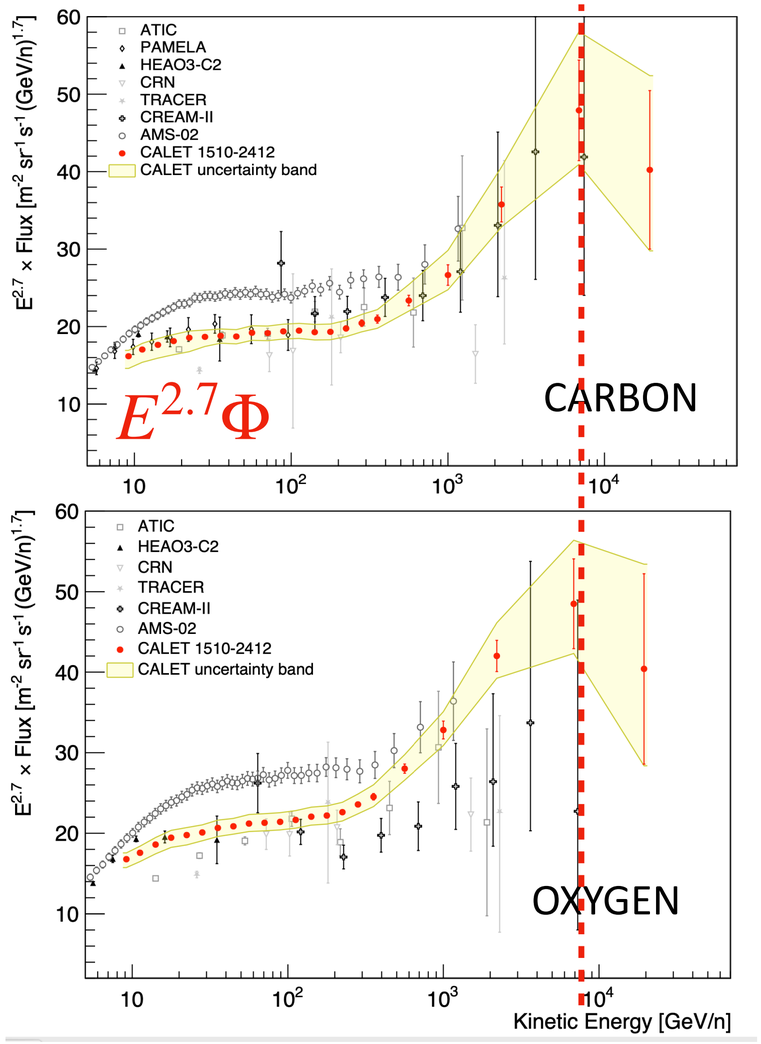

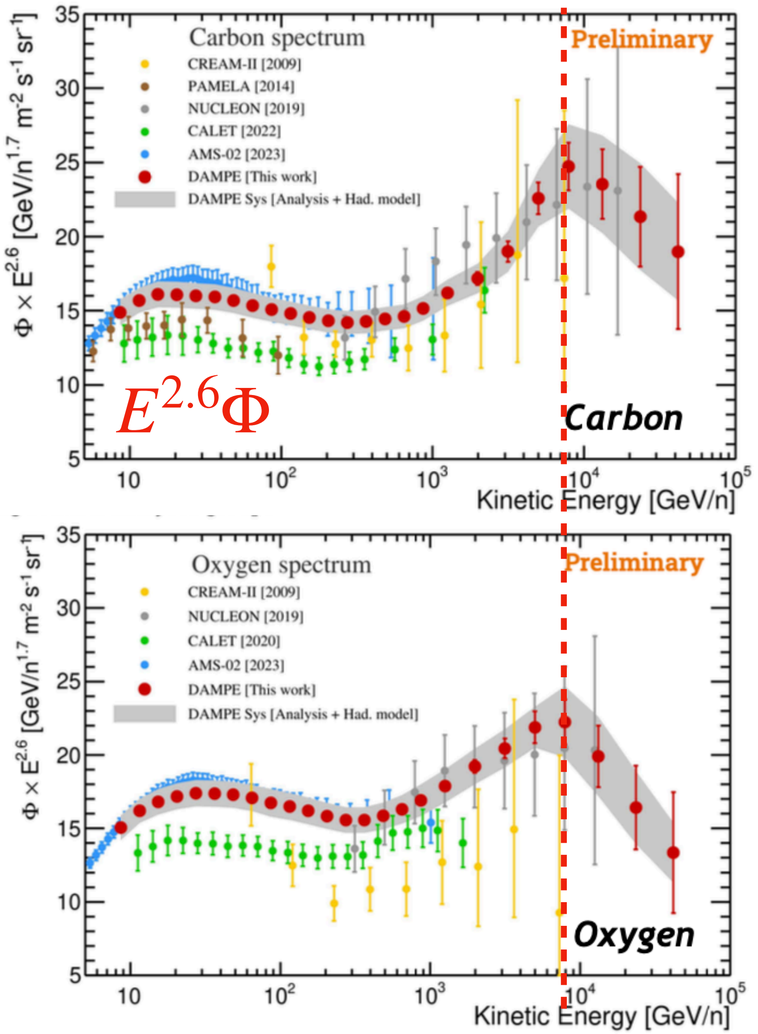

First direct evidence of break in rigidity by DAMPE

Cosmic rays

Energy content of extragalactic cosmic rays

$$\rho_E = \frac{4\pi}{c} \int \frac{E}{\beta} \frac{dN}{dE} dE$$

ρ_E=3.7 10^{-7} eV/cm^3

total power

P=5.5 10^{37} erg/(s Mpc^3)

→ ~2 10^{44} erg/s per active galaxy

→ ~2 10^{52} erg/s per cosmol. GRB

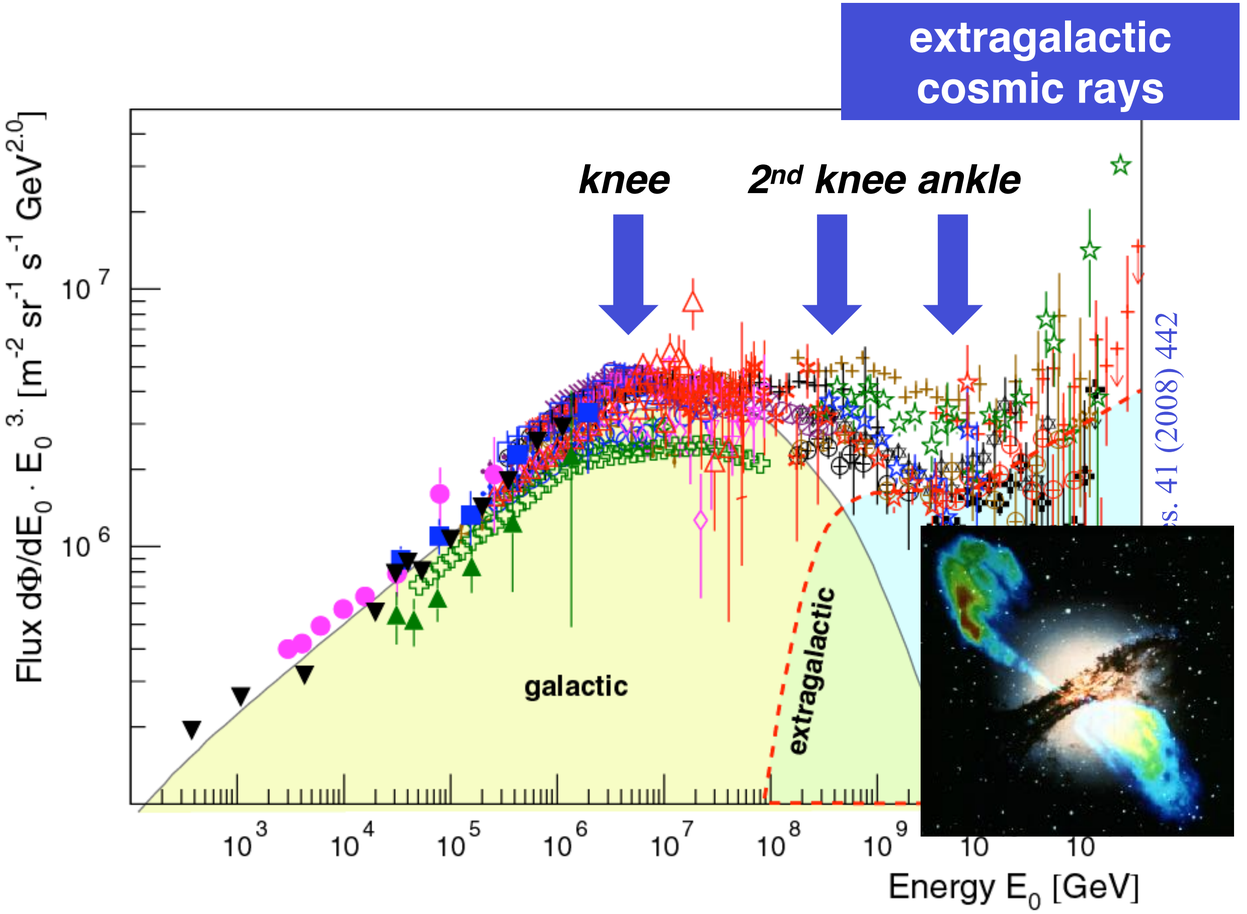

10^{20} eV = 16 J (macroscopic energy)

Hillas diagram

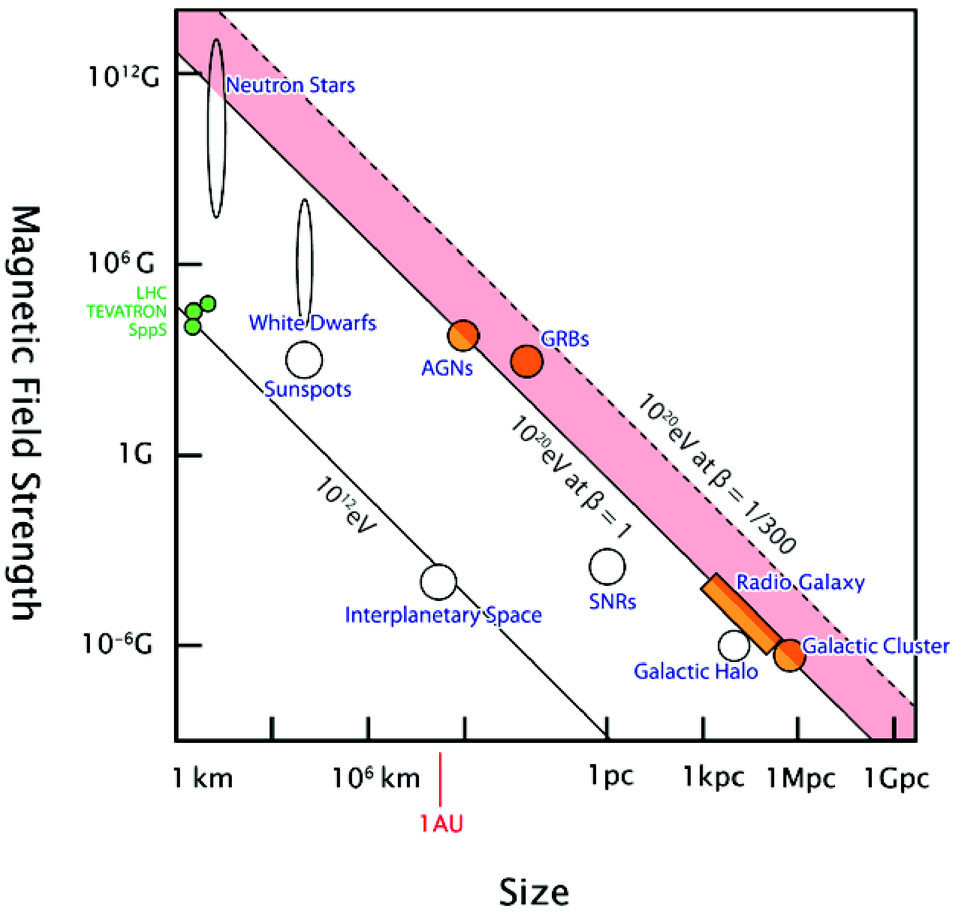

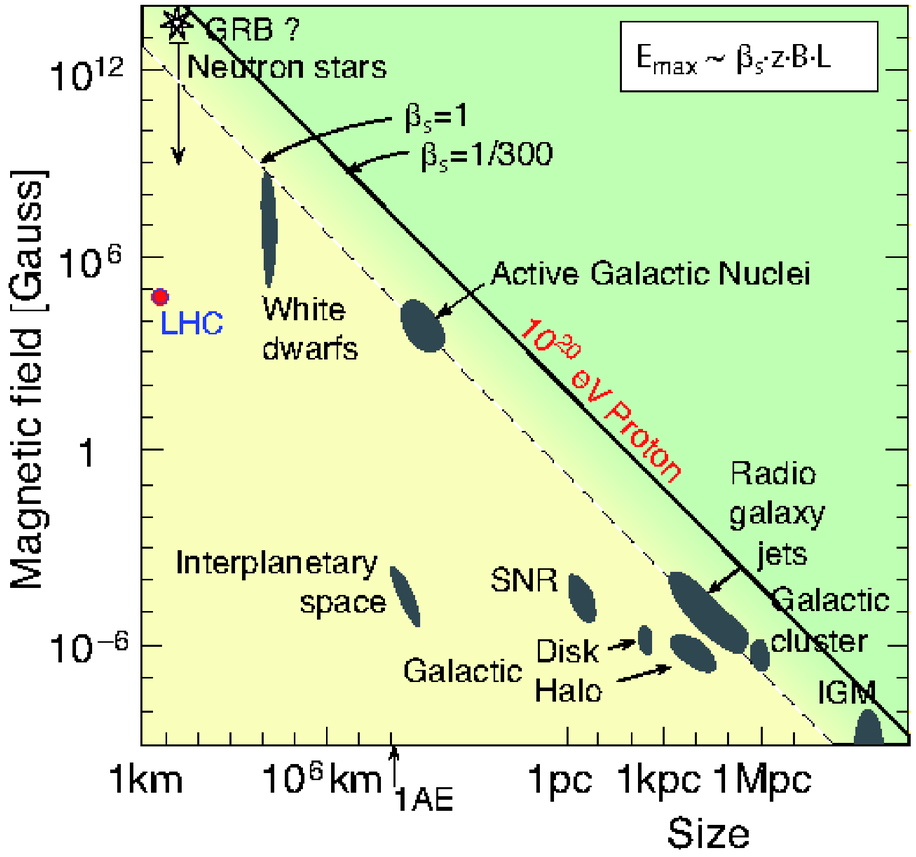

$$B \cdot L > \frac{2 \cdot p}{z \cdot e \cdot \beta}$$

Hillas criterion

model of AGN

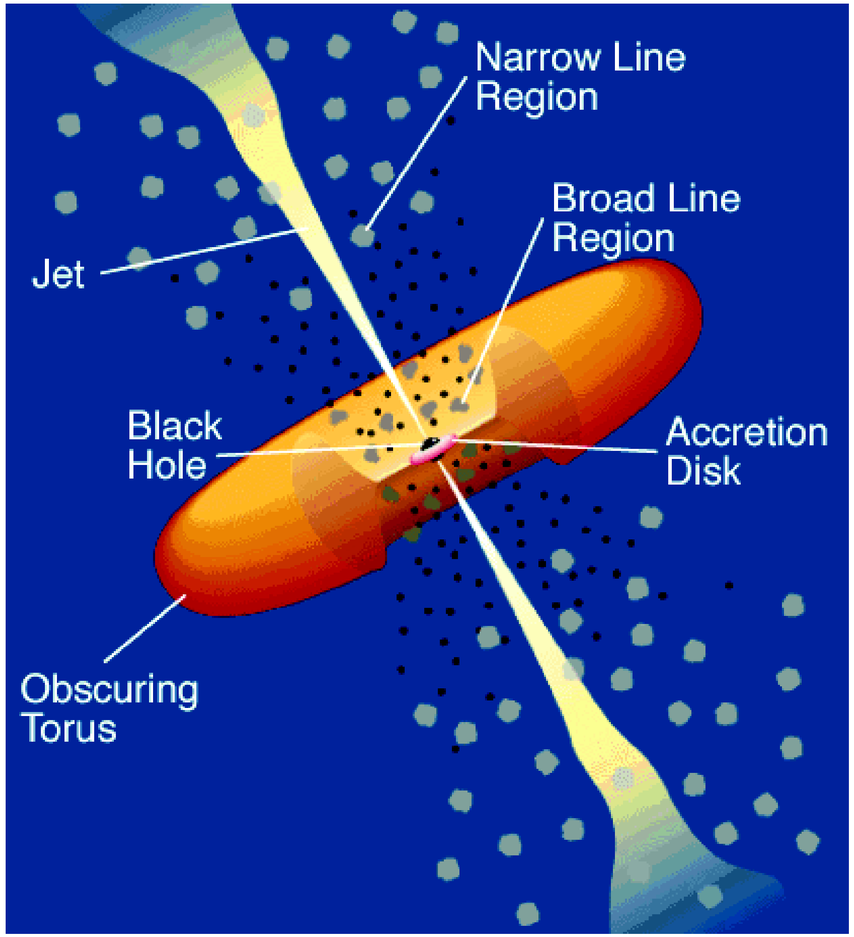
Narrow Line Region
Broad Line Region
Jet
Black Hole
Accretion Disk
Obscuring Torus

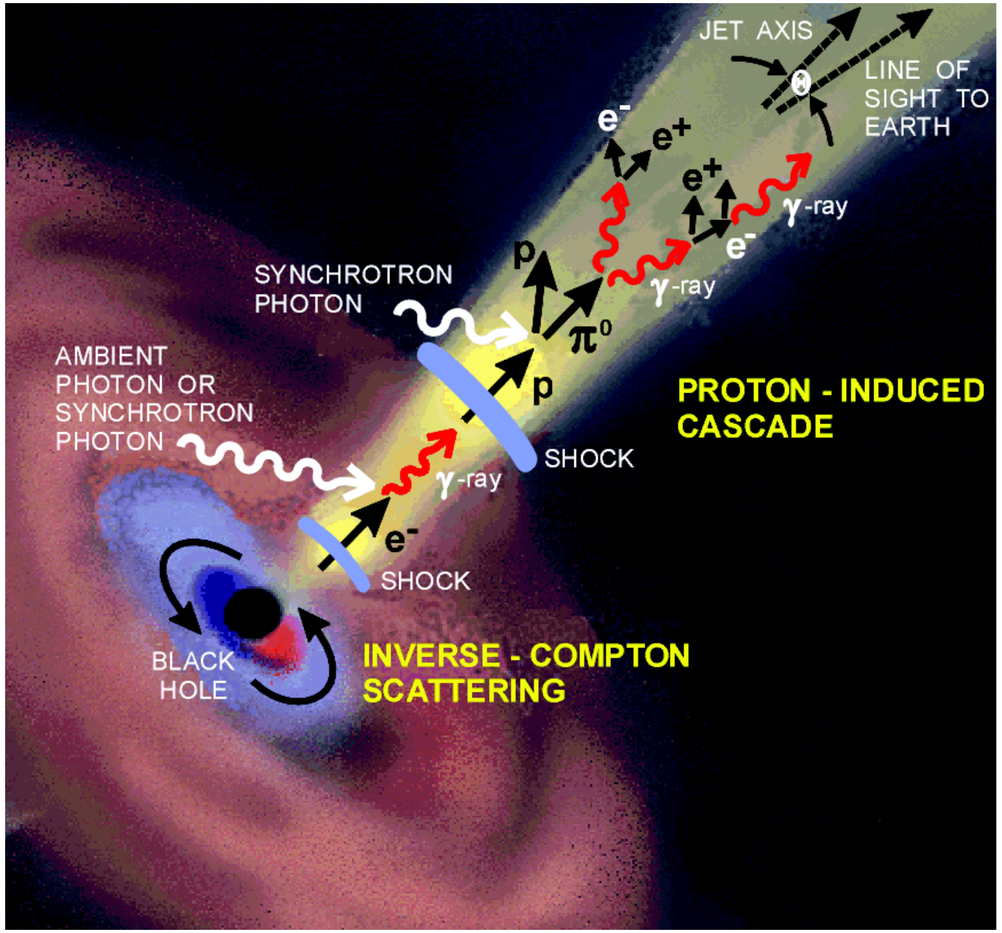
JET AXIS
LINE OF SIGHT TO EARTH
θ
e⁻
e⁺
e⁺
e⁻
γ-ray
γ-ray
SYNCHROTRON PHOTON
p
π⁰
p
AMBIENT PHOTON OR SYNCHROTRON PHOTON
PROTON - INDUCED CASCADE
SHOCK
γ-ray
e⁻
SHOCK
BLACK HOLE
INVERSE - COMPTON SCATTERING

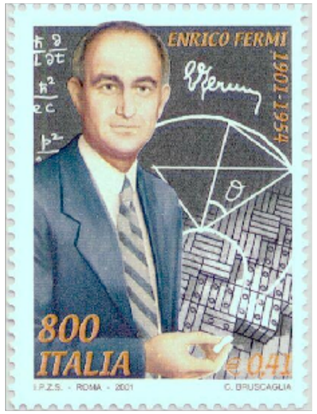
ENRICO FERMI
1901-1954
800
ITALIA
0,41

Cen A

Ultra High Energy Cosmic Rays

Noémie Globus[1,2,3] and Roger Blandford[2]

[1]Instituto de Astronomía, Universidad Nacional Autónoma de México Campus Ensenada, A.P. 106, Ensenada, BC 22860, México
[2]Kavli Institute for Particle Astrophysics and Cosmology, Stanford University, Stanford, CA 94305, USA
[3]Astrophysical Big Bang Laboratory, RIKEN, Wako, Saitama, Japan

Xxxx. Xxx. Xxx. Xxx. YYYY. AA:1–33

This article's doi:
10.1146/((please add article doi))

Keywords

cosmic accelerators, magnetic fields, particle astrophysics, particle detection, neutrinos, gamma-rays

Abstract

Ultra High Energy Cosmic Rays, UHECR, are charged particles with energies between $\sim 10^{18}$ eV and $\sim 3 \times 10^{20}$ eV ~ 50 J. They exhibit fundamental physics at energies inaccessible to terrestrial accelerators, challenge experimental physics and connect strongly to astronomical observations through electromagnetic, neutrino and even gravitational wave channels. There has been much theoretical and observational progress in the sixty years that have elapsed since the discovery of UHECR, to divine their nature and identify their sources.

- The highest energy UHECR appear to be heavy nuclei with rigidity extending up to ~ 10 EV;
- A significant (6.9σ) dipole anisotropy has been measured but our poor understanding of the Galactic magnetic fields makes this hard to interpret;
- The UHECR luminosity density is $\sim 10^{44}$ erg Mpc^{-3} yr^{-1} which constrains explanations of their origin;
- The most promising acceleration mechanisms involve diffusive shock acceleration and unipolar induction;
- The most promising sources include intergalactic accretion shocks, and relativistic jets from stellar-mass or supermassive black holes.

We explore the prospects for using the highest energy events, combined with multimessenger astronomy, to help us solve the riddle of UHECR.

Propagation of UHECRs

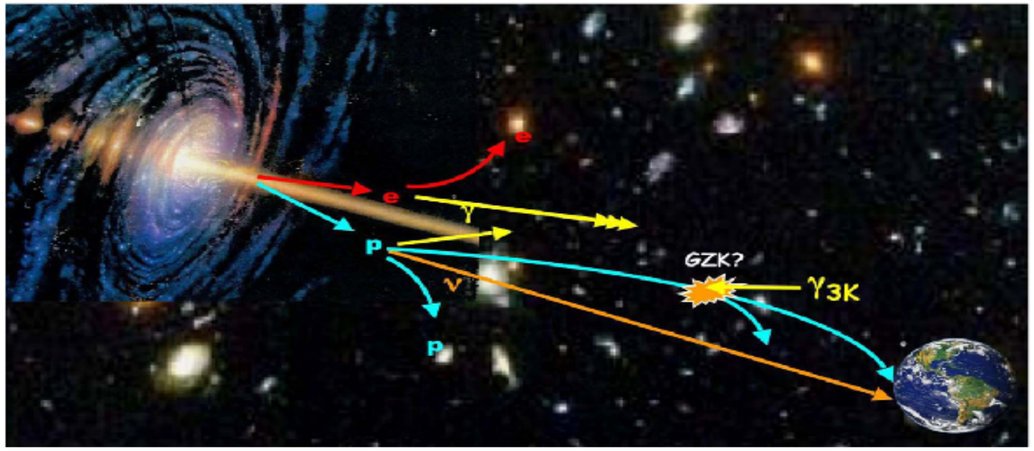

Fe-gamma cross section

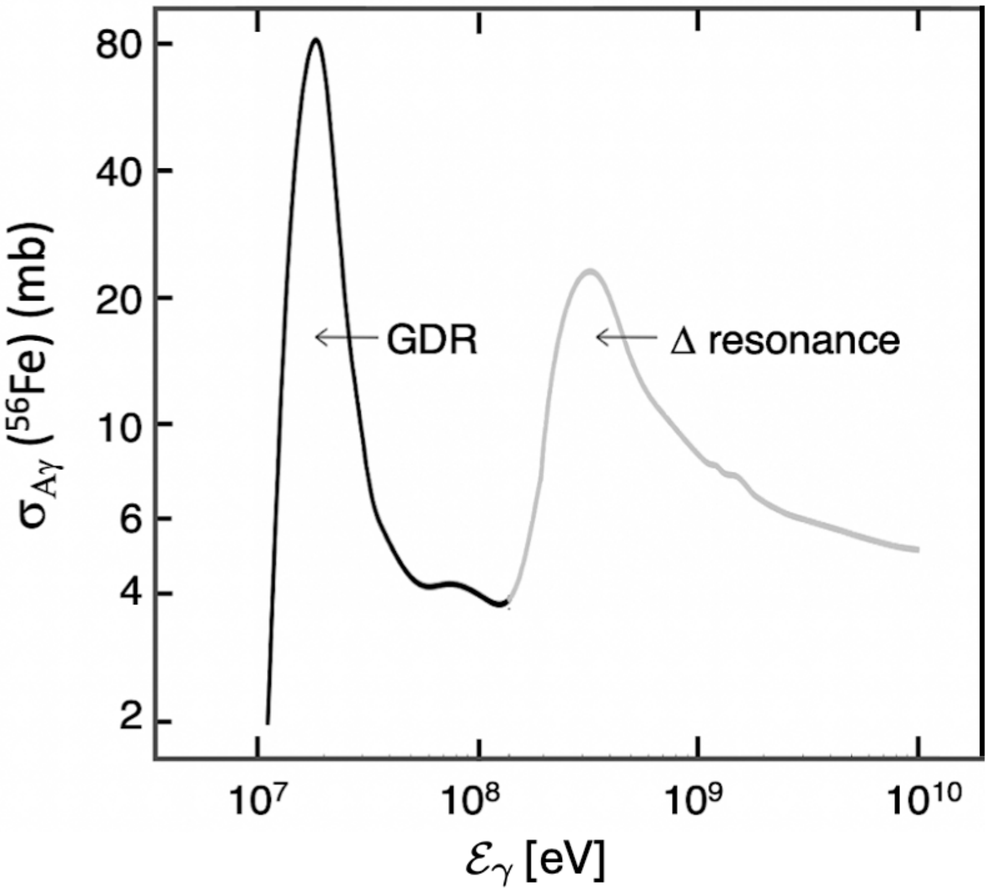

diffuse photon backgrounds

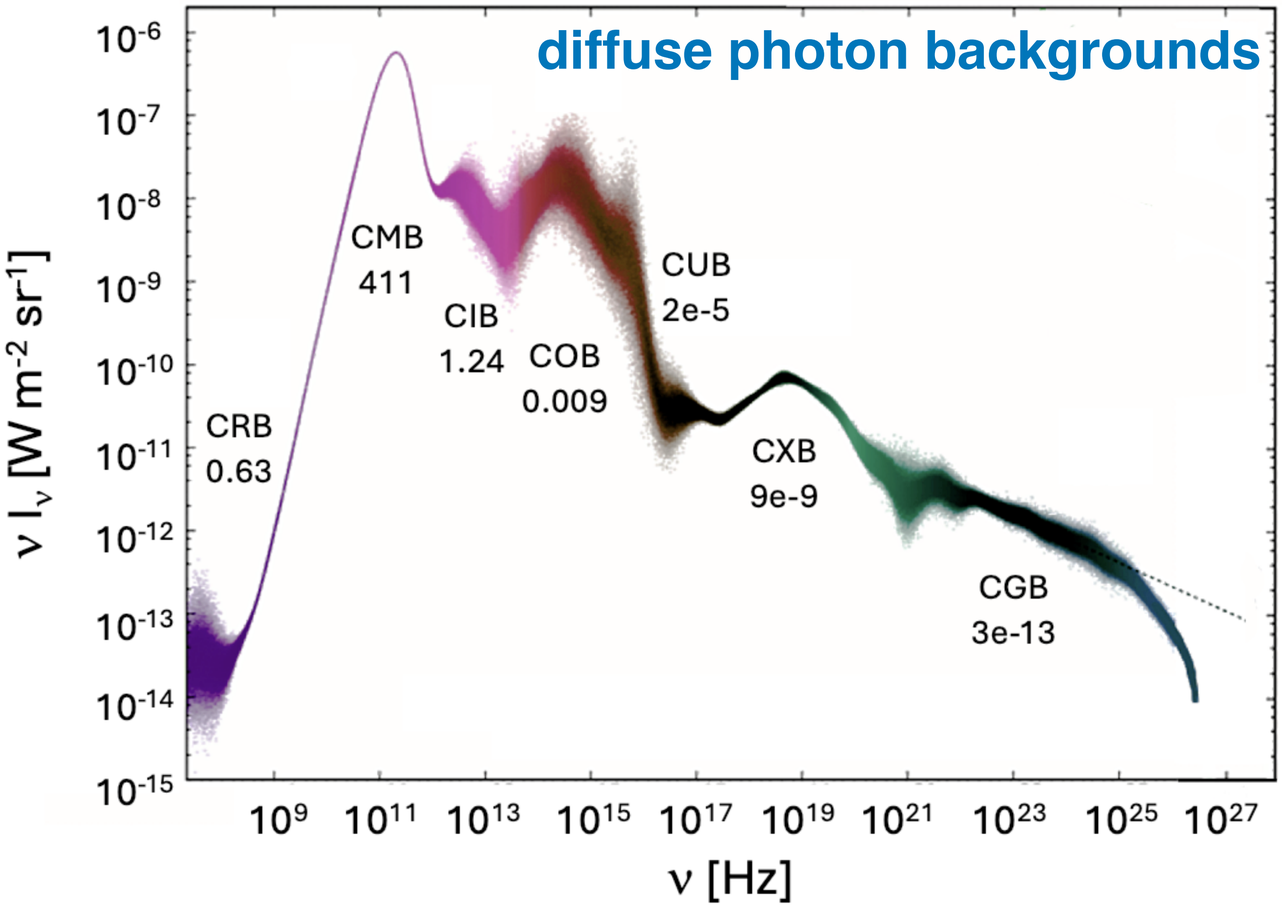

Energy loss lengths

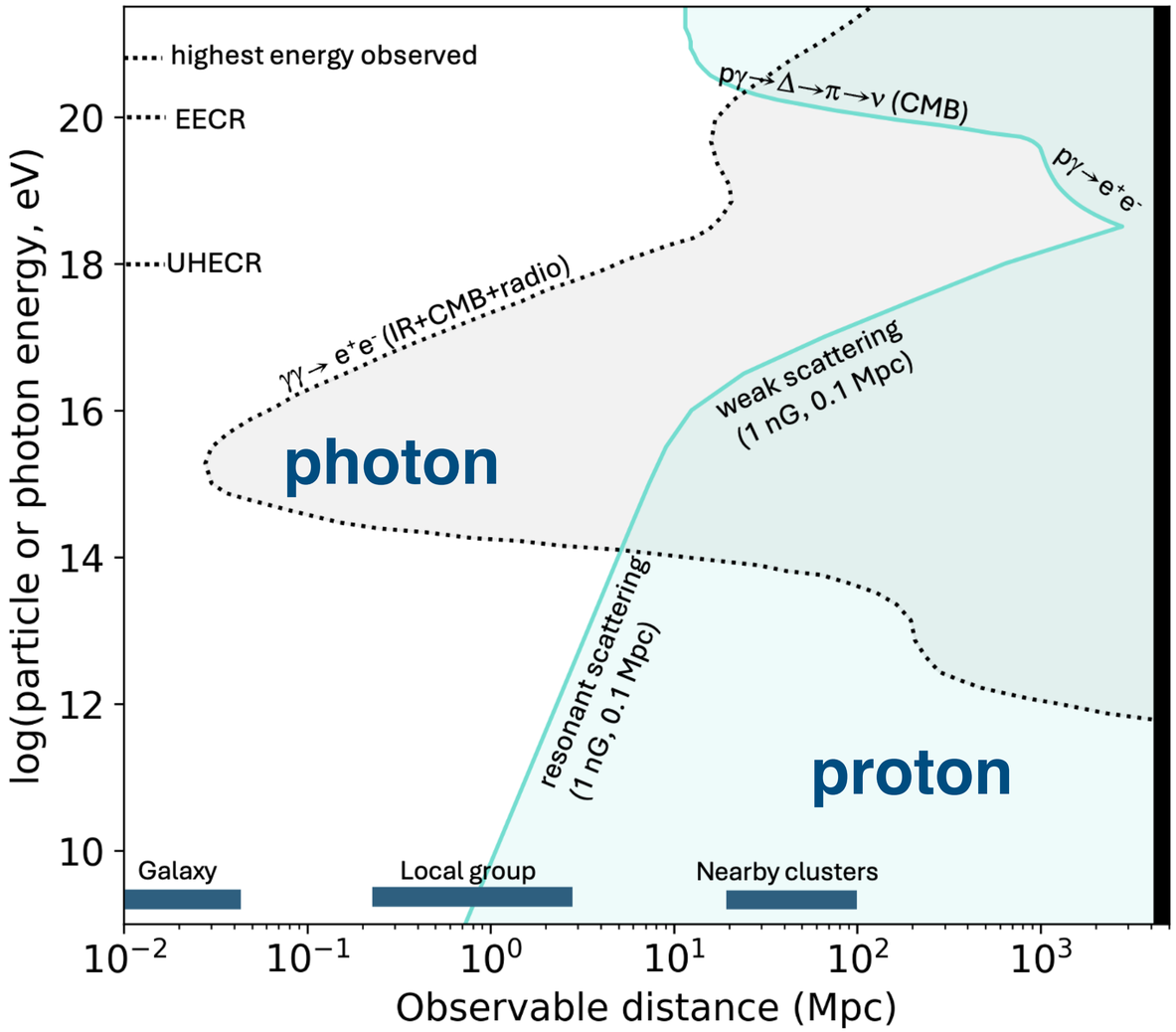

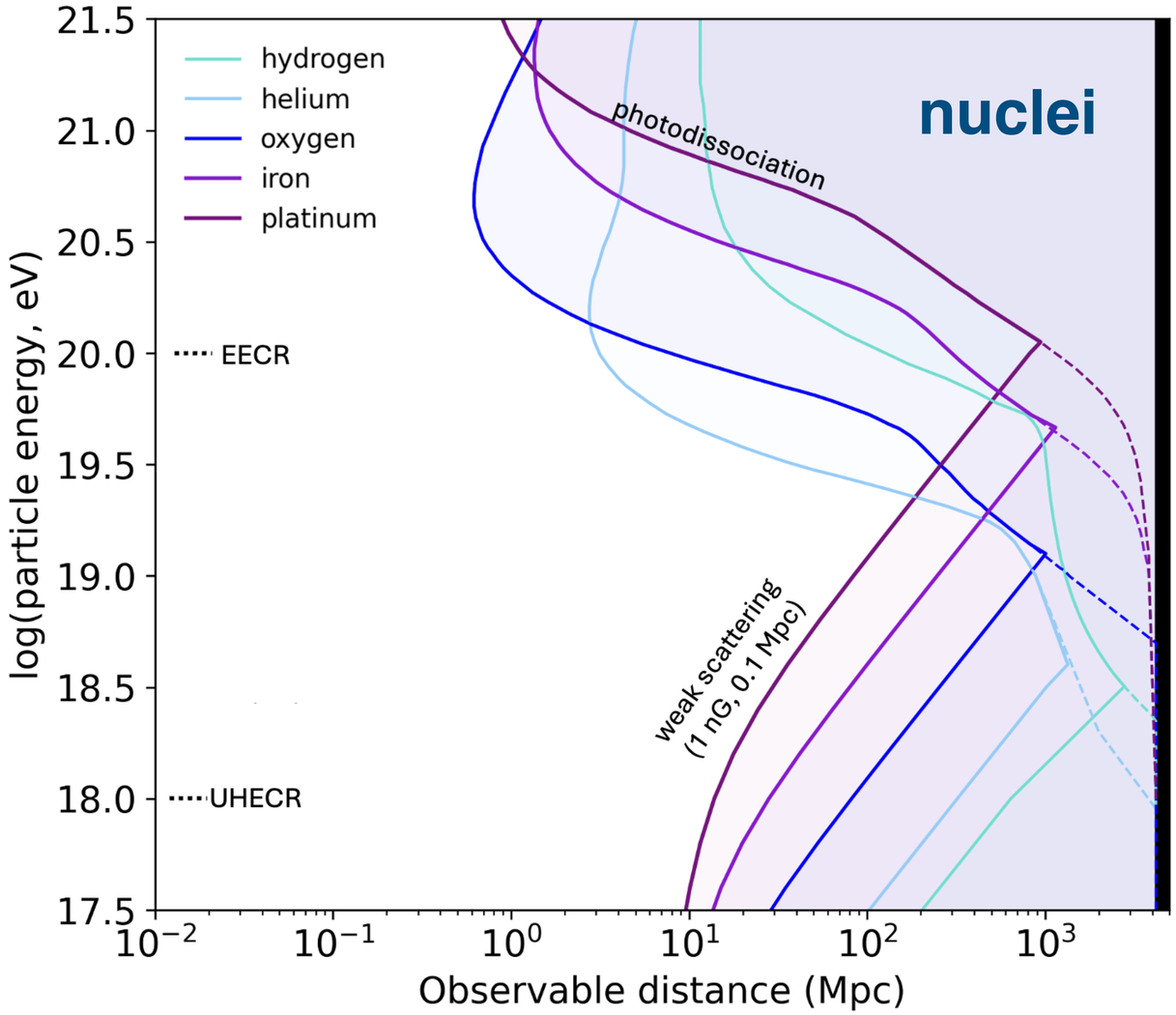

Sky map

Sky map in Galactic coordinates of the different types of galaxies within 40 Mpc that could host the sources of UHECR

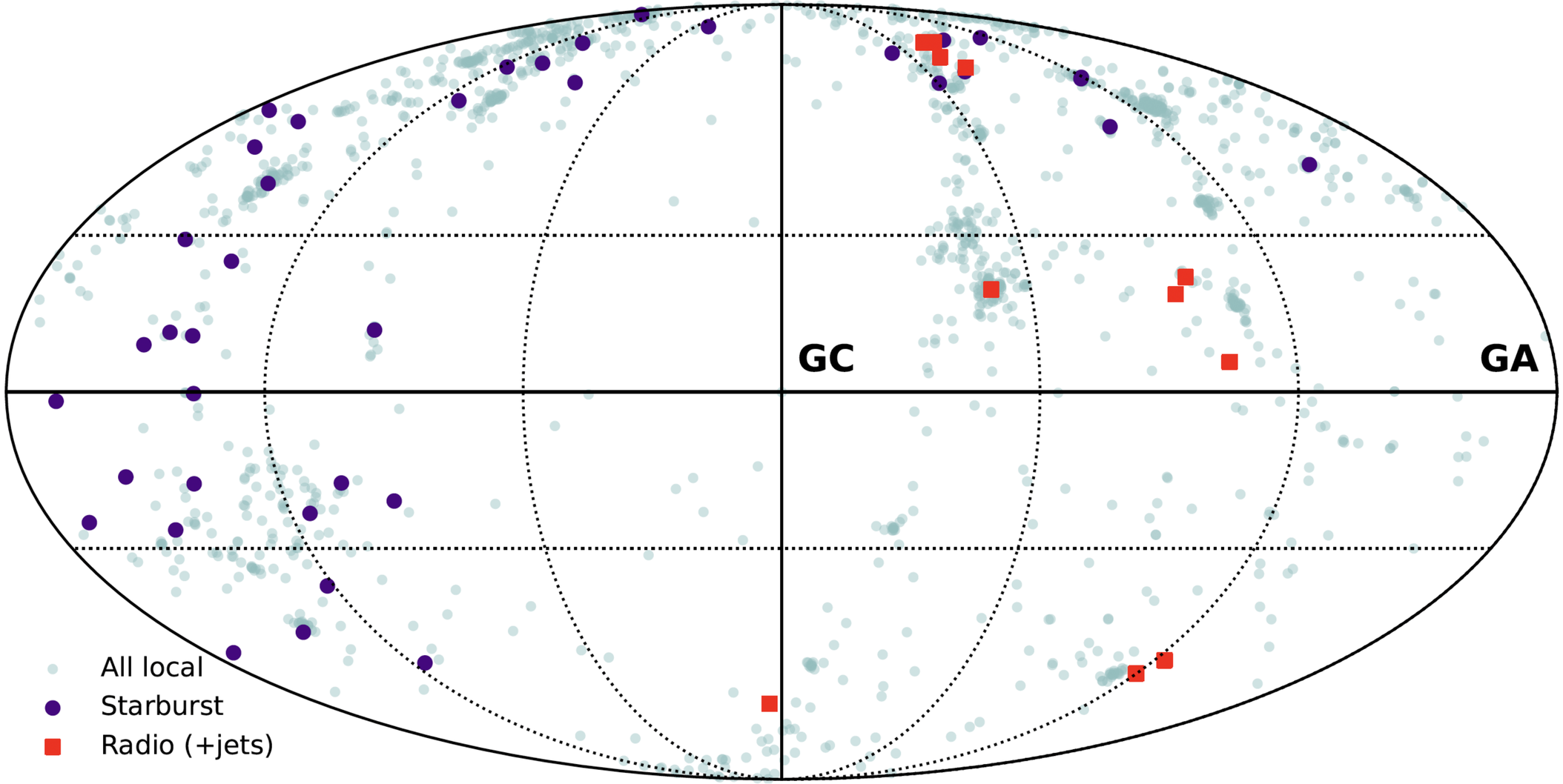

Starburst galaxies

exceptionally high rate of star formation

e.g. Milky Way 3 M_0/yr

starburst galaxy: >100 M_0/yr

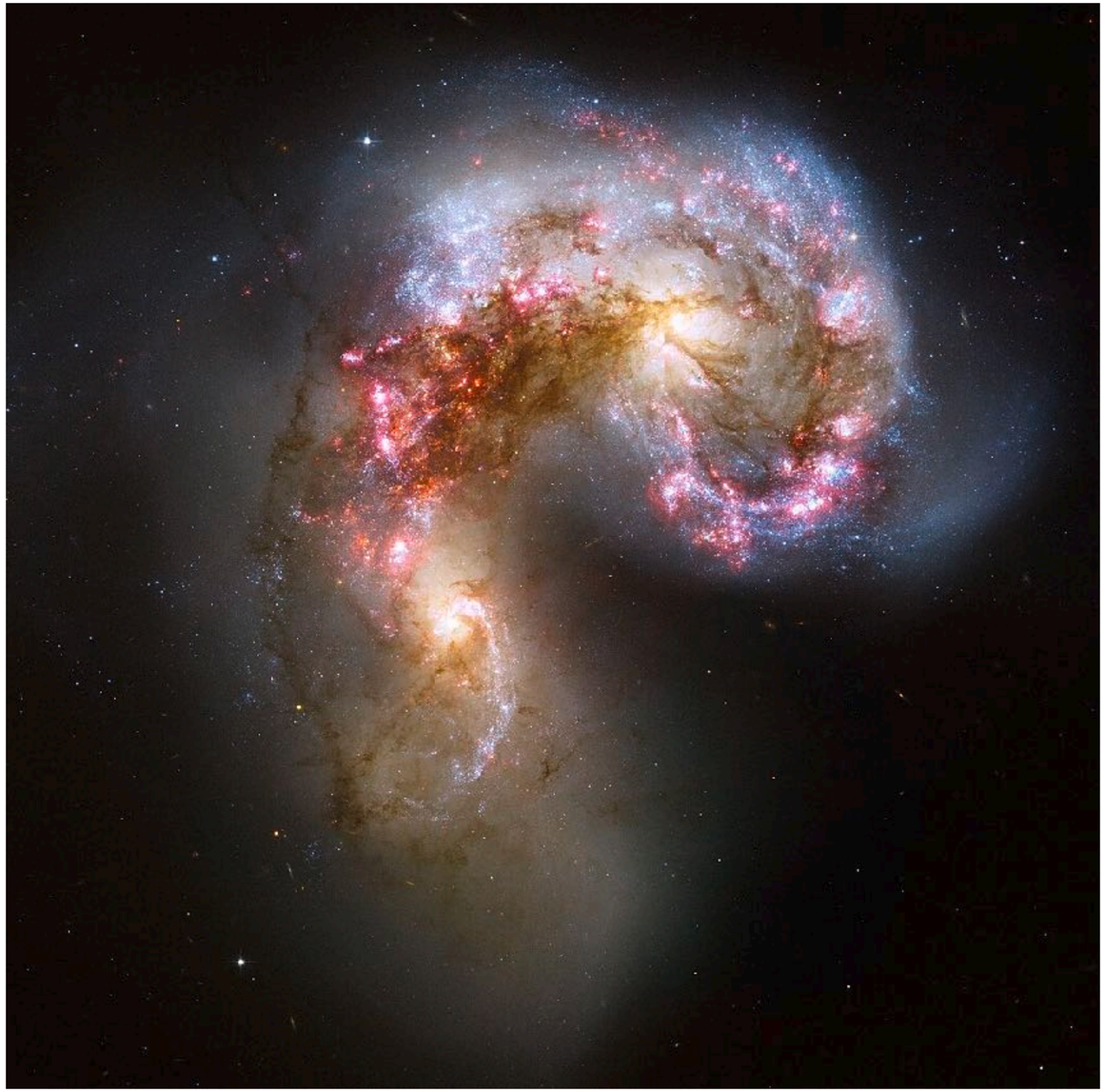

The Antennae Galaxies are an example of a starburst galaxy occurring from the collision of NGC 4038/NGC 4039.

J. Blümer et al. / Progress in Particle and Nuclear Physics 63 (2009) 293–338

~1000/m² s

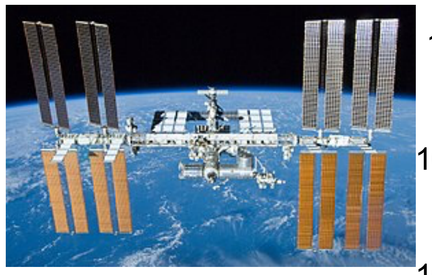

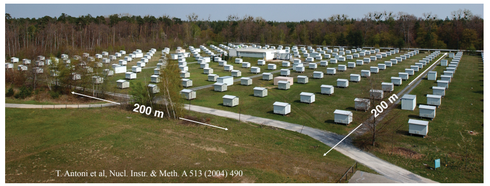

air shower measurements

~1/m² yr

direct measurements

knee

2nd knee

ankle

~1/km² century

Flux $d\Phi/dE_0 \cdot E_0$ [m^{-2} sr^{-1} s^{-1}]

Energy E_0 [GeV]

direct measurements (protons)

direct measurements (all particles)

air shower data (all particles)

The Pierre Auger Observatory

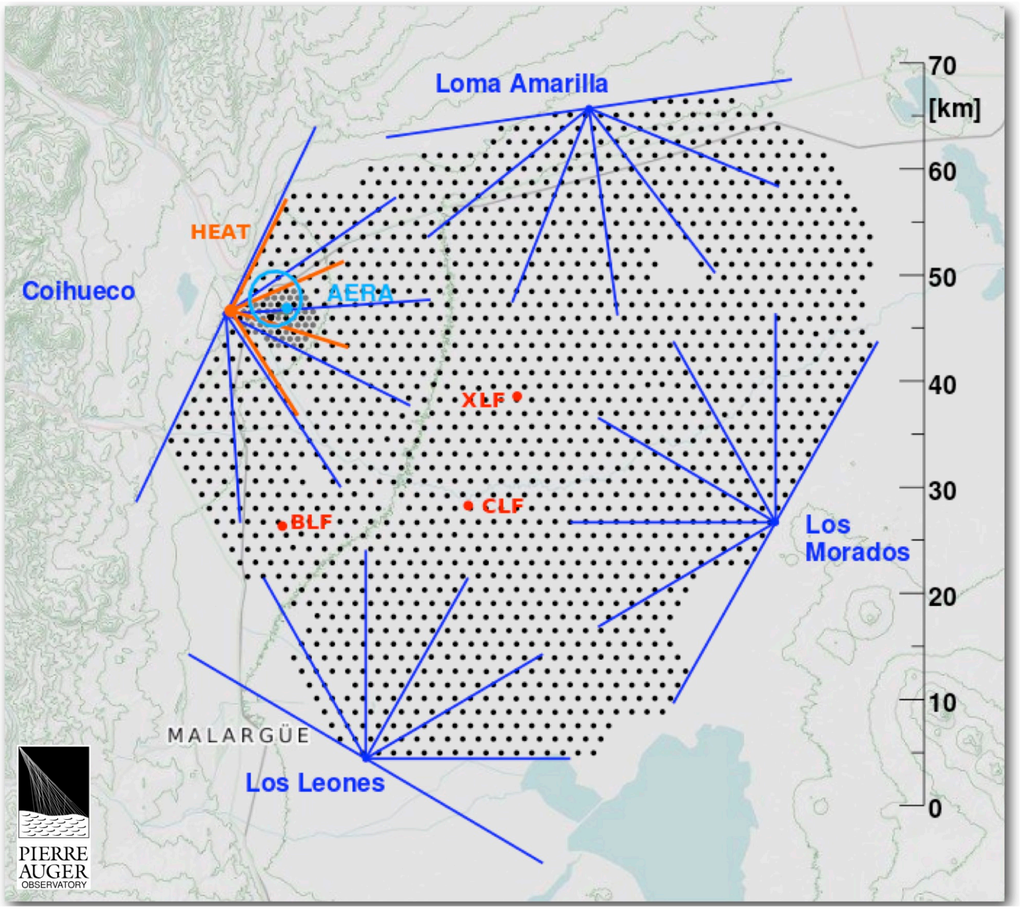

3000 km²
SD: 1660 positions, spacing 1500 m, 750 m, 433 m

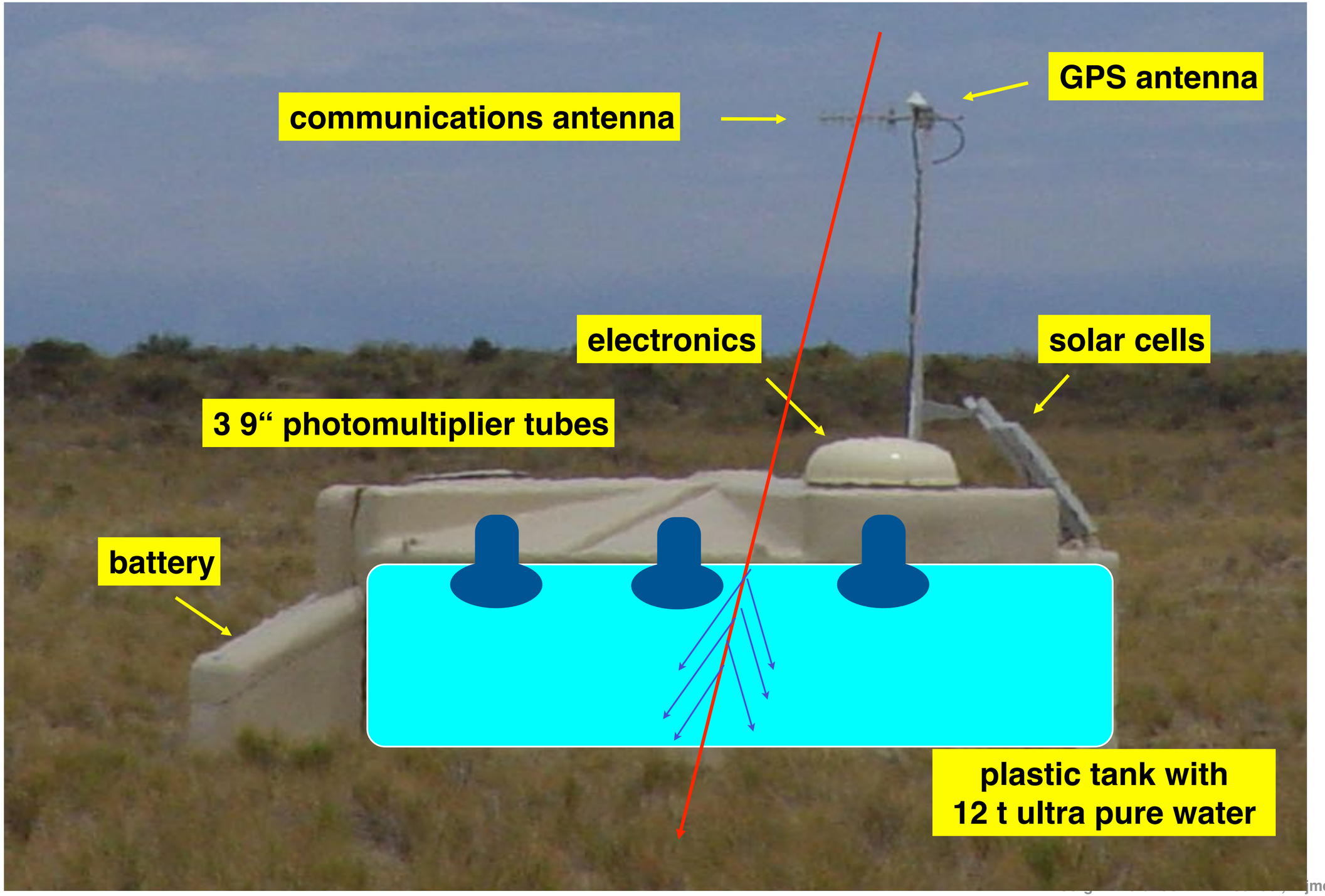
communications antenna
GPS antenna
electronics
solar cells
3 9“ photomultiplier tubes
battery
plastic tank with
12 t ultra pure water

Air shower registered with water Cherenkov detectors

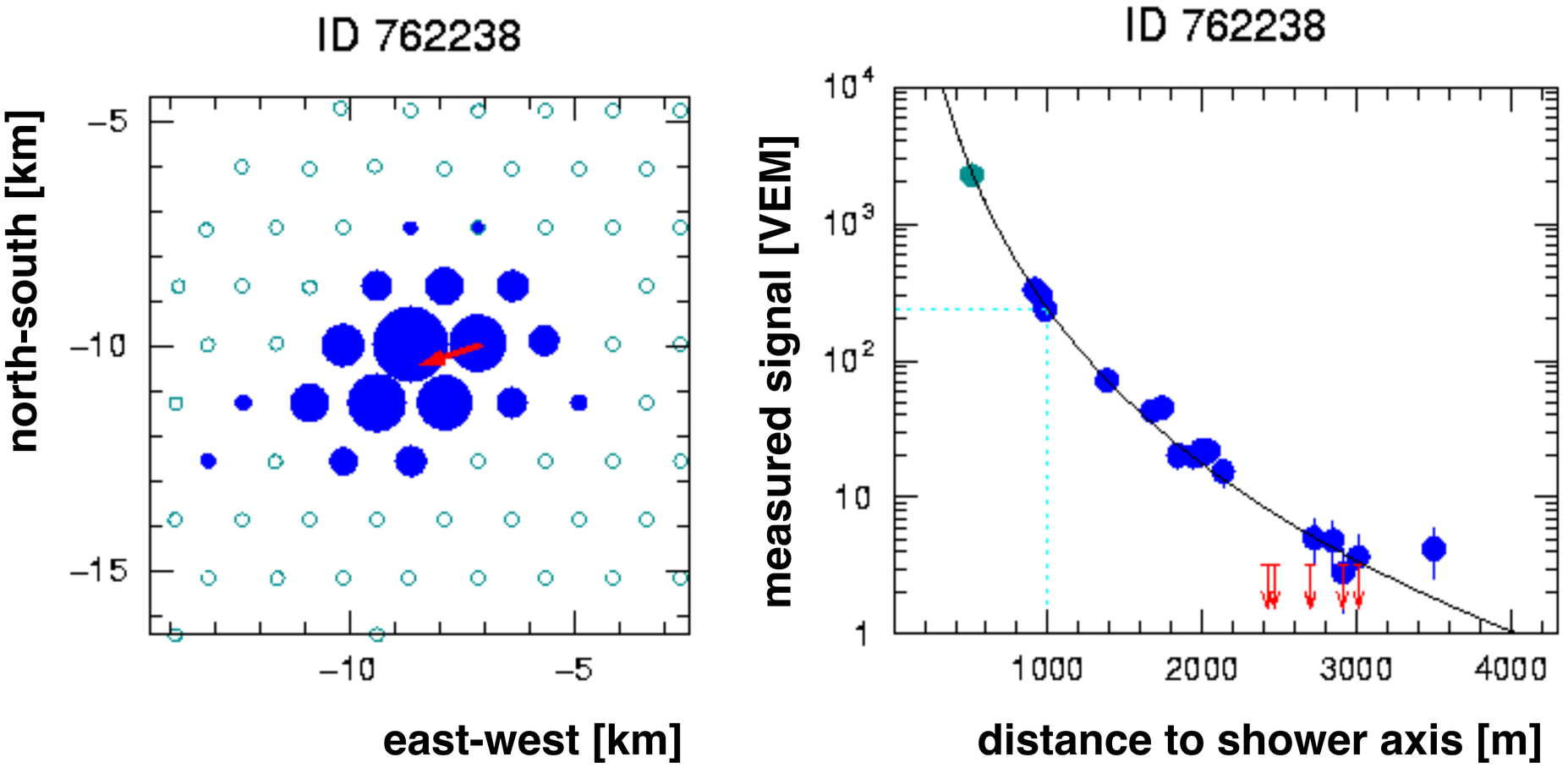

Fluorescence Detector

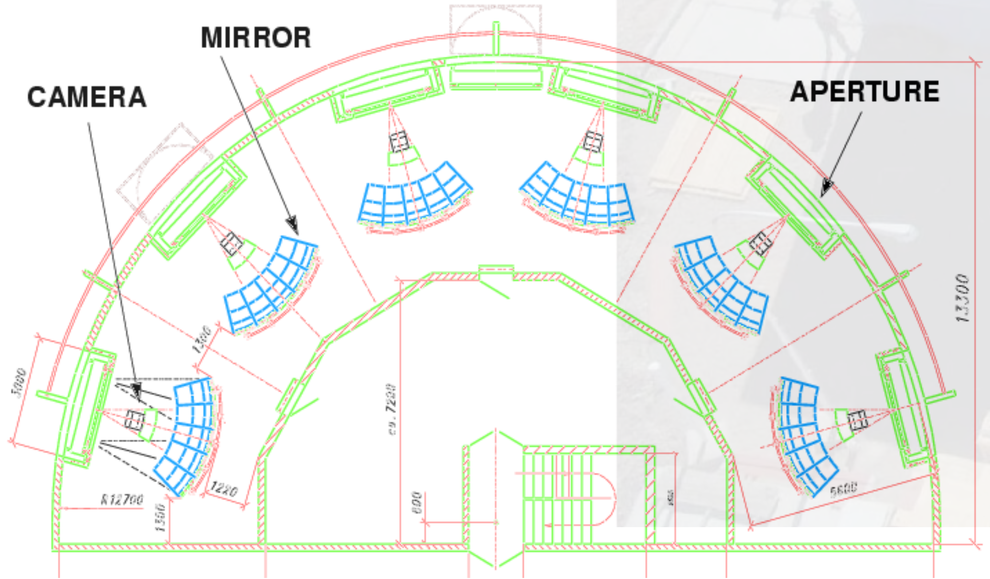

Four sites
Six telescopes
viewing 30°x30° each

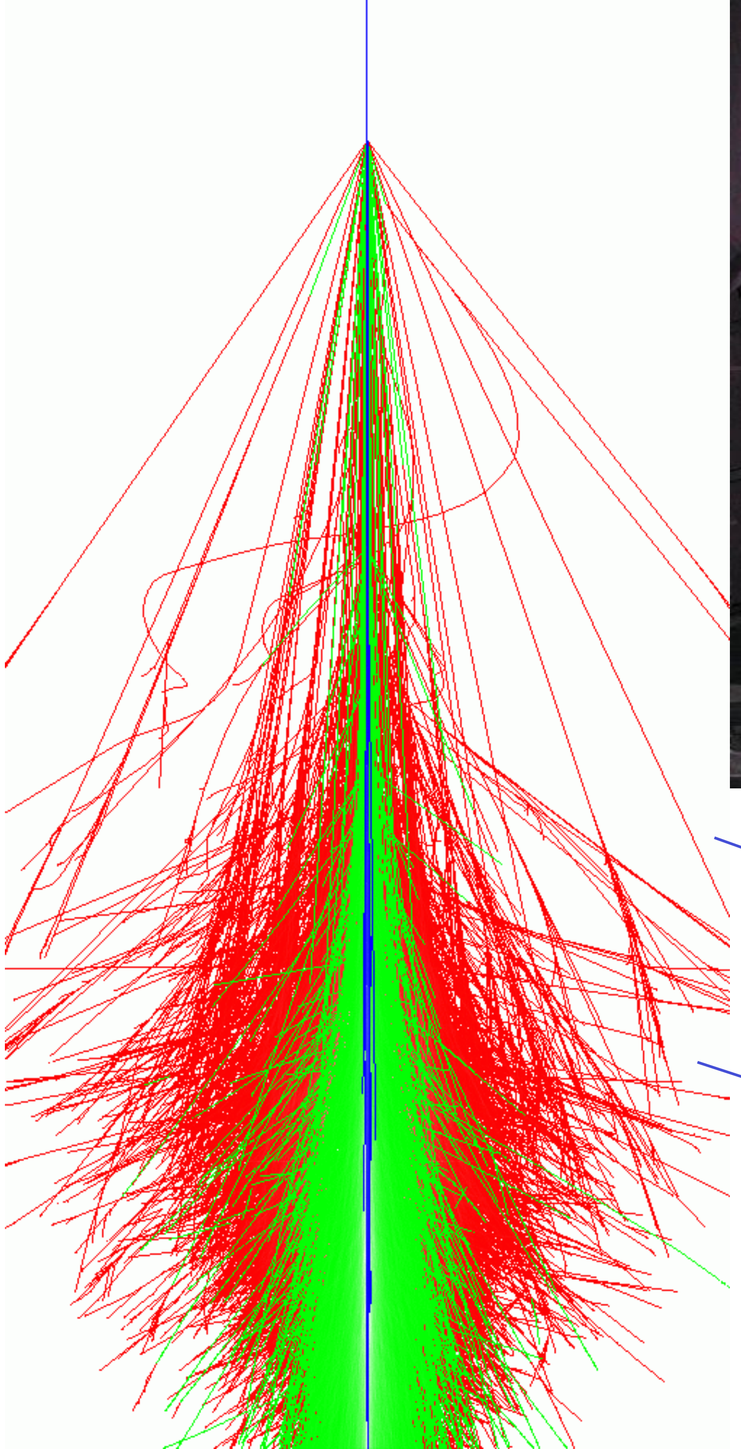

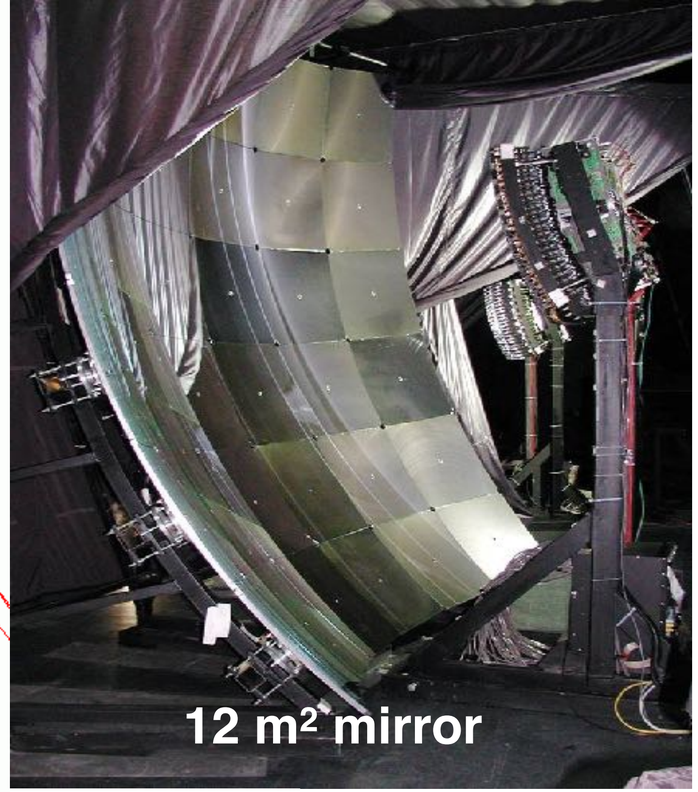
12 m² mirror

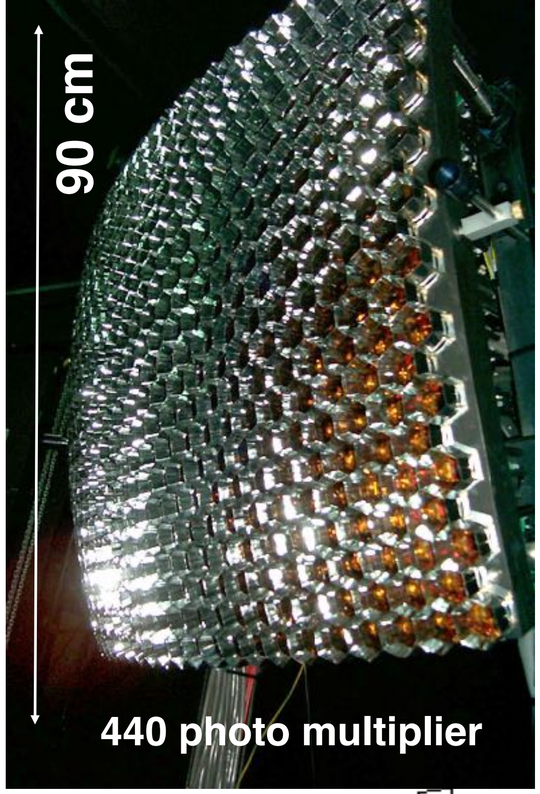
90 cm
440 photo multiplier

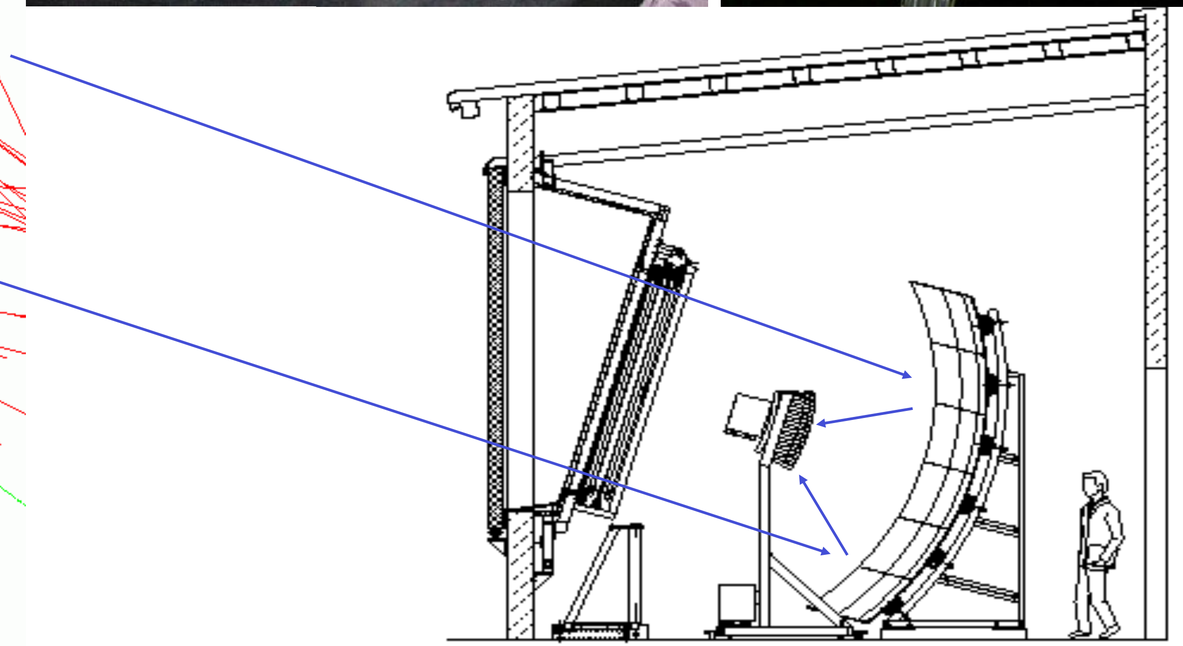

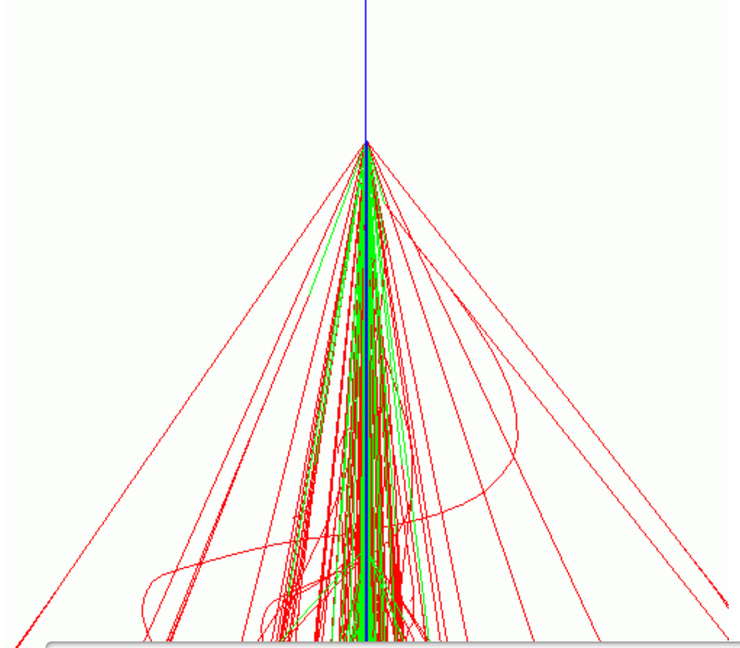

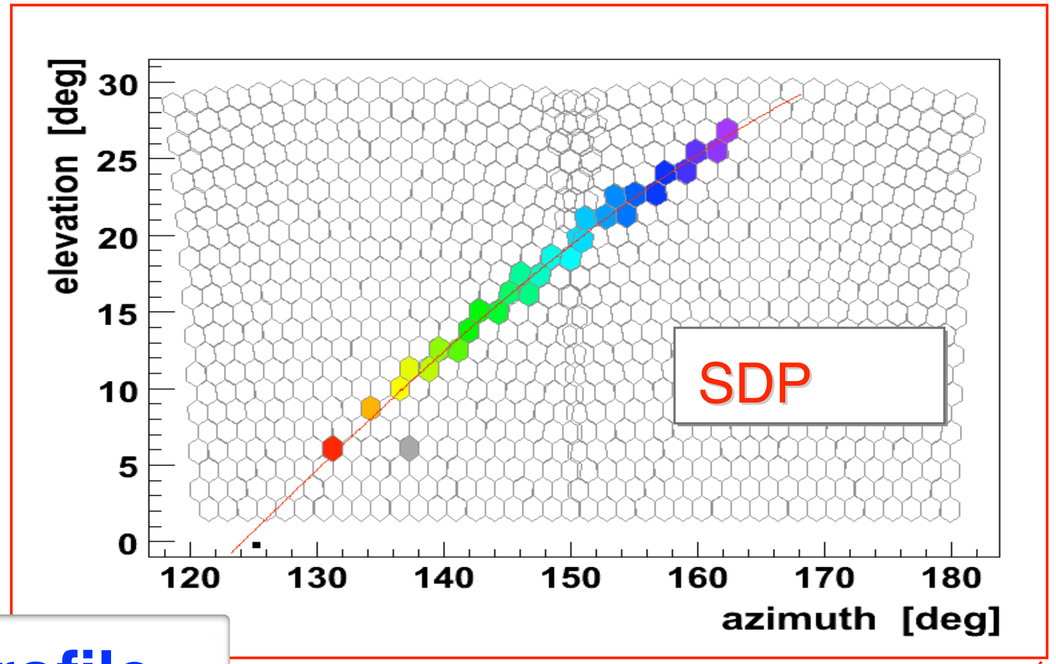

longitudinal shower profile

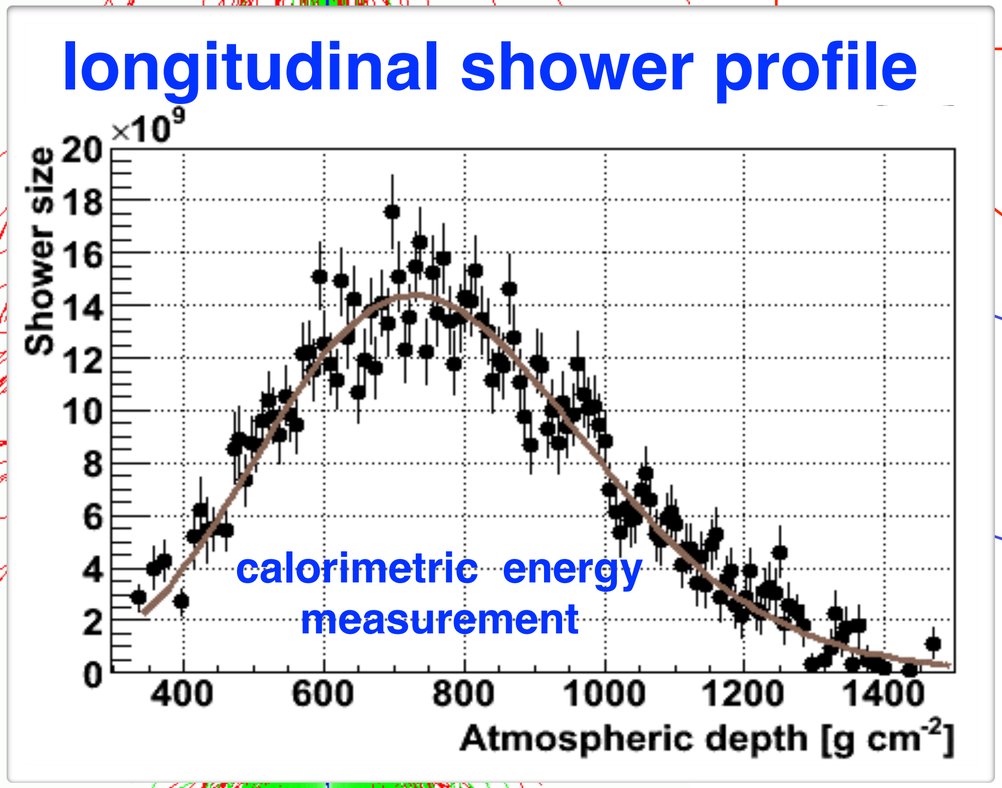

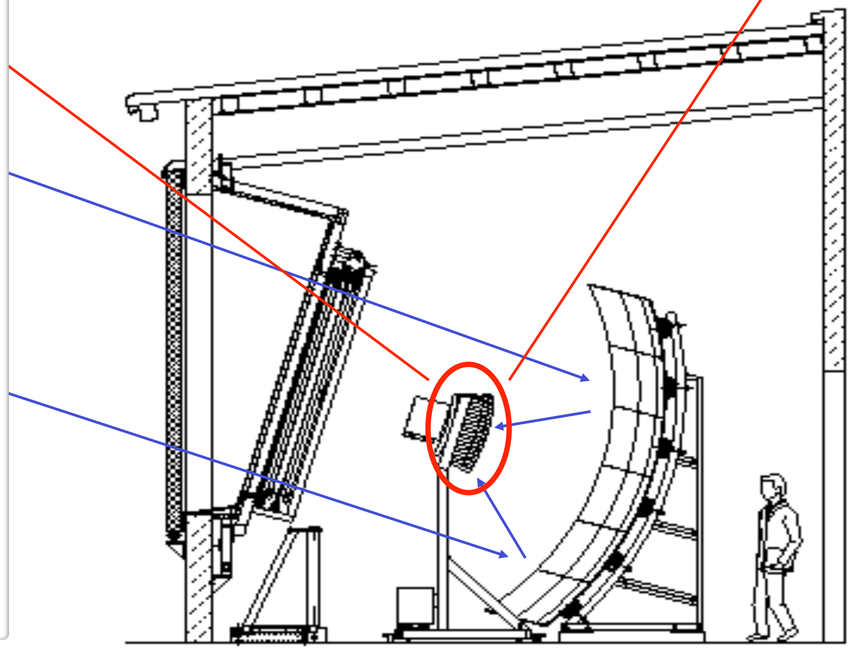

Measuring air showers with multiple techniques

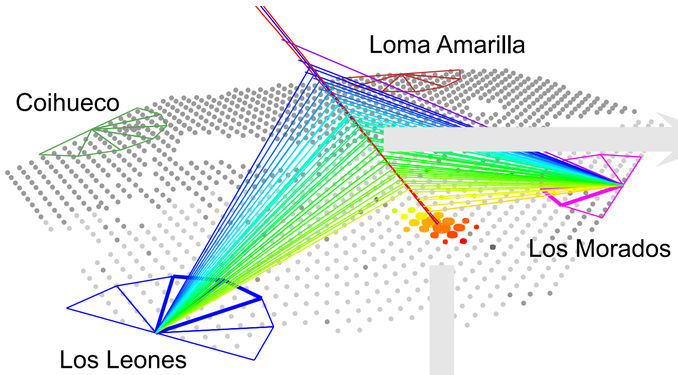

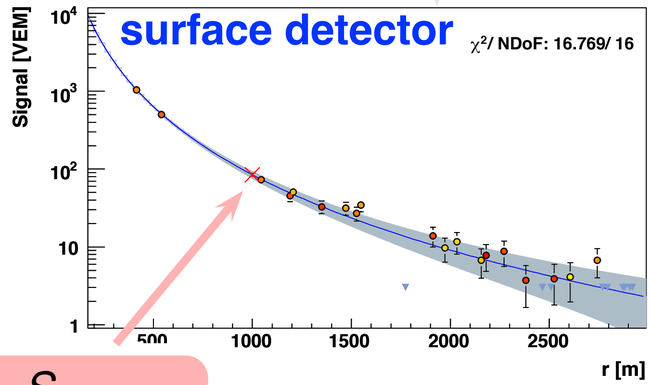

S_{1000}

$E_{\mathrm{surface}} = f(S_{1000}, \theta)$

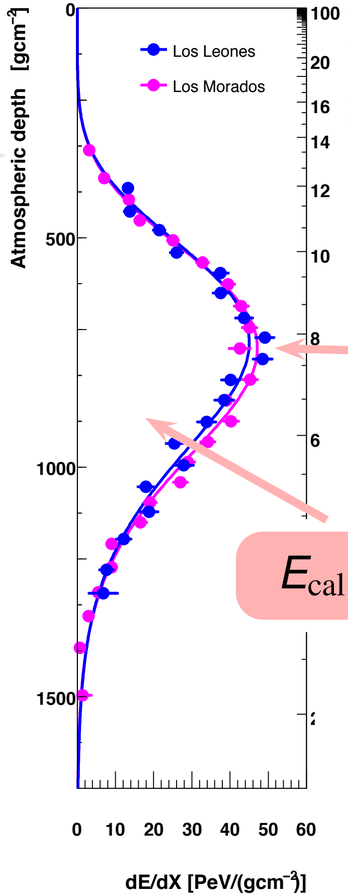

$\sigma X_{\mathrm{max}} \leq 20\,\mathrm{g/cm^2}$
$\Delta_{\mathrm{sys}} \leq 10\,\mathrm{g/cm^2}$

X_{max}

$E_{\mathrm{cal}} = \int \frac{\mathrm{d}E}{\mathrm{d}X}\,\mathrm{d}X$

$\sigma_E/E \sim 8\,\%$
$\Delta_{\mathrm{sys}} \approx 15\,\%$

fluorescence detector

radio detector

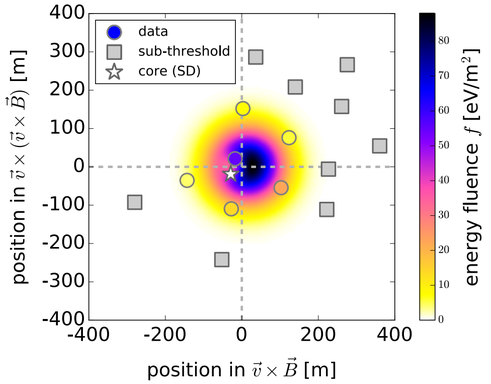

X_{max}, E_{cal}

exposure

Auger 9.0*10⁴ km² sr yr

TA 0.8*10⁴ km² sr

[6 of 30]

PIERRE
AUGER
OBSERVATORY

Energy spectrum

ENERGY SPECTRUM OVER 3 DECADES IN ENERGY

PIERRE AUGER OBSERVATORY

SD vertical

energy thr. 3 EeV

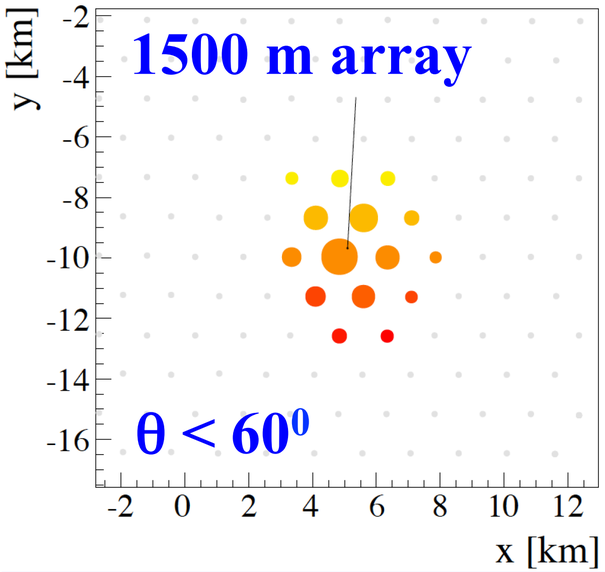

SD Inclined

energy thr. 4 EeV

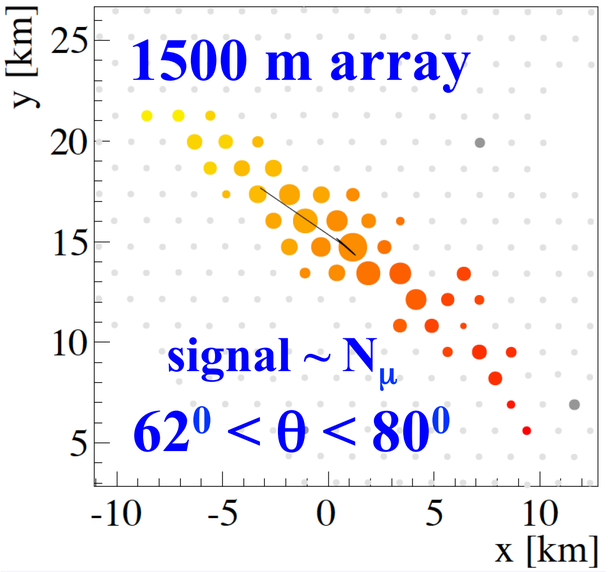

SD infill

energy thr. 0.3 EeV

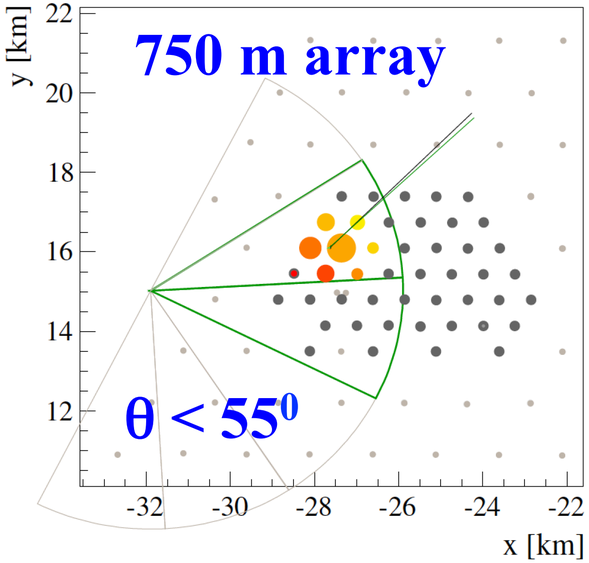

hybrid

13% duty cycle

energy thr. 1 EeV

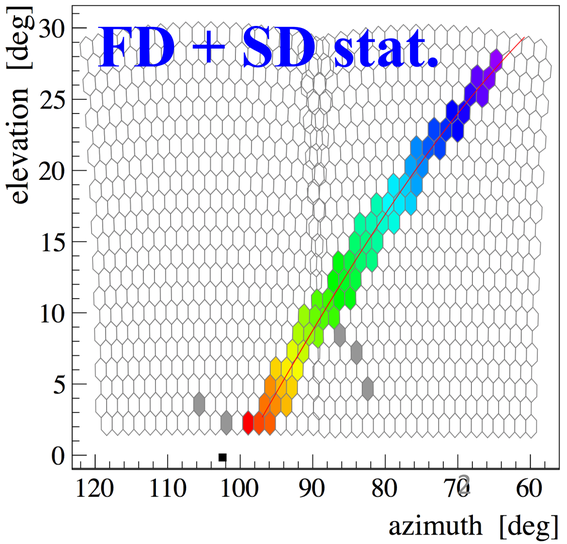

Auger (V. Verzi) UHECR2014

FD ENERGY SCALE

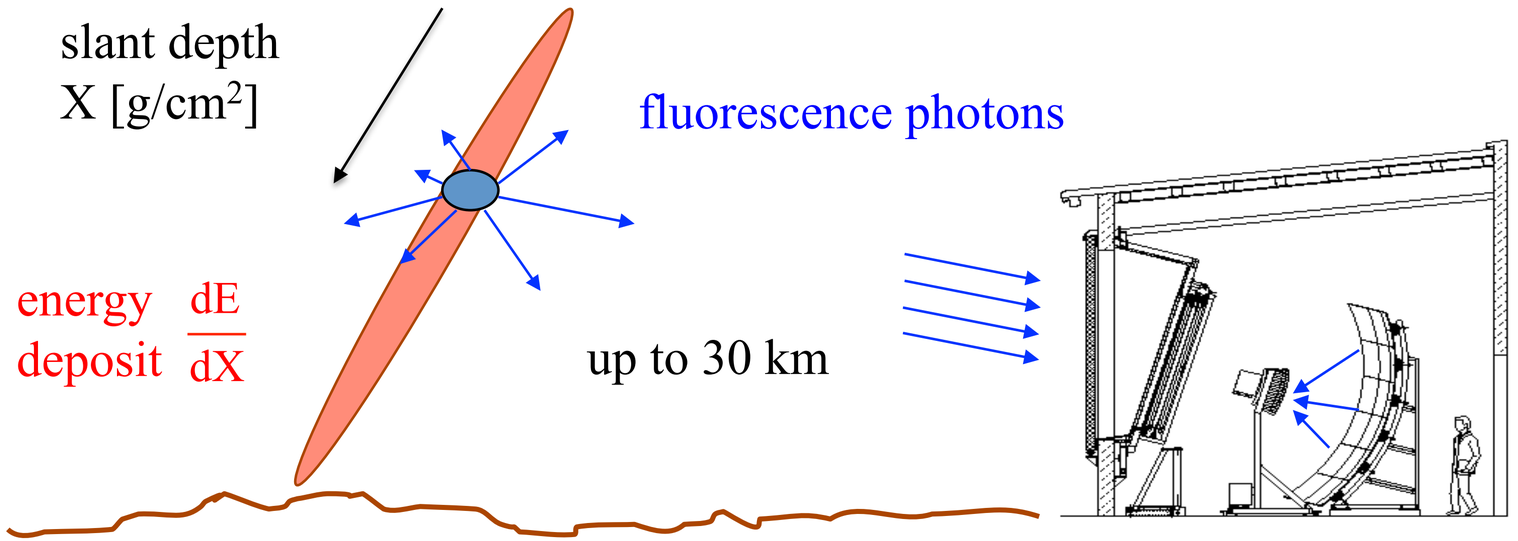

Fluorescence yield

Atmosphere

FD calibration

dE/dX reconstruction $\Rightarrow E_{cal} = \int \frac{dE}{dX} dX$

Invisible energy (ν, μ, ..) $\Rightarrow E_{inv}$

$$E = E_{cal} + E_{inv}$$

systematic uncertainties correlated and uncorrelated among different showers (crucial to correctly propagate the FD uncertainties to SD energies)

AIRFLY - FLUORESCENCE YIELD

The Airfly Collaboration: Astropart. Phys. **42** (2013) 90. Astropart. Phys. **28** (2007) 41.
Nucl. Inst.. Meth. A 597 (2008) 50. M. Bohacova talk at 6th Air Fluor. Workshop

- **relative spectrum and its pressure dependence**
- **humidity and temperature dependence of collisional cross sections**
- **absolute intensity of the 337 nm line**

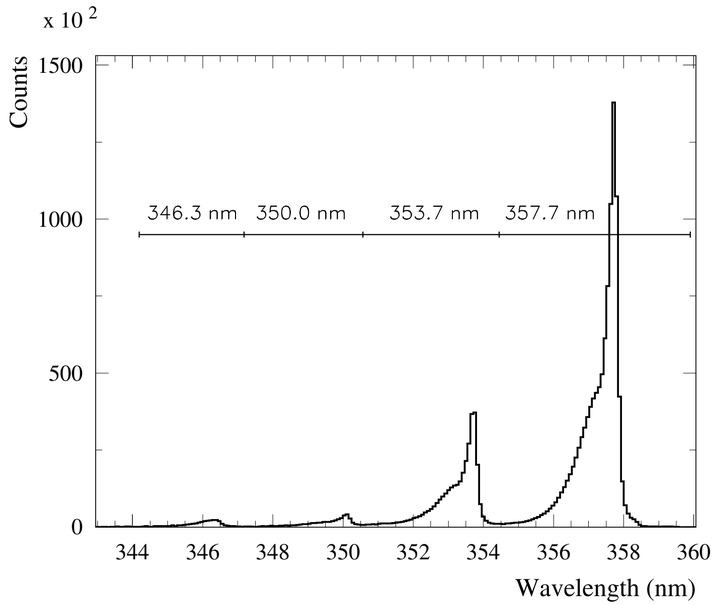

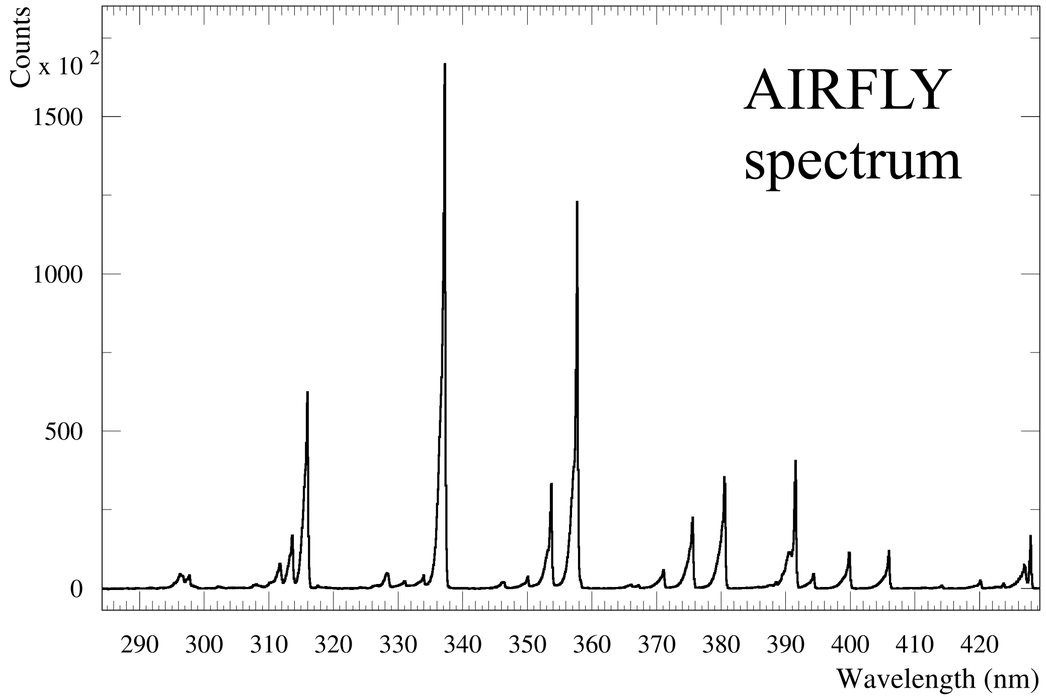

“effective” definition of the wavelength bands

- **don’t care of possible contaminations between nearby bands**
- **straightforward and correct propagation of Airfly measurement uncertainties**

ATMOSPHERE

production and transmission of the light (aerosols and molecular scattering)

- **atmospheric profiles from Global Data Assimilation System (GDAS)**
- **hourly aerosol optical depth profiles**
- **aerosol phase function**
- **λ dependence of aerosol scattering cross sec.**
- **cloud coverage**

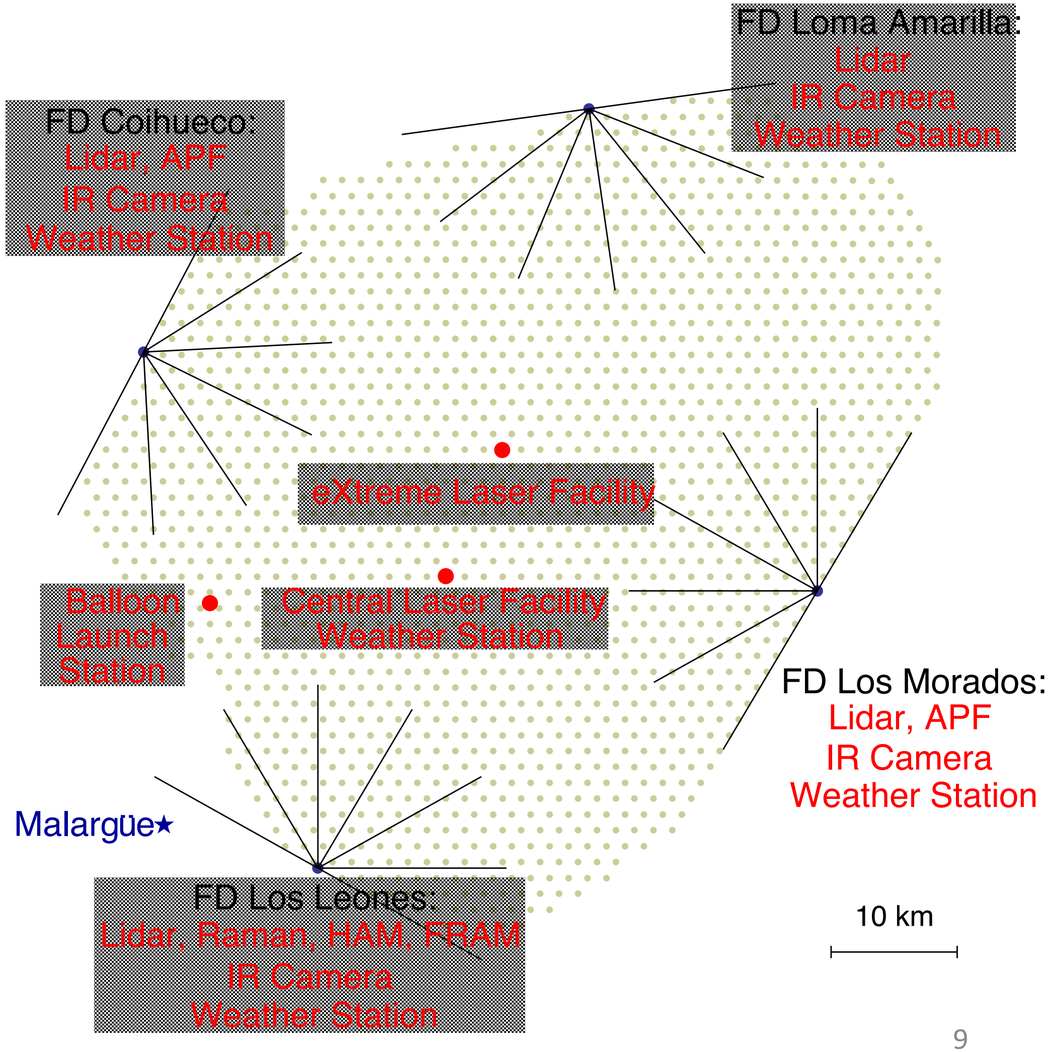

The Pierre Auger Collaboration
Astropart. Phys. **33** (2010) 108
Astropart. Phys. **35** (2012) 591
JINST **8** (2013) P04009
L. Valore ICRC 2013 #0920

SD Energy Calibration

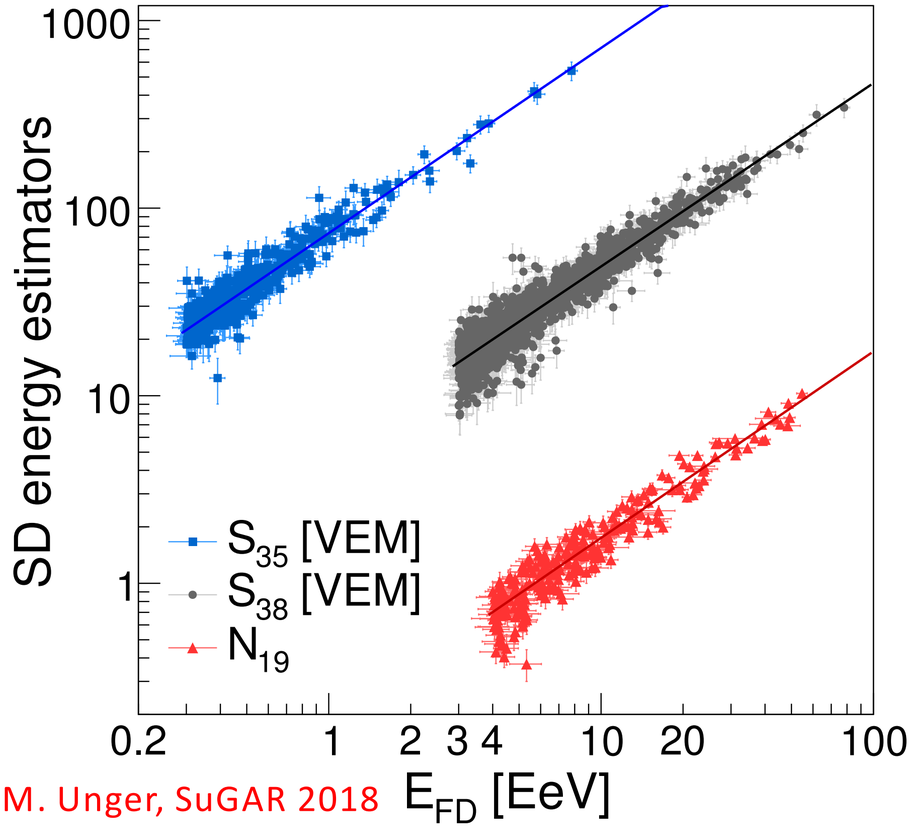

M. Unger, SuGAR 2018

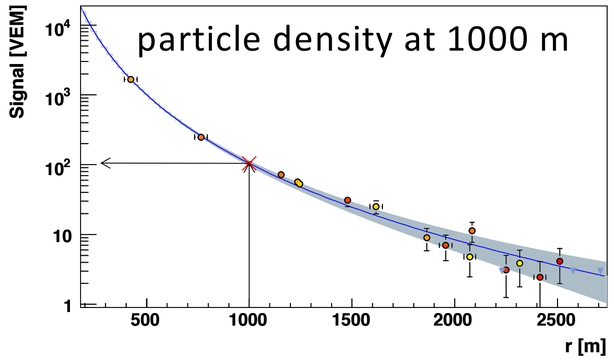

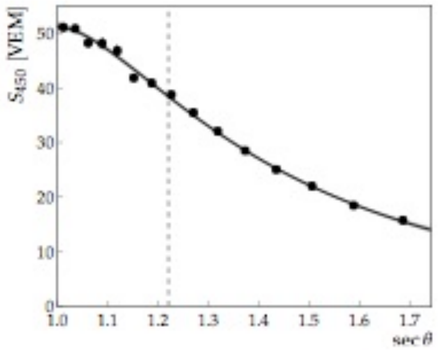

Infill: particle density at 400 m

FD longitudinal profiles

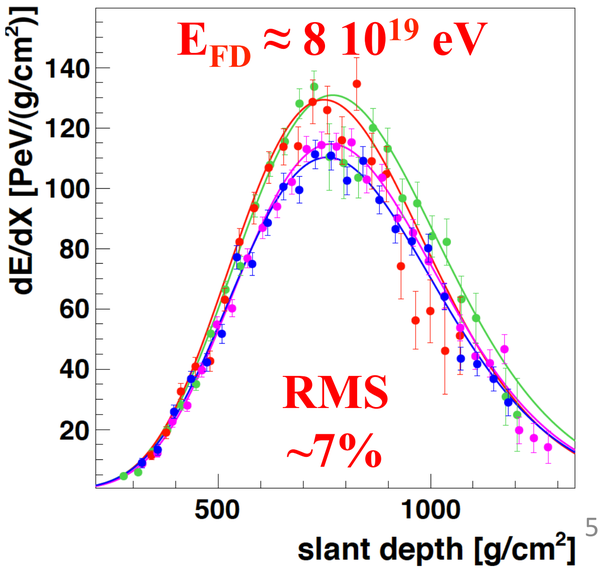

ENERGY SPECTRA

- SD 750 m spectrum: 29585 events above 3×10^{17} eV (08/2008 – 12/2012)
- correction for bin-to-bin migrations due to the detector resolution and steepness of spectrum (< 15%)

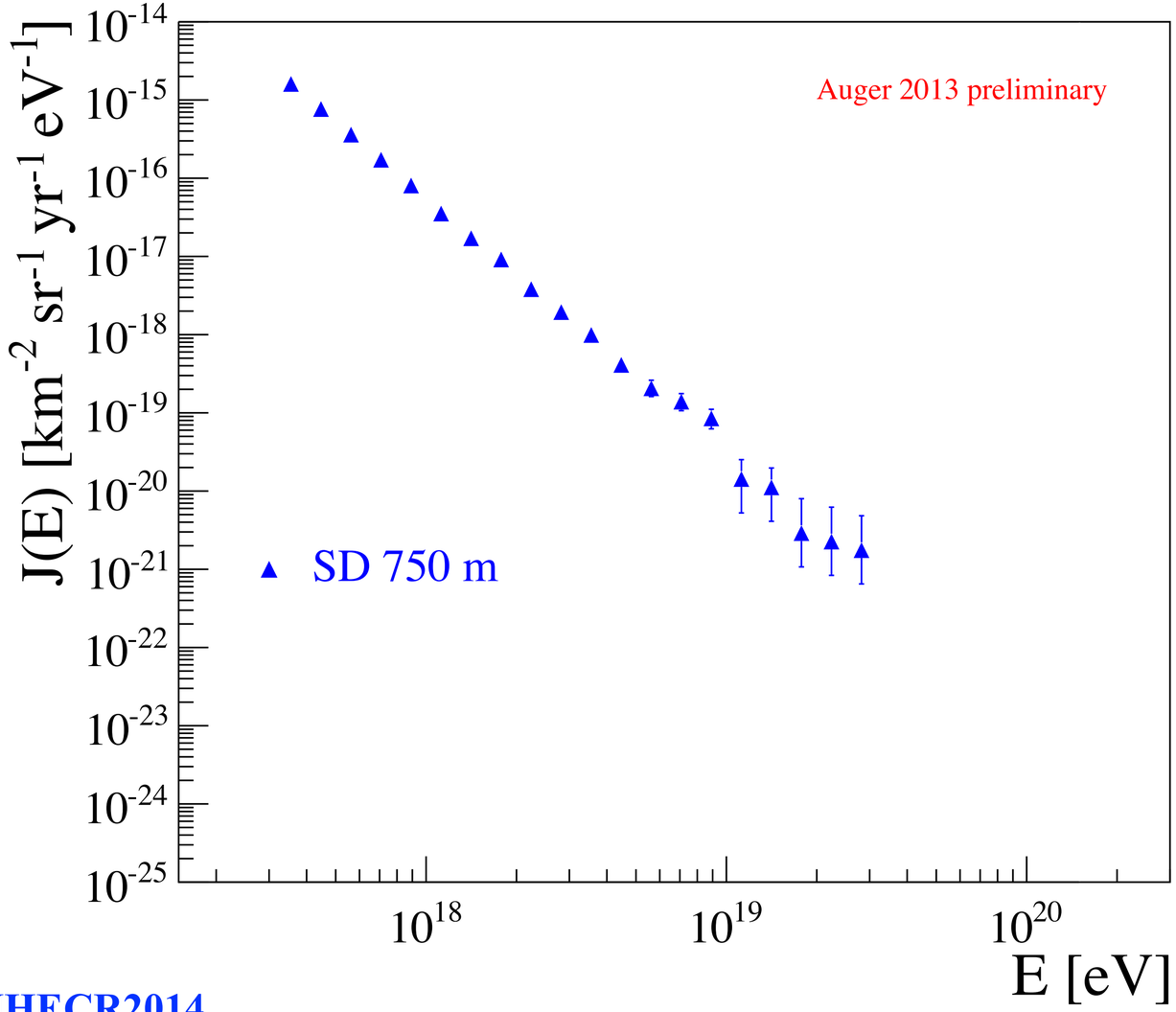

Auger (V. Verzi) UHECR2014

ENERGY SPECTRA

- hybrid spectrum: 11155 events above 10^{18} eV (11/2005 – 12/2012)
- correction for bin-to-bin migrations due to the detector resolution and steepness of spectrum (< 3%)

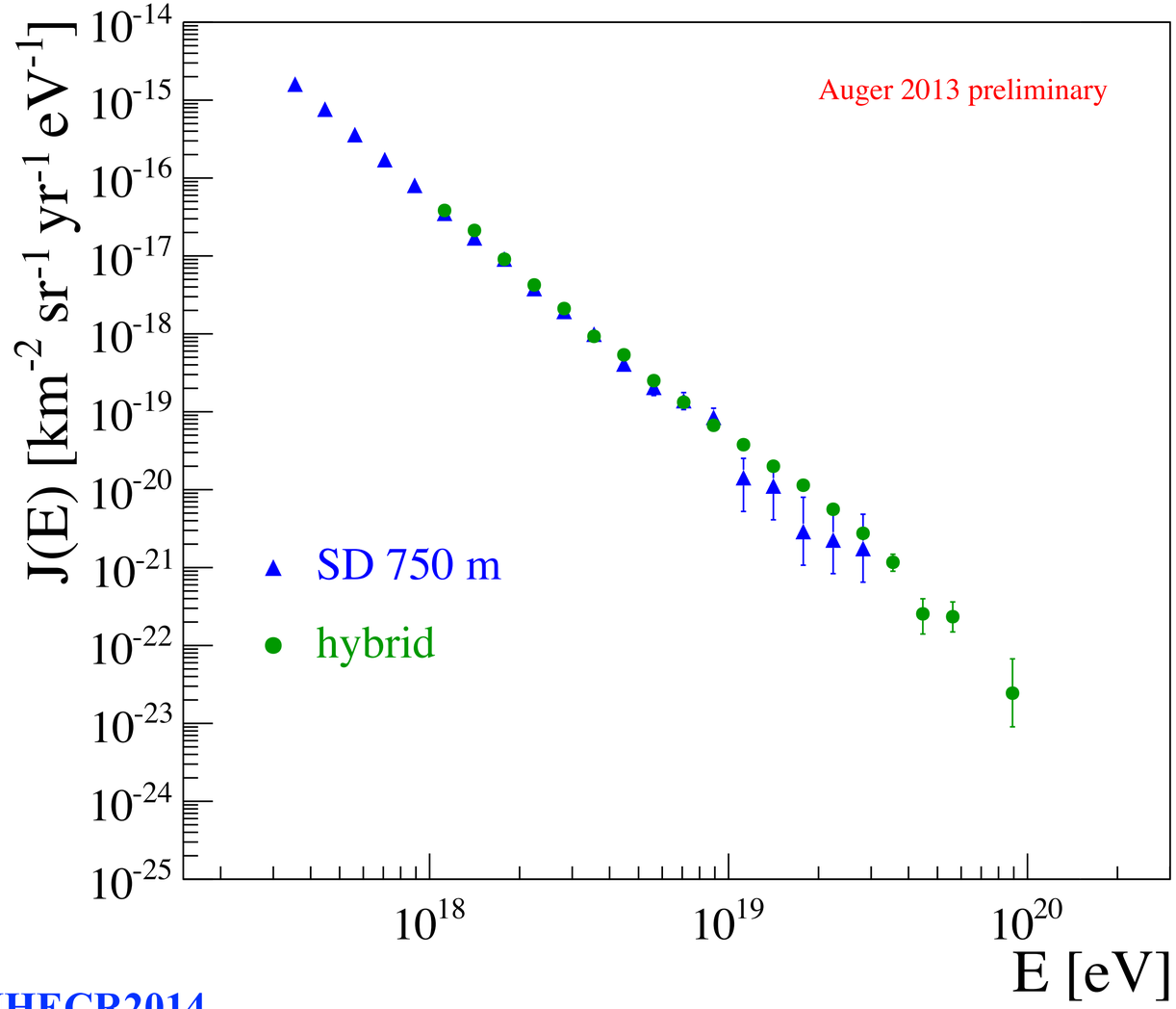

Auger (V. Verzi) UHECR2014

ENERGY SPECTRA

- SD inclined: 11074 events above 4×10^{18} eV (01/2004 – 12/2012)
- correction for bin-to-bin migrations due to the detector resolution and steepness of spectrum (< 12%)

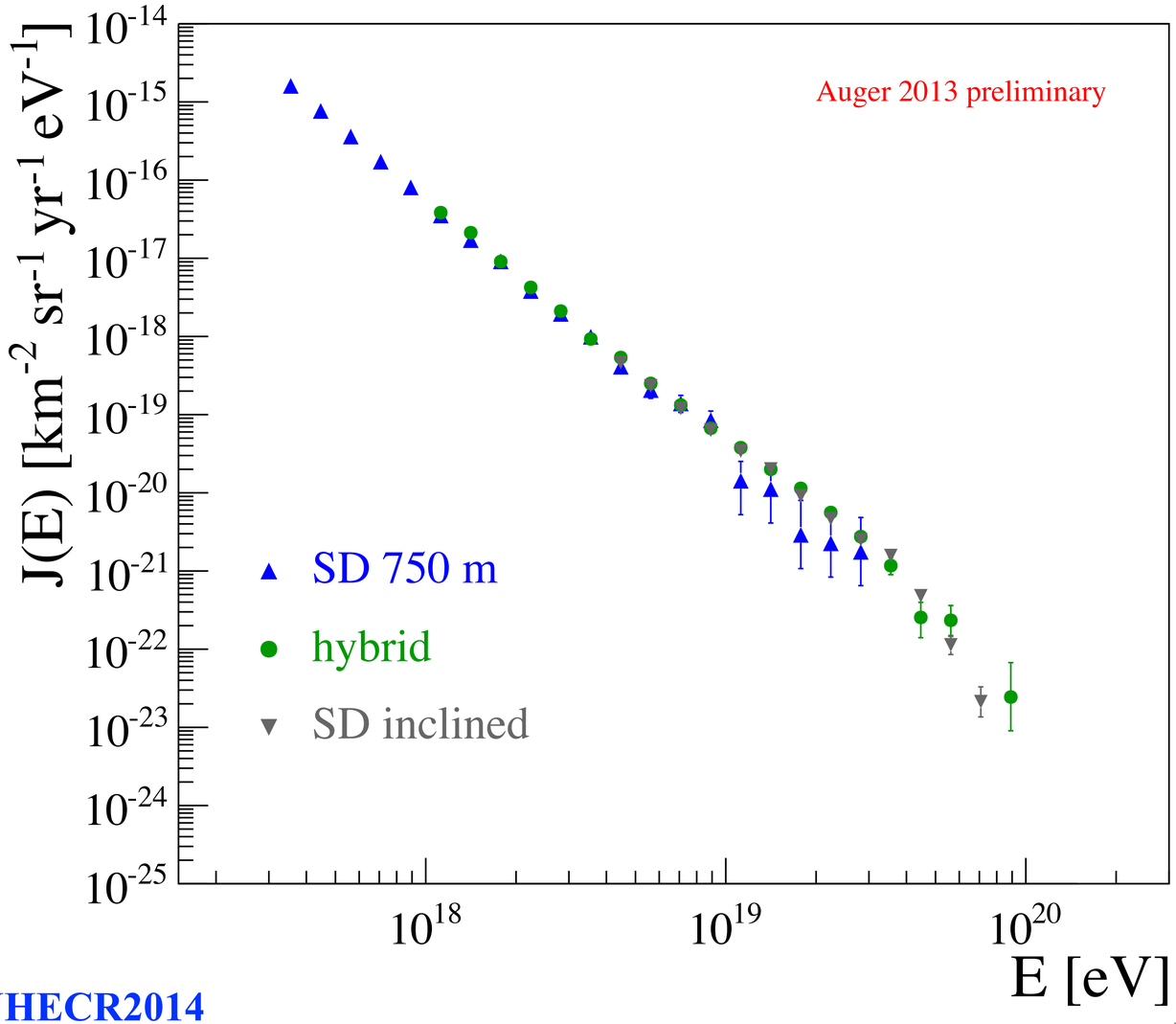

Auger (V. Verzi) UHECR2014

ENERGY SPECTRA

- SD inclined: 82318 events above 3×10^{18} eV (01/2004 – 12/2012)
- correction for bin-to-bin migrations due to the detector resolution and steepness of spectrum (< 17%)

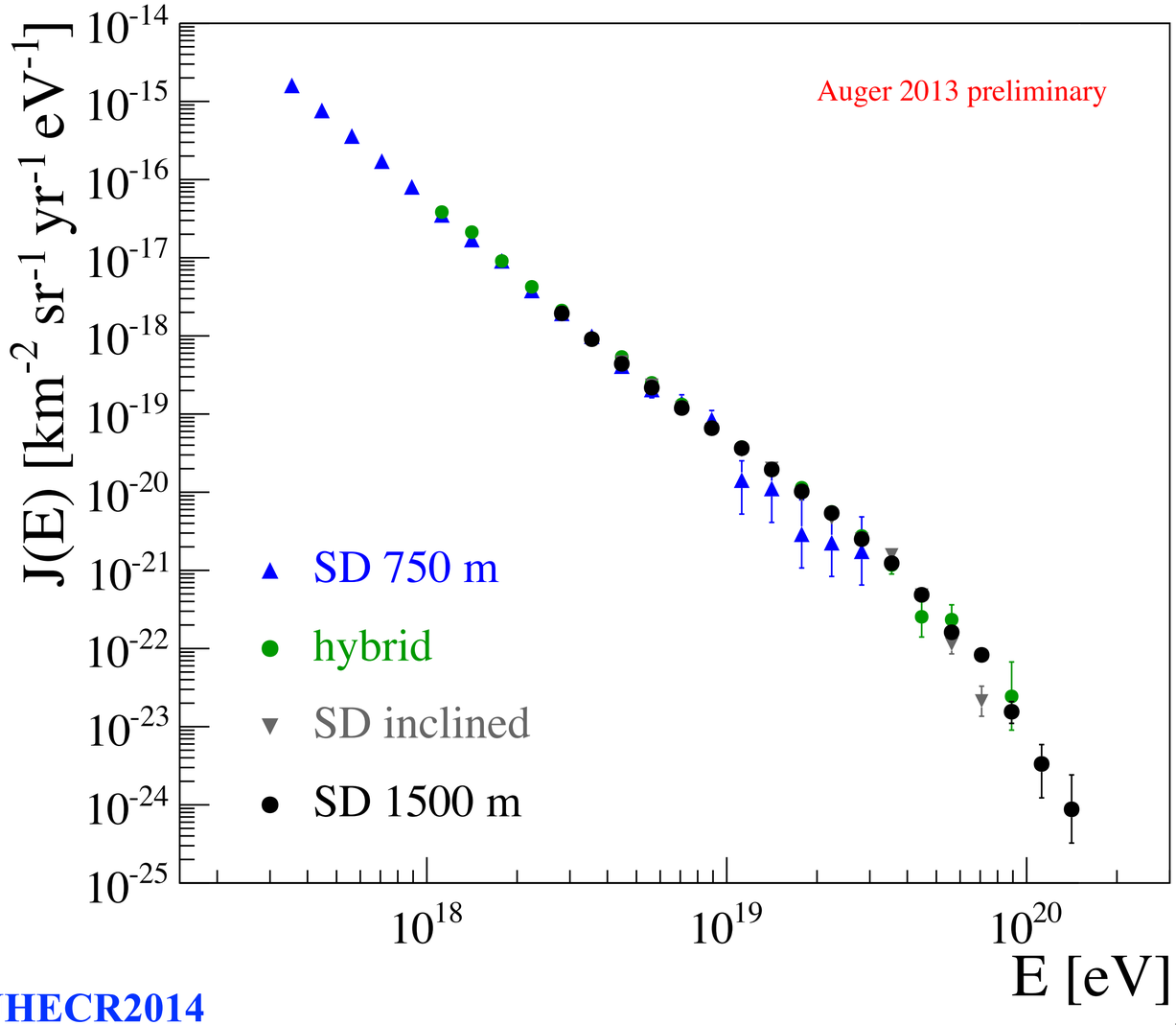

Auger (V. Verzi) UHECR2014

COMBINED ENERGY SPECTRA

- combination after few % correction to the normalizations

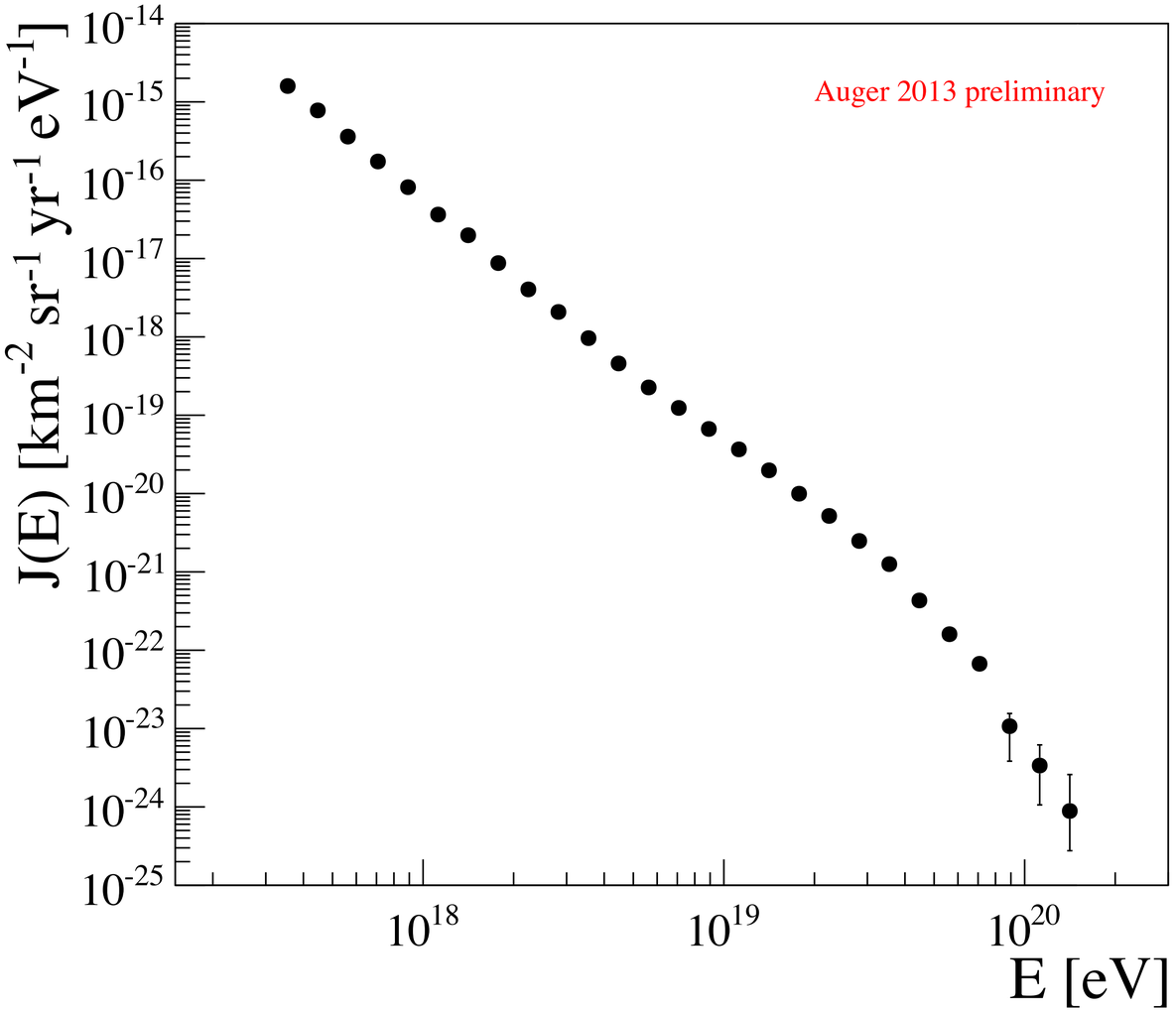

Auger (V. Verzi) UHECR2014

COMBINED ENERGY SPECTRA

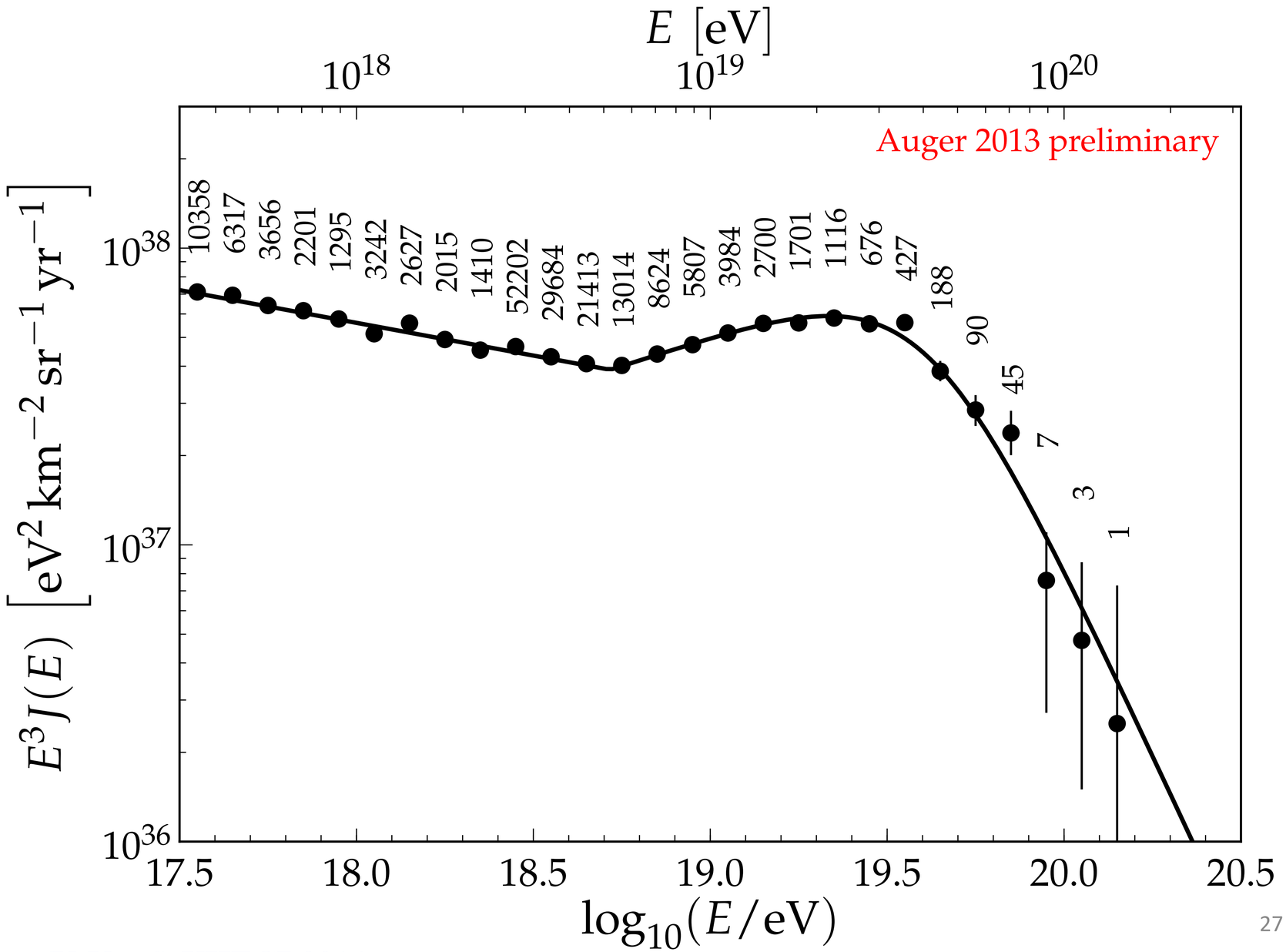

Auger (V. Verzi) UHECR2014

Editors' Suggestion Featured in Physics

Features of the Energy Spectrum of Cosmic Rays above 2.5×10^{18} eV Using the Pierre Auger Observatory

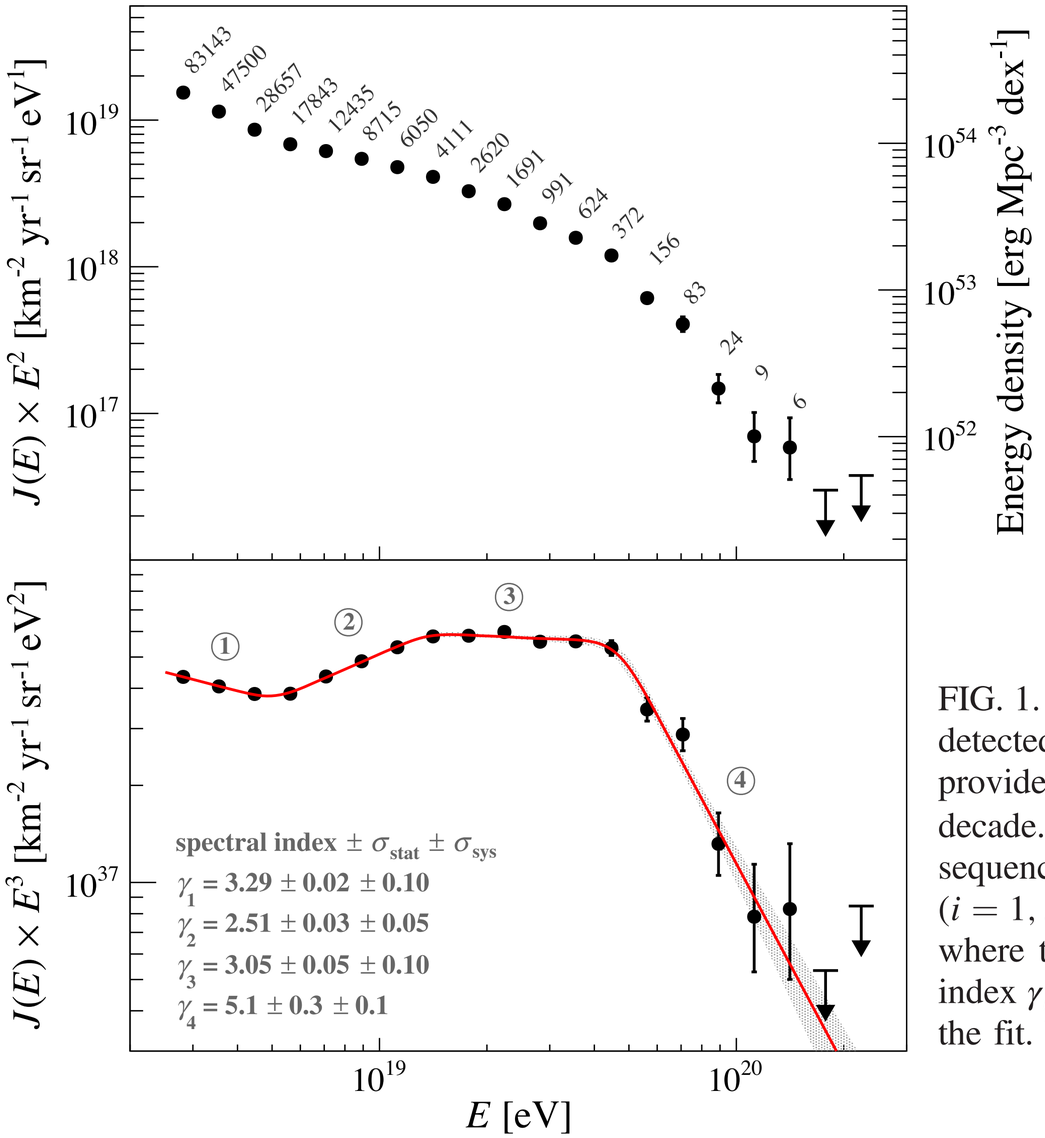

FIG. 1. Top: energy spectrum scaled by E^2 with the number of detected events in each energy bin. In this representation the data provide an estimation of the differential energy density per decade. Bottom: energy spectrum scaled by E^3 fitted with a sequence of four power laws (red line). The numbers ($i = 1, \ldots, 4$) enclosed in the circles identify the energy intervals where the spectrum is described by a power law with spectral index γ_i. The shaded band indicates the statistical uncertainty of the fit. Upper limits are at the 90% confidence level.

Energy spectrum

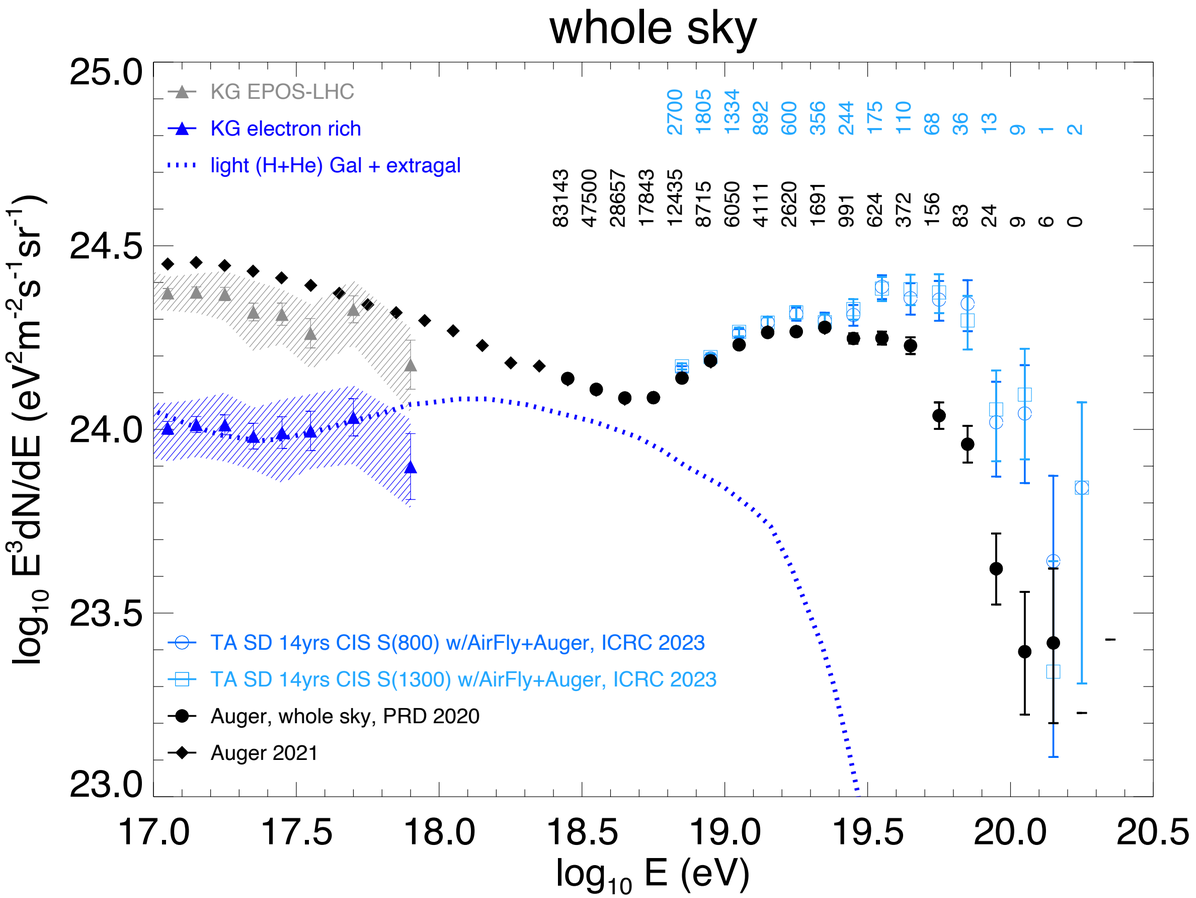

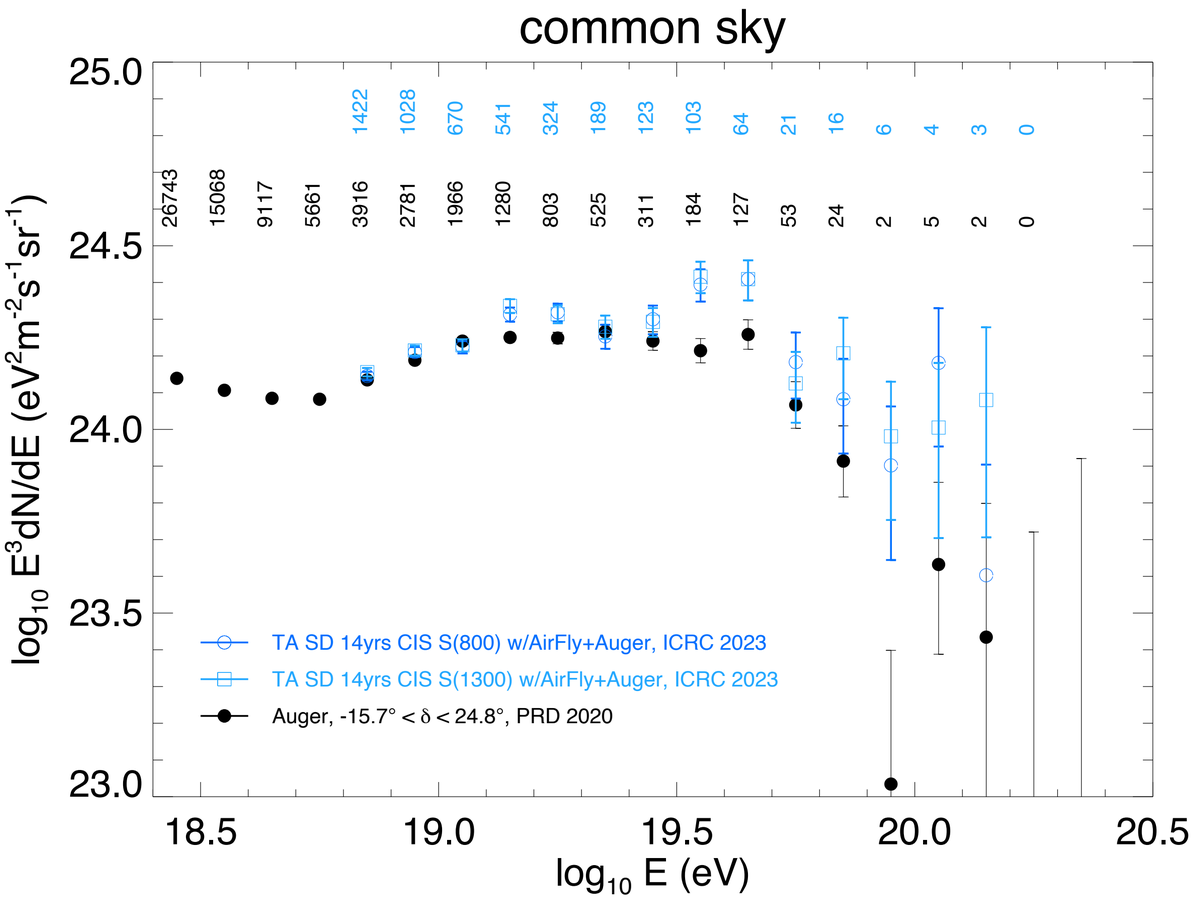

Mass composition

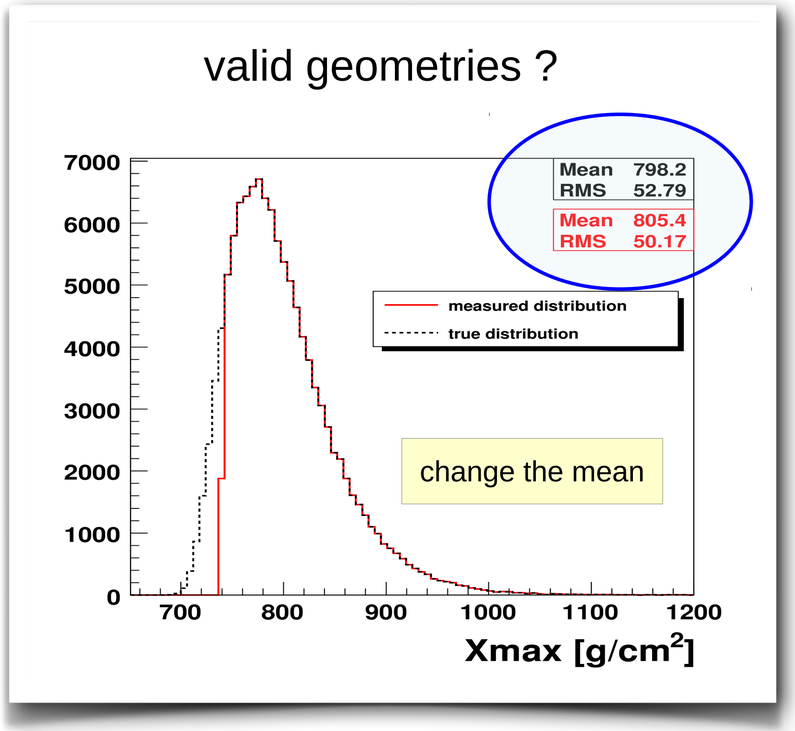

fiducial field of view

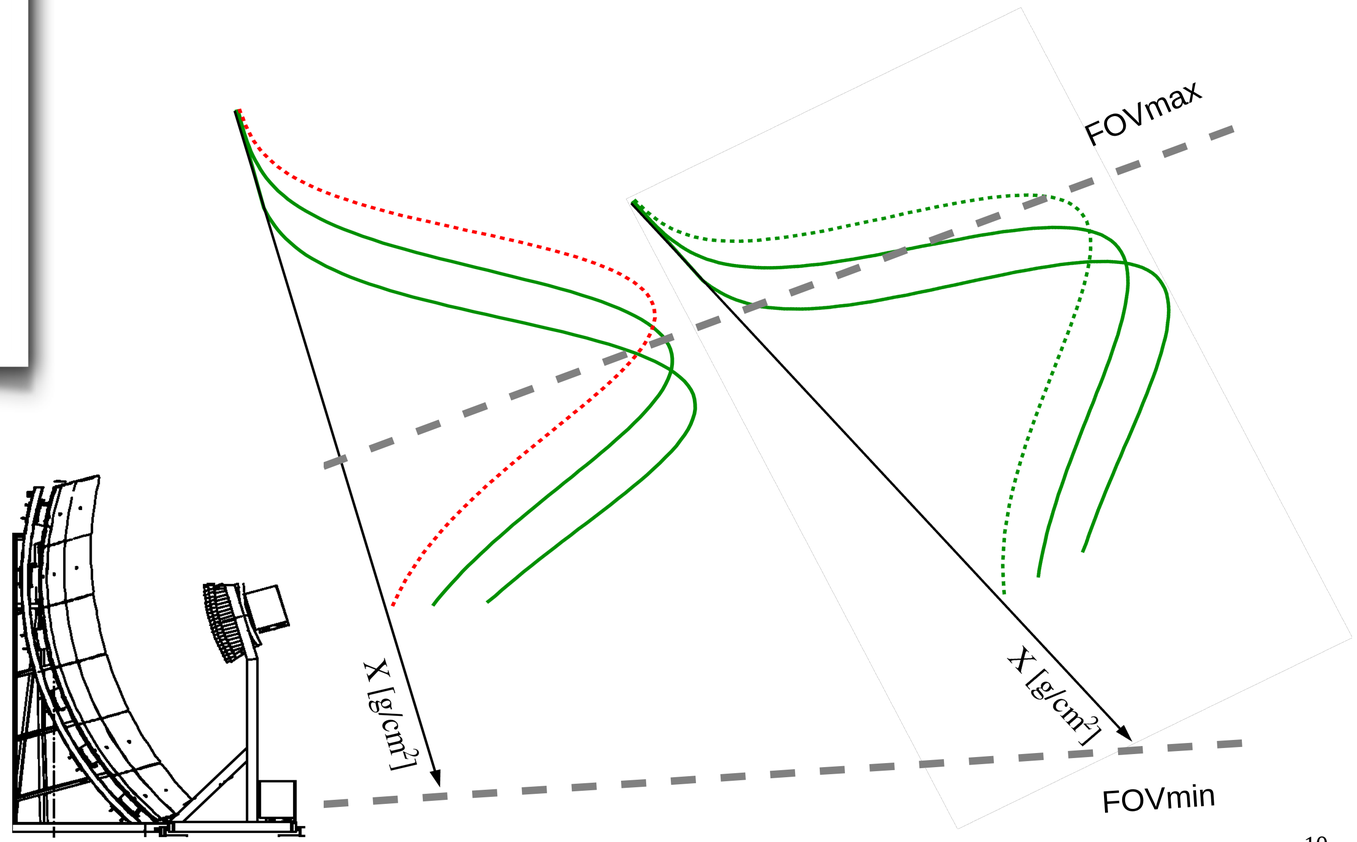

Auger (V. de Souza) UHECR2014

valid geometries ?

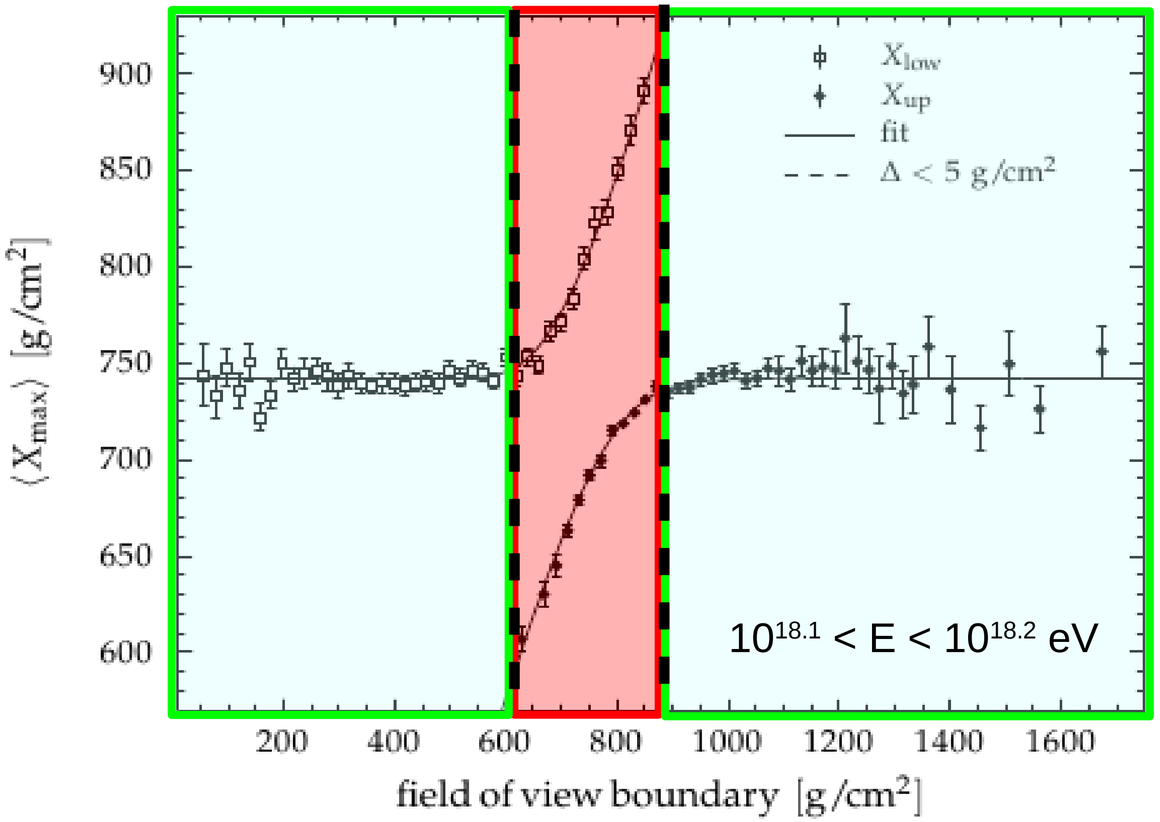

Auger (V. de Souza) UHECR2014

this is the valid geometry that assures unbiased Xmax distributions

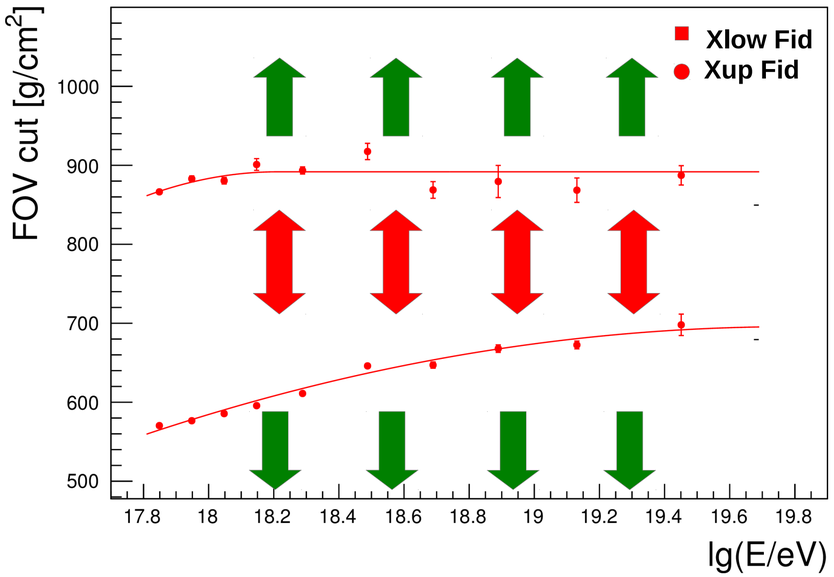

First 2 moments of X_{max} distributions

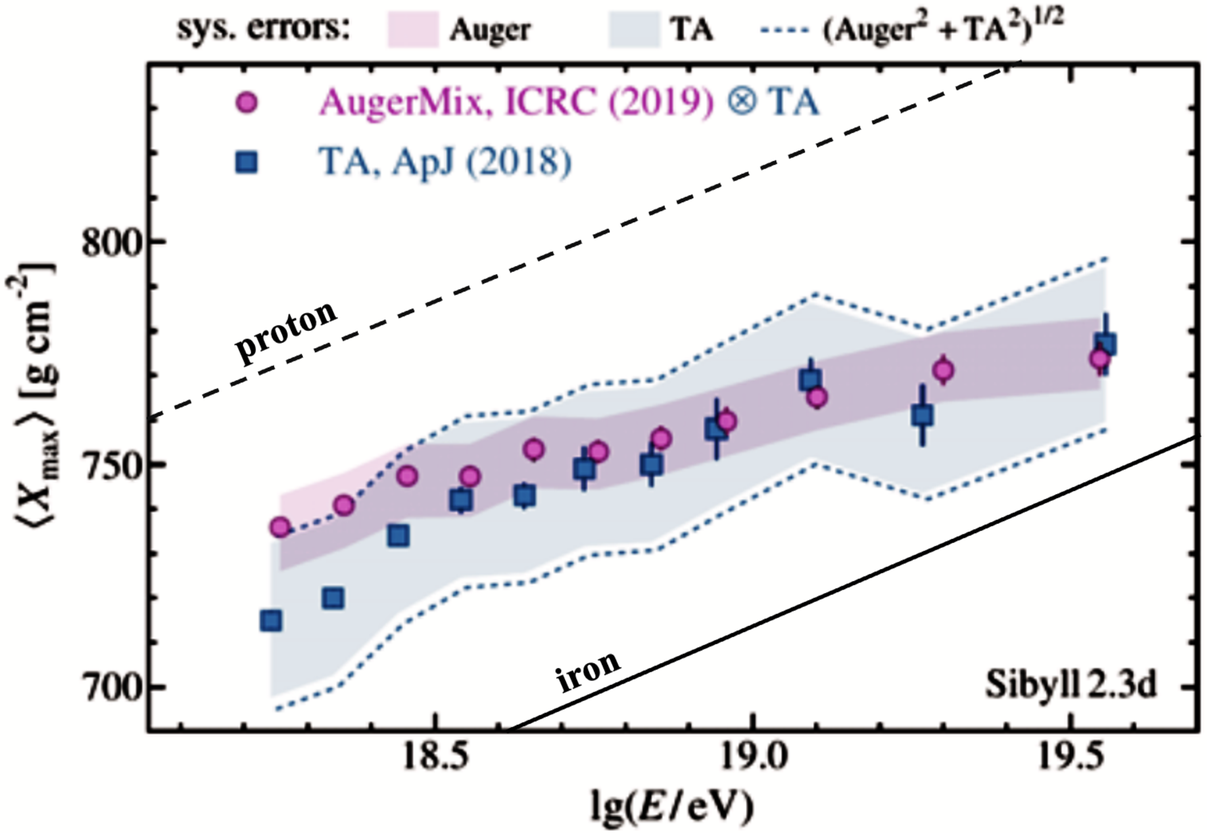

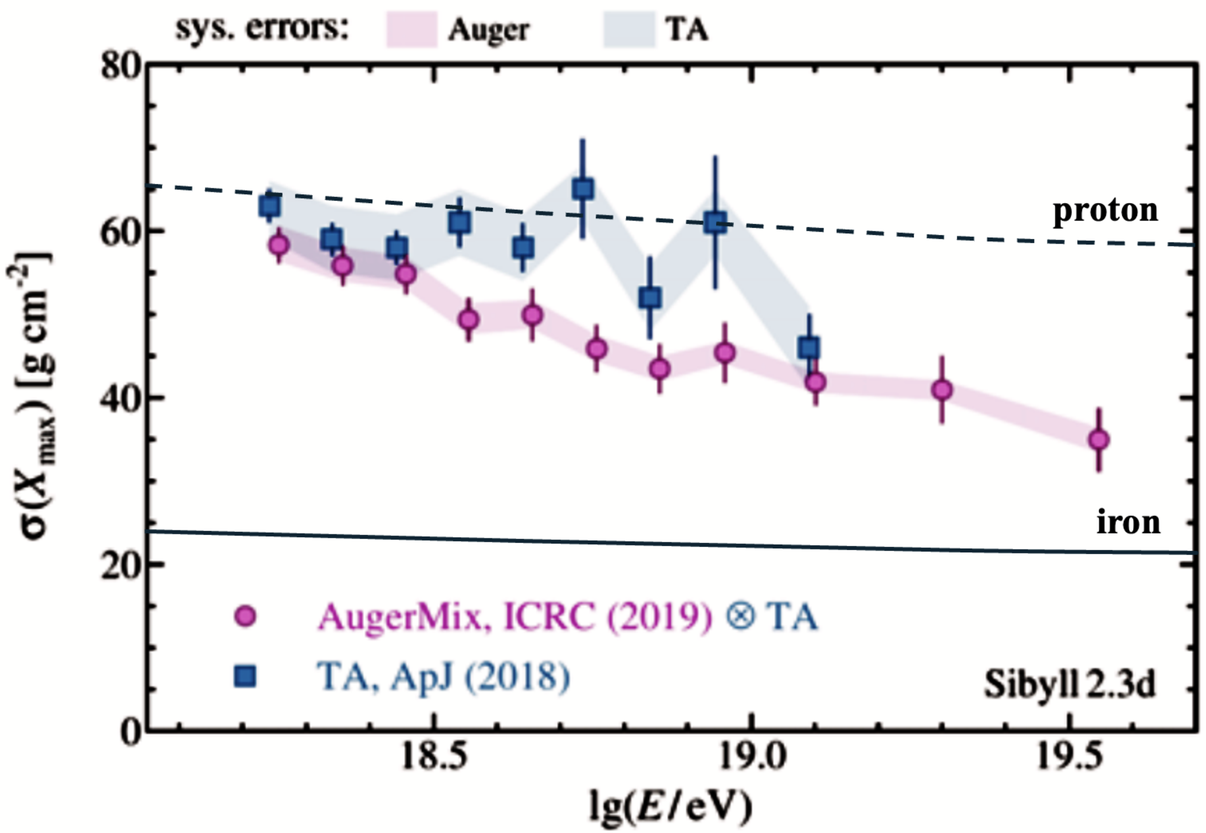

Journal of Cosmology and Astroparticle Physics
An IOP and SISSA journal

Combined fit of spectrum and composition data as measured by the Pierre Auger Observatory

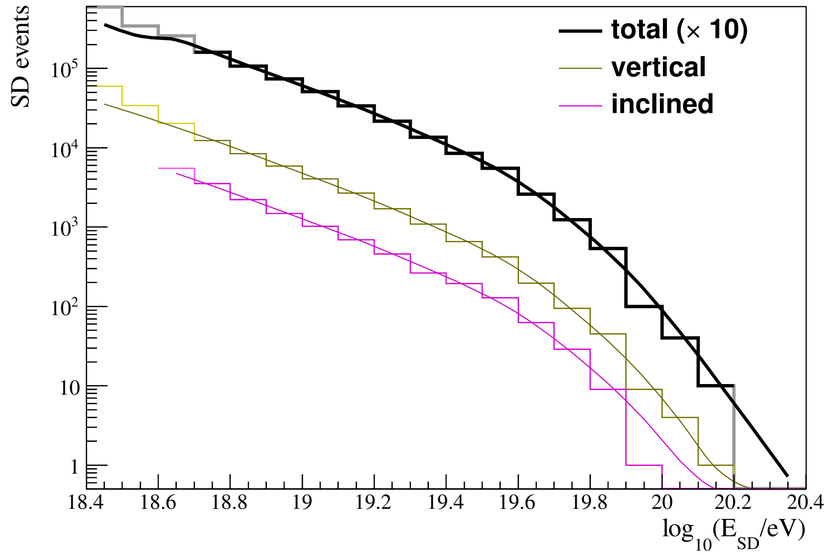

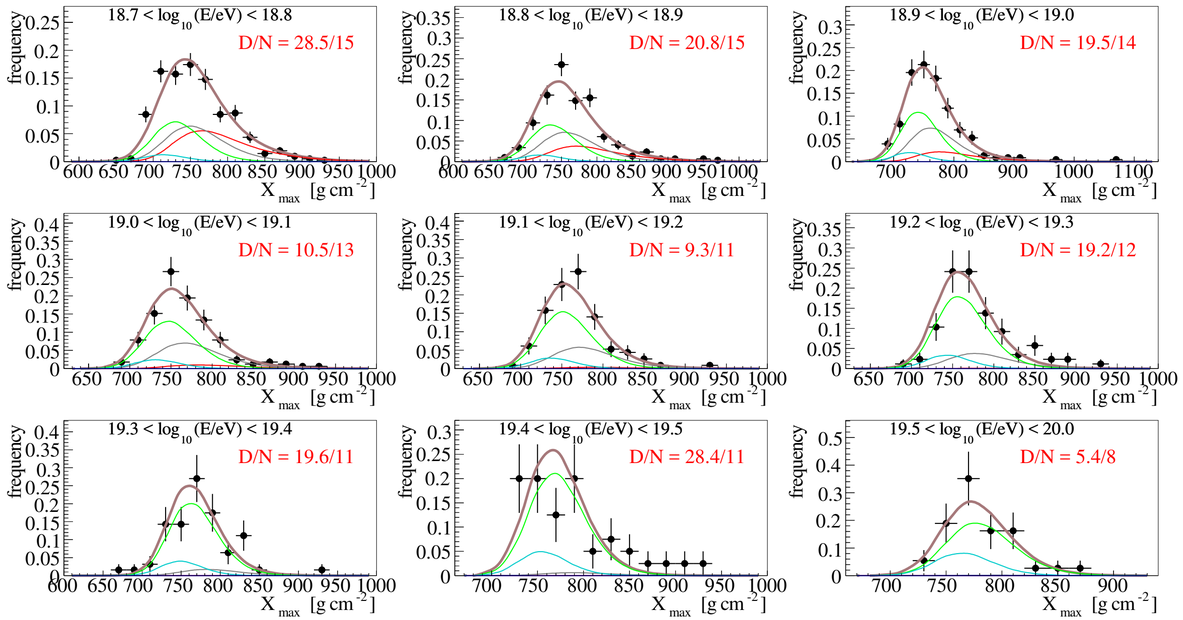

Figure 2. Top: fitted spectra, as function of *reconstructed* energy, compared to experimental coun The sum of horizontal and vertical counts has been multiplied by 10 for clarity. Bottom: the dist butions of $X_{\max}$ in the fitted energy bins, best fit minimum, SPG propagation model, EPOS-LI UHECR-air interactions. Partial distributions are grouped according to the mass number as follo $A = 1$ (red), $2 \leq A \leq 4$ (grey), $5 \leq A \leq 22$ (green), $23 \leq A \leq 38$ (cyan), total (brown).

JCAP04(2017)038

Combined fit of spectrum and composition data as measured by the Pierre Auger Observatory

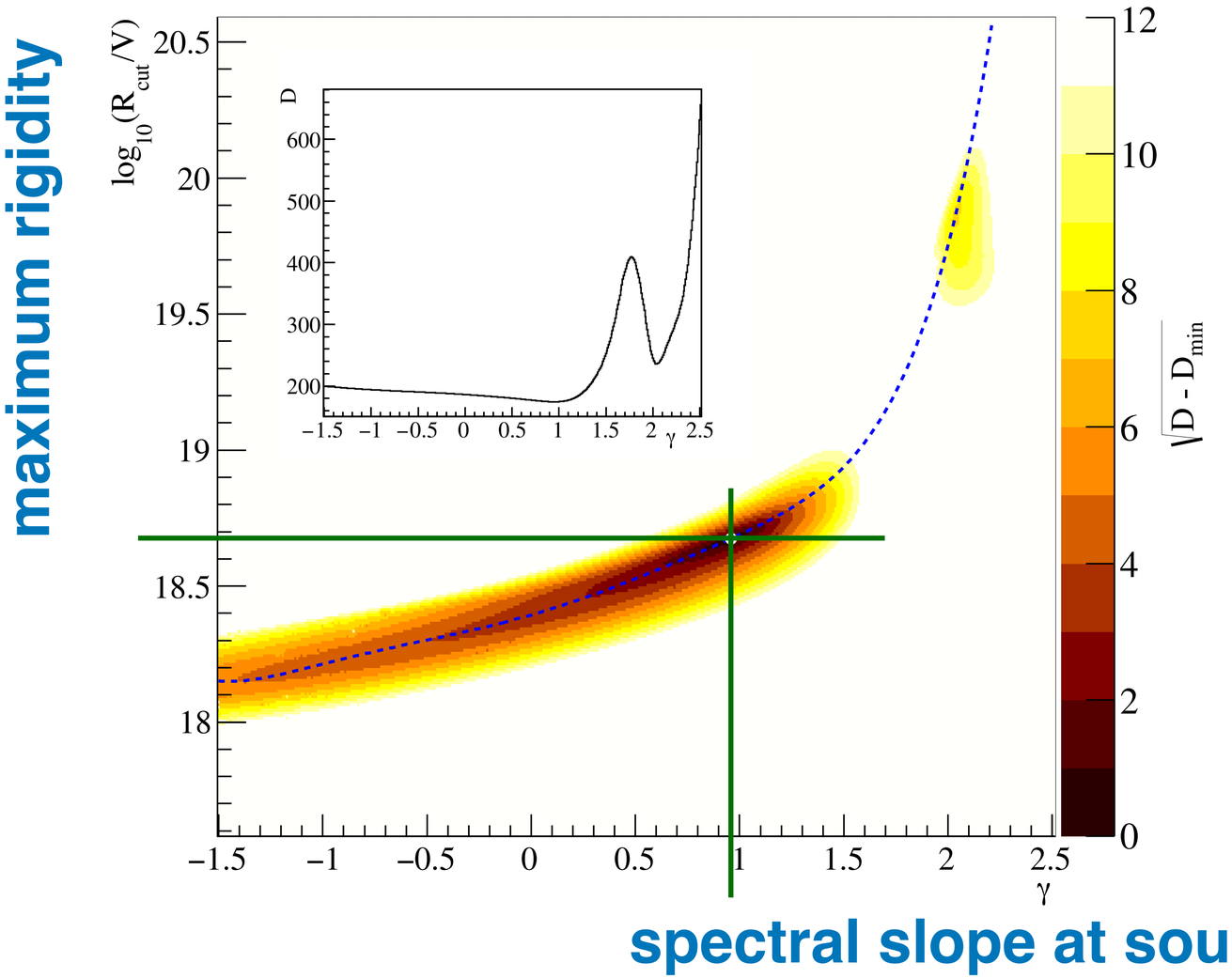

Figure 1. Deviance $\sqrt{D - D_{\rm min}}$, as function of γ and $\log_{10}(R_{\rm cut}/{\rm V})$. The dot indicates the position of the best minimum, while the dashed line connects the relative minima of D (valley line). In the inset, the distribution of $D_{\rm min}$ in function of γ along this line.

JCAP04(2017)038

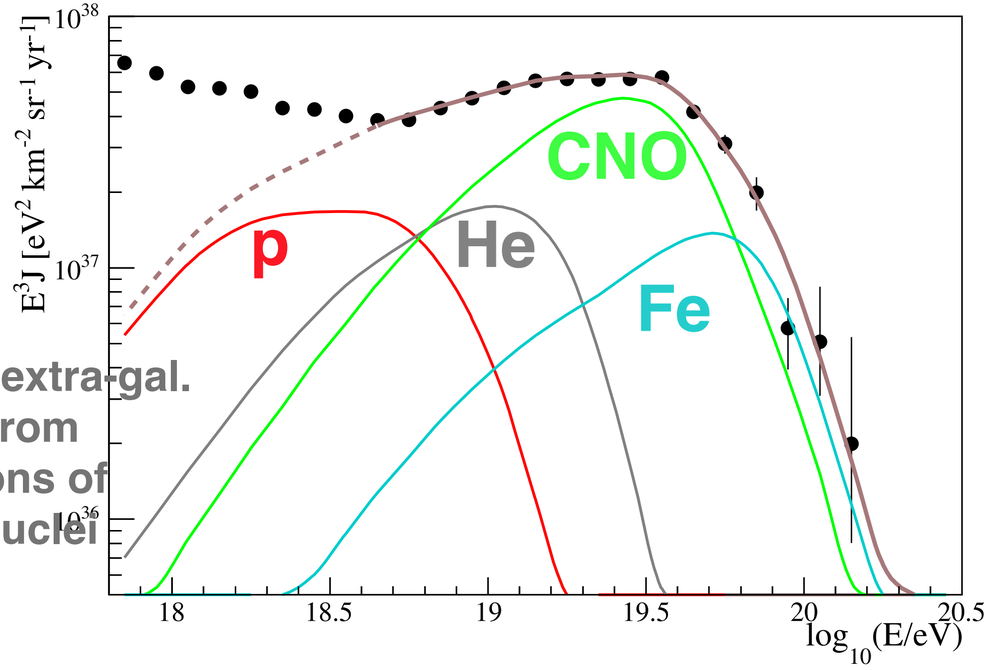

Sub-EeV extra-gal. protons from interactions of heavier nuclei

Combined fit of spectrum and composition data as measured by the Pierre Auger Observatory

$$\begin{aligned} \textbf{p} \quad & A = 1 \\ \textbf{He} \quad & 2 \leq A \leq 4 \\ \textbf{CNO} \quad & 5 \leq A \leq 22 \\ \textbf{Fe} \quad & 27 \leq A \leq 56 \end{aligned}$$

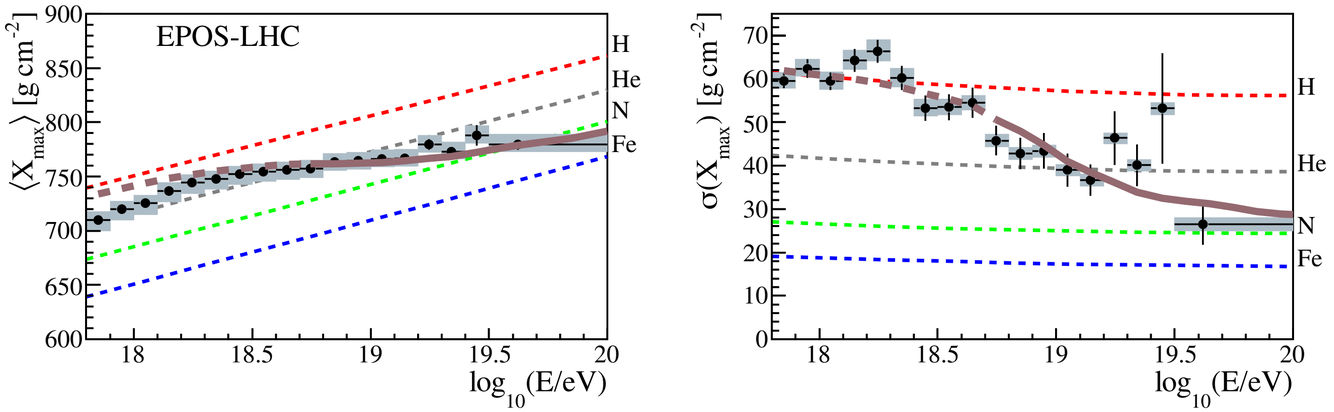

Figure 3. Top: simulated energy spectrum of UHECRs (multiplied by E^3) at the top of the Earth's atmosphere, obtained with the best-fit parameters for the reference model using the procedure described in section 3. Partial spectra are grouped as in figure 2. For comparison the fitted spectrum is reported together with the spectrum in [4] (filled circles). Bottom: average and standard deviation of the $X_{\rm max}$ distribution as predicted (assuming EPOS-LHC UHECR-air interactions) for the model (brown) versus pure ^{1}H (red), ^{4}He (grey), ^{14}N (green) and ^{56}Fe (blue), dashed lines. Only the energy range where the brown lines are solid is included in the fit.

JCAP04(2017)038

PIERRE AUGER OBSERVATORY

Combined fit of spectrum and composition data as measured by the Pierre Auger Observatory

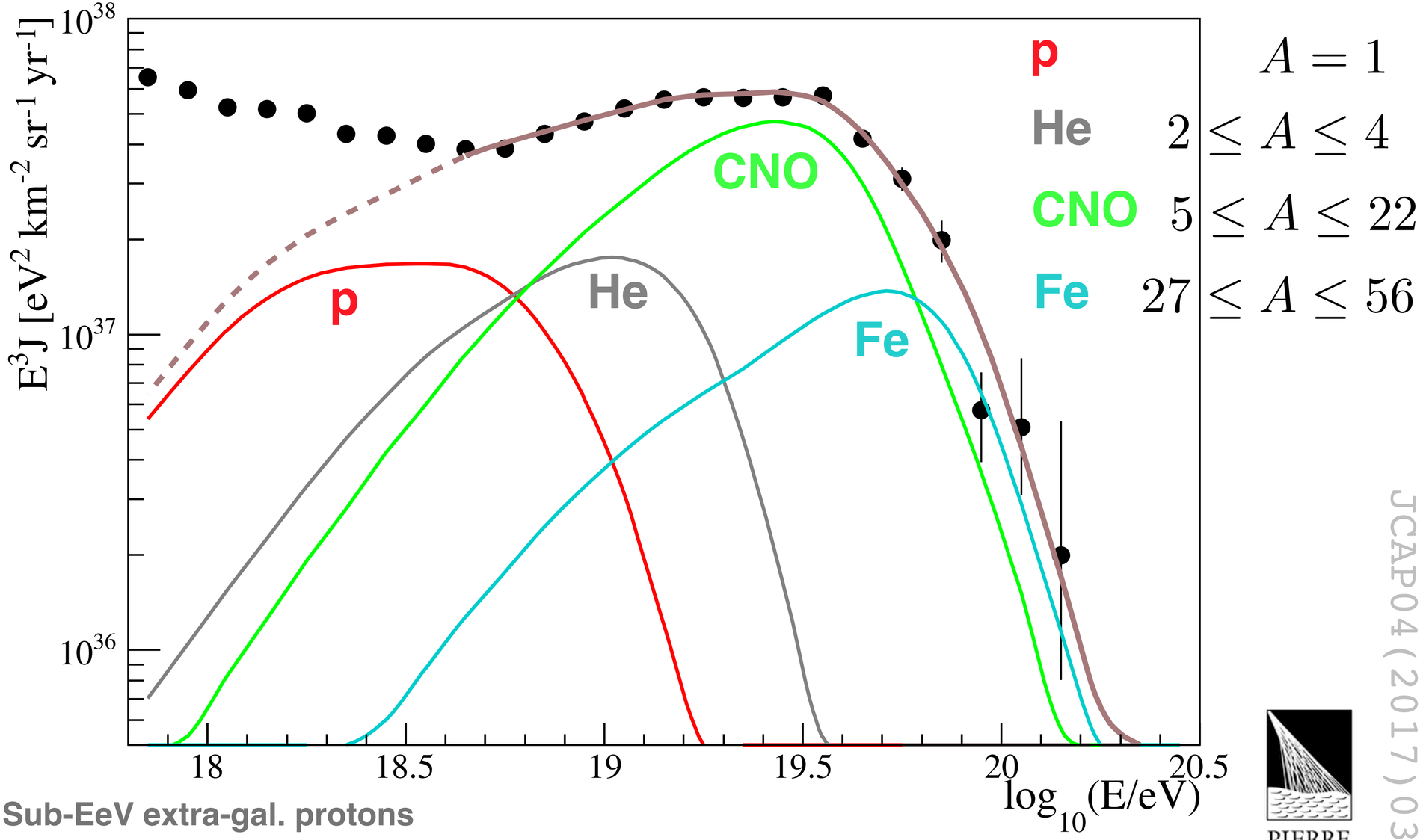

JCAP04(2017)038

Sub-EeV extra-gal. protons from interactions of heavier nuclei

PIERRE
AUGER
OBSERVATORY

Arrival direction

COSMIC RAYS

Observation of a large-scale anisotropy in the arrival directions of cosmic rays above 8×10^{18} eV

The Pierre Auger Collaboration*†

Anisotropy detected at >5.2 sigma
dipole amplitude 6.5%

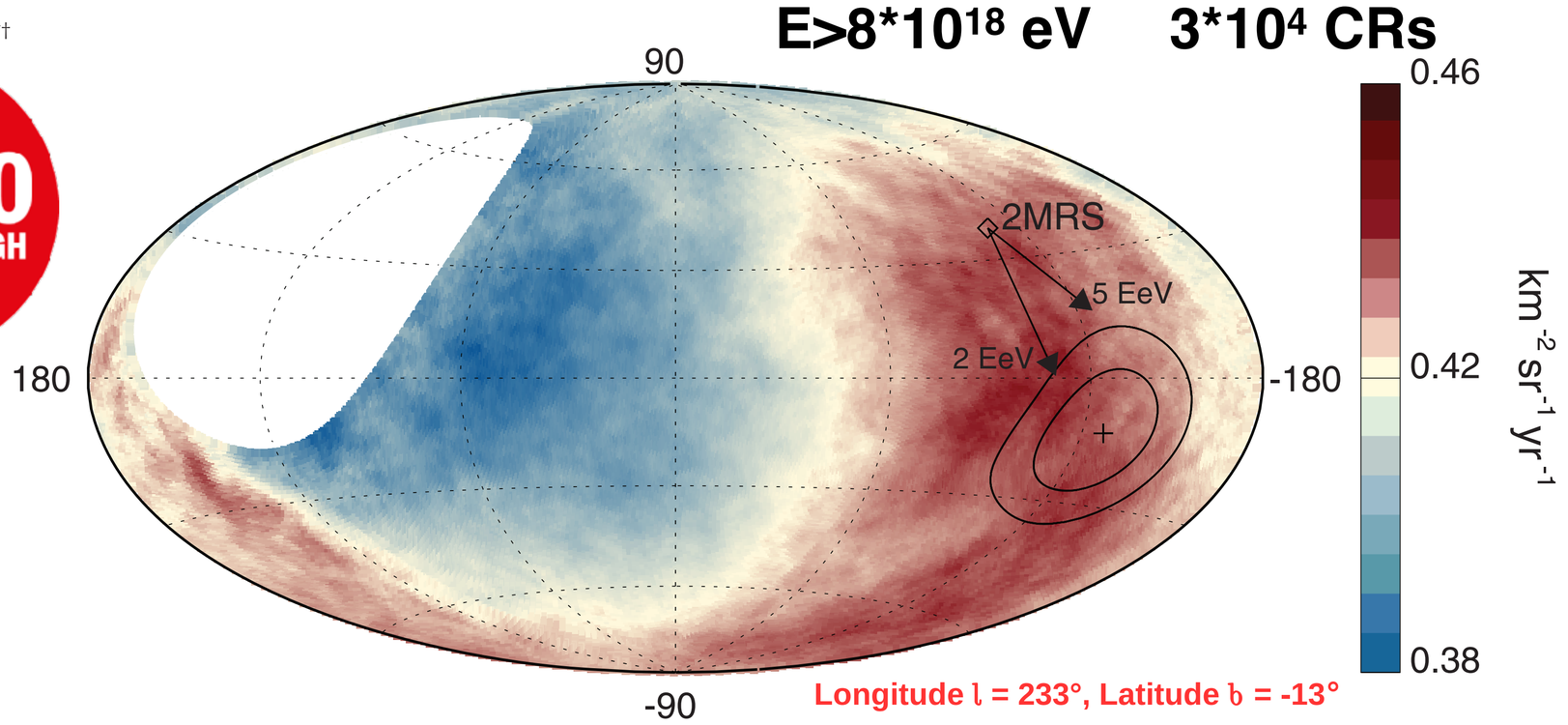

physicsworld TOP 10 BREAKTHROUGH 2017

Fig. 3. Map showing the fluxes of particles in galactic coordinates. Sky map in galactic coordinates showing the cosmic-ray flux for $E \geq 8$ EeV smoothed with a 45° top-hat function. The galactic center is at the origin. The cross indicates the measured dipole direction; the contours denote the 68% and 95% confidence level regions. The dipole in the 2MRS galaxy distribution is indicated. Arrows show the deflections expected for a particular model of the galactic magnetic field (*8*) on particles with E/Z = 5 or 2 EeV.

A. Aab et al., Science 357 (2017) 1266

Sky maps

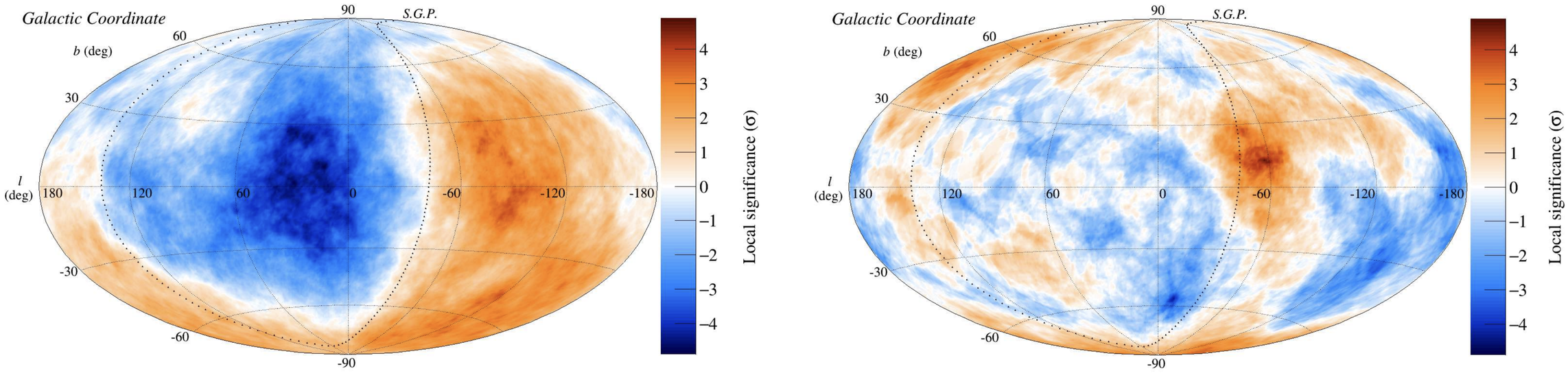

Figure 7

Left: Significance sky-map of 45^o oversamplings of events above the ankle energy. The distribution of UHECR appears to be dipolar with respect to the supergalactic plane, SGP. The dipole is the only significant UHECR anisotropy (6.9σ). *Right*: Significance sky-map of 20^o oversamplings above the cutoff energy. The post-trial significance of the intermediate-scale anisotropies are $\lesssim 4\sigma$. The sky maps are in in galactic coordinates (Fujii et al. 2022).

Journal of Cosmology and Astroparticle Physics
An IOP and SISSA journal

Received: *May 29, 2023*
Revised: *October 5, 2023*
Accepted: *December 2, 2023*
Published: *January 11, 2024*

Constraining models for the origin of ultra-high-energy cosmic rays with a novel combined analysis of arrival directions, spectrum, and composition data measured at the Pierre Auger Observatory

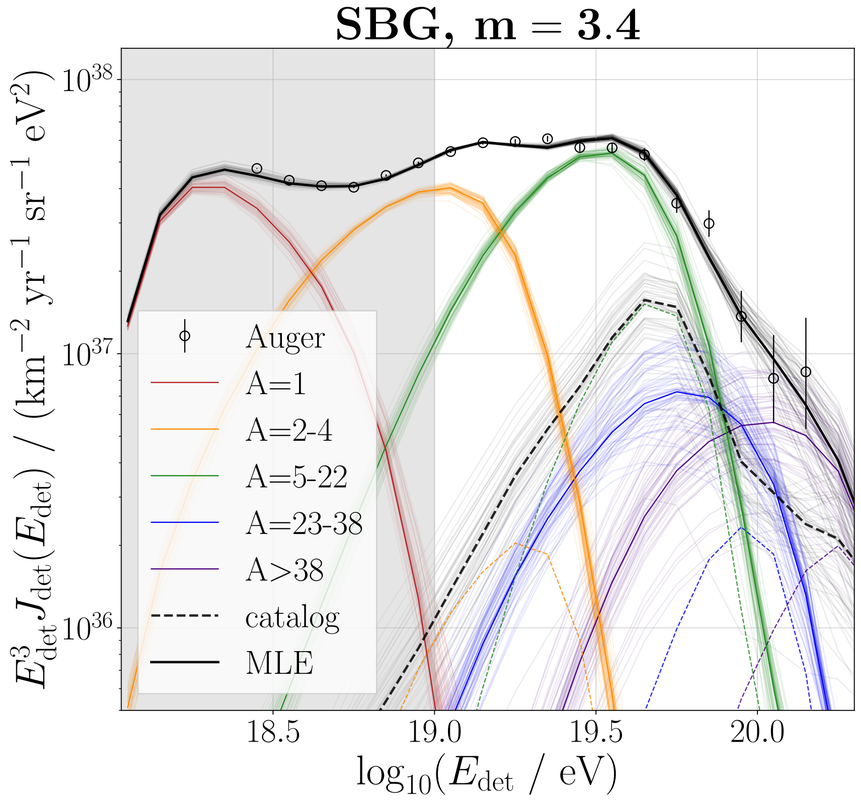

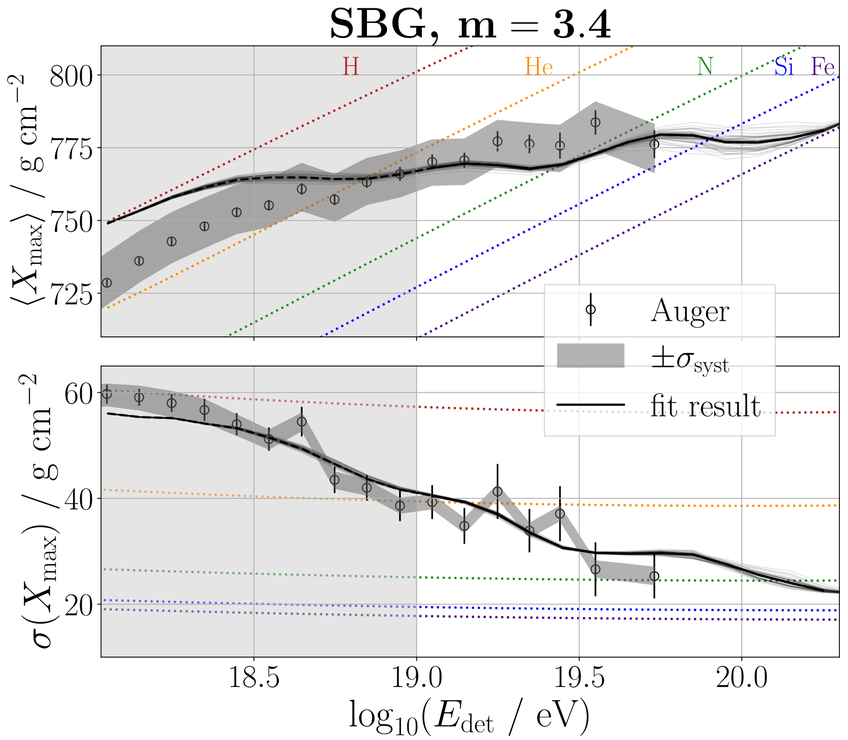

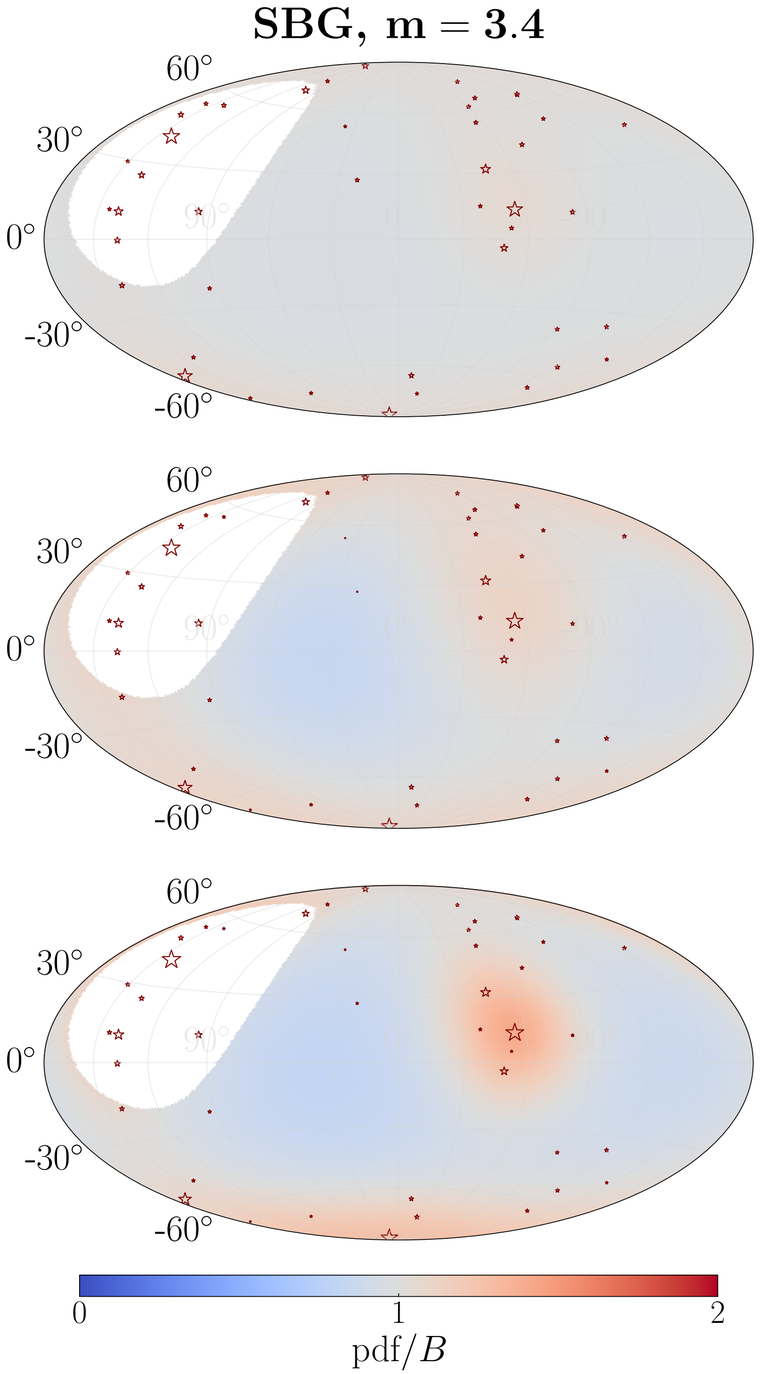

Journal of Cosmology and Astroparticle Physics
An IOP and SISSA journal

Received: *May 29, 2023*
Revised: *October 5, 2023*
Accepted: *December 2, 2023*
Published: *January 11, 2024*

Constraining models for the origin of ultra-high-energy cosmic rays with a novel combined analysis of arrival directions, spectrum, and composition data measured at the Pierre Auger Observatory

We find that a model containing a flux contribution from the starburst galaxy catalog of around 20% at 40 EeV with a magnetic field blurring of around 20° for a rigidity of 10 EV provides a fair simultaneous description of all three observables. The starburst galaxy model is favored with a significance of 4.5σ (considering experimental systematic effects) compared to a reference model with only homogeneously distributed background sources. By investigating a scenario with Centaurus A as a single source in combination with the homogeneous background, we confirm that this region of the sky provides the dominant contribution to the observed anisotropy signal. Models containing a catalog of jetted active galactic nuclei whose flux scales with the γ-ray emission are, however, disfavored as they cannot adequately describe the measured arrival directions.

JCAP01(2024)022

Origin of cosmic rays
multi messenger technique

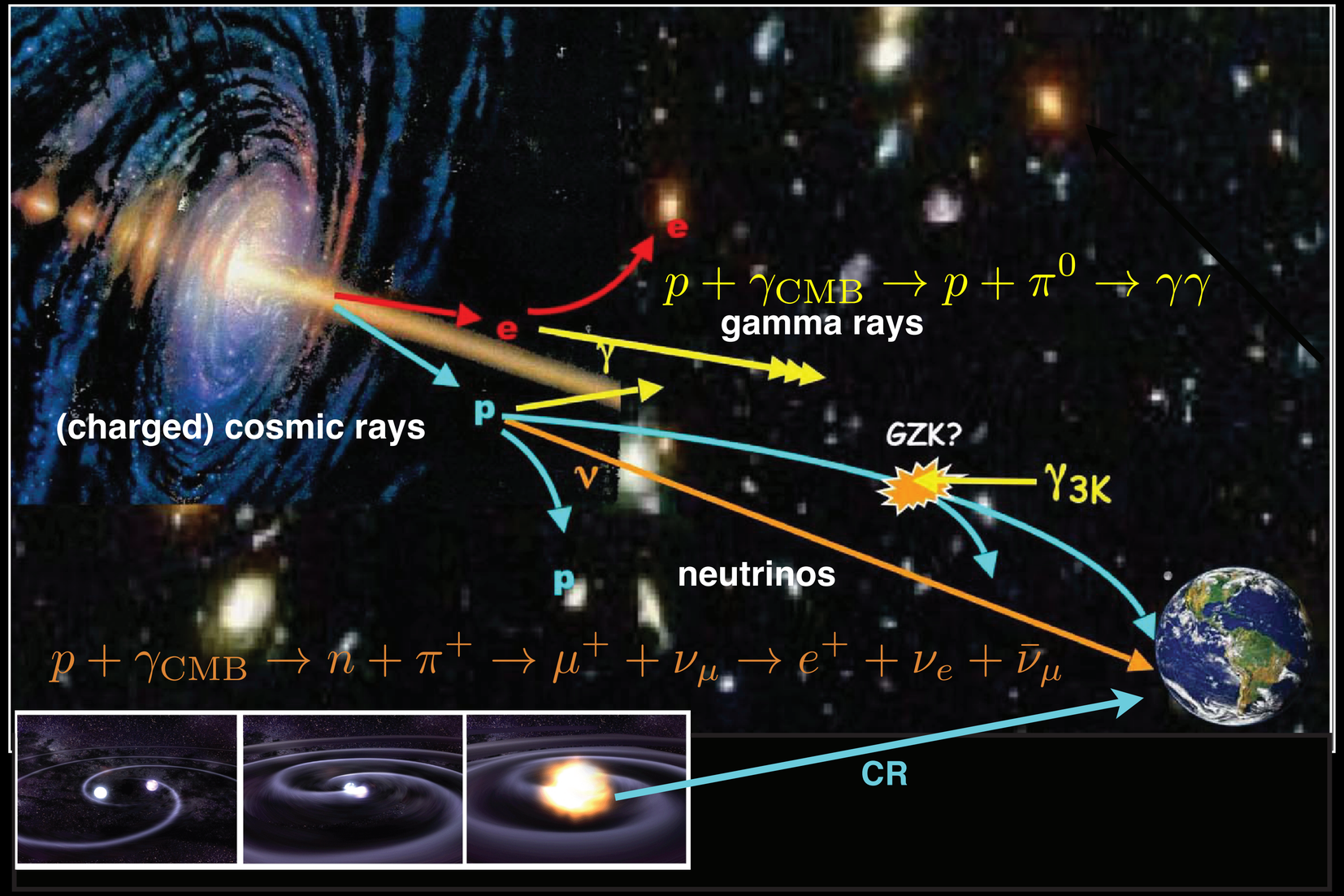

Journal of Cosmology and Astroparticle Physics
An IOP and SISSA journal

Search for correlations between the arrival directions of IceCube neutrino events and ultrahigh-energy cosmic rays detected by the Pierre Auger Observatory and the Telescope Array

JCAP01(2016)037

IceCube

TA

PAO

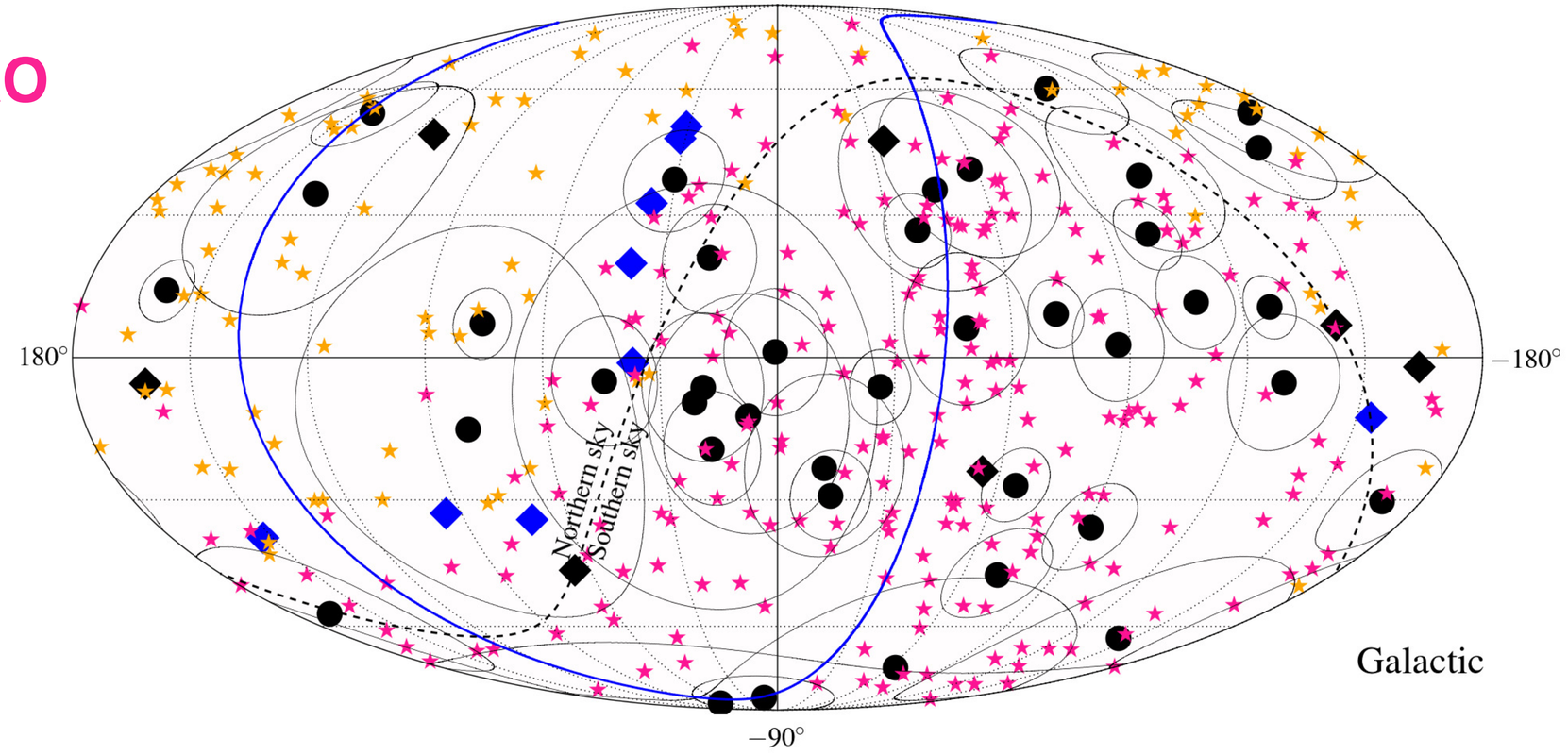

Figure 7. Maps in Equatorial and Galactic coordinates showing the arrival directions of the IceCube cascades (black dots) and tracks (diamonds), as well as those of the UHECRs detected by the Pierre Auger Observatory (magenta stars) and Telescope Array (orange stars). The circles around the showers indicate angular errors. The black diamonds are the HESE tracks while the blue diamonds stand for the tracks from the through-going muon sample. The blue curve indicates the Super-Galactic plane.

Neutrino detection with the Pierre Auger SD

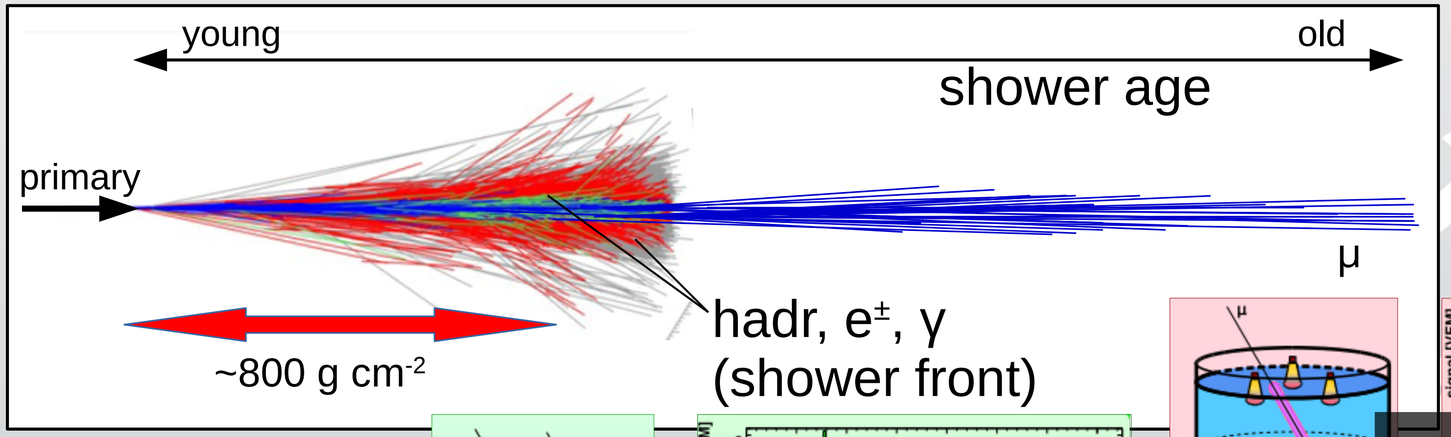

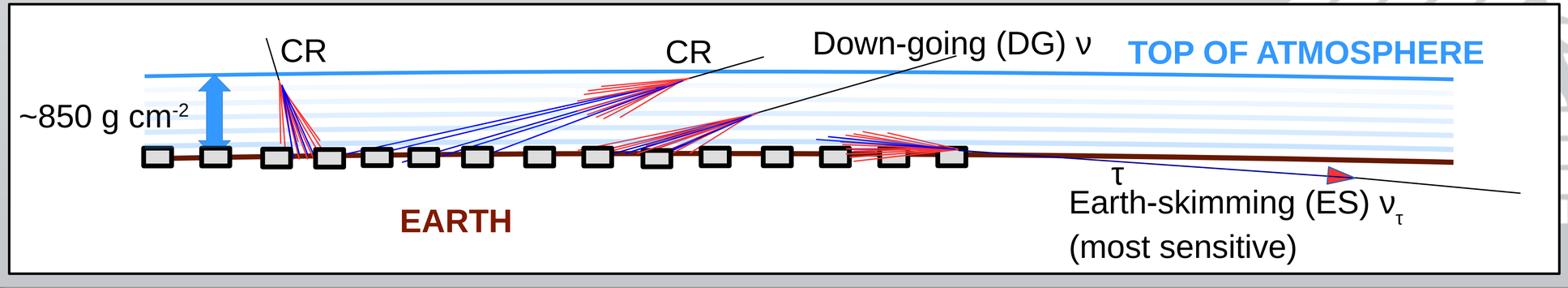

Neutrinos

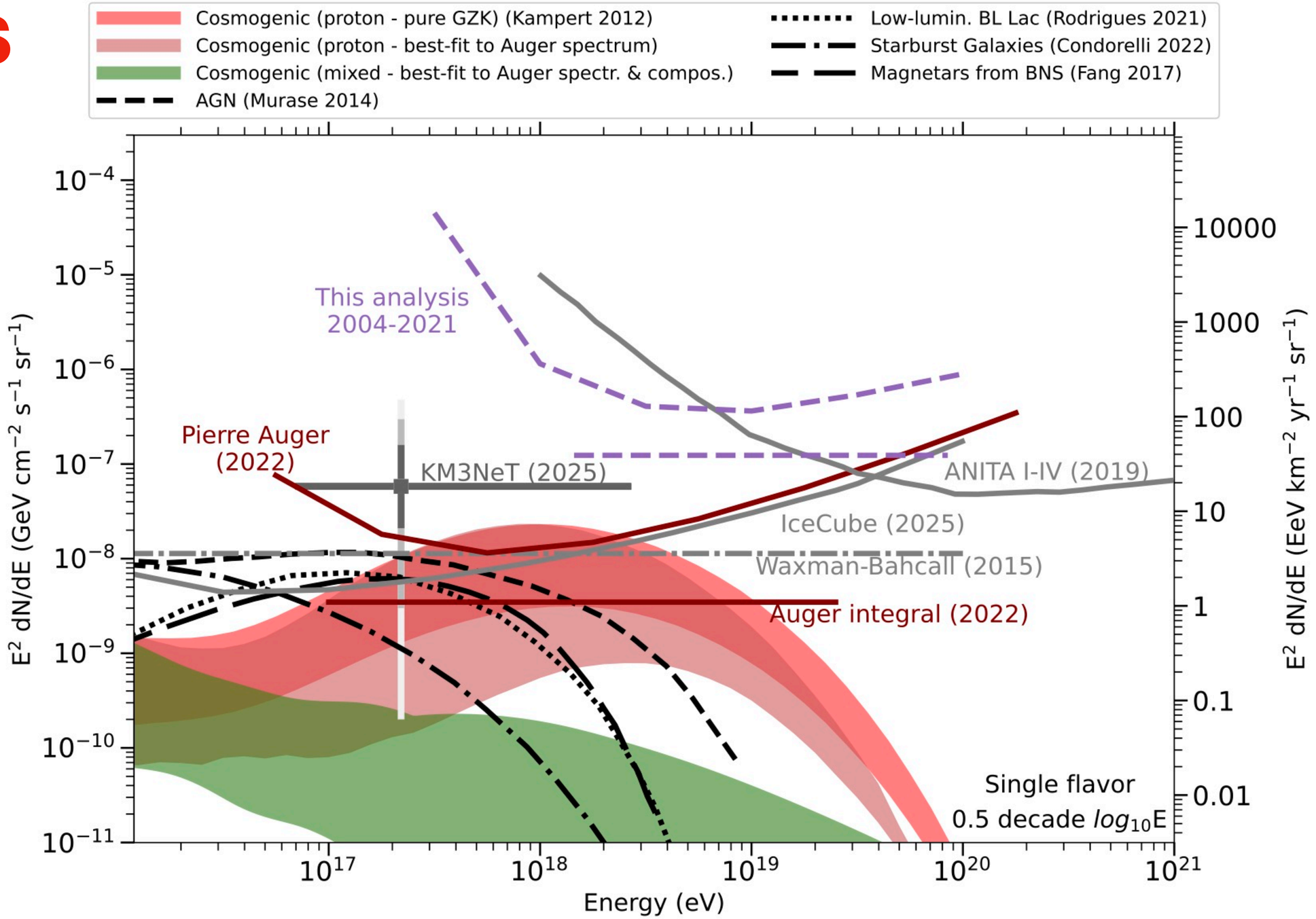
Cosmogenic (proton - pure GZK) (Kampert 2012)
Cosmogenic (proton - best-fit to Auger spectrum)
Cosmogenic (mixed - best-fit to Auger spectr. & compos.)
AGN (Murase 2014)
Low-lumin. BL Lac (Rodrigues 2021)
Starburst Galaxies (Condorelli 2022)
Magnetars from BNS (Fang 2017)
This analysis
2004-2021
Pierre Auger
(2022)
KM3NeT (2025)
ANITA I-IV (2019)
IceCube (2025)
Waxman-Bahcall (2015)
Auger integral (2022)
Single flavor
0.5 decade log10E
E² dN/dE (GeV cm⁻² s⁻¹ sr⁻¹)
E² dN/dE (EeV km⁻² yr⁻¹ sr⁻¹)
Energy (eV)

Gamma rays

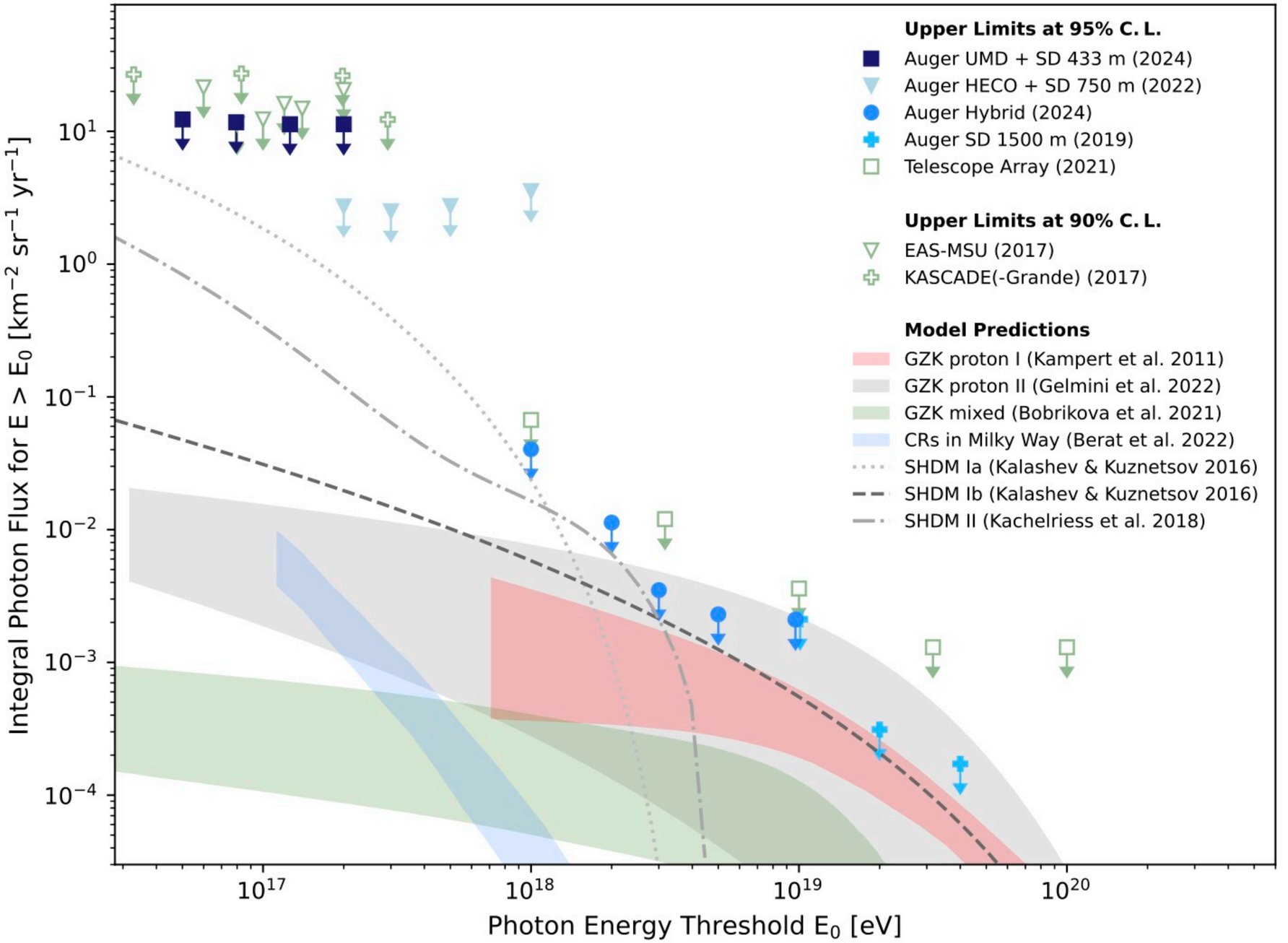
Upper Limits at 95% C. L.
Auger UMD + SD 433 m (2024)
Auger HECO + SD 750 m (2022)
Auger Hybrid (2024)
Auger SD 1500 m (2019)
Telescope Array (2021)
Upper Limits at 90% C. L.
EAS-MSU (2017)
KASCADE(-Grande) (2017)
Model Predictions
GZK proton I (Kampert et al. 2011)
GZK proton II (Gelmini et al. 2022)
GZK mixed (Bobrikova et al. 2021)
CRs in Milky Way (Berat et al. 2022)
SHDM Ia (Kalashev & Kuznetsov 2016)
SHDM Ib (Kalashev & Kuznetsov 2016)
SHDM II (Kachelriess et al. 2018)
Integral Photon Flux for E > E0 [km−2 sr−1 yr−1]
Photon Energy Threshold E0 [eV]

Follow-up of GW170817 with PAO (neutrinos)

Fermi

LIGO

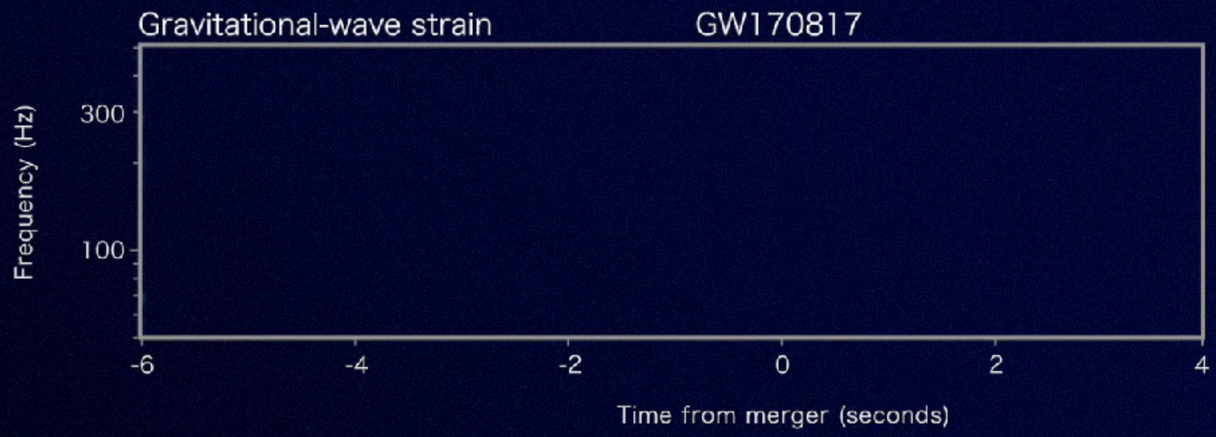

Follow-up of GW170817 with PAO (neutrinos)

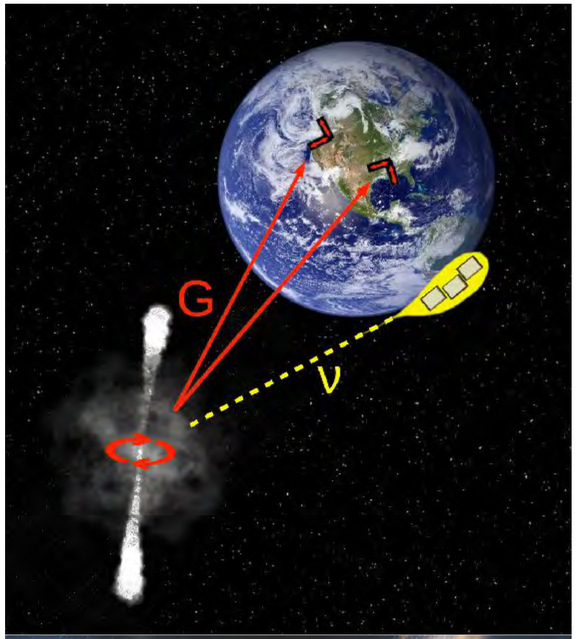

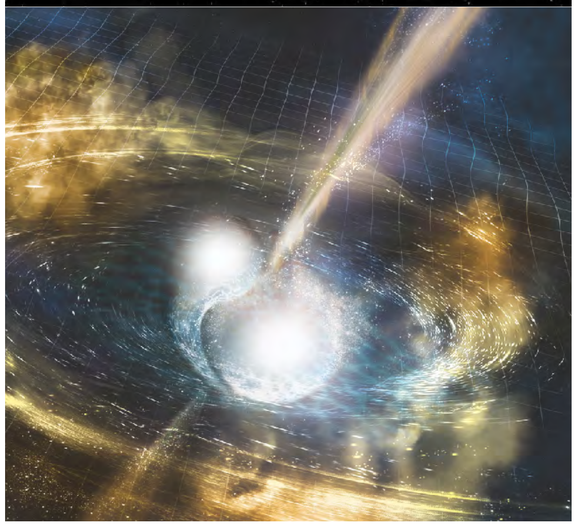

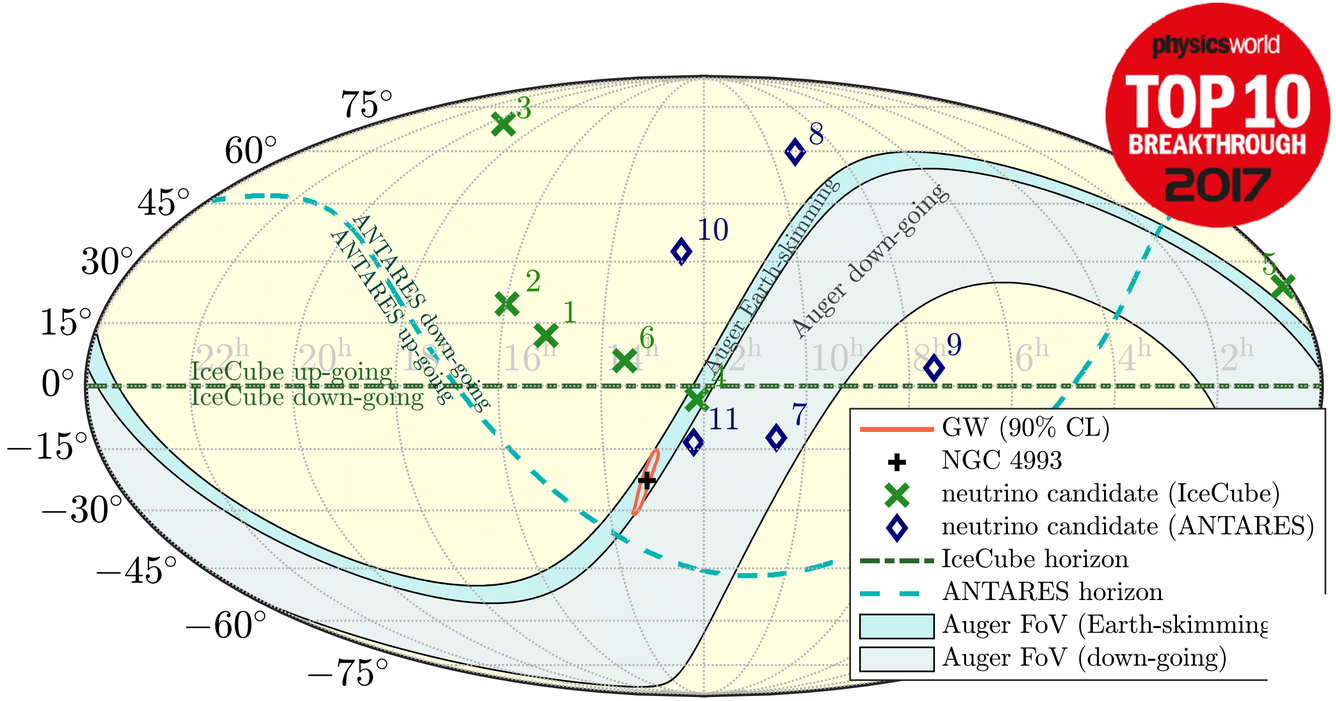

The Astrophysical Journal Letters, 848:L12 (59pp), 2017 October 20 https://doi.org/10.3847/2041-8213/aa91c9

OPEN ACCESS

Multi-messenger Observations of a Binary Neutron Star Merger

LIGO Scientific Collaboration and Virgo Collaboration, Fermi GBM, INTEGRAL, IceCube Collaboration, AstroSat Cadmium Zinc Telluride Imager Team, IPN Collaboration, The Insight-Hxmt Collaboration, ANTARES Collaboration, The Swift Collaboration, AGILE Team, The 1M2H Team, The Dark Energy Camera GW-EM Collaboration and the DES Collaboration, The DLT40 Collaboration, GRAWITA: GRAvitational Wave Inaf TeAm, The Fermi Large Area Telescope Collaboration, ATCA: Australia Telescope Compact Array, ASKAP: Australian SKA Pathfinder, Las Cumbres Observatory Group, OzGrav, DWF (Deeper, Wider, Faster Program), AST3, and CAASTRO Collaborations, The VINROUGE Collaboration, MASTER Collaboration, J-GEM, GROWTH, JAGWAR, Caltech-NRAO, TTU-NRAO, and NuSTAR Collaborations, Pan-STARRS, The MAXI Team, TZAC Consortium, KU Collaboration, Nordic Optical Telescope, ePESSTO, GROND, Texas Tech University, SALT Group, TOROS: Transient Robotic Observatory of the South Collaboration, The BOOTES Collaboration, MWA: Murchison Widefield Array, The CALET Collaboration, IKI-GW Follow-up Collaboration, H.E.S.S. Collaboration, LOFAR Collaboration, LWA: Long Wavelength Array, HAWC Collaboration, The Pierre Auger Collaboration, ALMA Collaboration, Euro VLBI Team, Pi of the Sky Collaboration, The Chandra Team at McGill University, DFN: Desert Fireball Network, ATLAS, High Time Resolution Universe Survey, RIMAS and RATIR, and SKA South Africa/MeerKAT
(See the end matter for the full list of authors.)

Received 2017 October 3; revised 2017 October 6; accepted 2017 October 6; published 2017 October 16

Malargüe, Nc

Follow-up of GW170817 with PAO (neutrinos)

The Astrophysical Journal Letters, 850:L35 (18pp), 2017 December 1 https://doi.org/10.3847/2041-8213/aa9aed

Search for High-energy Neutrinos from Binary Neutron Star Merger GW170817 with ANTARES, IceCube, and the Pierre Auger Observatory

ANTARES Collaboration, IceCube Collaboration, The Pierre Auger Collaboration, and LIGO Scientific Collaboration and Virgo Collaboration

PAO in pre-defined +/- 500 s window as sensitive as IceCube

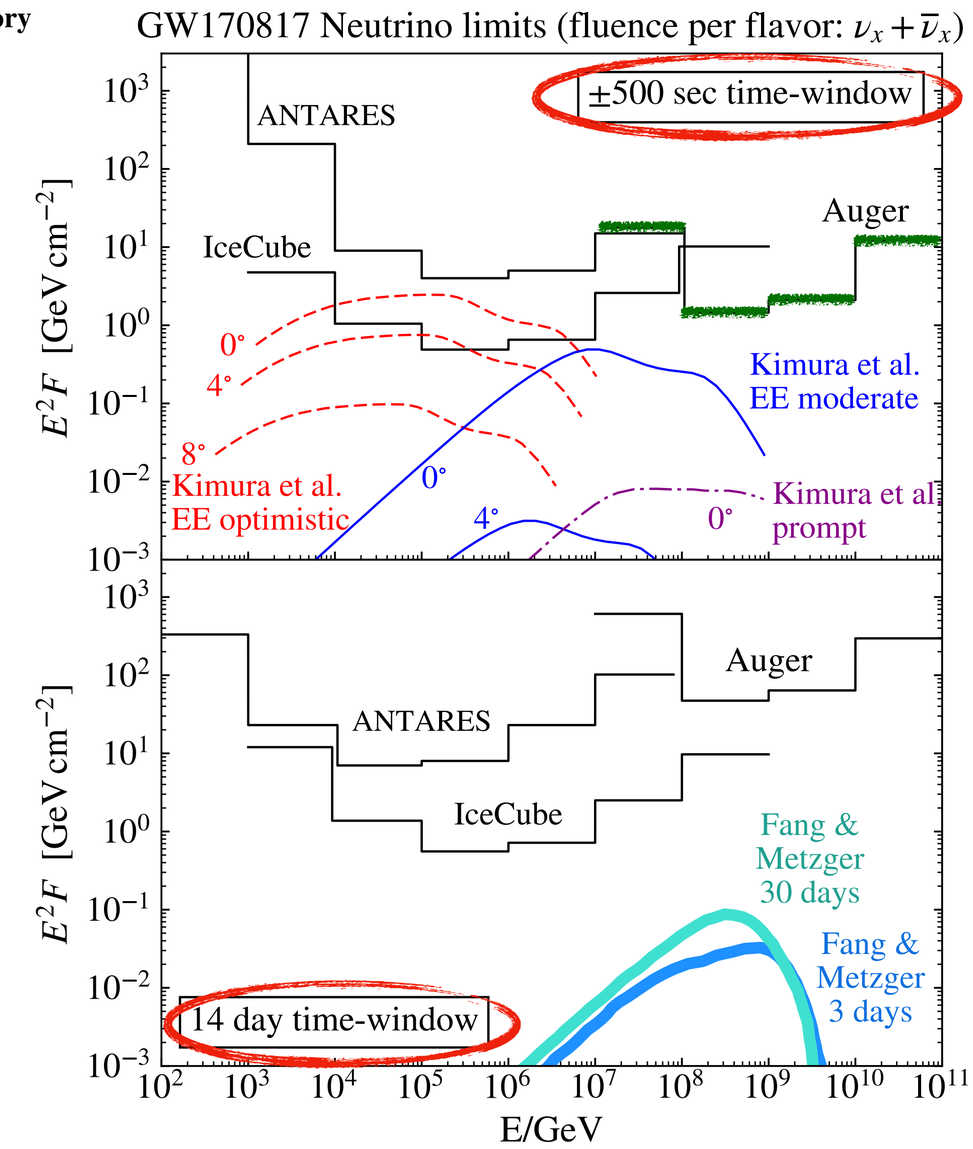

Pierre Auger Observatory - upgrade

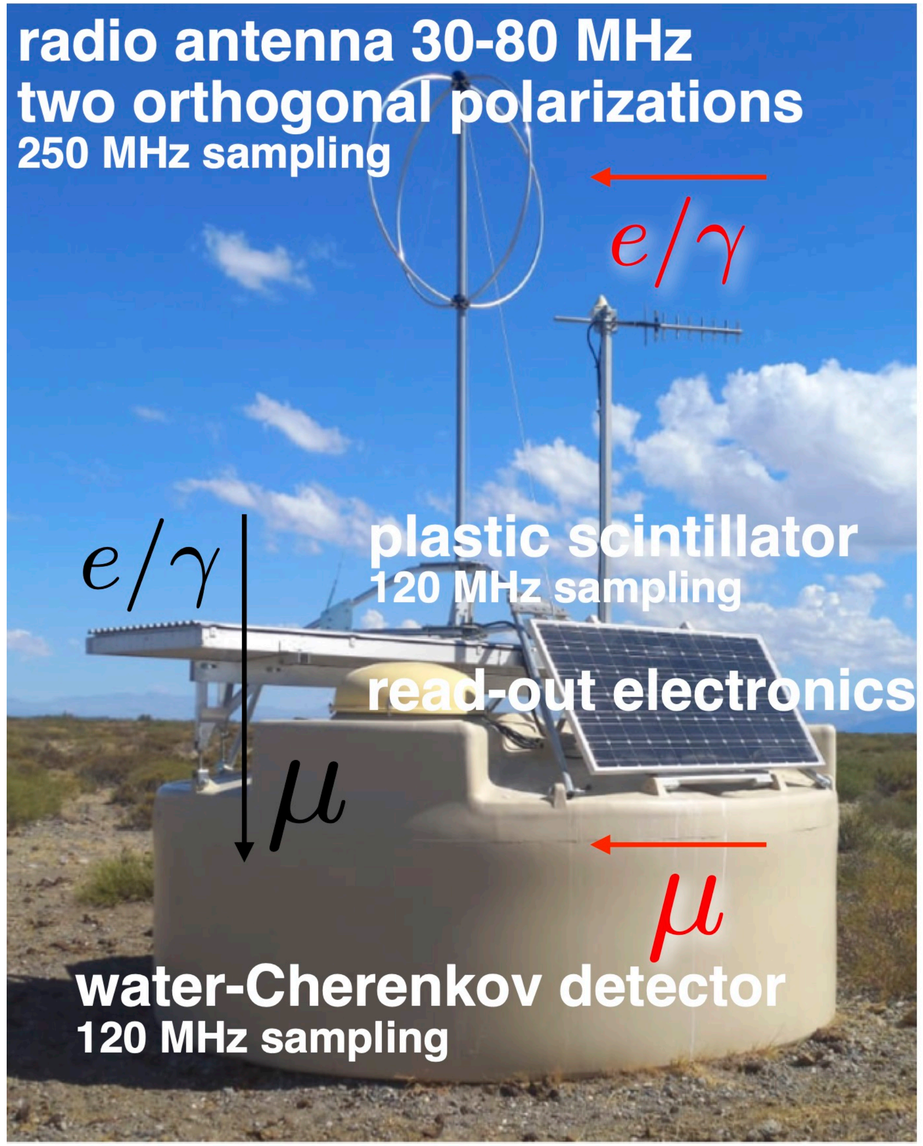

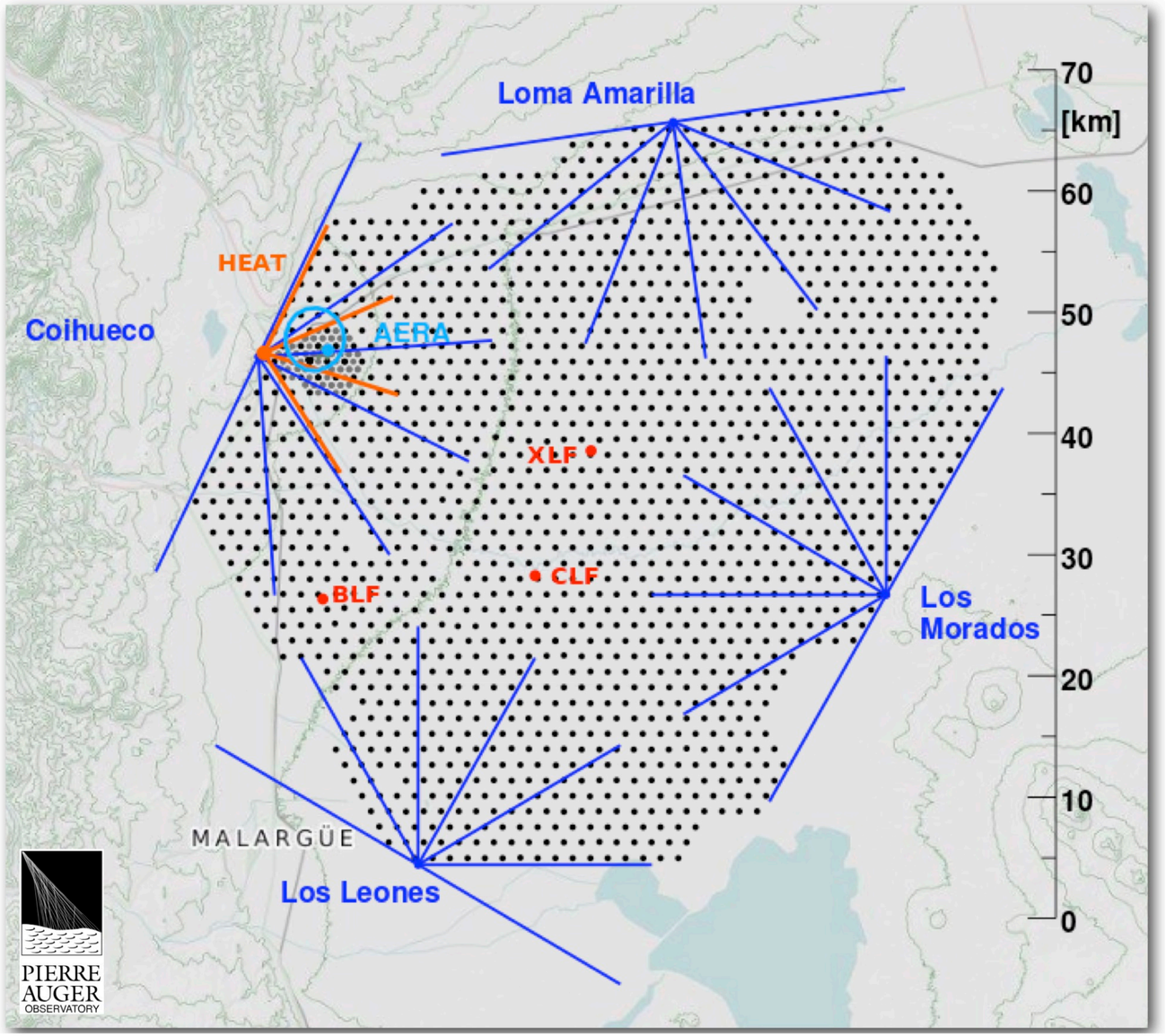

A measured air shower

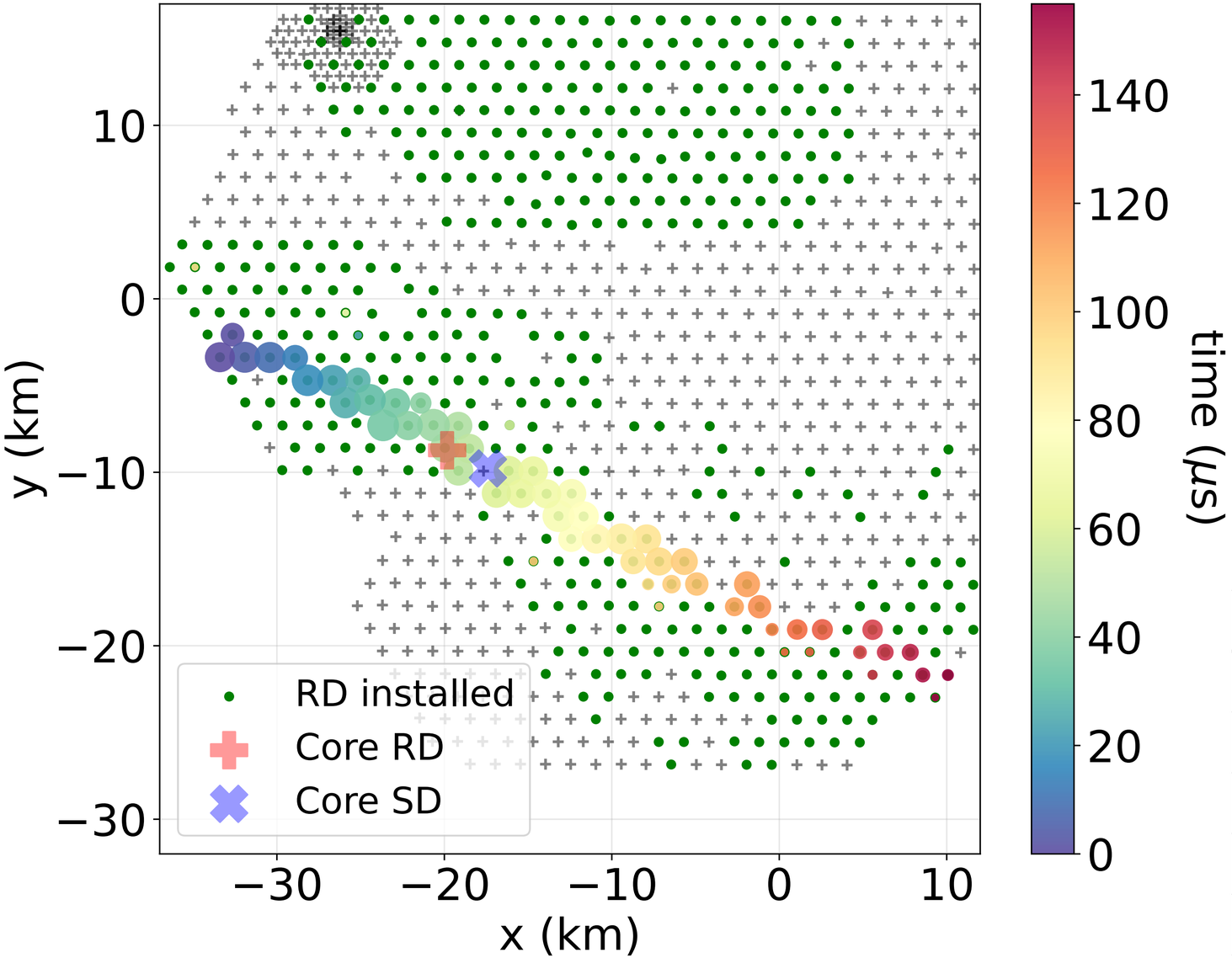

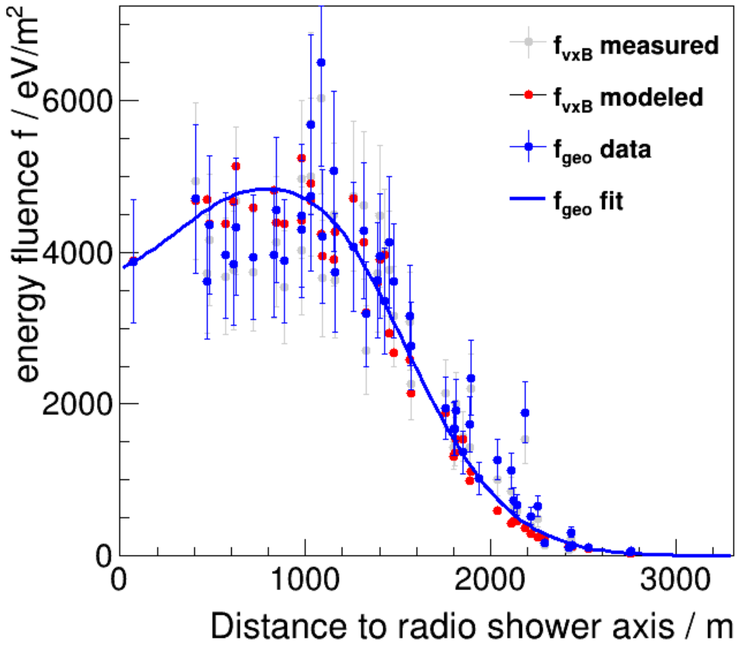

	RD	WCD
Azimuth (deg)	156.99±0.01	157±0.1
Zenith (deg)	84.7±0.01	84.7±0.1
Energy (EeV)	36.23 ± 3.34	38.55 ± 2.92
Core X (km)	-19.8	-17.40±0.88
Core Y (km)	-8.73	-9.78±0.45

Deflection of CRs in Galactic B-field

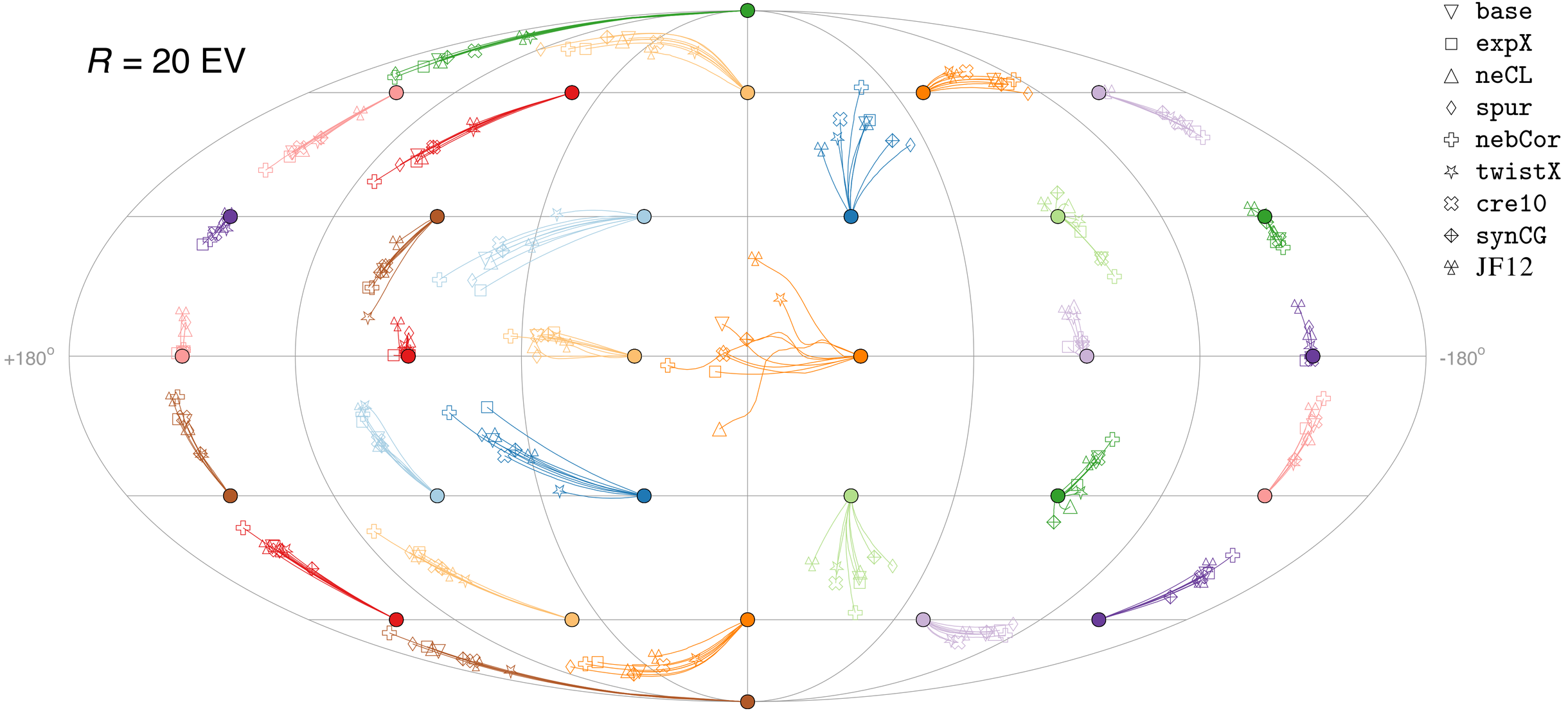

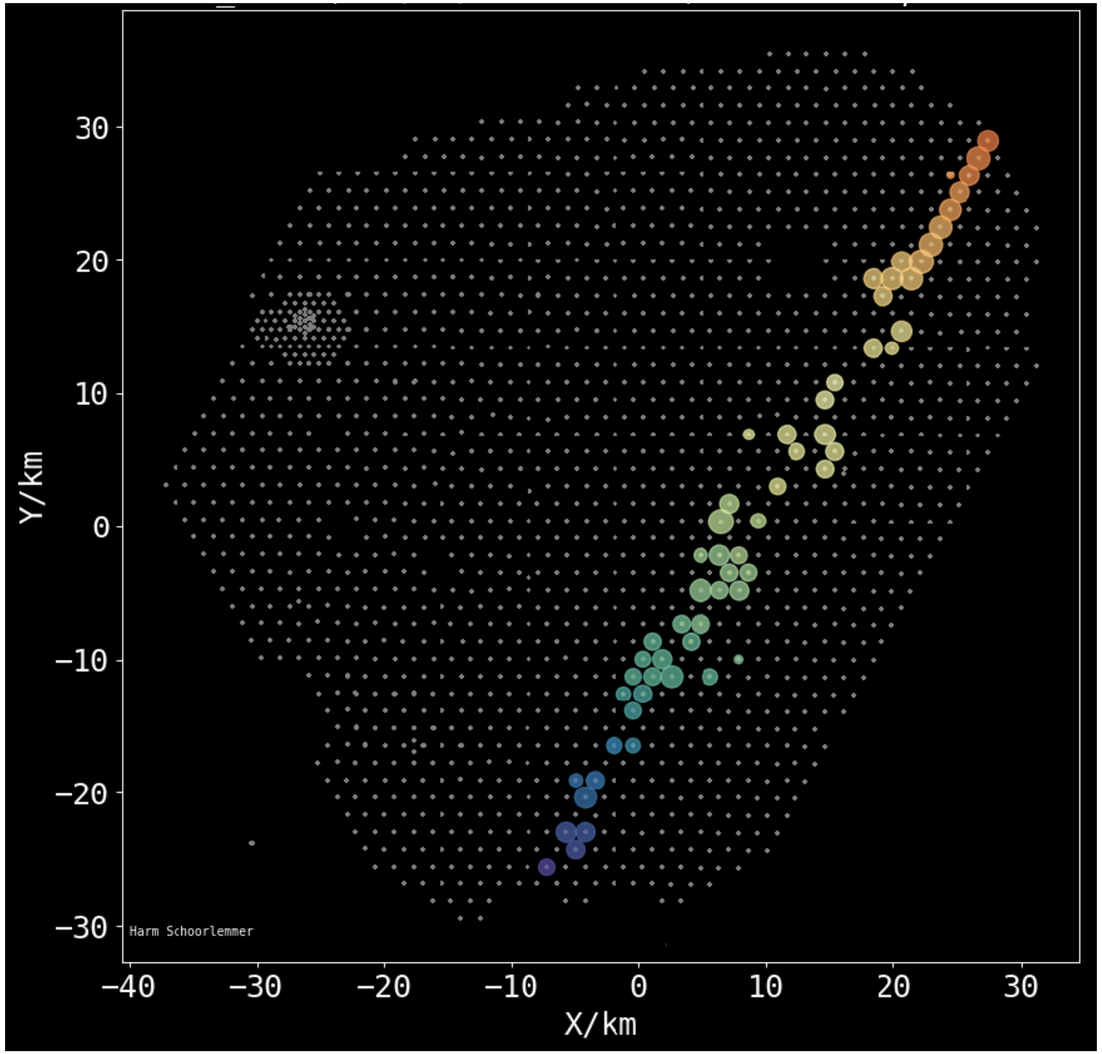

Figure 11: Measured HAS arriving 0.5° above the horizon. The footprint has a length of ∼65 km, crossing the complete array. The energy reconstructed form the RD is 52 EeV.